Statistics of intrinsic alignments and weak lensing

Federica Capranico

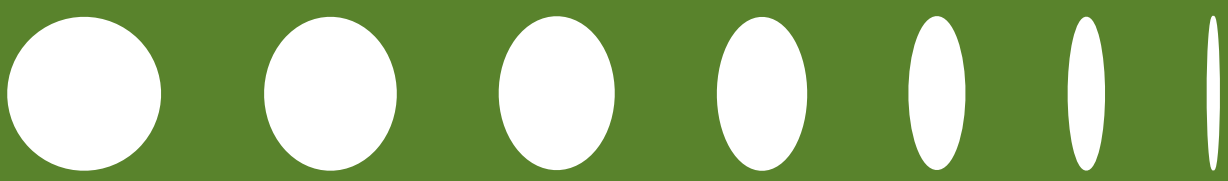

Dissertation
submitted to the
Combined Faculties of the Natural Sciences and
Mathematics
of the Ruperto-Carola-University of Heidelberg. Germany
for the degree of
Doctor of Natural Sciences

Put forward by
Federica Capranico
born in: Turin, Italy
Oral examination: 25 July 2013

Statistics of Intrinsic Alignments and Weak Lensing

Referees: Prof. Dr. Björn Malte Schäfer
Prof. Dr. Luca Amendola

To what I have lost, to what I have found.

ABSTRACT

The content of this work is two-fold. In the first part we present a study on the contamination of the intrinsic alignments to weak lensing measurements in the future survey Euclid. On the grounds of the tidal torque theory, we have adopted from the literature two related prescriptions for modeling the intrinsic alignment signal and computed for both the resulting biases in the cosmological parameters. We find a slight discrepancy among the two models, which both significantly (up to $> 3\sigma$) contaminate the estimates for Ω_m and σ_8. The other parameters h, n_s and w appear less affected. In the second part we present results based on an innovative statistical approach, the extreme value statistics. We investigate up to which level the primordial non-Gaussianities parameters $f_{\rm NL}$ and $g_{\rm NL}$ inherited by the bi- and trispectra of the weak lensing convergence can be constrained by the most extreme values of the convergence field. We find constraints of the order of 10^2 for $f_{\rm NL}$ and 10^5 for $g_{\rm NL}$ if individual extreme values are considered, therefore sadly showing only a relatively weak constraining power.

Meine Dissertation beschäftigt sich mit zwei Themen. In dem ersten Teil untersuche ich die Kontamination von Daten des schwachen Linseneffekts durch intrinsische Formkorrelationen von Galaxien für die Euclid-Mission. Die Beschreibung der intrinsischen Korrelationen basiert auf Modellen, bei denen die Galaxien ihren Drehimpuls durch Gezeitenwechselwirkungen mit der kosmischen großskaligen Struktur. Ich schätze den Fehler ab, der bei der Bestimmung kosmologischer Parameter auftritt. Obwohl es eine kleine Diskrepanz zwischen den Modellvorhersagen gibt, sind bei beiden Modellen die Messungen von Ω_m und σ_8 auf dem Niveau von $> 3\sigma$ beeinflusst, während andere Parameter wie h, n_s und w schwächer beeinflusst werden. Im zweiten Teil untersuche ich eine innovative Technik, mittels der Extremwertstatistik des schwachen Linseneffekts Einschränkungen auf die inflationären Nicht-Gaussianitätsparameter $f_{\rm NL}$ und $g_{\rm NL}$ zu gewinnen. Die Sensitivität ist von der Größenordnung 10^2 für $f_{\rm NL}$ und 10^5 für $g_{\rm NL}$, wenn individuelle Extremwerte herangezogen werden, was leider hinter anderen Methoden zurückbleibt.

Contents

List of Figures

LIST OF ACRONYMS

GR General Relativity

CMB Cosmic Microwave Background

CDM Cold Dark Matter

LSS Large Scale Structure

BBN Big Bang Nucleosynthesis

IA Intrinsic Alignments

LPT Lagrangian Perturbation Theory

EPT Eulerian Perturbation Theory

TTT Tidal Torque Theory

CKB Catelan, Kamionkowski, Blandford

CNPT Crittenden, Natarajan, Pen, Theuns model

MWK Mackey, White, Kamionkowski model

EVS Extreme Value Statistics

PDF Probability Distribution Function

GEV Generalised Extreme Value distribution

GDP Generalised Pareto Distribution

NG Non-Gaussianities

MOTIVATION

Our current knowledge about cosmology is the sum of the work and motivation prompted by the curiosity and commitment of thousands of scientists throughout almost one century (one century if we consider just cosmology!). This sum can be summarised in the current paradigm for the Universe, the ΛCDM model, for which the Universe started from a Big Bang, cooled and diluted due to its expansion, slowly having the chance to build itself up from the most basic building blocks: particles and atoms. After a long way lasted almost 14 billion years, today we can admire the result of such an intricate and complex development under the guise of very diverse objects ranging from planets, stars, galaxies, and large scale structure in general to the CMB. The Universe is thus a unique and single laboratory, in which we find combined all the physics from microscopical to macroscopical scales.

This work, which is two-fold, straddles the very early history and the present of the Universe, aiming to give a contribution in answering questions such as: What gave start to the inflationary early epoch of the Universe which created the seed fluctuations that we believe have grown up to becom the galaxies, clusters of galaxies and large scale structure we see today? And furthermore: how did galaxies form? Are we able to give a picture of this formation consistent with the ΛCDM? Are ellipticals and spirals completely different and unrelated families of galaxies? What are the physical processes intervening in the formation of a galaxy and its angular momentum?

In Chapter 1 we review the fundamental observations and theoretical tools leading to the current ΛCDM paradigm describing the Universe. We summarise the fundamental epochs the Universe is believed to have undergone and we finally describe in more detail the formation of the structure. This gives us a background to study the formation of the galaxies, topic upon which we dwell in Chapter 2. There, we address in more detail different possible scenarios, consistent with ΛCDM paradigm, of formation of both elliptical and spiral galaxies, particularly focussing on one aspect of galaxy formation: the source of their rotation. We discuss how ellipticals and spiral galaxies intrinsically differ in how their rotation is supported. The deep understanding of these processes has noticeable consequences also concerning the question of whether spiral and elliptical galaxies simply represent different stages of the life of a galaxy which, by

evolving and interacting with the surroundings and with other galaxies, experiences processes (such as mergers) able to drastically modify its morphological and physical features. Stress is put specifically on the Lagrangian description of the tidal torque theory which, being characterised by the interplay between short and long-ranged processes driven respectively by inertia and tidal shear tensors, reveals the double nature - local and non-local - intervening in the ultimate determination of the spin, and currently offers a very good understanding of the reasons for the induced rotation in spiral galaxies.

The key role played by the tidal shear tensor is even more far-reaching, since its long-ranged nature leads to its ability to mould not only one galaxy at a certain position, but also other galaxies in the close surroundings. Acting as a parent, the tidal shear imprints its features in its off-spring: the "sibling" neighbouring galaxies, whose similarities encode this common origin and show up in a correlation among their shapes. This correlation goes by the name of *intrinsic alignments*, and is thoroughly discussed in Chapter 3. We discuss the leading role of tidal correlation lengths in shaping both early- and late-type galaxies alignments and we present the current models used for linking the ellipticity to the second derivatives of the potential: the quadratic model for spiral galaxies, in which the ellipticity is proportional to the square of the tidal shear, and the linear model for elliptical galaxies, whose ellipticity is considered to scale linearly with the tidal tensor. In the framework of the quadratic model, we describe more in detail two prescriptions used in literature (which we will refer to as the *CNPT* and *MWK* models Crittenden et al., 2001; Mackey et al., 2002).

We furthermore discuss in both Chapters 2 and 3 the prominent role of numerical simulations in confirming and validating the tidal torque theory, by reproducing the typical scaling relations with mass and time it predicts for the angular momentum, and by investigating its efficacy in producing intrinsic alignments able to be tracked back to the gravitational tidal tensor. In this direction N-body simulations appear to be essential to investigate the difficult grounds of non-linearities which evolution of galaxies certainly introduces and which are expected to play an important role in the determination of the final spin of a galaxy and hence also the intrinsic alignments signal. The reason for deepening numerical simulations is even more reinforced by the fact that non-linearities constitute a complicated task to be achieved analytically, although studies have also been made in this direction.

Weak lensing represents the essential node between the two parts in which this thesis is developed, and constitutes the grounds of this work. On the one hand, cosmic shear produces a distortion in the images of background sources, therefore inducing a statistical correlation among the observed images which can be easily mimicked by intrinsic correlations, which are also capable to produce such correlations but upon a physically different process, as already mentioned. Intrinsic correlations, accounting for $\sim 10\%$ of the cosmic shear signal, therefore constitute a severe contaminant to weak lensing. Mostly in this era of high-precision surveys, such as Euclid, which aim to measure the weak lensing

signal up to 1% accuracy, intrinsic alignments can jeopardise our ability of pinpointing cosmological parameters from weak cosmic shear. On the other hand, since the weak lensing essentially provides a measurement of the density field of the visible Universe, the convergences measured therefrom are expected to be distributed according to a probability distribution which reflects the probability distribution of the density. Both non-linear evolution on large scales and primordial non-Gaussianities are thought to be possible sources of any departure from the original Gaussian shape of this distribution, and to yield to a weakly non-Gaussian distribution of the convergence, which would then be asymmetric and thus able to enhance the probability of extreme events or, equivalently, the tails of the distribution. This statistical feature of the convergence distribution can be conveniently exploited by analysing the occurrence of such extreme values with the Extreme Value Statistics. These are the grounds for our investigations, whose core is contained in Chapters 5 and 8, which reproduce the articles Capranico et al. (2012) and Capranico et al. (2013) respectively.

A description of the physical processes inducing weak lensing and the reasons why intrinsic alignments constitute a contamination to this signal are discussed in Chapter 4, where we address the basics of gravitational lensing. We include a description of tomographic weak lensing, technique nowadays broadly used due to the enhancement in the amplitude of the signal it produces. In this context we show the results we have obtained by applying the tomography technique to intrinsic ellipticities modelled with the CNPT prescription, confirming how and quantifying how much the tomographic approach can lead to significant improvement in results.

In Chapter 5 we show how, by means of a Fisher matrix analysis, we can give an estimation of the biases on the cosmological parameters which would be caused by not including the intrinsic alignments contribution to theoretical weak lensing signal used to model the data. We consider only late-type galaxies and therefore restrict ourselves on the framework given by the quadratic modelling of intrinsic alignments, thereby comparing the effectiveness of CNPT and MWK models in describing the physics intervening in the formation of intrinsic ellipticities. We compare these results with some of the other analyses conducted in literature.

The description of the methods and physics used for the second part of this thesis starts in Chapter 6, which provides a basic toolkit for an appropriate understanding of the statistics of extremes. Extreme Value Statistics is a relatively new tool to cosmology, and appears to be very powerful mostly when applied to distributions which enhance the probability of the tails of the ditributions, such as asymmetric distributions and, very generically speaking, distributions deviating from Gaussianity. In order to describe why we would expect physically to encounter in cosmology such statistical distributions, we put emphasis, in Chapter 7, on the primordial type of non-Gaussianities (which, we repeat, provide just one of the possible ways of recovering non-Gaussianity), which we address in our work concerning extreme values. We begin with an initial discussion

about inflation, and then continue by incorporating a general description about different models for primordial non-Gaussianties. Chapter 8 shows our results on extreme values and concludes all our analyses. By modelling the distribution of the convergences with a Gram-Charlier distribution, we sample from this distribution obtaining the distributions of maxima and minima both numerically and analytically. We show how the latter tend to a specific distribution, the Gumbel distribution, for larger and larger values of the number of samples, and we study the dependence of the position and shape of the extreme distributions for the case of inflationary non-Gaussianities on the number of available samples. Finally, we attempt to find the constraints on the non-Gaussianity amplitudes $f_{\rm NL}$ and $g_{\rm NL}$ which would be set by the single values for the extremes measured in the Euclid weak lensing survey. We end this thesis with a discussion about the results and conlcusions.

Chapter 1

THE COSMOLOGY BEHIND

1.1 Introduction

This chapter is meant to provide a basic cosmological background and tools to understand the history and the physics of the Universe according to the current paradigm of its formation and evolution, the ΛCDM model. The ΛCDM model is based on Einstein's theory of General Relativity, it postulates a Universe with a flat geometry, expanding with a cosmological constant Λ, and constituted by Cold Dark Matter (CDM) apart from the visible baryonic matter. Science managed to attain this current state of knowledge in a remarkably short time, mainly due to technological improvements which allowed for more detailed measurements, therefore shedding the light on new problems and creating a favourable ground for proliferation of new models and theories. We will start by discussing first the observational and then the theoretical pillars of modern cosmology (Sec. 1.2 and 1.3), thereby trying to provide a chronological picture. We will then focus on the parameters used to describe the Universe and its evolution (Sec. 1.4), the definitions of distances and scaling relations (Sec. 1.5 and 1.6) and finally, after having given a very brief summary of the main steps of the evolution of the Universe in Sec. 1.7, we deepen the theory of large scale structure formation in the last section, which constitutes the framework of this research project. The compilation of this chapter has been carried out by consulting one of the many available books on cosmology, Dodelson (2003). The notes on the cosmology lectures of Prof. Dr. M. Bartelmann were also used. [1]

1.2 Observational pillars

Modern cosmology, as all other sciences, finds its roots both in theoretical developments and observational evidences. We will start with the observational evidences, since these provided throughout time important evidences and prompted

[1] http://www.ita.uni-heidelberg.de/research/bartelmann/Lectures/cosmology/cosmology.pdf

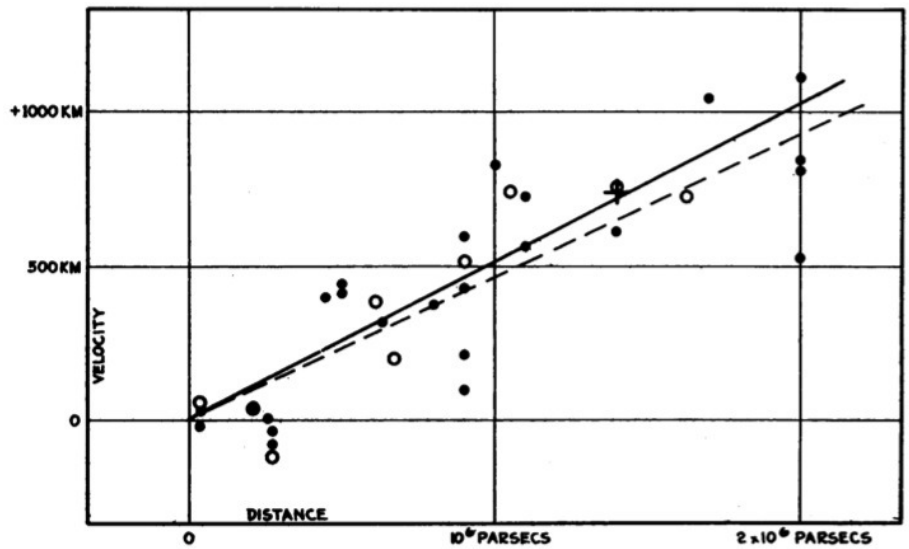

FIGURE 1
Velocity-Distance Relation among Extra-Galactic Nebulae.

Figure 1.1: Original Hubble diagram from (Hubble, 1929).

deeper studies on the origin and structure of the Universe.

Hubble law and the expansion of the Universe. Although carrying today the name of Edwin Hubble, the idea of an expanding Universe had been already proposed by Georges Lemaître in 1927 (Lemaître, 1927). Two years later Edwin Hubble (Hubble, 1929), by measuring the distances and redshifts (part of the latter observations had already been carried out by V. Slipher in 1917 (Slipher, 1917)) of a sample twenty-four "nebulae", showed that the recession velocity of the nebulae was in linear relation to their distance at any distance. All objects appeared to recede from the Earth and from each other with a recession velocity higher at higher distances, fact which confirmed Lemaître's idea of an *expanding Universe*, and yielded to the very well know Hubble law:

$$v_r = H_0 d, \tag{1.1}$$

where v_r is the recessional velocity, d is the distance of the object, and H_0 is the value of the Hubble parameter today, measured in (km/s)Mpc^{-1} and accounting for the rate at which the Universe is expanding today.

For measuring distances Hubble used first Cepheids and, much later, also Press-Schechter's luminosity function (Press & Schechter, 1974), whereas he used the shift of spectral lines of the objects, interpreted as Doppler redshift, to mea-

sure velocities through the relations:

$$z = \frac{\lambda_{obs} - \lambda_{em}}{\lambda_{em}} \tag{1.2}$$

$$1 + z = \sqrt{\left(\frac{1+\beta}{1-\beta}\right)} \overset{\beta \ll 1}{\longrightarrow} z \sim \beta = \frac{v}{c}. \tag{1.3}$$

Cosmic Microwave Background: homogeneity and isotropy. In 1964, at the Bell Laboratories and working at a horn antenna, A. Penzias and R. Wilson accidentally discovered the Cosmic Microwave Background (CMB), the relic radiation of photons emitted at a time in which the Universe was only 3×10^5 years old: the last scattering surface, when photons decoupled from electrons and started to free stream (cfr. Sec.1.7). The CMB has two properties: The spectrum of the photons from the last scattering surface is an extraordinarily perfect blackbody spectrum, showing that the photons were in equilibrium due to interactions with the electrons before decoupling. The second is that this picture of the youngest Universe we can possibly see shows the remarkable feature of homogeneity and isotropy on large scales, giving very solid observational grounds to the Cosmological Principle (see the next Section for more detailed discussion).

Light element abundances: dark matter. If the Universe expanded it implies it was hotter and denser at early times, up to a point where the temperature, being even higher than the typical binding energy of nuclei, would not allow them to be stable. Due to the expansion the temperature cooled, eventually allowing first the nuclei of light elements, and later atoms to form. Therefore any model for the Universe has to describe these early times, from which the abundances of the light elements can be predicted. Usually, for the Big Bang theory, we talk about *Big Bang Nucleosynthesis* (BBN), precisely meaning the synthesis of the baryonic matter. Burles et al. (1999) predicted the abundances for light elements in the Big Bang theory. Their main result is depicted in Fig. (1.2) and indeed represents one of the major successes of the Big Bang theory. The observations (boxes) very well fit the predictions for every light element. Since from the density of protons and neutrons it is possible to extract the density of the baryons, the BBN provides us with a measurement of the total density of baryon in the Universe at the time of the nucleosynthesis, which can be turned into the value today with scaling arguments (cfr. Sec.1.6). If this quantity is calculated it can be seen that the ordinary matter just accounts for a very small percentage of total matter density, which today is larger than this, thus making it necessary to invoke the presence of another form of matter: the *dark matter* (DM). An important remark is that, although being one of the arguments in favour of the dark matter, the BBN is not the only one. Kinematic velocity curves of galaxies and mass-to-light ratios of clusters of galaxies provide same predictions. Furthermore, also the amplitudes of fluctuations we observe in the CMB show indication of dark matter, since they would be incompatible with the presence of the

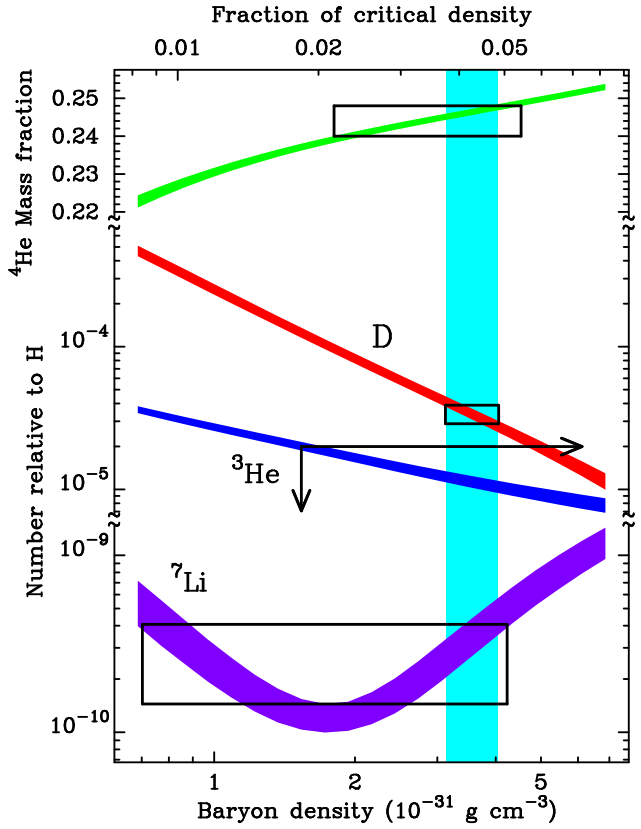

Figure 1.2: Big Bang Nucleosynthesis predictions for four elements: ^{4}He, deuterium, ^{3}He and lithium, taken from Burles et al. (1999).The observations are shown as boxes, whereas the vertical stripe represents the limits for primordial deuterium measurements.

amount of the already-formed structures we also observe, unless dark matter is accounted for.

Matter density distribution: inhomogeneity. The CMB represents a striking evidence for homogeneity and isotropy of the Universe on large scales ($\gtrsim 100$ Mpc h^{-1}). On smaller scales, as certainly is noticeable just by looking to the surroundings of the Milky Way, we find a matter distribution which is not at all homogeneous: this is the Large Scale Structure (LSS). The Two Degree Filed Galaxy Redshift Survey (2dF) (Colless et al., 2001) catalogued redshifts and positions of 2.5×10^5 galaxies, reaching redshifts of $z = 0.3$, and showing the aspect of the close-by Universe in terms of its inhomogeneities.

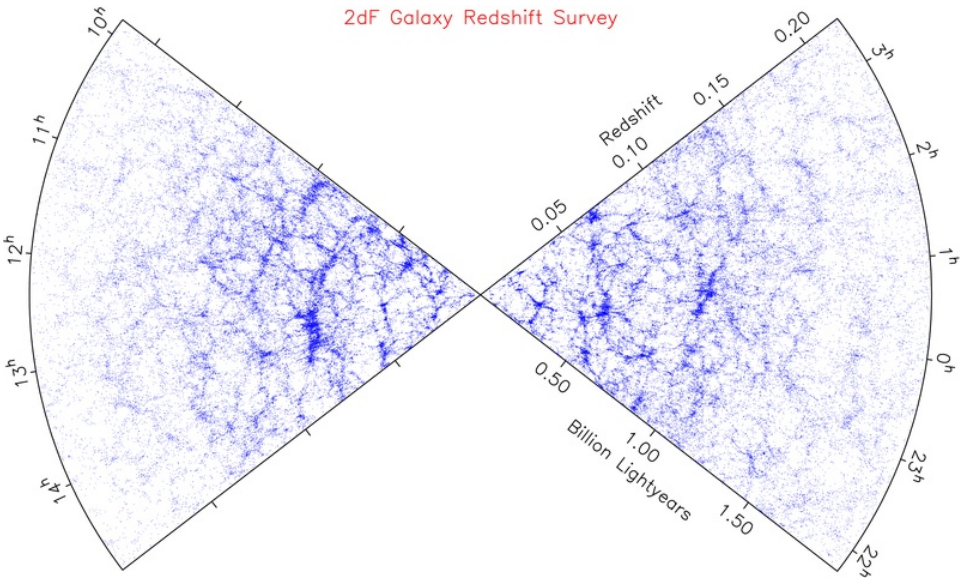

Figure 1.3: Distribution of galaxies from the 2dF survey. Image taken from `http://www2.aao.gov.au/~TDFgg/`

Supernovae Ia: accelerated expansion. Between 1998 and 1999 two groups, the Supernova Cosmology Project and the High-z Supernova Search Team (Riess et al., 1998; Perlmutter et al., 1999), were engaged with measurements of Supernovae Ia (SNIa) at high redshift to analyse the relation between their apparent luminosity and redshift. Based on their observation that distant supernovae appear to be dimmer than in an empty Universe with no cosmological constant, they find evidence for an accelerated expansion of the Universe due to the presence of *dark energy*, which in its simplest form is the cosmological constant Λ. Their results are shown in Fig. (1.4) and Fig. (1.5).

Any good explanation of the Universe's evolution has to account for these obser-

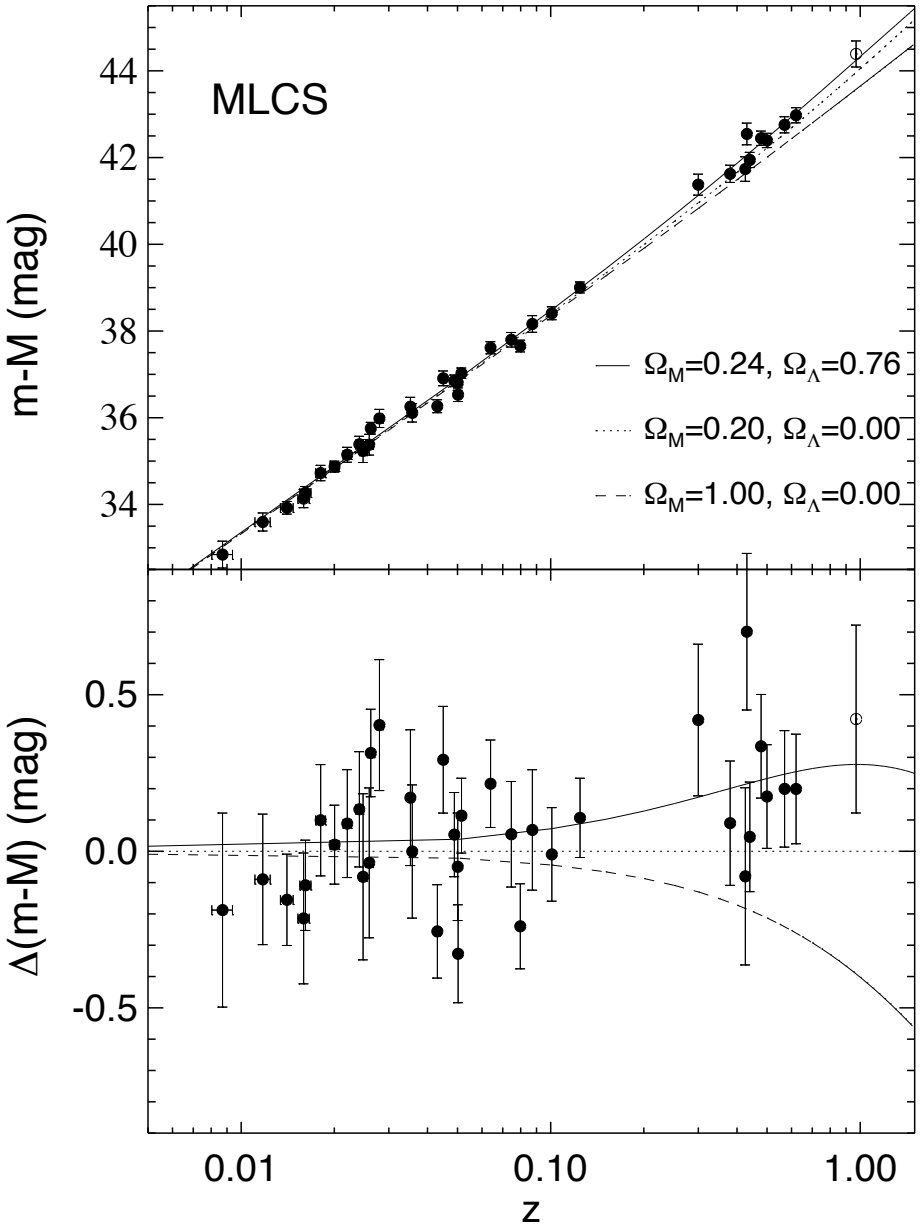

Figure 1.4: Measurements of SNIa between redshifts $0.16 \leq z \leq 0.97$ as measured by Riess et al. (1998), from which this figure is taken. The distance modulus is plotted against redshift. The curves represent theoretical estimations of the distance modulus for different models. The bottom plot is a comparison of the data with the Einstein-de Sitter model with $\Omega_m = 0.2$ and $\Omega_\Lambda = 0$.

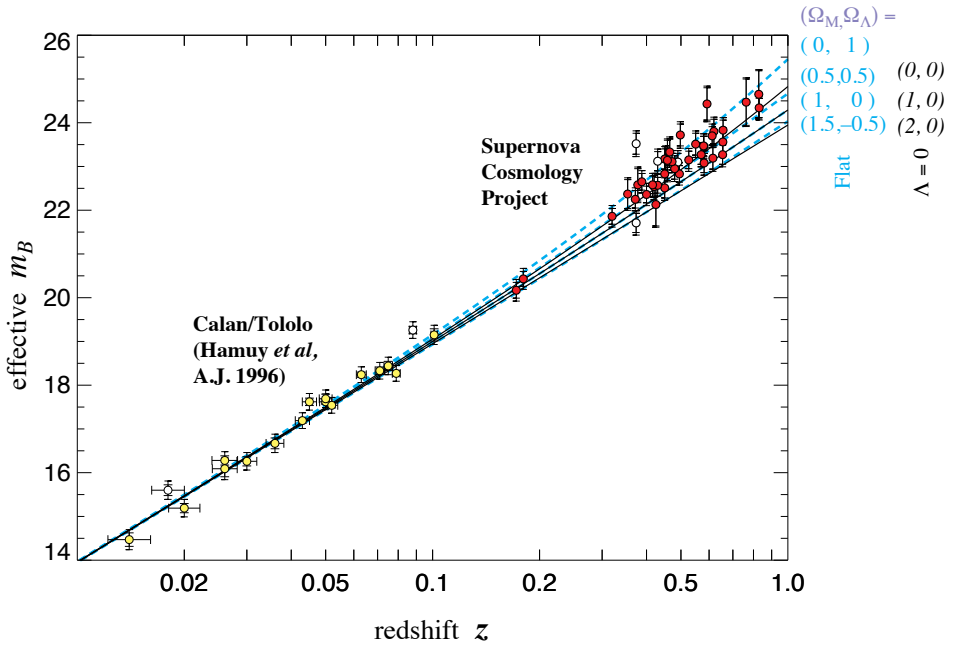

Figure 1.5: Measurements of SNIa between redshifts $0.18 \leq z \leq 0.83$ as measured by Perlmutter et al. (1999), from which this figure is taken. The effective magnitude is plotted versus redshift: The dashed and solid curves are the theoretical effective magnitudes expected for different cosmological models.

vations and their interpretation, i.e. that the Universe appears to expand in an accelerated fashion driven by dark energy or the cosmological constant, shows evidence for dark matter, is homogeneous and isotropic on large scales, but inhomogeneous on small scales.

1.3 Theoretical pillars

Cosmology lays its groundwork essentially on two theoretical milestones: The validity of Einstein's theory of General Relativity, and the validity of the Cosmological Principle.

General Relativity and Einstein's equations: Of the four forces we know, gravity is outstanding in the implications it has for the Universe, in how it shaped it up to now, and in how it will drive it in the future. Therefore it is unquestionable that any cosmological theory starts from the theory for gravity: Einstein's theory of General Relativity (GR) (Einstein, 1916). GR essentially gives a geometric interpretation of gravity by describing the space-time as a manifold with a metric $g_{\mu\nu}$:

$$ds^2 = g_{\mu\nu} \mathrm{d}x^\mu \mathrm{d}x^\nu, \tag{1.4}$$

whose dynamics is determined by Einstein's field equations, which relate the mass-energy content to the geometry of the manifold:

$$G_{\mu\nu} = \frac{8\pi G}{c^2} T_{\mu\nu} + \Lambda g_{\mu\nu}, \tag{1.5}$$

where G is the Newtonian constant, and Λ is the cosmological constant, a term which was originally put in the equations from Einstein to construct a static Universe. The structure of the space-time, described by the Einstein tensor $G_{\mu\nu}$, is determined by $T_{\mu\nu}$, the energy-momentum tensor for ideal (isotropic and dissipation-free) fluids with pressure p and density ρ (which are functions only of time because of homogeneity), but determines at the same time the motion of the matter.

Cosmological Principle: The Cosmological Principle makes two assumptions:

- *The Universe is homogeneous*: were we to sit, in a comoving frame, on another galaxy or in any other position in the Universe, we would observe, on sufficiently large scales, the same features of the Universe. The philosophical implication of this is that the portion of the Universe we see is a fair sample, and that our position in the Universe is not preferred to another.
- *The Universe is isotropic*: in any direction we look, the properties of the Universe viewed on large scales are the same.

The second assumption binds the first to also be valid: If the Universe is isotropic, then it must also be homogeneous. Note that the homogeneity is meant to be in space but not in time. In fact, the properties of the Universe at high redshift are very different from the properties of the Universe today.

It must be noted that the cosmological principle was an assumption made long earlier than any observational evidence for it was found. It constituted, though, a theoretically necessary assumption for simplifying Einstein's equations and to be thus able to find an analytical solution describing the evolution of the Universe.

Lemaître-Friedmann-Robertson-Walker metric and Friedmann's equations: The metric fulfilling the requirements of the Cosmological Principle is the Lamaître-Friedmann-Robertson-Walker (FLRW or simply FRW) metric, which enters the line element:

$$ds^2 = c^2 \mathrm{d}t^2 - a^2(t)\left[\mathrm{d}\chi^2 + f_K^2(\chi)\left(\mathrm{d}\phi^2 + \sin^2\theta \mathrm{d}\theta^2\right)\right], \tag{1.6}$$

where (t, χ, θ, ϕ) are the *comoving coordinates*, $a(t)$ is the *scale factor*, which accounts for the expansion of the Universe in time and, as a consequence of homogeneity, $f_K(\chi)$ is a function which can be trigonometric, hyperbolic or linear:

$$f_K(\chi) = \begin{cases} K^{-1/2}\sin(K^{1/2}\chi) & K > 0 \\ \chi & K = 0 \\ |K|^{-1/2}\sinh(K^{1/2}\chi) & K < 0, \end{cases} \tag{1.7}$$

and describes the geometry of the spacetime. If we use the FRW metric, then the Einstein's equations simplify to the *Friedmann's equations*:

$$\left(\frac{\dot{a}}{a}\right)^2 = \frac{8\pi G}{3}\rho - \frac{Kc^2}{a^2} + \frac{\Lambda}{3} \tag{1.8}$$

$$\frac{\ddot{a}}{a} = -\frac{4\pi G}{3}\rho\left(\rho + \frac{3p}{c^2}\right) + \frac{\Lambda}{3}, \tag{1.9}$$

where Λ is the cosmological constant, G the constant of Newtonian gravity, ρ is the density, p the pressure and $a(t)$ the scale factor. Freidmann's equations tell how the scale factor $a(t)$ evolves with time. By definition, the scale factor is set today to be $a_0 \equiv 1$.

1.4 Cosmological Parameters

In order to characterise the content of the Universe and its evolution it is useful to define some parameters. A table of the values of these parameters according to the latest results of the Planck mission (Planck Collaboration et al., 2013a) can be found in Table (1.1).

Hubble parameter: it is defined as the logarithmic change in the expansion rate, and is a function of time:

$$H(t) \equiv \frac{\dot{a}}{a}. \tag{1.10}$$

Critical density: it is defined as:

$$\rho_{\rm cr}(t) \equiv \frac{3H^2(t)}{8\pi G}, \tag{1.11}$$

and it is the density the Universe would need to have to be geometrically flat. It is also a function of time, and its value today is:

$$\rho_{\rm cr0} \equiv \frac{3H_0^2}{8\pi G} = 1.86 \times 10^{-29} h^2 \,{\rm g\,cm^{-3}}. \tag{1.12}$$

Density parameter: It is natural to associate to the density a parameter which is the dimensionless ratio between the matter density (baryonic and dark) of the Universe and the critical density, and therefore roughly tells how the matter content is related to the geometry of the space-time:

$$\Omega_m(t) \equiv \frac{\rho_m(t)}{\rho_{\rm cr}(t)}. \tag{1.13}$$

It is usually also customary to distinguish the contributions of ordinary matter and dark matter, and split this parameter into two: $\Omega_b(t)$ and $\Omega_{\rm CDM}(t)$.

Radiation density parameter: The matter (dark and baryonic) is not the only constituent of the Universe: Radiation is an important part of the cosmic inventory, and the dimensionless density parameter associated to radiation is

$$\Omega_r(t) \equiv \frac{\rho_r(t)}{\rho_{\rm cr}(t)}. \tag{1.14}$$

Note that the radiation and matter density parameters have same operational definitions, but they differ by their equation of states. This results in a different scaling of $\rho_m(t)$ and $\rho_r(t)$ with a (cfr. Sec. 1.6)

Cosmological constant density: A density parameter can also be associated to the cosmological constant:

$$\Omega_\Lambda(t) \equiv \frac{\Lambda}{3H^2(t)}. \tag{1.15}$$

Curvature parameter: The last important parametrisation to be made concerns the curvature of the space-time. The curvature parameter is therefore defined as:

$$\Omega_K(t) \equiv -\frac{Kc^2}{H^2(t)}. \tag{1.16}$$

	Planck	Planck + lensing	Planck + WP
H_0	67.4 ± 1.4	67.9 ± 1.5	67.3 ± 1.2
Ω_Λ	0.686 ± 0.02	0.693 ± 0.019	$0.685^{0.018}_{-0.016}$
Ω_m	0.314 ± 0.02	0.307 ± 0.019	$0.315^{0.016}_{-0.018}$
σ_8	0.834 ± 0.0027	0.823 ± 0.018	0.829 ± 0.012
n_s	0.9616 ± 0.0094	0.9635 ± 0.0094	0.9603 ± 0.0073

Table 1.1: Set of cosmological parameters as measured by the Planck mission (Planck Collaboration et al., 2013a). Best fits for the parameters are shown when only Planck temperature power spectrum data are used (first column), Planck temperature data and Planck lensing, and Planck data and WMAP polarisation at low multipoles.

Rewritten in terms of these parameters, Friedmann's equation can be expressed as:

$$H^2(a) = H_0^2 E^2(a) = H_0^2 \left[\Omega_{r0} a^{-4} + \Omega_{m0} a^{-3} + \Omega_{\Lambda 0} + \Omega_K a^{-2}\right] \tag{1.17}$$

Since the Friedmann's equations are valid at any time, they must be valid also today. By taking $a(t) = a_0 = 1$, we find a link between all the cosmological parameters:

$$\Omega_K = 1 - \Omega_{r0} - \Omega_{m0} - \Omega_{\Lambda 0}. \tag{1.18}$$

Redshift and scale factor: Finally, the redshift we have introduced in Eqn.(1.2) can be related to the scale factor:

$$a(t) = \frac{1}{1+z} \tag{1.19}$$

1.5 Distances in Cosmology

A consequence of the fact that the Universe can have curvatures different from the flat one is that the distance between two events is no longer uniquely defined. The distance can depend on the quantity we are measuring (as in the case of luminosity and angular diameter distances) or on the "system of reference" we imagine to use (comoving and proper distance):

Proper distance: This is the distance that the light covers to go from a source at z_2 to the observer at $z_1 < z_2$:

$$D_{\rm prop}(z_1, z_2) = c \int_{a(z_1)}^{a(z_2)} \frac{{\rm d}a}{\dot{a}} = \frac{c}{H_0} \int_{a(z_2)}^{a(z_1)} \frac{{\rm d}a}{a\,E(a)}. \tag{1.20}$$

Comoving distance: This is the distance measured by an observer which is comoving with the cosmic flow:

$$D_{\rm com}(z_1, z_2) = c \int_{a(z_1)}^{a(z_2)} \frac{{\rm d}a}{a\dot{a}} = \frac{c}{H_0} \int_{a(z_1)}^{a(z_2)} \frac{{\rm d}a}{a^2 E(a)} = \chi(z_1, z_2). \tag{1.21}$$

Angular diameter distance: It represents the distance related to the solid angle $\delta\omega$ subtended to the physical dimension of the object on the sky, δA. This definition is analogous to the same definition in Euclidian space, in which case we have $\delta\omega D_{\rm ang}^2 = \delta A$. The object is at redshift z_2 and the observer at z_1. For a generic space we then have:

$$\frac{\delta A}{4\pi a^2(z_2) f_K^2(\chi(z_1, z_2))} = \frac{\delta\omega}{4\pi}, \tag{1.22}$$

and therefore:

$$D_{\rm ang}(z_1, z_2) = \left(\frac{\delta A}{\delta\omega}\right)^{1/2} = \frac{a(z_2)}{a(z_1)} f_K[\chi(z_1, z_2)]. \tag{1.23}$$

Luminosity distance: This distance is also inherited by a definition in Euclidian space, specifically the relation between the luminosity L of a source at redshift z_2 and the flux F received by an observer at z_1:

$$D_{\mathrm{L}} = \sqrt{\frac{L}{4\pi F}}. \tag{1.24}$$

The *Etherington relation* puts into connection the angular and luminosity distances:

$$D_{\mathrm{L}}(z_1, z_2) = \left[\frac{a(z_1)}{a(z_2)}\right]^2 D_{\mathrm{ang}}(z_1, z_2). \tag{1.25}$$

In the limit of low redshift all the distances are the same, and one recovers Hubble's expansion law:

$$D = \frac{cz}{H_0} + \mathcal{O}(z^2). \tag{1.26}$$

1.6 Important scalings

In this section we summarise the most important scalings of various quantities in the cases of a matter- and radiation-dominated Universes. These scalings represent a fundamental tool in cosmology.

Scaling of density From the conservation of the energy-momentum tensor for a perfect fluid and with a FLRW metric, we obtain the so-called *adiabatic equation*, which describes how the energy density changes if pressure changes:

$$\frac{\mathrm{d}}{\mathrm{d}t}(a^3\rho c^2) + p\frac{\mathrm{d}}{\mathrm{d}t}(a^3) = 0 \tag{1.27}$$

If we write the equation of state as:

$$p = w\rho c^2, \tag{1.28}$$

then we obtain the scaling of the density with a:

$$\rho \propto a^{-3(w+1)}, \tag{1.29}$$

which leads to the cases:

$w = 0$	$\rho \propto a^{-3}$	Matter
$w = \frac{1}{3}$	$\rho \propto a^{-4}$	Radiation
$w = -\frac{1}{3}$	$\rho \propto a^{-2}$	Curvature
$w = -1$	$\rho = \mathrm{const}$	Cosmological Constant

(1.30)

Scalings for an Einstein-de Sitter Universe: In an Einstein-de Sitter Universe, for which $\Omega_\Lambda = 0$ and $\Omega_m = 1$ we have that, for a fluid with $w = 0$, i.e. for matter:

$$\begin{aligned} a &\propto t^{2/3} \\ H &\propto t^{-1} \propto (1+z)^{3/2} \\ \rho &\propto t^{-2} \propto (1+z)^3. \end{aligned} \tag{1.31}$$

Instead, for a relativistic degenerate fluid with $w = 1/3$, i.e. for radiation, we have:

$$\begin{aligned} a &\propto t^{1/2} \\ H &\propto t^{-1} \propto (1+z)^2 \\ \rho &\propto t^{-2} \propto (1+z)^4 \propto a^{-4}. \end{aligned} \tag{1.32}$$

It is important to notice that the case of an Einstein-de Sitter Universe does not correspond to the model of the Universe we measure today (which has indeed a $\Lambda \neq 0$ and $\Omega_0 \neq 1$), but yet represents a good approximation to the Universe as it was in its history.

Scaling of temperature: Knowing that for an adiabatic transformation from the first law of thermodynamics we have:

$$TV^{\gamma-1} = const, \tag{1.33}$$

and that the volume scales as $V \propto a^3$, we find that the scaling of the temperature with a depends on the adiabatic indexes for non-relativistic and relativistic particles, which are resepctively $\gamma = 5/3$ and $\gamma = 4/3$ and follows:

$$\begin{aligned} T &\propto a^{-1} \quad \text{Radiation} \\ T &\propto a^{-2} \quad \text{Matter} \end{aligned} \tag{1.34}$$

1.7 Tracing the history of the Universe

We can trace the history of the Universe very coarsely in the following steps and eras:

- **Big Bang** ($t = 0$): The Big Bang constitutes in Friedmann's equations a singularity, which basically tells that the laws we are using do not hold anymore at this time. In fact the Planck time $t_{\rm PL} = 10^{-43}$s sets a threshold to what we can observe, due to the Indetermination Principle, and at the same time sets the time at which General Relativity breaks down and some other, unknown, physics linking Quantum Field Theory to General Relativity must hold. The Big Bang and the expansion imply that at earlier times the Universe must have been much denser and hotter.

- **Inflation**: the earliest time of the Universe is characterised by an exponential expansion which cooled and rarefied very much the Universe. The subsequent period of reheating re-established the temperature to higher values. We will talk more extensively about the Inflation in Chap. 7

- **Adronic ($t \sim 10^{-5}s$) and leptonic era ($t \sim 10s$)**: These eras see the formation of all the elementary particles as we know them from the Standard Model. The synthesis of light elements (BBN) also starts and the neutrino ν decouples (i.e. stops interacting) from the other species ($t \sim 1$s). We refer to a "decoupling", or a "freeze-out" when the rate of interactions Γ between the species is lower than the rate of expansion of the Universe, which is given by the Hubble parameter H.

- **Radiation dominated era**: It is the longest lasting era we know, and it starts when the electrons e^- and positrons e^+ annihilate, which takes place shortly after the neutrino freeze-out. The radiation era also sees the end of the BBN, at $t \sim 100s$. The so-called *time of equivalence*, or just *equivalence* also falls within the radiation dominated era. It refers to the time the radiation density equals the matter density. Given the different scaling of the radiation and matter densities with the scale factor, $\rho_r \propto a^{-4}$ and $\rho_m \propto a^{-3}$, there must be a time in which the two are equal. This time corresponds to $t \sim 10^{12}$s $\sim 3\times10^4$yrs after the Big Bang.

- **Matter dominated era**: Starting with the *recombination*, i.e. the formation of the first atoms from the binding of electrons and protons, the beginning of the matter domination era coincides with the decoupling of the photons and the formation of the CMB. The matter dominated era is characterised by the formation of all the structure we can see today: stars, galaxies form due to the clumping of the matter driven by gravitational attraction. The most accredited scenario today is the so-called *bottom→up* scenario, for which first the small objects formed, aggregating in time into larger and larger objects.

- **Cosmological constant era**: This is the epoch of the Universe in which we live, dominated by dark energy, which drives the accelerated expansion. In it simplest, constant form, the dark energy coincides with the cosmological constant. The beginning of this era can be traced back as the time at which Ω_Λ and Ω_m coincide, which is $t = 11\times10^9$yrs.

1.8 Large Scale Structure: the evolution of perturbations

The main quantity which is always addressed in Large Scale Structure (LSS hereafter) studies is the *density contrast*, defined as the difference between the density at a certain coordinate and the mean density, normalised by the mean den-

sity:

$$\delta(\mathbf{x},t)=\frac{\rho(\mathbf{x},t)-\bar{\rho}(t)}{\bar{\rho}(t)}=\frac{\delta\rho}{\rho_0} \tag{1.35}$$

When observed on scales $\lesssim 100$ Mpc h^{-1} the Universe appears far from homogeneous, whereas it actually reveals structures such as filaments and voids (~ 50 Mpch^{-1}), clusters and superclusters of galaxies ($\sim 1\div 10$ Mpc h^{-1}), down to galaxies (~ 10 Kpc h^{-1}). When considering the Universe as a fluid it obeys the following equations, which determine and specify the evolution of the system:

- *continuity equation*, standing for the mass conservation:

$$\frac{\partial\rho}{\partial t}+\nabla\cdot(\rho\mathbf{v})=0; \tag{1.36}$$

- *Euler's equation*, describing how the velocity field $\mathbf{v}$ evolves due to forces induced by pressure and gravitational potential, and standing for momentum conservation:

$$\frac{\partial\mathbf{v}}{\partial t}+(\nabla\cdot\mathbf{v})\mathbf{v}=-\frac{1}{\rho}\nabla P-\nabla\Phi \tag{1.37}$$

- *Poisson's equation*, linking the mass density to the gravitational potential:

$$\nabla^2\Phi=4\pi G\rho \tag{1.38}$$

- *equation of state*, determining the relation between pressure and density Eqn. (1.28):

$$p=p(\rho) \tag{1.39}$$

The evolution of the perturbations can be described in two regimes: the *linear* and *nonlinear* regimes.

1.8.1 Linear evolution

For $\delta\ll 1$ one can rewrite the density and the velocity fields as a perturbation ($\delta\rho$ and $\delta\mathbf{v}$) to their background values ρ_0 and $\mathbf{v}_0$:

$$\begin{aligned}\rho(\mathbf{x},t) &= \rho_0(t)+\delta\rho(\mathbf{x},t)\\ \mathbf{v}(\mathbf{x},t) &= \mathbf{v}_0(t)+\delta\mathbf{v}(\mathbf{x},t).\end{aligned} \tag{1.40}$$

By inserting these in Eqns. (1.36) and (1.37), and by making use also of the other Eqns.(1.38) and (1.39) we find an equation for the evolution of the density contrast:

$$\ddot{\delta}+2H\dot{\delta}=\frac{c_s^2}{a^2}\nabla^2\delta+4\pi G\rho_0\delta, \tag{1.41}$$

where c_s is the speed of sound and comes from the equation of state (1.39). By passing to Fourier space and decomposing the density contrast:

$$\delta(\mathbf{x},t) = \int \frac{\mathrm{d}^3 k}{(2\pi)^3} \hat{\delta}(\mathbf{k},t) e^{-i\mathbf{k}\cdot\mathbf{x}} \tag{1.42}$$

we find that real oscillations occur for values of $k > k_J$, value corresponding to the Jeans length λ_J:

$$k_J \equiv \frac{2\sqrt{\pi G \rho_0}}{c_s} \quad \lambda_J := \frac{2\pi}{k_J}. \tag{1.43}$$

For an Einstein-de Sitter Universe, during radiation- and matter-dominated eras we have, respectively, $a \propto t^{1/2}$ and $a \propto t^{2/3}$ (see Sec. 1.6), which substituted in Eqn.(1.41) yield to an equation written in terms of the time variable, and whose sought solution is of the type $\hat{\delta} \propto t^n$. This yields to an equation for n:

$$n^2 + \frac{n}{3} - \frac{2}{3} = 0, \tag{1.44}$$

which translates into the growing solutions for the radiation and matter dominated Universe:

$$\begin{aligned} \hat{\delta}_+ &\propto a^2 \quad \text{radiation domination} \\ \hat{\delta}_+ &\propto a \quad \text{matter domination} \end{aligned} \tag{1.45}$$

In the case of Universes with $\Omega_{m0} \neq 1$, $\Omega_{\Lambda 0} \neq 0$ we have, for the matter domination era:

$$\delta(a) = \delta_0 D_+(a), \tag{1.46}$$

where $D_+(a)$ is the *growth factor* (Carroll et al., 1992):

$$D_+(a) = \frac{5a}{2}\Omega_m \left[\Omega_m^{4/7} - \Omega_\Lambda + \left(1 + \frac{1}{2}\Omega_m\right)\left(1 + \frac{1}{70}\Omega_\Lambda\right)\right]^{-1} \tag{1.47}$$

1.8.2 The evolution of the velocity field

Also the velocity field can be explored in its evolution which, if pressure gradients are neglected, reads:

$$\dot{\mathbf{u}} + 2H\mathbf{u} = \frac{\nabla\delta\Phi}{a^2}, \tag{1.48}$$

where we have decomposed the potential field in analogy to Eqn.(1.40): $\Phi = \Phi_0 + \delta\Phi$, and $\delta\Phi$ is the perturbation term, and $\mathbf{u}$ is the peculiar velocity given from the derivative of the space coordinate r: $\dot{\mathrm{r}} = \mathbf{v} = \dot{a}\mathbf{x} + a\dot{\mathbf{x}} = \dot{a}\mathbf{x} + \mathbf{u}$. We can further decompose the velocity in two components: one perpendicular and the other parallel to the gradient $\nabla\delta\Phi$, $\mathbf{u}_\perp$ and $\mathbf{u}_{//}$, for which we find:

$$\begin{aligned} \mathbf{u}_\perp &\propto a^{-1} \\ \mathbf{u}_{//} &= \frac{\dot{\delta}}{k} = \dot{D}_+\delta_0 \frac{a}{k_c} = \frac{a(t)H(t)}{k_c}\delta(t)\frac{\mathrm{d}\ln D_+(a)}{\mathrm{d}\ln a}, \end{aligned} \tag{1.49}$$

where we have defined $k = k_c/a$ and where:

$$\frac{\mathrm{d}\ln D_+(a)}{\mathrm{d}\ln a} \approx \Omega^{0.6} \tag{1.50}$$

It is important to note that turbulent motion $\mathbf{u}_\perp$ gets smoothed out quite rapidly with the evolution of the Universe, resolving any doubt that rotation of galaxies might have originated by the original turbulence in the velocity field. This will be useful when we study the origin of galactic rotation, in Chap. 2

1.8.3 Non-linear evolution

When the condition $\delta \ll 1$ is not verified anymore, the assumptions of small perturbations of the background fields are no longer valid, and we enter the non-linear regime of perturbations, in which the equations are very complicated to solve analytically. It is though still possible to give an analytical treatment of the mildly non-linear regime (corresponding to $\delta \sim 1$) by means of the *Zel'dovich approximation*, which we will extensively discuss in Chap. 2 in the framework of how galaxies acquire their angular momentum. Another possible way is to consider the so-called *spherical collapse* model which describes the evolution of an homogeneous overdensity with spherical symmetry . When also the mildly non-linear regime drops and $\delta \geq 1$ there is no longer chance treat analytically the equations, and hence a numerical approach is required. N-body simulations have in fact become the standard tool adopted for studying the evolution of the density field at later times. A very famous example for such techniques is given by the Millennium Simulations [2], of which we show a series of images in Fig. (1.6).

1.9 Statistical properties: the power spectrum

A very useful tool to study the large scale structure and the inhomogeneities of the Universe (in the temperature for the CMB and in the density field for the LSS) is to study the statistical properties of these fields. The first quantity we would investigate is the average of the observable we are interested in, e.g. the density contrast. By definition this quantity is zero:

$$\langle\delta\rangle = \langle\frac{\rho-\rho_0}{\rho_0}\rangle = \frac{\langle\rho\rangle}{\rho_0} - 1 = 0. \tag{1.51}$$

The further step to take is to measure the variance of the density field, to quantify how much, on average, the density field moves away from its mean value. This implicitly measures the degree of clumpiness of the field, since for a perfectly homogeneous field the variance would be zero, whereas for a field with more

[2] For more details see http://www.mpa-garching.mpg.de/millennium/ and the list of references therein.

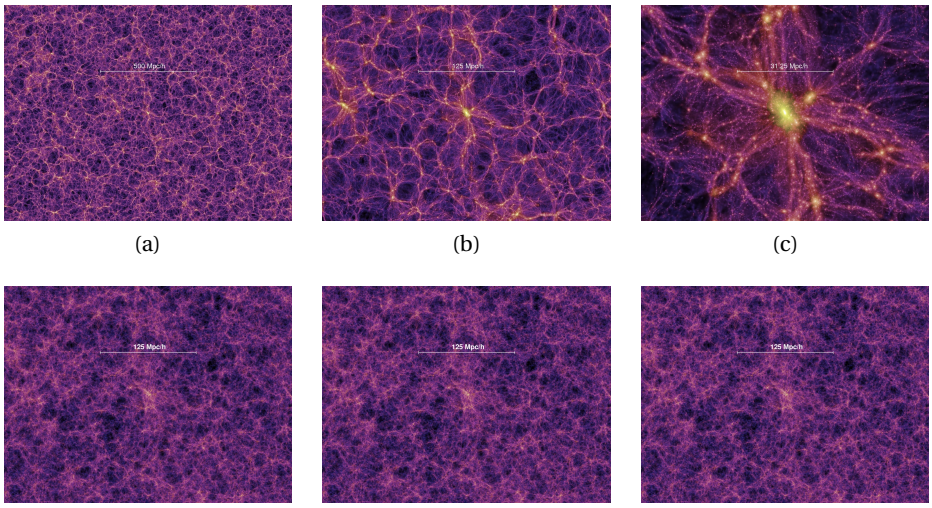

(a) (b) (c)

(d) (e) (f)

Figure 1.6: Millennium simulation snapshots taken from http://www.mpa-garching.mpg.de/galform/virgo/millennium/. The three top panels represent the simulation box at $z = 0$, i.e. today, at different resolutions. The three bottom panels are snapshots taken when the simulated Universe is much younger, at $z = 5.7$

over- and under-dense regions the variance increases. The variance in real space is related to the *correlation function*, defined as:

$$\xi(y) \equiv \langle \delta(\mathbf{x})\delta(\mathbf{x}+\mathbf{y})\rangle, \tag{1.52}$$

where the $\langle\cdot\rangle$ represents the average over the all realisations. Notice that for isotropy arguments the correlation function does not depend on the direction of $\mathbf{y}$ but only on its magnitude y. The variance of δ is then the correlation function at $\mathbf{y} = 0$:

$$\sigma^2 = \langle \delta(\mathbf{x})^2\rangle, \tag{1.53}$$

which is the correct expression if the mean is zero, as it is in our case.

The Fourier pair of the correlation function is the power spectrum [3], which defines the variance in Fourier space:

$$\langle \hat{\delta}(\mathbf{k})\hat{\delta^*}(\mathbf{k}')\rangle \equiv (2\pi)^3 P(k)\delta_D(\mathbf{k}+\mathbf{k}'), \tag{1.54}$$

where δ_D is the Dirac distribution and is there to guarantee that the different modes are uncorrelated, and where we have used the the Fourier transform $\hat{\delta}$ of the density contrast:

$$\delta(\mathbf{x}) = \int \frac{\mathrm{d}^3k}{(2\pi)^3}\hat{\delta}(\mathbf{k})e^{-i\mathbf{k}\cdot\mathbf{x}}; \quad \hat{\delta}(\mathbf{k}) = \int \frac{\mathrm{d}^3k}{(2\pi)^3}\delta(\mathbf{x})e^{i\mathbf{k}\cdot\mathbf{x}}. \tag{1.55}$$

[3] This is also known as Wiener-Khintchine theorem

The power spectrum therefore has dimensions of k^{-3}, or equivalently, of $[L]^3$. It is therefore customary to plot the dimensionless quantity $\Delta^2(k) = k^3 P(k)/(2\pi)^3$ as a function of k. Usually one identifies the infinitesimal quantity $\mathrm{d}^3 k P(k)/(2\pi)^3$ with the excess power in a bin of width k centred at k.

In principle if the field we are describing is a Gaussian field, it will be completely described by its first two moments, the mean and the variance. If the field is non-Gaussian, which is a situation often encountered in Nature, then higher-order moments are necessary (i.e. skewness, kurtosis, etc.). These quantities can be investigated by means of higher-order correlators: the three-, four-, N-point correlation function, defined as:

$$\xi_N(\mathbf{x}_1, ..., \mathbf{x}_N) = \langle \delta(\mathbf{x}_1) ... \delta(\mathbf{x}_N) \rangle, \tag{1.56}$$

(for a more detailed description of higher-order statistics see Bernardeau et al., 2002a). For the case of the three- and four-point correlator functions the correspondent Fourier functions are the bi- and trispectra $B(k)$ and $T(k)$.

1.10 Philosophical considerations

Some considerations based on basic philosophical grounds can be made in cosmology. Here we report the ergodic theorem and the anthropic principle.

Ergodic theorem: What really distinguishes cosmology from other sciences and other fields within physics stems from a particularly simple consideration about the Universe: it is just one, i.e., we have just *one* realisation of the Universe. Since the natural grounds for developing science are both theory and observations, and even more precisely the *repeatability* of the measurements, we must make sure that this can be granted when observing the single realisation of the Universe. Since we inspect, as we have seen, the statistical properties of the Universe, then the cosmological statements are essentially statistical in nature. This implies, as we have seen, the need for statistical tools, such as the moments of a distribution, i.e. mean and the variance if the distribution is purely Gaussian. When computing these quantities, an operation of *averaging* is always made, denoted by the symbol $\langle \cdot \rangle$. This average is meant to be an *ensemble average*, which means that the average is made over many realisations of the distribution. Since, as said before, we do not have this possibility to calculate this average for the Universe, we need to resort to another definition of the average, the *sample average*, which takes different samples within *one* single realisation. If the samples are uncorrelated, then the two averages coincide. This is what the ergodic theorem states, and what we assume for our Universe.

Anthropic Principle: The cosmological principle is an extension of the Copernican Principle in the sense that it also asserts that our position in the Universe is not privileged, i.e. all positions are equivalent. A variation of this, the *Anthropic Cosmological Principle*, aims to find a connection between the structure of the Universe and the development of forms of intelligent life within it (Coles

& Lucchin, 2002). Specifically, there are two anthropic principles. The *Weak Anthropic Principle* remarks that our existence cannot be a privileged condition, since it is only due to how the Universe is shaped and how it has evolved. In equivalence, we could not have possibly evolved in another time and in other conditions, and we must be aware of this when we interpret cosmological data. The *Strong Anthropic Principle* is teleological in its foundation and is related to the fine tuning of natural constants. In fact, were the constants be be even slightly different from what we know them to be, we could not exist. This constitutes for some reason to believe that there must be some sort of purpose, even though, speculatively, one can construct models of the Universe such that only the weak explanation suffices. The strong anthropic principle is still very controversial and debated.

Chapter 2

THE PHYSICS OF GALACTIC ANGULAR MOMENTA

2.1 Introduction

Due to its generality, the very wide context of structure formation somehow imposed us, in the last chapter, to gloss over the details of the formation processes of galaxies themselves, which constitutes itself a deep and large matter of study. It is indeed striking to see that in all we have understood about the Universe, its formation and its evolution, the topic of galaxy formation still constitutes an open question mark involving a wide range of physical aspects, from the baryonic dissipation processes and feedbacks to the dark matter dissipationless processes. Galaxies not only formed through highly non-linear physical processes, but very likely interacted during their long lives, such that today it is an even harder work for us, gazing at the sky, to establish their formation history.

In particular a deeper aspect of galaxy formation concerns the fact that they rotate, and that they therefore have a net angular momentum. The mechanism through which this angular momentum is acquired is yet to be understood in detail, also given the fact that different prescriptions for galaxy assembly seem to be needed for different morphologies. Late-type and early-type galaxies are assumed to acquire angular momentum in different ways, spiral galaxies being supported by their angular momentum, ellipticals having it instead dissipated in mergers and being supported by random motion of stars. This appears obvious when considering observational properties of early- and late-type galaxies concerning not only their luminosity, velocity dispersion profiles and rotation curves, but also the quantification of their rotational support. The latter can in fact be defined by the dimensionless *spin parameter* λ, first introduced by Peebles (1969), and defined as:

$$\lambda = \frac{L|E|^{1/2}}{GM^{5/2}}, \tag{2.1}$$

where L, E, M are respectively the angular momentum, the energy and the mass

of the system, and G is the Newtonian gravitational constant. The spin parameter can be interpreted as a measure of the degree of rotational support of the system, being the ratio between the observed angular velocity ω of a galaxy and the angular velocity needed for the rotational support ω_0 (Mo et al., 1998):

$$\lambda = \frac{\omega}{\omega_0} = \frac{L/(MR^2)}{\sqrt{GM/R^3}}. \tag{2.2}$$

Throughout time, there have been several measurements of the statistical properties of the spin parameter (which appears to be distributed as a lognormal Warren et al., 1992), and its typical values from N-body simulations, which was found to be $\lambda = 0.05 \div 0.08$ (Peebles, 1969, 1971a; Bullock et al., 2001; Efstathiou & Jones, 1979; Barnes & Efstathiou, 1987; Warren et al., 1992). Observations showed that spiral galaxies, which rotate very fast and whose rotation is supported by angular momentum, had a typical value of $\lambda \sim 0.5$, whereas ellipticals were shown to have $\lambda < 0.1$ (Davies et al., 1983). This result showed two mismatches at the same time and on different levels: in general, ellipticals appeared to behave very differently compared to spirals in terms of their rotational support and, on the other hand, observations of spiral galaxies were in contrast with N-body simulations (this problem is called *angular momentum problem*, or *angular momentum catastrophe*, and will be discussed in more detail in Sec. 2.5).

This paved the way to many possible scenarios of formation of early- and late-type galaxies, which will be quickly reviewed respectively in Sec. 2.2 and Sec. 2.3. Sec. 2.4 will focus respectively on the theory of tidal torques, which is currently the most accredited theory at the basis of spiral disk formation and angular momentum acquisition. This theory also constitutes a basilar tool we will need in the next chapter to revisit the intrinsic alignments models for late-type galaxies. We will dedicate a special section, Sec. 2.5, to numerical simulations carried out to test the theory of tidal torques and the analytical models for disk formation, and finally we will summarise the content of this chapter in Sec. 2.6. [1]

2.2 Early-type galaxies

As mentioned above, elliptical galaxies showed to have much smaller spin parameter than spirals, and this suggested that they could not be rotationally supported as spirals, and that the flattening of their halos due to their slow rotation

[1] Some of the content of this chapter was assembled by consulting the following webpages:
http://ned.ipac.caltech.edu/level5/Sept11/Benson/Benson_contents.html
http://ned.ipac.caltech.edu/level5/March02/Efstathiou/Efst_contents.html
and the online material of Prof. Dr. Trager and Prof. Dr. Mo:
http://www.astro.rug.nl/~sctrager/teaching/formation_and_evolution/2003/lecture1.pdf
http://www.astro.umass.edu/~hjmo/astro850/lecture9_3.pdf
http://www.astro.umass.edu/~hjmo/astro850/lecture9_1.pdf

could be ascribable to velocity dispersions (see also Binney, 1978). In some way dissipation and loss of angular momentum seem to have had a major role in the rotational properties that ellipticals show today. In order to explain loss of angular momentum the simplest way would be to assume that elliptical galaxies formed from mergers. This, though, is not the only possible speculated scenario. Nowadays there are in fact mainly three models for the formation of ellipticals, which we are going to briefly describe in what follows (see also Binney & Tremaine, 2008).

Merging scenario: This umbrella term actually includes two kind of models: the *major merger model*, for which the main characters of the merging are two disk galaxies of comparable mass, and the *minor mergers model*, for which an elliptical might form from several mergers between individual galaxies with much lower mass than the remnant.
Mergers were first studied in N-body simulations by Toomre & Toomre (1972), and then proposed as possible viable ways to describe early-type galaxies' formation by Toomre (1977), given the fact that mergers between disk galaxies appeared to be able to produce galaxies with similar properties to ellipticals. In order to recover ellipticals' properties, it was also found that dissipationless dark matter halo mergers (also called gas-free mergers) alone were not enough. Instead, disks (i.e. the baryonic component) needed to be accounted for in simulations and needed to have a pre-existing bulge with stars. This prescription is in fact able to recover both the observation of old stellar populations in ellipticals and their low angular momentum. To sketch the picture we could say that the halos would initially interact, followed only in a second moment by the disks with their bulges. During this latter interaction the luminous components would transfer lot of their angular momentum to their dark halos, conserving therefore angular momentum, but redistributing it to the dark, unobservable, component. The remaining angular momentum in the luminous and visible component is therefore much lower. Among others, Steinmetz & Navarro (2002); Meza et al. (2003) carried out cosmological numerical simulations showing the merging scenario to be consistent with observed or expected properties of ellipticals, such as mass accretion and star formation history, structure and kinematics. Within framework of galaxy mergers Lynden-Bell (1967), trying to find an explanation for the observed light distributions of elliptical galaxies, suggested that, during mergers, the orbits of the stars are so heavily affected by the change in the potential due to the merging process that they lose memory of their previous ordered motion, becoming random. In other words, the change in potential is much more rapid than the dynamical timescale of the stars producing a *violent relaxation*.

Monolithic model: This latter model prescribes the easiest way to form an elliptical galaxy, i.e. by mean of a collapse of a big gas cloud. It was proposed by (Larson, 1969; Larson & Tinsley, 1974; Larson, 1974, 1975), and mostly motivated by

the fact that it could plainly explain some features of the ellipticals, i.e. that they appear to be very stabilised stellar systems with an old stellar population. In the monolithic scenario, in fact, the gas cloud collapses yielding to star formation in short timescales. The problem with this model is that the initial conditions are not well motivated, and that other models, such as the merging scenario, can recover the same observational features by invoking other mechanisms (i.e. the old star population can be easily explained by the fact that stars could be already present in galaxies that merged in a second moment). In addition to this, such a model would be in contradiction with the hierarchical CDM model providing the "bottom→up" scenario, for which structures rather formed by the clustering of smaller objects than from collapse of bigger structures which then fragmented into their constituents.

2.3 Late-type galaxies

It was already in the time interval spanning between the end of 40s and beginning of 50s that first Hoyle (1949) and then Sciama (1955) suggested that the mechanism enabling rotation in galaxies had to be inherent to the way the galaxies themselves formed. Hoyle and Sciama were pioneers in realising that, during the formation of a protogalaxy, the tidal torques created by the neighbouring structures could produce a velocity shear in the protogalactic object, inducing its rotation. This original idea, then further developed by Peebles (1969); Doroshkevich (1970) and White (1984) well suits the hierarchical CDM structure formation scenario (in this case, in fact, galaxies are a first product of structure formation), setting the grounds for explanations both concerning the spin-up of the galaxies and the development of their disk-like structures and morphology.

Although the theory of tidal torques is nowadays widely accepted and accredited, it has not been the only proposed mechanism for angular momentum build-up. Vitvitska et al. (2002) proposed a *satellite accretion model*, which believes that dark halos gain angular momentum cumulatively via accretion of small satellite halos, yielding to an angular momentum associated with the assembly history of the halo's major progenitor. Vitvitska et al. (2002) and D'Onghia & Navarro (2007) find in N-body simulations that the accretion of satellites is enough to provide the galaxy with angular momentum, and are able to reproduce the lognormal distribution for the spin parameter λ (D'Onghia & Navarro, 2007). We will give further details on these numerical results compared to tidal torques simulation results in Sec. 2.5.

Note that the possibility of rotation due to some primeval vorticity field (von Weizsäcker, 1951; Gamow, 1952) was ruled out (Peebles, 1967; Efstathiou & Silk, 1983) as the vortical component of the velocity field in linear regime scales with the inverse of the scale factor a, and would have either needed galaxies to form too soon (Peebles, 1967) or it would have been damped too soon, leaving for no possible vorticity today. Also other possible argumentations, such as the in-

fluence of primordial magnetic fields on angular momentum acquisition, have been ruled out (Peebles, 1969), as the contribution of gravity to angular momentum formation is several orders of magnitude larger than the one due to magnetic fields.

It is worth stressing that one fundamental aspect to explain the spin parameter of spirals and the sizes of the disks has been to assume that galaxies formed within dark halos (Fall & Efstathiou, 1980). Models for disk formation within a dark halo have been proposed by Dalcanton et al. (1997) and Mo et al. (1998), who both try to find a solution fitting observations by including the interplay between the halo to the disk, disk stability and the cosmological evolution of the disk parameters. They both predict a Tully-Fisher relation with its scatter, and manage to track the evolution of the disks, and substantially find that the properties of the halo and how these properties vary with the environment determine the properties of the galaxy forming at its centre. So the density profile, its shape and the distribution of angular momentum determine structure, size and rotation curve of the galaxy (Lemson & Kauffmann, 1999).

2.4 Tidal Torque Theory

The mechanism proposed by Hoyle, the *Tidal Torque Theory* (TTT hereafter), is a rather simple and elegant way to describe the process of angular momentum formation for late-type galaxies compared to the very complex suite of overlapping physical aspects which are expected to go into such a theory, as we have seen in the last section, but yet it yields to a strikingly good description of this process. The plain idea is that, during the galaxy formation phase, when the regime of structure formation is still linear and mildly linear, the protogalaxies undergo the gravitational potential of the surrounding large scale structure, which exerts torques on the protogalactic object eventually setting it into rotation. When self gravitation starts dominating over the tidal torques the protogalaxy collapses, and its size diminishes. This reduces the lever arms and consequently the tidal torquing efficiency. This is when the galaxy decouples from the tidal field and binds into a defined object (this corresponds to the so-called turn-around, which occurs in the weakly non-linear regime Sugerman et al., 2000) which conserves the net angular momentum accumulated up to that point. A deeper consequence of the last mentioned feature is the scaling of the angular momentum with the mass $L \propto M^{5/3}$, already shown by Peebles (1969) in an SCDM cosmology. In fact the turn-around, which ultimately defines the angular momentum of an object, depends on the halo mass, in such a way that higher masses will acquire larger angular momenta.

TTT is a *perturbative* process described in the framework of *Lagrangian coordinates* based on the following ideas (see Porciani et al., 2002a,b):

- most of the angular momentum **L** is gained in linear or mildly non linear regime by tidal torques;

- only a small amount of angular momentum is exchanged between halos in the non-linear regime;
- baryonic material gains an angular momentum similar to the one gained by the dark matter halo.

In order to obtain an expression for the angular momentum we will make use of four assumptions nicely summarised by Porciani et al. (2002a,b):

- the flow is laminar, with a one to one correspondence between Eulerian and Lagrangian description;
- the velocities obey the so-called Zel'dovich approximation;
- the potential can be approximated by its second order Taylor expansion about the centre of mass of the protogalactic object;
- there is only a little contribution to the halo's angular momentum by nonlinear effects.

2.4.1 Lagrangian Perturbation Theory

Lagrangian and Eulerian perturbation theories (LPT and EPT hereafter) have been widely discussed in the framework of structure formation (see Bouchet (1996); Buchert (1996) and Bernardeau et al. (2002a) for extensive reviews). In fluid dynamics, the Eulerian frame of reference corresponds to the laboratory frame, and describes each field as a function of position and time ($\mathbf{x}$, t), whereas the Lagrangian frame of reference follows an individual fluid parcel throughout time. Consistently, while the Eulerian description follows the perturbations of the entire fields (density field $\delta(\mathbf{x}, t)$, or velocity field $\mathbf{v}(\mathbf{x}, t)$), the Lagrangian description follows the perturbations in the particle trajectories (Bouchet, 1996).

The reason to choose the Lagrangian framework over the Eulerian is in synthesis due to the regime of validity of the approximations used to guarantee linearity. In fact in the Eulerian framework the assumption is $\delta \ll 1$ (note this is an assumption about the field), which ceases very rapidly to be true, whereas Lagrangian perturbation theory, as we will see, relies on the assumption of small Lagrangian displacements and gradients, which turns out to be a weaker requirement (Bouchet, 1996; Buchert, 1996). Moreover, calculations in Lagrangian framework are less cumbersome, so that also enhancements of the theory up to non-linear regimes become affordable (Catelan, 1995; Catelan & Theuns, 1996b, 1997). We will therefore focus on Lagrangian coordinates, with the aim of finding a description of the angular momentum and its evolution in time within this framework, although the same calculations in Eulerian coordinates were carried out by Heavens & Peacock (1988).

Considering a collisionless fluid under Newtonian gravity (as has been done by Catelan, 1995), the key quantities in the Lagrangian description are therefore

the *trajectories of the particles* or, equivalently, individual fluid parcels (whereas in the Eulerian coordinate system it is the entire field as a function of position and time), which put into relation their initial (Lagrangian) coordinate $\mathbf{q}$ with their final (Eulerian) comoving coordinate $\mathbf{x}$ at a certain time t by means of a displacement field $\mathbf{S}$:

$$\mathbf{x}(\mathbf{q},t) = \mathbf{q} + \mathbf{S}(\mathbf{q},t) = \mathbf{q} + \nabla\Psi(\mathbf{q},t). \tag{2.3}$$

A Jacobian $J(\mathbf{q},t)$ is associated to this mapping $\mathbf{q} \mapsto \mathbf{x}(\mathbf{q},t)$, and it represents the change in volume between Eulerian and Lagrangian coordinates. Given that the Eulerian and Lagrangian coordinates are the same at $t = 0$, the Jacobian at that time is $J(t=0) = 1$, and $\rho/\rho_0 = J(0)/J(t)$. By considering the mass conservation condition:

$$d^3\mathbf{q} = (1+\delta)d^3\mathbf{x} \tag{2.4}$$

we immediately find a link between the Jacobian $J(\mathbf{q},t)$ and the density field $\delta[\mathbf{x},t]$:

$$1 + \delta[\mathbf{x}(\mathbf{q},t),t] = J^{-1}(\mathbf{q},t) \tag{2.5}$$

where the Jacobian is the following:

$$J(\mathbf{q},t) \equiv \frac{d\mathbf{x}}{d\mathbf{q}} = \left(\det\left[\delta_{ij} + \partial_i\partial_j\Psi\right]\right). \tag{2.6}$$

One can notice that when J vanishes the density field δ diverges, which is the typical condition of caustic formation process, and corresponds in this case to the occurrence of *shell crossing*.

The perturbation approach consists in expanding the displacement potential $\mathbf{S}$ in a perturbative series: $\mathbf{S} = \mathbf{S}_1 + \mathbf{S}_2 + \mathbf{S}_3 + ...$, where $\mathbf{S}_n = O(\Psi_1^n)$ is the n-th order approximation (Catelan, 1995; Catelan & Theuns, 1996b), whose first term gives the linear Lagrangian perturbation, and corresponds to the *Zel'dovich approximation*, strictly valid for $\delta \ll 1$:

$$\mathbf{S}(\mathbf{q},t) \sim \mathbf{S}^{(1)}(\mathbf{q},t) = D_+(t)\nabla\Psi_1(\mathbf{q}), \tag{2.7}$$

where $D_+(t)$ is the growth function which describes the cosmic evolution of the displacement field $\mathbf{S}$, and $\Psi_1(\mathbf{q})$ is the linear gravitational potential. Notice that the approximation made is two-fold: not only we consider a linear gravitational potential, but we consider it to be also constant in time, so that the temporal dependency present in Eqn. (2.3) is dropped in the latter expression.

Linear Lagrangian perturbation theory and angular momentum

The first one to apply LPT to obtain a formula for the angular momentum has been Peebles (1969). He considered the case of a spherical volume and found that such an object would gain angular momentum from tidal torques just in the case of second order perturbative description. One year later Doroshkevich

(Doroshkevich, 1970) showed that only the special symmetry given by a spherical volume would require a second order perturbative approach, but instead, in the more general case of a non-spherical volume, the angular momentum arises already in linear approximation (examples of why this holds will be given). We are interested in an expression for the angular momentum as a function of time, so by following the notation of Catelan & Theuns (1996a) we write first the angular momentum $\mathbf{L}$ of the matter contained in the volume V in Eulerian coordinates:

$$\mathbf{L}(t) = \int_{a^3V} d^3r\,\rho(\mathbf{r},t)(\mathbf{r}-\bar{\mathbf{r}})\times\mathbf{v}(\mathbf{r},t) = \rho_b a^4 \int_V d\mathbf{x}(1+\delta)(\mathbf{x}-\bar{\mathbf{x}})\times\mathbf{u}, \tag{2.8}$$

where $\mathbf{r}$ is the position around the centre of gravity $\bar{\mathbf{r}}$, $\rho = \rho_b(1+\delta)$ is the matter density field, ρ_b the background mean density, δ is the density contrast, and $\mathbf{v} = d\mathbf{r}/dt = \dot{a}\mathbf{x} + \mathbf{u}$ is the velocity field composed by the sum of the Universe expansion and the peculiar velocity $\mathbf{u} = a\dot{\mathbf{x}}$. It is important to notice that we do *not* know the volume V on which we are integrating but yet we can refer to the centre of mass of the object to define an angular momentum *relative to* the object.

Given the one-to-one relation between Eulerian and Lagrangian coordinates given in Eqn. (2.3) we rewrite the expression (2.8) in these coordinates:

$$\mathbf{L}(t) = \rho_0 a^5 \int_{V_L} d^3q(\mathbf{q}-\bar{\mathbf{q}}+\mathbf{S}(\mathbf{q},t))\times\dot{\mathbf{S}}(\mathbf{q},t) \tag{2.9}$$

where the Lagrangian volume V_L is in comoving coordinates and is a fixed initial region, which can be identified with a density peak region (from which a halo will eventually form from collapse). An important note to this expression is that it is still an *exact* expression for the angular momentum of a protogalactic object, since no approximation has been done yet.

Now, by applying the Zel'dovich approximation in Eqn. (2.7) the equation for the angular momentum simplifies to:

$$\mathbf{L}(t) \sim \mathbf{L}^{(1)}(t) = \rho_0 a^5 \int_{V_L} d^3q(\mathbf{q}-\bar{\mathbf{q}}+\mathbf{S}^{(1)})\times\dot{\mathbf{S}}^{(1)}dt = \rho_0 a^5 \dot{D}_+(t)\int_{V_L} d^3q(\mathbf{q}-\bar{\mathbf{q}})\times\nabla\boldsymbol{\Psi}_1(\mathbf{q}) \tag{2.10}$$

where we have used the relation:

$$\dot{\mathbf{x}}(\mathbf{q},t) = \dot{\boldsymbol{\Psi}}(\mathbf{q},t) \sim \dot{D}_+(t)\nabla\boldsymbol{\Psi}_1(\mathbf{q}) \tag{2.11}$$

obtained by the temporal derivation of Eqn. (2.3) and Eqn. (2.7) and the fact that the fact that $\nabla\boldsymbol{\Psi}_1\times\nabla\boldsymbol{\Psi}_1 = 0$.

The second approximation we make is to consider that the gradient of the displacement field $\Psi_1(\mathbf{q})$, where we will drop the subscript and which we will write $\Psi(\mathbf{q})$ for simplicity, does not vary too much across the Lagrangian volume V_L, in which case we are free to Taylor-expand it about the centre of mass $\bar{\mathbf{q}}$:

$$\partial_\alpha\Psi(\mathbf{q}) \simeq \partial_\alpha\Psi(\bar{\mathbf{q}}) + \sum_\beta(\mathbf{q}-\bar{\mathbf{q}})_\beta\Psi_{\alpha\beta}, \tag{2.12}$$

where $\Psi_{\alpha\beta}$ is the tidal shear at the point $\bar{\mathbf{q}}$:

$$\Psi_{\alpha\beta}(\bar{\mathbf{q}}) = \partial_\alpha \partial_\beta \Psi_{\alpha\beta}(\bar{\mathbf{q}}), \tag{2.13}$$

and is the only part really contributing to rotation build-up of the protogalaxy, since the gradient of the displacement field $\partial_\alpha \Psi(\bar{\mathbf{q}})$ only displaces it. The displacement field $\mathbf{\Psi}$ is related to the gravitational potential $\mathbf{\Phi}$, and can be computed as the solution of Poisson's equation $\triangle \mathbf{\Psi} = \delta$ from the cosmological density field δ. By now recognising now the quadrupole of the mass distribution, or the inertia tensor $I_{\beta\sigma}$, as:

$$I_{\beta\sigma} = \rho_0 a^3 \int_{V_L} d^3q (\mathbf{q} - \bar{\mathbf{q}})_\beta (\mathbf{q} - \bar{\mathbf{q}})_\sigma \tag{2.14}$$

one obtains the final expression for the angular momentum components:

$$L_\alpha(t) = a^2(t)\dot{D}_+(t) \sum_\beta \sum_\gamma \epsilon_{\alpha\beta\gamma} \sum_\sigma I_{\beta\sigma} \Psi_{\sigma\gamma}, \tag{2.15}$$

which basically states that the tidal field of an inhomogeneous distribution of matter couples to the inertia tensor of the protogalactic object therefore inducing a rotation or, otherwise said, a net angular momentum relative to its centre of gravity. $\epsilon_{\alpha\beta\gamma}$ is the Levi-Civita antisymmetric tensor. We dropped the superscript indicating that this expression for the angular momentum is a first order approximation.

It is very useful to consider the case in which we write the angular momentum in the eigenframe of the tidal shear (Dubinski, 1992; Porciani et al., 2002a; Schäfer, 2009). The components are then:

$$L_\alpha \propto I_{\beta\gamma}(\Psi_{\beta\beta} - \Psi_{\gamma\gamma}). \tag{2.16}$$

The largest component of $\mathbf{L}$ will be the one with the largest value if $|\Psi_{\beta\beta} - \Psi_{\gamma\gamma}|$. Given $\Psi_1 \leq \Psi_2 \leq \Psi_3$, the largest component ought to be $L_2 \propto |\Psi_3 - \Psi_1|$. This means that we expect the angular momentum to align itself parallel to the intermediate axis of the tidal shear. We will see in Sec 2.5 that this very important feature has been checked in numerical simulations.

It is insightful to rewrite the expression in Eqn. (2.10) (Bouchet, 1996):

$$\begin{aligned} \mathbf{L}(t) &= \rho_0 a^5 \dot{D}_+(t) \int_{V_L} d^3q (\mathbf{q} - \bar{\mathbf{q}}) \times \nabla \mathbf{\Psi}_1(\mathbf{q}) = \\ &= \rho_0 a^5 \dot{D}_+(t) \int_\Gamma \mathbf{\Psi}_1(\mathbf{q} - \bar{\mathbf{q}}) \times \mathrm{d}\mathbf{\Gamma}, \end{aligned} \tag{2.17}$$

where we have used Gauss' divergence theorem transforming the volume integral into an integral over the boundary surface Γ of the Lagrangian volume containing the protogalaxy. It is thus immediately clear that when the protogalactic

object is spherical the integral vanishes, therefore leading to a zero angular momentum at first order. The same can be seen by calculating the inertia tensor of a spherical volume, which is (Catelan & Theuns, 1996a):

$$I_{\beta\sigma} = \frac{4\pi}{15}\rho_0 a^3 (q-\bar{q})^5 \delta_{\beta\sigma} \tag{2.18}$$

and therefore the angular momentum $L_\alpha \propto \epsilon_{\alpha\beta\gamma}\Psi_{\beta\gamma} = 0$.

The general condition under which the angular momentum vanishes can be shown by following the notation of Schäfer (2009). By rewriting the tensorial product of the inertia and shear tensors as the tensor $\mathbf{X} = \mathbf{I\Psi}$, one can divide the latter in two components, a symmetric and an antisymmetric one:

$$\mathbf{X} = \mathbf{X}^+ + \mathbf{X}^-, \tag{2.19}$$

defined by means of the commutator and the anticommutator as follows:

$$\begin{aligned} \mathbf{X}^+ &\equiv \frac{1}{2}\{\mathbf{I},\mathbf{\Psi}\} \\ \mathbf{X}^- &\equiv \frac{1}{2}[\mathbf{I},\mathbf{\Psi}], \end{aligned} \tag{2.20}$$

and whose components are:

$$\begin{aligned} X^+_{\beta\gamma} &= \frac{1}{2}\sum_\sigma (I_{\beta\sigma}\Psi_{\sigma\gamma} + \Psi_{\beta\sigma}I_{\sigma\gamma}) \\ X^-_{\beta\gamma} &= \frac{1}{2}\sum_\sigma (I_{\beta\sigma}\Psi_{\sigma\gamma} - \Psi_{\beta\sigma}I_{\sigma\gamma}). \end{aligned} \tag{2.21}$$

The symmetry properties of these components are:

$$\begin{aligned} (\mathbf{X}^+)^t &= \frac{1}{2}(\mathbf{I\Psi} + \mathbf{\Psi I})^t = \frac{1}{2}(\mathbf{\Psi I} + \mathbf{I\Psi}) = +\mathbf{X}^+ \\ (\mathbf{X}^-)^t &= \frac{1}{2}(\mathbf{I\Psi} - \mathbf{\Psi I})^t = \frac{1}{2}(\mathbf{\Psi I} - \mathbf{I\Psi}) = -\mathbf{X}^-. \end{aligned} \tag{2.22}$$

When inserting these components in the relation for the angular momentum (Eqn. 2.15) we obtain:

$$L_\alpha = a^2\dot{D}_+\epsilon_{\alpha\beta\gamma}(X^+_{\beta\gamma} + X^-_{\beta\gamma}) = a^2\dot{D}_+\epsilon_{\alpha\beta\gamma}X^-_{\beta\gamma}, \tag{2.23}$$

since the multiplication of an antisymmetric tensor by a symmetric one is always zero. Eqn. (2.23) very nicely shows that the condition of having a perfect alignment between the principal axes of the inertia and shear tensors, i.e. the two tensors sharing common eigensystems and being simultaneously diagonsable, yields to a vanishing commutator and therefore to no angular momentum. In order to have a non-zero angular momentum, the commutator between inertia and deformation tensor must not vanish, meaning that the eigensystems of the tensors must be skewed relative to each other. As discussed in Catelan &

Theuns (1996a), this situation is usually fulfilled since the principal axes of the inertia tensor depend on a very irregular shape of the initial volume V_L of the protogalaxy, whereas the principal axes of the shear tensor depend on the location of neighbour matter fluctuations (White, 1984). We are going to go back to this "sine qua non" condition for angular momentum build-up when talking about angular momentum correlations between close-by galaxies, as this feature has been parametrized as an average effect in N-body simulations within this context.

The symmetric component $\mathbf{X}^+$, even though not being responsible for the galaxy spin-up, contributes in anisotropically deforming the protogalactic region prior to collapse, when the assumption of linear structure formation holds.

The time evolution of the angular momentum is completely described by the term $a(t)\dot{D}(t)$ containing the scale factor and the time derivative of the growth factor. In an Einstein-de-Sitter model this equals $2(t/t_0^2)/3$, which makes $L(t) \propto t$ in linear theory, as shown by Doroshkevich (1970).

As already mentioned, during its lifetime a galaxy undergoes several processes such as dynamical friction of infalling gas clumps, major mergers, star formation and feedback many of which introduce strong non-linearities in the game able to dissipate the previously generated angular momentum. Furthermore, non-linearities in the density field itself would lead to results departing from the standard ones obtained in linear approximation.

Non-linear Lagrangian perturbation theory

A step further was taken by Catelan & Theuns (1996b) and Catelan & Theuns (1997) who considered two possible ways of departing from linearity. Based on the previous work of Bouchet et al. (1992); Buchert (1994); Catelan (1995), in the first paper the authors applied further perturbative corrections to the displacement potential while still considering the matter density perturbations to be Gaussian distributed, and in the second they considered instead the case of a non-Gaussian initial density field.

With the aim of studying the non-linear spin dynamics in the mildly non-linear regime, Catelan & Theuns (1996b) rewrite the angular momentum as:

$$\mathbf{L}(t) = \eta_0 \int_{V_L} d\mathbf{q} \left[\sum_{i=0}^{\infty} \mathbf{\Psi}_i(\mathbf{q},t) \right] \times \frac{d}{dt} \left[\sum_{j=0}^{\infty} \mathbf{\Psi}_j(\mathbf{q},t) \right] \equiv \sum_{h=0}^{\infty} \mathbf{L}^{(h)}(t), \tag{2.24}$$

where

$$\sum_{h=0}^{\infty} \mathbf{L}^{(h)}(t) \equiv \sum_{j=0}^{h} \eta_0 \int_{V_L} d\mathbf{q} \mathbf{\Psi}_j(\mathbf{q},t) \times \frac{d\mathbf{\Psi}_{h-j}(\mathbf{q},t)}{dt} \tag{2.25}$$

with $\mathbf{\Psi}_0 \equiv \mathbf{q}$ and hence $\mathbf{L}^{(0)} = 0$. In order to calculate the second order corrections to the ensemble average $\langle \mathbf{L}^2 \rangle$ they need corrections to $\mathbf{L}$ up to the third order. They recover the growth of the perturbative corrections to $\langle \mathbf{L}^{(1)2} \rangle^{1/2}$ to be proportional to $t^{5/3}$ in an Einstein-de-Sitter Universe, as previously shown

by Peebles (1969). Furthermore, given the proportionality of these corrections to the invariant of the inertia tensor $\mu_1^2 - 3\mu_2$, where $\mu_1 \equiv \iota_1 + \iota_2 + \iota_3$ and $\mu_2 \equiv \iota_1\iota_2 + \iota_1\iota_3 + \iota_2\iota_3$ are the first and second invariant of the inertia tensor [2], they manage to express the order of magnitude of the nonlinear correction to the linear one: In fact they find that the variance $\langle \mathbf{L}^{(1)2} \rangle$ increases by a factor of 1.6 in their third order calculations compared the first order ones. This result, in addition to the linear (and therefore mild) growth of the angular momentum with time, yields to the conclusion that the initial torque is a good estimate for the tidal torque in mildly non-linear regimes, i.e. until turn-around.

Catelan & Theuns (1997) instead considered another possible source of non-linearities, aiming to answer to the question whether initial non-Gaussian conditions might make the analytical linear calculation of the angular momentum deviate strongly during mildly non-linear regime. For this purpose they consider multiplicative models, i.e. non-Gaussian models obtained by the non-linear transformation of an underlying Gaussian random field (examples of these are the χ^2 and lognormal distributions, which are used by the authors). They find a lower growth of the perturbative corrections with time, $\propto t^{4/3}$ instead of $\propto t^{5/3}$ of the Gaussian case for an Einstein-de-Sitter model. They furthermore find that for χ^2 and linearised lognormal distributions the deviation is of the order of the first linear term, i.e. these statistics induce $O(1)$ corrections to the linear angular momentum, and deduct that higher order contributions might well likely be non-negligible.

2.5 Numerical simulations

A great deal of effort has been put into numerical studies of TTT, angular momentum acquisition and disk formation, mostly aimed to confirm the validity of analytical results and approximations, and to shed light on other possible important missing tiles. In this section we will skim through the numerical simulations which have been carried out throughout time. The investigations concerning TTT have in common the attempt of recovering features such as the relation between angular momentum and mass, specifically the proportionality $L \propto M^{5/3}$, growth of the spin in time, recovery of the spin parameter lognormal distribution, and in general tests on the approximations made by the TTT theory involving the hypothesis of linearity and Zel'dovich approximation (shell crossing), direction and magnitude of spin, and importance of nonlinear effects. We also quickly review other numerical investigations about spin and local environment and simulations including baryonic physics separately.

[2] We remind that the n-th invariant of a symmetric matrix (in this case the inertia I), can be found by calculating the trace $\mathrm{tr}(I^n)$

2.5.1 TTT simulations

The very first simulations applied to TTT were carried out by Peebles (1971b), with a series of small numerical experiments (where the number of particles used was $N = 100$) which confirmed his previous calculations. Soon after Efstathiou & Jones (1979) increased the number of particles used for the simulation, recovering the fact that most of the angular momentum of the galaxy was acquired during early stages, and confirming that deviations at later stages were due to nonlinear effects. They also recovered the expected $L \propto M^{5/3}$ and $L \propto t^{5/3}$ scaling relations. The same was found by White (1984) too, who also added that the total final spin can be correctly estimated only to order of magnitude due to final non-linear effects.

Barnes & Efstathiou (1987) confirm the low values of the spin parameter for ellipticals ($\lambda \sim 0.05$), the linear growth with time of the spin, and reproduce the scaling relation $L \propto M^{5/3}$. They furthermore find a tendency of spins to be perpendicular to major axes of the object, while finding that tidal torque produces no significant spin orientation effect (lack of spin alignment). Dubinski (1992) study the effects of tidal shear on dark halos, since tidal shear could in principle determine both the shape of the final object (i.e. its structure) and change the kinematics of dark halos. They find no relationship between the initial shape of the density peak and the final dark halo one, whereas they do find the importance of tidal torques in establishing the kinematics of dark halos. They also find a strong tendency of the spin to align with the dark halo's intrinsic minor axis. Sugerman et al. (2000) find that the angular momentum grows linearly until turn-around, turns over during shell crossing (i.e. when the inner mass shells pass throughout the centre) and remains constant after, when virialization and relaxation occur. The linear tidal torquing therefore overestimates the magnitude of the spin and the true turn-around. The scaling relation between mass and spin is also retrieved. Porciani et al. (2002a,b) argue that TTT is good for the estimation of the spin amplitude in terms of its order of magnitude, and that non-linearities induce significant (up to 50°) changes in the spin direction and weaken spin correlations too. This general trend is better at high redshift because nonlinearities are not yet present at high redshifts.

An important finding, to be stressed here, concerns the fact that the standard approximations of TTT (second order expansion of potential, Zel'dovich approximation and smoothing of the shear tensor on the protohalo scale) are good and cannot really be improved. They therefore deduce that the emergence of non-linearities constitute the only problem for which final spins deviate from the linear ones.

Concerning non-linearities, Lee & Pen (2008) parametrise the degree of dependence of the orientations of the halo spins on the linear and non-linear tidal field such that any deviation from linearity involves a nonzero value of the defined parameter. By using halo catalogues from the Millennium Run Simulation for a ΛCDM cosmology, they find an increase of linearity with redshift, such

that linear tidal fields are more representative of the high redshift population, whereas the non-linear parameter strongly deviates from zero today ($z = 0$), which implies that the non-linear tidal effects are dominant today, inducing correlations on larger scales ($\sim 10h^{-1}$Mpc) than predicted by linear TTT ($\sim 1h^{-1}$Mpc, see Schäfer & Merkel, 2012). Furthermore the non-linear parameter grows with the specific angular momentum.

Libeskind et al. (2013) focus their attention on non-linearities induced by the vorticity flow. In fact they argue that halos find themselves embedded in vorticity flows after the linear and mildly non-linear regimes (i.e. after the regime of validity of TTT), and they expect therefore the angular momentum growth to be affected by this vorticity. They actually find that the curl of the velocity field is very important in the determination of the spin of the halo, and find a significant alignment signal: the vorticity tends to be perpendicular to the axis of the fastest collapse of the velocity shear tensor, independent of the mass of the halo and its environment. They therefore propose that the angular momentum growth can be divided in two steps: one well described by TTT, and the second (close to virialization time) in which the spin partially aligns with the vorticity.

This has been observationally supported by Lee (2013), who actually finds a very strong alignment between galaxy spins and the local vorticity field, and study how the alignment strength depends on the environment. Different behaviours appear between knot and filament regions (vorticity vectors are found to be anti-aligned with the directions of maximal volume compression) and sheets and voids (the anti-alignment is found here with the direction of the minimal volume compression).

2.5.2 Angular momentum and cosmic web

Another filed of research developed on the basics of TTT has been devoted to possible alignments between angular momenta and the ambient large scale structure in terms of the sheets, voids and filaments forming the cosmic web as we know it from simulations and observations. The alignments of the dark halo axes with the large scale structure and the orientation of the galactic disks constitute main subject of these studies conducted by means of numerical simulations.

Navarro et al. (2004), other than recovering the alignment of the spin with the intermediate principal axis of the inertia tensor, numerically study the orientations of galactic disks relative to the surrounding large scale structure, finding that there is a tendency of the rotation axis of the disk to be aligned perpendicularly to the minor axis of the surrounding structure, as a consequence of angular momentum acquisition at early stages by TTT. A trend in the alignment of galactic spin with the minor axes of the neighbouring structure was found by Bailin & Steinmetz (2005), who find it to lie perpendicular to the filaments.

A very organic study in this sense was carried out by Aragón-Calvo et al. (2007), who separate the cosmic structure in wall-like and filament-like structures and study the correlations between spins and shapes of dark halos and the

orientation of their host structure. Again the perpendicular alignment is strongly found in both cases of walls and filaments and, furthermore, it is found that the orientation of the spin depends on the mass, such that low mass halos are more likely to be oriented with the parent substructure. A categorisation of the position of halos, i.e. whether in clusters, filaments, sheets or voids is carried out by Hahn et al. (2007), who also try to grasp the relation between halo masses in clusters, and properties such as the degree of sphericity or the magnitude of the spin, finding that low mass halos are more prolate and have higher median spin in clusters than in filaments. Moreover, they find that halo spins tend to lie within the plane of symmetry of the mass distribution in sheets. Specific attention to voids was given by Patiri et al. (2006) and Brunino et al. (2007), who study the alignment of halo spins with voids, finding that the minor axis of the halos point preferentially in the direction of the centres of the voids.

Sousbie et al. (2008) find perpendicular spins to filaments, whileSousbie et al. (2009) show that the Zel'dovich approximation is able to well reproduce the time evolution of the cosmic web, regardless of the non-linearities induced today.

Another comprehensive description is given by Libeskind et al. (2012). They assign to each halo a "web-type": knot, filament, sheet or void, and analyse the orientation of the halos spin with the velocity shear field eigenvectors, finding that there is an alignment of subhalos' spins with the intermediate eigenvector in knots, filaments and sheets, which is interpreted as the role played by the tidal velocity shear on the infall kinematics of substructures within virialised objects. They also find the halo spin axis to point along filaments and to lie in the plane of cosmic walls for low mass halos.

Lastly, Codis et al. (2012) investigate correlations between spin of dark halos and their large-scale environment. They find a significant signal for filaments over a smoothing scale of $5h^{-1}$ Mpc: they deduce therefore that the orientation of the spin is sensitive to the environment. The signal is also mass-dependent: low masses are usually found to be aligned with large-scale filaments, more massive objects tend to be perpendicular to these. In general the mass transition is redshift dependent.

2.5.3 Dependency of the spin on local environment

Lemson & Kauffmann (1999), based on the fact that the structure and history of a galaxy can be fully determined by the history of its surrounding halo, study the properties of DM halos as a function of local density and environment. They specifically look at correlations between some halo properties (mass, formation redshift, concentration, shape and spins) and both their environment and the surrounding tidal field, finding that the mass is the only property depending on the environment. The hight of a peak is found to be anticorrelated with its angular momentum (because high peaks collapse early, so there is no time for tidal torques to act). On the other hand, though, it is expected to be correlated, since high peaks experience higher tidal fields. These two behaviours are expected to

cancel out in order to Heavens & Peacock (1988), and as is confirmed by Steinmetz & Bartelmann (1995), so that there is a very weak dependence of the spin on the environment. This weak correlation was confirmed by N-body simulations of Dubinski (1992), who find no correlation between the shape of the initial density peak and the shape of the final collapsed halo.

2.5.4 Simulations on dark halos and gas: angular momentum catastrophe

There have been also attempts to study the formation of disks in N-body simulations accounting for the baryonic component within a ΛCDM cosmology, as for instance Steinmetz & Navarro (2002). Although an exhaustive compilation of all the work carried out in this direction is impossible and out of track in this context, it is interesting to focus the attention on one of the major problems encountered by these numerical simulations, i.e. the *angular momentum catastrophe*. As also Mayer et al. (2008) very well summarised, the predictions of the analytical disk models within the framework of the ΛCDM model match the real size of galaxies disks, but it was found that simulations consistently underproduced the scalelengths of real observed galaxies. This mismatch lead people to question the validity of the ΛCDM paradigm. Further simulations and studies (Governato et al., 2004; D'Onghia, 2008; Governato et al., 2007, 2008; Zavala et al., 2008; Scannapieco et al., 2008; Burkert, 2009) showed the root of this mismatch to be found in the fact that, in numerical simulations, baryons collapse too early and cool too much. Consequently the disks collapse too much and, while still allowing for later mergers, they also allow for angular momentum redistribution (or transfer) from baryons to dark halos.

2.6 Summary

This chapter summarises the physical mechanisms which enabled galaxies to acquire their current morphology and their angular momentum. We therefore review the differences between elliptical and spiral galaxies mainly in what concerns their rotation, trying to create a link between this observational property and possible formation scenarios. Other observational features discriminating between the two galaxy types are not further discussed here, so we stress that this chapter does not represent a full and thorough description of elliptical and spiral galaxies.

Great attention is devoted to the theory of tidal torques both in terms of analytical analysis and numerical simulations. The main points of the chapter can be summarised as follows:

- the rotational support of a galaxy can be well described by the spin parameter λ, which assumes typical values of $\lambda \sim 0.5$ for late-type galaxies and $\lambda \sim 0.05$ for early-type galaxies.

- in the attempt of explaining such difference among galaxy types in terms of rotation, several possible scenarios arise: ellipticals seem to have formed in the so-called *merging scenario*, and appear to be remnants of mergers of disk-like galaxies, whereas spirals seem to be spun up by tidal fields from the large scale structure acting at the very early stages of their formation, i.e. at the stage of protogalaxies. The latter model goes by the name of tidal torque theory (TTT).

- TTT is a perturbative process which applies in the linear and mildly non-linear regime of density fluctuations. It assumes no substantial difference in the spin acquired by the baryonic and non-baryonic component, and that non-linear effects leading to exchange of angular momentum to be negligible.

- Given that the description of spin acquisition is equivalent in Lagrangian and Eulerian coordinates, Lagrangian coordinates appear to be a preferable framework to work in, mostly due to the much easier calculus level offered. Also, the key assumption of linear regime, phrased as $\delta \ll 1$ in an Eulerian context, becomes a weaker and longer lasting requirement in Lagrangian coordinates (displacements of the particles are required to be small and the gradients of the gravitational potential to be smooth).

- Tidal torques act on the protogalactic object setting it in rotation until the gravitational collapse decouples the object from its background (turn-around time). This reduces the lever arm of the torques, reducing its efficiency, and leaves the object with a spin acquired up to that point.

- The angular momentum, as developed in linear Lagrangian perturbation theory, is proportional to the tensorial product of inertia $\mathbf{I}$ and the tidal shear $\mathbf{T}$ tensors, which need to have misaligned eigensystems in order not to produce a vanishing spin. Furthermore, the spin is found to grow linearly in time ($L \propto t$) in an SCDM cosmology, and have a specific scaling relation with mass ($L \propto M^{5/3}$).

- Numerical simulations widely agree in the finding that TTT gives a fairly good description of the spins of galaxies up to turnaround (Dubinski, 1992; Sugerman et al., 2000; Porciani et al., 2002a,b), when non-linear effects due to mergers (angular momentum exchange), feedbacks and baryonic dissipation processes are found to become more important and non-negligible. Lately it has been found that vortices arising very close to the virialization time and embedding the halos show a significant correlation with the spins of the objects (Libeskind et al., 2013; Lee, 2013).

- In all TTT simulations the spin axis has been found to be parallel to the intermediate principal axis of the tidal shear tensor (as an example see Dubinski, 1992), due to the fact that the largest component of the angular momentum is proportional to the largest discrepancy between the tidal field eigenvalues.

- Numerical investigations of the alignment of the spins with the cosmic web in non-linear structure formation have also been carried out throughout the years, leading to the the results that: spins tend to lie perpendicular to filaments and sheets if the halo mass is high, but aligned to these for lower masses, and point preferentially radially to voids.

Chapter 3

THE PHYSICS OF INTRINSIC ALIGNMENTS

3.1 Introduction

As much as the offspring contains imprints of the parents in terms of its genetic makeup, galaxies born close by share information about the initial conditions they underwent during the very beginning of their formation process. These initial conditions - the "parents" of sibling galaxies - plainly are the gravitational potentials around them at the moment of their birth. Following this analogy this means that, as much as we would expect to find correlations among brothers and sisters (at least) in terms of their appearance, we will indeed expect to find correlations between neighbouring galaxies once again in terms of their appearance, although, in this case, their appearance is not constituted by their luminosity, but rather their *shape*. These correlations go by the name of *Intrinsic Alignments* (IA hereafter), *shape alignments*, or *intrinsic correlations*. In fact, whatever the galaxy type, luminosity and colour is, we expect that galaxies which formed in spatially close locations were moulded in similar ways or underwent similar conditions once formed, and therefore still bear, at least partly, this information codified in their shape.

In the case of late-type galaxies, correlations among the shapes indicate correlations among their angular momenta, provided that, for each galaxy, the spin is perpendicular to the galactic disk (Dalcanton et al., 1997; Mo et al., 1998; Buchalter et al., 2001) and that the spin of the baryonic disk corresponds to the spin of the dark matter halo in which the galaxy is embedded. In other words, the galaxies experienced similar tidal torques, which led to angular momenta similar in direction.

In the case of early-type galaxies, the orientation of the galaxy image can be determined by the shape of the halo in which the galaxy formed (Catelan et al., 2001). In fact, as already said, the angular momentum in elliptical galaxies is not dominant and the rotation is mainly supported by the dispersion of the stellar

velocities, so that the shape cannot be determined by the spin as is the case for spiral galaxies. As will be discussed in Sec. (3.6), the idea behind this picture is that the tidal fields acting on the galaxies can either stretch or compress them producing respectively prolate or oblate halos and will, on average, lead to a net elongation of the halos.

We can therefore see that there is a common denominator for the origin of IA, in both the cases of late-type and early-type galaxies: Specifically, whatever the origin for the spins of the galaxies, the correlations of the underlying tidal field (Catelan & Porciani, 2001; Catelan et al., 2001; Crittenden et al., 2001) will contribute to the IA.

Intrinsic correlations thus have to do with the correlation length of the tidal field, as will be discussed in Sec. 3.2. Sec. 3.4 and 3.6 will deal with the modelling of, respectively, the late-type and the early-type IA, which differ in the assumptions they make, as already mentioned above. In Sec. 3.7 we will provide a round up of N-body simulations applied to IA, while Sec. **??** offers an overview on IA detections. Finally we summarise the basic ideas of this chapter in Sec. 3.8.

3.2 Tidal correlation lengths

Any attempt to evaluate the correlations between the spins of galaxies at a given separation θ on the sky must rely on considerations about the range of "influence" of what contributes in the first place to the formation of the spins, namely the inertia of the object and the external tidal field. In particular the latter has been shown to correlate over distances much larger than the mass-density (or inertia) correlation length (Catelan & Porciani, 2001), and appears to be a salient feature in explaining not only spins and IA, but more in general also galaxy formation. In other words the feature of spatial locality of such processes and their apparent independency one from another actually mask a correlation at a deeper level which eventually shows up in the IA.

From the Fourier space perspective, one could say that in the process of formation of a galaxy (or a protogalaxy) all the modes in the initial density field contribute: the short wavelengths contributing to the shape of the object, and the long wavelengths contributing to the tidal field. Notice that tidal shear field has the same correlation length of the density field (due to Poisson's equation the trace of the tidal field gives the density field), whereas the inertia has the correlation length of the curvature of the density field, that is its second derivative (Schäfer, 2009).

Catelan & Porciani (2001) measured the correlation length for tidal shear fields without any assumption given about whether the distribution of the gravitational potential is Gaussian or not. Quantitatively they achieve a study of the correlations of the tidal field by carrying out a decomposition of the tidal tensor, and by calculating the correlator among the different components at two different points in space. Furthermore they also define a scalar quantity, dimen-

sionally the square of the correlation function, which is meant to carry the information about the size of the tidally correlated sphere about any given point. All these correlation functions give rise to correlation lengths roughly between 1 and 30 Mpch^{-1} on cluster scales. The mass correlations appear instead to be much weaker, up to only 15 Mpch^{-1}.

These scales appear therefore to be fundamental for the study of IA. We will see in the following sections how this interplay between the different correlation lengths of inertia and tidal shear can be used to simplify otherwise very cumbersome calculations.

3.3 Intrinsic ellipticity correlations

The aim of this chapter is to study correlations between galaxy shapes, which equivalently means that we would like to study the statistics of a field of images of galaxies. In order to achieve this the first goal is to define the ellipticity of a galaxy, which must be a two-dimensional quantity derived by the projection of a three-dimensional ellipsoid onto the celestial sphere. This projected shape of the galaxy on the sky is an ellipse with semi-axes a, b, ($a > b$). Once the coordinate system is chosen, the orientation of the ellipse will depend on the angle ϕ between the major axis of the ellipse and the coordinate system, and the magnitude instead is:

$$|\epsilon| = \frac{a^2 - b^2}{a^2 + b^2}. \tag{3.1}$$

The ellipticity can be well and synthetically quantified by the relation (Crittenden et al., 2001):

$$\epsilon = \epsilon_+ + i\epsilon_\times = |\epsilon| e^{2i\phi}, \tag{3.2}$$

where i is the imaginary unit: The ellipticity is thus a complex quantity able to reproduce the symmetry property that, if an ellipse is rotated by 180°, its shape will not be affected.

The two point correlation function of the shapes of two galaxies positioned at angular positions θ' and θ'', separated by a distance $\theta = \theta' - \theta''$ on the sky, will be denoted as $\langle \epsilon(\theta')\epsilon^*(\theta'')\rangle$, and is defined as the average over all possible realisations of the product between the ellipticity of a galaxy at a position θ' and the ellipticity of another galaxy at position θ'':

$$\langle \epsilon(\theta')\epsilon^*(\theta'')\rangle = \langle \epsilon'\epsilon''^*\rangle = C(\theta) \tag{3.3}$$

Due to the fact that the ellipticity has two components, the intrinsic correlation will be a four-point correlator which can be though simplified to the sum of two two-point correlation contributions (Wick's theorem, Wick, 1950):

$$\langle \epsilon'\epsilon''^*\rangle = \langle \epsilon'_+\epsilon''^*_+\epsilon'_\times\epsilon''^*_\times\rangle = \langle \epsilon'_+\epsilon''^*_+\rangle + \langle \epsilon'_\times\epsilon''^*_\times\rangle. \tag{3.4}$$

Note the fact that the cross-correlations $\langle \epsilon'_+ \epsilon''^*_\times \rangle = \langle \epsilon'_\times \epsilon''^*_+ \rangle = 0$ by definition if statistical parity invariance holds. Being the components of the complex ellipticity, they are independent one from another.

These correlations between the two ellipticity components ϵ_+ and $\epsilon_\times$ can be described using two correlation functions $C_{++}(\theta) = \langle \epsilon_+(\theta')\epsilon_+(\theta'') \rangle$ and $C_{\times\times}(\theta) = \langle \epsilon_\times(\theta')\epsilon_\times(\theta'') \rangle$, which are conveniently combined into two correlation functions $C_\pm(\theta)$:

$$C_+(\theta) = C_{++}(\theta) + C_{\times\times}(\theta) \tag{3.5}$$

$$C_-(\theta) = C_{++}(\theta) - C_{\times\times}(\theta) \tag{3.6}$$

Finally, ellipticity correlation functions can be transformed to the spectra $C^\epsilon_E(\ell)$ and $C^\epsilon_B(\ell)$ of the gradient and vorticity modes of the ellipticity field,

$$C^\epsilon_E(\ell) = \pi \int \theta \mathrm{d}\theta \, [C_+(\theta) J_0(\ell\theta) + C_-(\theta) J_4(\ell\theta)] \,, \tag{3.7}$$

$$C^\epsilon_B(\ell) = \pi \int \theta \mathrm{d}\theta \, [C_+(\theta) J_0(\ell\theta) - C_-(\theta) J_4(\ell\theta)] \,, \tag{3.8}$$

by Fourier transform (Kaiser, 1992; Schneider et al., 2002; Schneider & Kilbinger, 2007; Fu & Kilbinger, 2010). C_E and C_B, the so-called $E-$ and $B-$modes, will mostly be used when we will talk about IA and weak lensing in Chap. 4.

In this section we have presented the basis for any model of IA. In the next sections we are going to talk about the two basilar models for IA, the so-called "*quadratic*" and "*linear*" models.

3.4 Late-type galaxies: the quadratic model

The fundamental idea of the quadratic model is that the orientation of the galaxy image is determined by the angular momentum of the three-dimensional halo in which the galaxy is formed. Another hypothesis at the basis of this model is the fact that the angular momentum is perpendicular to the disk of the galaxy, and that the angular momentum of the baryonic disk and that of the dark matter halo correspond. Note that already these assumptions are quite strong, but given the degree of complexity of the problem, and our little knowledge about galaxy formation, these assumptions seem reasonable. Within the framework of the quadratic model there are different possible ways of modelling the IA signal. We are are going to discuss in detail two quadratic models, upon which the results in Chap. 5 have been obtained. A first analysis of the quadratic model for intrinsic correlations has been carried out by (Crittenden et al., 2001), whose notation will be broadly used in this section.

3.4.1 Ellipticity of a spiral galaxy

In the previous section we have given a definition of the ellipticity as a spin-2 quantity coming from the projection of the three-dimensional ellipsoid onto

the two-dimensional sky. In the case of spiral galaxies the three-dimensional ellipsoid can be approximated to a thin disk, with the angular momentum perpendicular to the disk plane. If we think of projecting such a galaxy on the sky the shape of the galaxy will certainly depend on the angle under which it is observed. This situation is described in Fig. (3.1). In fact, if we consider a disk-like galaxy as a circle of radius R with a certain thickness α, and we define θ to be the angle between the angular momentum of the galaxy and the line of sight (which corresponds to the z-axis), by defining a, b to be respectively the major and the minor axis of the projected ellipse, we have:

$$\begin{aligned} a &= R \\ b &= R\cos(\theta) \end{aligned} \tag{3.9}$$

and the magnitude of the ellipticity is given by:

$$|\epsilon| = \alpha\frac{a^2-b^2}{a^2+b^2} = \alpha\frac{1-\cos^2(\theta)}{1+\cos^2(\theta)} = \alpha\frac{1-L_z^2}{1+L_z^2}, \tag{3.10}$$

where $0 < \alpha < 1$. There are two possible extreme situations:

- $\theta = 0°$, i.e. the z-axis coincides with the angular momentum, therefore $a = b = R$, and by definition the magnitude of the ellipticity is $|\epsilon| = 0$: The galaxy is face-on and seen as circular;
- $\theta = 90°$, i.e. the z-axis is perpendicular to the angular momentum, and in this case $a = R$ and $b \sim 0$ (because of the thickness α b will never be absolutely 0), so that the magnitude $|\epsilon| \sim 1$: The galaxy is edge-on, and appears as highly elliptical.

3.4.2 Intrinsic Alignments

The assumption is that the intrinsic ellipticity of a galaxy arises from its angular momentum, its shape and orientation, i.e. $\epsilon = \epsilon(\mathbf{S}, \hat{\mathbf{L}})$, where $\mathbf{S}$ denotes both the shape and the orientation of the ellipsoid, and $\hat{\mathbf{L}}$ is its angular momentum.

If we calculate now the correlation between ellipticities of galaxies at different positions we obtain:

$$\langle \epsilon\epsilon'^{*} \rangle = \int d\mathbf{S}d\mathbf{S}'\, d\hat{\mathbf{L}}d\hat{\mathbf{L}}'\, \epsilon(\mathbf{S}, \hat{\mathbf{L}})\epsilon(\mathbf{S}', \hat{\mathbf{L}}')P(\mathbf{S}, \hat{\mathbf{L}}, \mathbf{S}', \hat{\mathbf{L}}'), \tag{3.11}$$

where $P(\mathbf{S}, \hat{\mathbf{L}}, \mathbf{S}', \hat{\mathbf{L}}')$ denotes the joint probability distribution of finding the shapes and angular momenta of the first galaxy, $(\mathbf{S}, \hat{\mathbf{L}})$, and the second galaxy, $(\mathbf{S}', \hat{\mathbf{L}}')$. There are a few simplifications to this expression which can be made before we turn to talk about the different treatments of the two quadratic models we are going to consider. The following assumptions are valid for both these models.

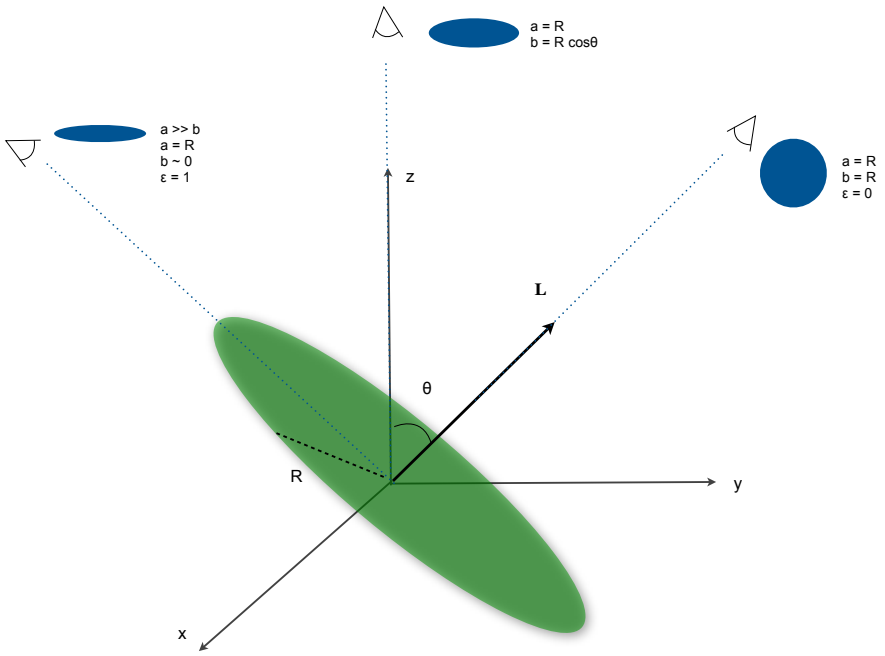

Figure 3.1: Sketch of ellipticities as viewed from an observer positioned at different angles.

Independent three dimensional shapes: We can assume that there is no correlation between the shapes of the two distinct galaxies, and this is justified by the fact that the shapes of the ellipsoids are determined by *local* processes (e.g. the dissipation processes during the collapse of the dark matter halo). Therefore the shapes of the two galaxies are independent, and the joint probability distribution simplifies to $P(\mathbf{S},\hat{\mathbf{L}},\mathbf{S}',\hat{\mathbf{L}}') = P(\hat{\mathbf{L}},\hat{\mathbf{L}}')P(\mathbf{S})P(\mathbf{S}')$, so that Eqn. (3.11) becomes:

$$\langle \epsilon\epsilon'^{*}\rangle = \int \mathrm{d}\mathbf{S}\mathrm{d}\mathbf{S}'\,\mathrm{d}\hat{\mathbf{L}}\mathrm{d}\hat{\mathbf{L}}'\,\epsilon(\mathbf{S},\hat{\mathbf{L}})\epsilon(\mathbf{S}',\hat{\mathbf{L}}')P(\mathbf{S})P(\mathbf{S}')P(\hat{\mathbf{L}},\hat{\mathbf{L}}'). \tag{3.12}$$

Average shape for each galaxy: Since the determination of a certain shape given the angular momentum's direction is difficult to obtain or to assume, it appears convenient to obtain an average ellipticity for a given direction of the spin for each galaxy. This is achieved by integrating over all possible shapes and orientations: $\bar{\epsilon}(\hat{\mathbf{L}}') = \int d\mathbf{S}\epsilon(\mathbf{S},\hat{\mathbf{L}})P(\mathbf{S})$ and results in the relation:

$$\langle \epsilon\epsilon'^{*}\rangle = \int \mathrm{d}\hat{\mathbf{L}}\mathrm{d}\hat{\mathbf{L}}'\,\bar{\epsilon}(\hat{\mathbf{L}})\bar{\epsilon}(\hat{\mathbf{L}}')P(\hat{\mathbf{L}},\hat{\mathbf{L}}'), \tag{3.13}$$

which contains the joint probability distribution $P(\hat{\mathbf{L}},\hat{\mathbf{L}}')$, key point of the quadratic model study. $P(\hat{\mathbf{L}},\hat{\mathbf{L}}')$ can be investigated by considering the definition of angu-

lar momentum in Eqn. (2.15), which shows the proportionality to the inertia and tidal shear tensors and allows a rewriting of the probability itself as $P(\hat{\mathbf{L}}, \hat{\mathbf{L}}') = P(\mathbf{I}, \mathbf{T}, \mathbf{I}', \mathbf{T})$, $\mathbf{I}$ being the inertia tensor and $\mathbf{T} \equiv \Phi_{,\alpha\beta}$ the tidal shear tensor.

Quite generally speaking, the treatment of this joint probability distribution $P(\mathbf{I}, \mathbf{T}, \mathbf{I}', \mathbf{T})$ is at the same time the starting point and the discriminator between the two quadratic models we are going to talk about in the next sections, respectively ascribable to (Crittenden et al., 2002, CNPT hereafter) and (Mackey et al., 2002, MWK hereafter).

It is worth stressing that *locality* is a key concept in providing any kind of description of IA. In both models, in fact, we are considering local processes (the formation of a galaxy with a certain inertia tensor, or a certain shape and angular momentum) which end up to be correlated due to the long-range correlation lengths of the tidal shear.

3.4.3 Modelling of intrinsic alignments I: CNPT model

As was just mentioned in the previous section, if we are interested in the full joint probability distribution of finding the angular momenta $\hat{\mathbf{L}}, \hat{\mathbf{L}}'$ of two galaxies at a certain distance one from another, we need to consider the full joint probability distribution $P(\mathbf{I}, \mathbf{T}, \mathbf{I}', \mathbf{T}')$. Again some considerations can be made in order to lighten this expression:

Indipendent inertia tensors: CNPT assume that the moment of inertia of a given galaxy is only correlated to the shear tensor of the galaxy, such that $P(\mathbf{I}, \mathbf{T}, \mathbf{I}', \mathbf{T}') = P(\mathbf{I}|\mathbf{T})P(\mathbf{I}'|\mathbf{T}')P(\mathbf{T}, \mathbf{T}')$. Equivalently, this translates into omitting the conditional probability $P(\mathbf{I}|\mathbf{I}')$ by considering $\mathbf{I}, \mathbf{I}'$ independent. This assumption derives from considerations about the different correlation lengths of the quantities involved: Since the correlation length of the inertia tensor is significantly smaller than the correlation length of the shear tensor, we expect the inertia of one galaxy not to be correlated with the inertia of the second galaxy.

Definition of protogalaxy boundaries: The conditional probability distribution $P(\mathbf{I}|\mathbf{T})$, namely the probability of finding an inertia tensor $\mathbf{I}$ given the tidal shear tensor $\mathbf{T}$, is very difficult to retrieve, since it contains one of the major unsolved problems of the TTT, which is the fact that the inertia tensor of a protogalactic object, which is caused by the tidal shear of the surrounding regions, can be defined only by defining the boundaries of the object itself, but these boundaries in turn depend on the evolution of the gravitational potential and on the mass distribution outside the collapsed object as well. In other words it appears very intricate to encode all the information about inertia and tidal shear tensors and their interdependencies. A possible way out was suggested by Lee & Pen (2000, 2001) who considered the conditional probability $P(\hat{\mathbf{L}}|\mathbf{T})$ (the probability of finding the spin $\hat{\mathbf{L}}$ given the tidal shear tensor $\mathbf{T}$) instead of $P(\mathbf{I}|\mathbf{T})$ (since $P(\hat{\mathbf{L}}|\mathbf{T}) \propto P(\mathbf{I}|\mathbf{T})$). This actually appears as a viable way if one considers the def-

inition of angular momentum and the fact that the probability of finding a certain angular momentum given a tidal field builds in the information contained in $P(\mathbf{I}|\mathbf{T})$ by construction. The reader may be convinced by the fact that, once again, we are talking about local, spatially separated processes taking place "on top" of an underlying common tidal field, which is able to affect in a similar way the above mentioned processes. If one allows for this rewriting, i.e. $P(\hat{\mathbf{L}}|\mathbf{T})$ instead of $P(\mathbf{I}|\mathbf{T})$, then it is also possible to express the average ellipticity in terms of the tidal tensor rather than the angular momentum: $\bar{\epsilon}(\mathbf{T}) = \int \mathrm{d}\hat{\mathbf{L}}\epsilon(\hat{\mathbf{L}})P(\hat{\mathbf{L}}|\mathbf{T})$, which is the expected average ellipticity given a tidal shear tensor.

In this way the ellipticity correlation becomes:

$$\langle \epsilon\epsilon'^{*}\rangle = \int \mathrm{d}\mathbf{T}\mathrm{d}\mathbf{T}'\,\bar{\epsilon}(\mathbf{T})\bar{\epsilon}(\mathbf{T}')P(\mathbf{T},\mathbf{T}'). \tag{3.14}$$

Finally, in order to be able to calculate this expression, the only ingredient needed is the tidal field and the correlation among the tidal field at different locations.

Notice that this ellipticity correlation is quadratic in the tidal shear, and asks for the computation of both the linear and the quadratic two point functions of the tidal shear $\langle \mathbf{T}\mathbf{T}'\rangle$ and $\langle \mathbf{T}\mathbf{T}\mathbf{T}'\mathbf{T}'\rangle$. Notice once again also that CNPT did *not* discard the information contained in $P(\mathbf{I}|\mathbf{T})$ and $P(\mathbf{I}'|\mathbf{T}')$, but have rather encoded this information inside $P(\hat{\mathbf{L}}|\mathbf{T})$.

In order to solve the integral in the last expression, one needs to find the dependency of the ellipticity on the tidal shear, and to assume some relation for $P(\hat{\mathbf{L}}|\mathbf{T})$. We address the first point by recalling the relation between the ellipticity and the angular momentum in Eqn. (3.10):

$$\begin{aligned}
\bar{\epsilon}_{+} &= |\bar{\epsilon}|\cos(2\phi) = \alpha\frac{1-\hat{L}_z^2}{1+\hat{L}_z^2}\frac{\hat{L}_y^2-\hat{L}_x^2}{\hat{L}_y^2+\hat{L}_x^2} = \alpha\frac{\hat{L}_y^2-\hat{L}_x^2}{1+\hat{L}_z^2} \\
\bar{\epsilon}_{\times} &= |\bar{\epsilon}|\sin(2\phi) = 2\alpha\frac{1-\hat{L}_z^2}{1+\hat{L}_z^2}\frac{\hat{L}_y\hat{L}_x}{\hat{L}_y^2+\hat{L}_x^2} = 2\alpha\frac{\hat{L}_y^2-\hat{L}_x^2}{1+\hat{L}_z^2}
\end{aligned} \tag{3.15}$$

such that $|\epsilon|^2 = |\epsilon_+ + i\epsilon_\times|^2$ and $\hat{L}_x^2+\hat{L}_y^2+\hat{L}_z^2 = 1$. It is interesting to notice that when the observer's frame of reference corresponds to the frame in which the shear tensor is diagonal, then the cross-correlations $\langle L_xL_y\rangle = 0$, and $\epsilon_\times = 0$, so that the distortions in the ellipticity are only real.

The probability distribution of finding the angular momentum $\hat{\mathbf{L}}$ given the shear field $\mathbf{T}$ was given by (Lee & Pen, 2000), who assumed this conditional probability to be a Gaussian, and since this probability distribution implicitly contains the probability distribution of the inertia tensor components $P(\mathbf{I}|\mathbf{T})$, this assumption corresponds to assuming that also the latter probability distribution is a Gaussian. So we have:

$$P(\hat{\mathbf{L}}|\mathbf{T}) = \frac{1}{(2\pi)^{3/2}|C|^{1/2}}\exp\left(-\frac{1}{2}\hat{\mathbf{L}}^T C^{-1}\hat{\mathbf{L}}\right), \tag{3.16}$$

where $C \equiv \langle L_\alpha L_\beta \rangle$ is the covariance matrix. Always (Lee & Pen, 2000) and (Crittenden et al., 2001) adopt a parametrisation for the degree of alignment between the inertia and shear tensors:

$$C = \langle \hat{L}_\alpha \hat{L}_\beta \rangle = \left\langle \frac{L^2}{3} \right\rangle \left(\frac{1+a}{3} \delta_{\alpha\beta} - a \hat{T}_{\alpha\gamma} \hat{T}_{\gamma\beta} \right) \tag{3.17}$$

where a is the so-called *misalignment parameter*, which encodes the information of $P(\mathbf{I}|\mathbf{T})$ as well as the information we lack about all the non linear processes, due both to baryonic dissipative processes going into the formation of the galaxy and to the natural transit to nonlinear regime (in which case the approximations used to recover the angular momentum are no longer valid and must be dropped). There term $\hat{T}$ is instead the unit-normalised ($\hat{T}_{\alpha\beta}\hat{T}_{\alpha\beta} = 1$) and traceless ($\mathrm{tr}\hat{T} = 0$) tidal shear tensor which can be derived by using:

$$\bar{T}_{\alpha\beta} = T_{\alpha\beta} - \frac{\mathrm{tr}T}{3} \delta_{\alpha\beta}, \tag{3.18}$$

and the rescaling $\hat{T} = \bar{T}/|\bar{T}|$. There are two extreme cases for the misalignment parameter, i.e. $0 \leq a \leq 3/5$:

- $a = 0$: In this case the inertia and tidal shear tensors are correlated, or equivalently, their eigensystems are perfectly aligned. This causes the covariance to be equal to $\langle L_\alpha L_\beta \rangle = \langle \frac{L^2}{3} \rangle \left(\frac{1}{3} \delta_{\alpha\beta} \right)$, which is the case for completely random angular momenta directions. If the angular momenta of neighbouring galaxies are completely uncorrelated one to another, then the signal, the correlation function, is zero.

- $a = 3/5$: This is the case in which the inertia and shear tensors are completely uncorrelated, otherwise said their eigensystems are maximally misaligned, in which case the angular momenta trace the underlying tensor field, and are therefore maximally correlated, meaning that the signal obtained, the correlation function, is maximum.

The maximum value $3/5$ for a can be bound by the requirement that the covariance matrix C is positive definite, which turns into the two requirement s that $\det C > 0$ and $\mathbf{L}^T C^{-1} \mathbf{L} > 0$ for any $\mathbf{L}$. In order to quantify the signal in these two extreme cases, it is useful to consider (Schäfer, 2009), who showed that the signal is maximised in the case of eigensystems completely unaligned:

$$\langle L_\alpha(\mathbf{x}) L_{\alpha'}(\mathbf{x}') \rangle = a^4 \dot{D}_+^2 \epsilon_{\alpha\beta\gamma} \epsilon_{\alpha'\beta'\gamma'} \langle X_{\beta\gamma}(\mathbf{x}) X'_{\beta'\gamma'}(\mathbf{x}') \rangle, \tag{3.19}$$

where X is the tensorial product we defined in eqn. (2.19). The correlation function can be written as:

$$C_L(r) = \mathrm{tr}\langle \mathbf{L}(\mathbf{x}) \mathbf{L}^t(\mathbf{x}') = a^4 \dot{D}_+^2 \mathrm{tr} \left[\langle \mathbf{X}(\mathbf{x}') \mathbf{X}(\mathbf{x}) \rangle - \langle \mathbf{X}(\mathbf{x}) \mathbf{X}^t(\mathbf{x}') \rangle \right]. \tag{3.20}$$

What was the property of the angular momentum to be proportional just to the antisymmetric part of the $\mathbf{X}$ tensor, $\mathbf{X}^-$, becomes in the correlation function of

the angular momenta an asymmetric quadratic form $\langle \mathbf{X}(\mathbf{x}')\mathbf{X}(\mathbf{x})\rangle - \langle \mathbf{X}(\mathbf{x})\mathbf{X}^t(\mathbf{x}')\rangle$, where the second term is carrying the signal. If the inertia and tidal shear have common eigensystems, then $\mathbf{X} = \mathbf{X}^+ = \mathbf{X}^{\mathbf{t}}$, where the last equivalence comes from the fact that the shear and inertia matrices are symmetric. In this case the correlation function would vanish. In the opposite case, case in which inertia and shear tensors are misaligned, $\mathbf{X} = \mathbf{X}^-$ and $\mathbf{X}^{\mathbf{t}} = (\mathbf{X}^-)^t = -\mathbf{X}$ and the correlation function, i.e. the signal, is maximised:

$$C_L(r) = 2a^4\dot{D}_+^2 \mathrm{tr}\left[\langle \mathbf{X}(\mathbf{x}')\mathbf{X}(\mathbf{x})\rangle\right] \tag{3.21}$$

Of course reality lies between these two extreme cases.

The conditional probability density can be used for establishing a direct relation between ellipticity ϵ and tidal shear $\hat{T}$ by integrating out angular momentum direction and magnitude:

$$\epsilon(\hat{T}) = \int \mathrm{d}\hat{\mathbf{L}}\,\epsilon(\hat{\mathbf{L}}) \int L^2 \mathrm{d}L\, p(\mathbf{L}|T) \tag{3.22}$$

With this relation, one can write down the two correlation functions $\langle \epsilon_+(\theta')\epsilon_+(\theta'')\rangle$ and $\langle \epsilon_\times(\theta')\epsilon_\times(\theta'')\rangle$ of the three-dimensional ellipticity field in terms of moments $\zeta_n(r)$ (see Crittenden et al., 2001) of the tidal shear field.

The correlation function of the three dimensional ellipticity field can then be projected onto the angular correlation function of the ellipticity components by using the configuration-space Limber-equation (Limber, 1954):

$$C_{++}(\theta) = \int \mathrm{d}\chi_1 W_\epsilon(\chi_1) \int \mathrm{d}\chi_2 W_\epsilon(\chi_2)\, \langle \epsilon_+(\theta')\epsilon_+(\theta'')\rangle \tag{3.23}$$

$$C_{\times\times}(\theta) = \int \mathrm{d}\chi_1 W_\epsilon(\chi_1) \int \mathrm{d}\chi_2 W_\epsilon(\chi_2)\, \langle \epsilon_\times(\theta')\epsilon_\times(\theta'')\rangle \tag{3.24}$$

with the distance distribution $W_\epsilon(\chi) = n(z(\chi))\mathrm{d}z/\mathrm{d}\chi$ resulting for a given cosmology from the observed redshift distribution $n(z)\mathrm{d}z$ of background galaxies, and where we have neglected the clustering of galaxies.

3.4.4 Modelling of intrinsic alignments II: MWK model

In the case of MWK the full joint probability distribution $P(\mathbf{I},\mathbf{T},\mathbf{I}',\mathbf{T}')$ encountered in Sec. 3.4.2 is treated in slightly a different way. As much as CNPT do, MWK also consider the inertia tensors $\mathbf{I},\mathbf{I}'$ of the two galaxies to be uncorrelated, therefore omitting the term $P(\mathbf{I}|\mathbf{I}')$.

But differently from CNPT, MWK also omit the conditional probabilities $P(\mathbf{I}|\mathbf{T})$, $P(\mathbf{I}'|\mathbf{T}')$, meaning that they consider the inertia and the tidal shear tensor to be completely uncorrelated. This approach, previously used by Catelan & Theuns (1996a), basically corresponds to the so called *peak-background split*, and is based once again on considerations on the interplay between the long-range correlations in the tidal field as opposed to the short-range correlations of the inertia tensors. In this perspective MWK argue that the large wavelengths Fourier

modes must be statistically independent of the smaller wavelength Fourier modes responsible for the inertia tensors.

Furthermore, they argue that this assumption would lead to an upper limit in the IA signal. Even though apparently counterintuitive, this fact can easily be understood by considering the following fact: We have seen that in order to have a non vanishing angular momentum the inertia and tidal tensors must not be aligned. We are therefore requiring that the eigensystems of the two tensors are not perfectly correlated (i.e. they must not be perfectly aligned), because in this picture we would have actually no angular momenta, and consequently the correlation function would also vanish. This constitutes, in a way, the lower (although unrealistic) limit of our calculations. But we do know, since we observe spins of galaxies, that the eigensystems of the two tensors must have a certain degree of misalignment, which equivalently means that they must be uncorrelated at a certain level. In this case the angular momenta of the galaxies are allowed to arise, and it is possible to calculate the correlation function among these (as discussed in Eqn.(3.20)), which is higher the more the angular momentum is able to trace the underlying tidal field. So the extreme situation, which then constitutes an upper limit to our predictions, is the case in which the eigensystems of inertia and tidal shear tensors are maximally uncorrelated, or equivalently maximally misaligned. In this case this maximum (and also unrealistic, as shown in N-body simulations, see Sec. 3.7) degree of misalignment leads the signal to be maximised.

They therefore proceed by performing, in Fourier space (differently from CNPT, who perform all the integrals in real space), an average over orientations of the inertia tensors first, and then separately an average over realisations of the tidal field (this last step is equivalent to considering the correlation function for the tidal shear), which corresponds to:

$$\langle \epsilon \epsilon'^{*} \rangle = \bar{\epsilon}\bar{\epsilon}' \langle \mathbf{T}\mathbf{T}' \rangle = \bar{\epsilon}\bar{\epsilon}' \int d\mathbf{T} d\mathbf{T}' P(\mathbf{T}, \mathbf{T}'). \tag{3.25}$$

Working therefore completely in harmonic space they aim at the power spectra of the intrinsic ellipticity, for which it is convenient to introduce the parity conserving (E-mode) and parity violating (B-mode) part (see Chap. 4 for further details on E- and B-modes) of the intrinsic ellipticity field:

$$\begin{aligned} E(\mathbf{k})\, k^2 &= \left(k_x^2 - k_y^2\right)\epsilon_+(\mathbf{k}) + 2k_x k_y \epsilon_\times(\mathbf{k}) \\ B(\mathbf{k})\, k^2 &= -2k_x k_y \epsilon_+(\mathbf{k}) + \left(k_x^2 - k_y^2\right)\epsilon_\times(\mathbf{k}). \end{aligned} \tag{3.26}$$

Focusing on modes perpendicular to the line of sight one can derive the following dimensionless ellipticity power spectra for the E- and B-mode, respectively

$$\begin{aligned} \Delta_X^2(k) &= \frac{C}{225}\left(\frac{3}{2}\Omega_m H_0^2\right)^4 \int_0^\infty \frac{\mathrm{d}\alpha}{\alpha}\Delta^2(\alpha k) \\ &\quad \times \int_{-1}^{1} \mathrm{d}\mu \frac{\Delta^2(k\sqrt{1+\alpha^2-2\alpha\mu})}{(1+\alpha^2-2\alpha\mu)^{7/2}} g_X(\alpha,\mu). \end{aligned} \tag{3.27}$$

Here $X \in \{E, B\}$ and g_X is a polynomial given in eqn. (17) of Mackey et al. (2002) together with a detailed derivation of the expressions given above.

Finally, in order to get the corresponding angular power spectra the Fourier-space variant of Limber's projection (Limber, 1954) is used:

$$\frac{\ell(2\ell+1)}{4\pi} C_X^{\epsilon}(\ell) = \frac{\pi}{\ell} \int_0^{\infty} \chi \, \mathrm{d}\chi \, W_{\epsilon}^2(\chi) \Delta_X^2(\ell/\chi) \tag{3.28}$$

with the weighting function $W_{\epsilon}(\chi)\mathrm{d}\chi = n(z)\mathrm{d}z$.

MWK determine the constant C by computing the expectation value of the squared angular momentum modulus and adjusting C to match the mean-square source ellipticity typically observed in galaxy surveys.

3.5 Drawing inertia tidal-shear tensors misalignments

In order to visually grasp the meaning of having a certain amount of misalignment between inertia and tidal shear tensor we computed the tidal shear tensors and galactic orientations of 2000 galaxies in a box of size 128 Mpc h^{-1} following the prescription of CNPT. We show here two plots. The first, in Fig. (3.2), shows the $+1\sigma$ and -1σ contours of the three dimensional density field respectively in blue and green. Disks represent galaxies and are meant to show exclusively the orientation of the galaxy rather than its shape. The smoothing scale used for the density field is of 8 Mpc h^{-1}.

The plot was obtained by using a structure formation code able to generate 3D random Gaussian density and potential fields. Galaxies are then positioned randomly on the density field, and the tidal shear components are computed from the potential field at each galaxy position. Angular momenta components are instead first generated randomly, being thus at first completely uncorrelated. We then modelled the covariance matrix by using Eqn. (3.17), and then rendered the angular momentum components correlated by means of a Cholesky decomposition. The ellipticity field is then easily obtained by using Eqn. (4.33), which relates the ellipticity components to the angular momenta components. We stress once more that only the direction of the galactic spin is important for the parametrisation in Eqn. (3.17) (Lee & Pen, 2000), and thus the spins are all normalised to 1.

In Fig. (3.3) we superimpose to the disks the tidal shear tensors. Although not being directly a measure of the shape of the galaxies, the disks represent the orientations of the galaxies, which are related to the observed shapes. One of the hypotheses made is that the spin is perpendicular to the disk of the galaxy, and is parallel to the spin of the dark halo in which the galaxy is embedded. Thus, effectively, Fig. (3.3) shows the misalignment between tidal shear and inertia tensors. It is very interesting to see how, in order to have non-vanishing angular momenta, and thus correlated disk images, it is necessary to have a certain degree of misalignment. In this case the misalignment parameter was set to

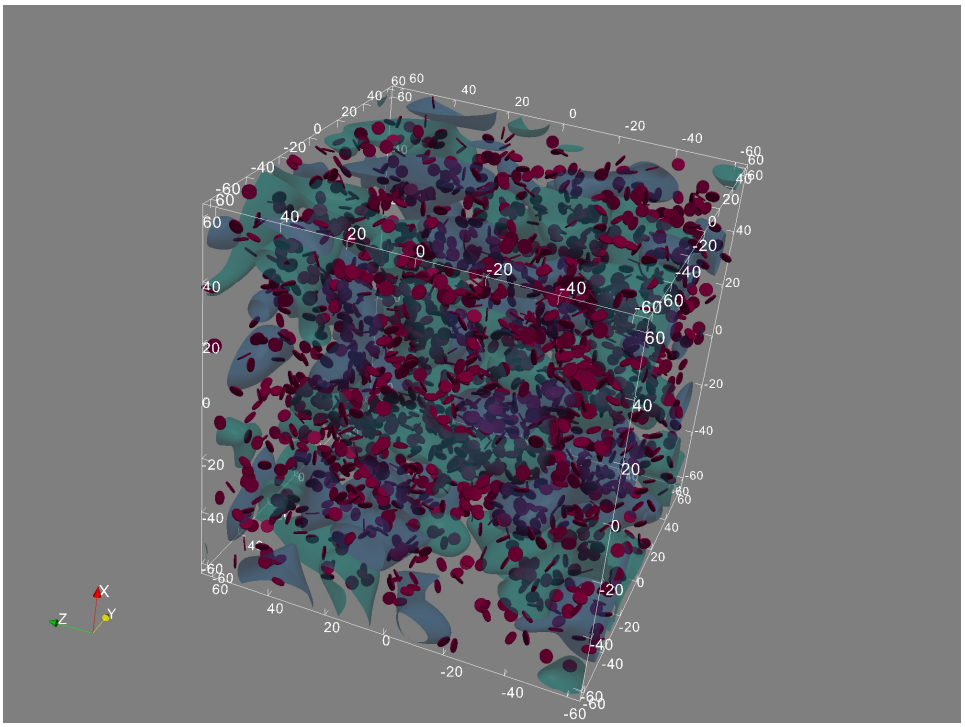

(a) Disk orientations of the galaxies on top of the density field

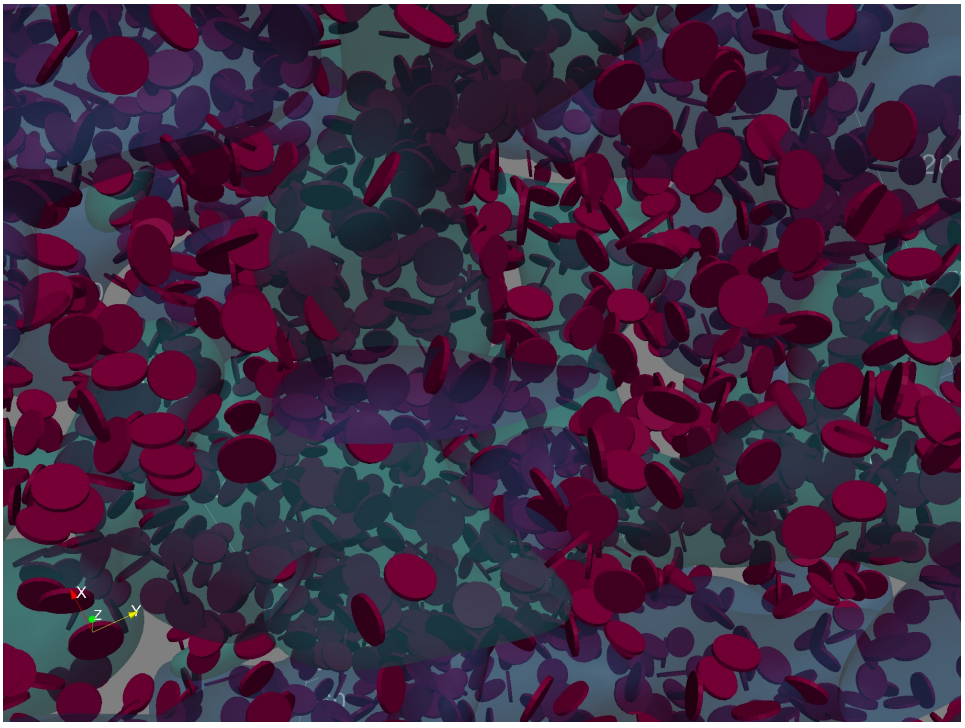

(b) Zoom in on the density field

Figure 3.2: 3D visualisation of the density field for a box of size 128Mpc h^{-1}. Blue and green contours correspond to $+1\sigma$ and -1σ contours of the density field. The smoothing scale is set to 8Mpc h^{-1}. The red disks show the orientations of the galaxies, not their 3D shapes. 2000 galaxies are shown.

$a = 0.25$, which is the value found in N-body simulations (Lee & Pen, 2000). We remind that a value of $a = 0$ would correspond to situation in which inertia and tidal shear eigensystems are completely correlated, and thus the resulting angular momenta are totally uncorrelated to the tidal shear and among each other. Equivalently, they are maximally randomised.

In order to study how the misalignment parameter affects the intrinsic alignments and the spin correlation we computed ellipticity and angular momentum correlation functions. We show the results for the ellipticity correlation functions in Fig. (3.4) and for the spin correlation function in Fig. (3.5). Ellipticity correlations increase with increasing value of a, except for the cross-term, which remains consistent with zero as expected in the case of statistical parity invariance. Values of a ranging between $0.0 \leq a \leq 0.8$ were considered, although values of $a \sim 0.8$ are unrealistic, as we will also discuss in Sec. 3.7 on the basis of N-body simulations. We strongly remark that there is no theoretical prediction for the misalignment parameter, which has only been investigated numerically, and represents a pure paramterisation.

3.6 Early-type galaxies: the linear model

For the elliptical galaxies the description is quite different. First of all, in what follows there is the assumption that the elliptical galaxy is already a bound object in equilibrium, which is not the case in TTT, where the focus is on the trajectories of the particles which will eventually form an object. So the image to bear in mind is that of an object with its own gravity exposed to external tidal fields, which deform its shape.

The original suggestion, proposed by Catelan et al. (2001) (hereafter CKB), and first applied by Hirata & Seljak (2004) (whose notation we are going to follow), is that the orientation of the galaxy image is determined by the shape of the halo in which the galaxy forms.

Thus, the very basic idea is that the elliptical galaxies trace the ellipticity of the dark matter halo in which they are embedded. But the dark matter, in turn, clumps in halos whose shape is ellipsoidal, and usually the major axis of this triaxial halo is aligned with the maximum curvature of the large scale gravitational potential. Roughly said, if the dark matter halo shape traces the curvature of the underlying gravitational potential, and the ellipticity of the galaxy traces in turn the shape of the dark matter halo, then the relation between ellipticity and curvature of the gravitational potential (tidal shear) must be a linear one (Kirk et al., 2012). From these purely qualitative considerations we can write:

$$\begin{aligned} \epsilon_+ &= C(\partial_y^2 - \partial_z^2)\Phi \\ \epsilon_\times &= 2C\partial_y\partial_z\Phi. \end{aligned} \tag{3.29}$$

CKB report the example of a sphere moving in a uniform (or spatially slowly varying) gravitational field, which can be therefore Taylor expanded about the

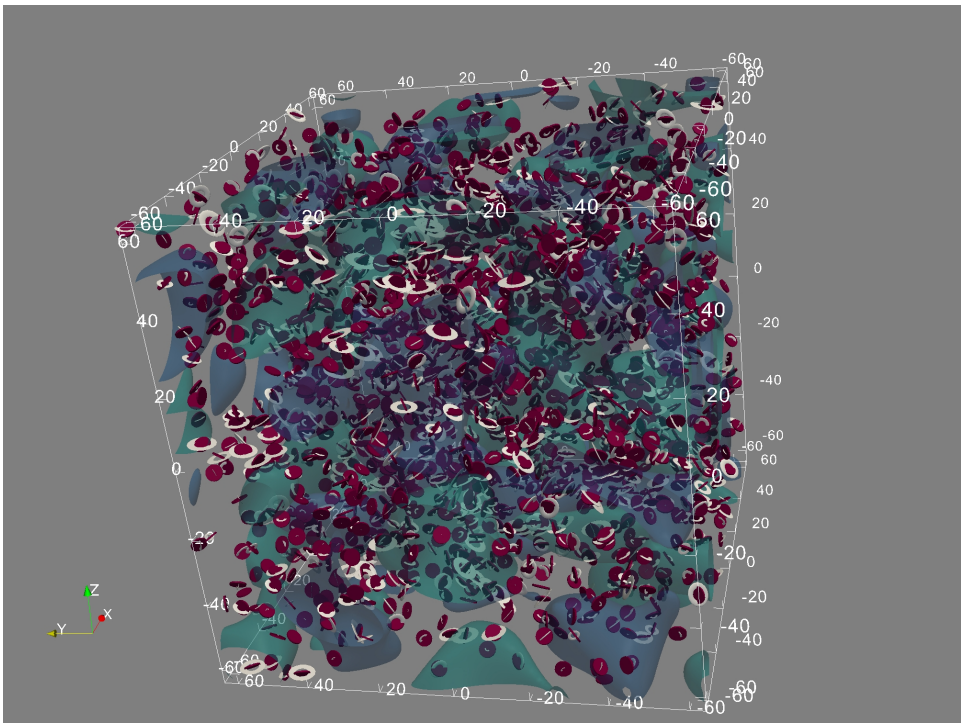

(a) Tidal shear tensors

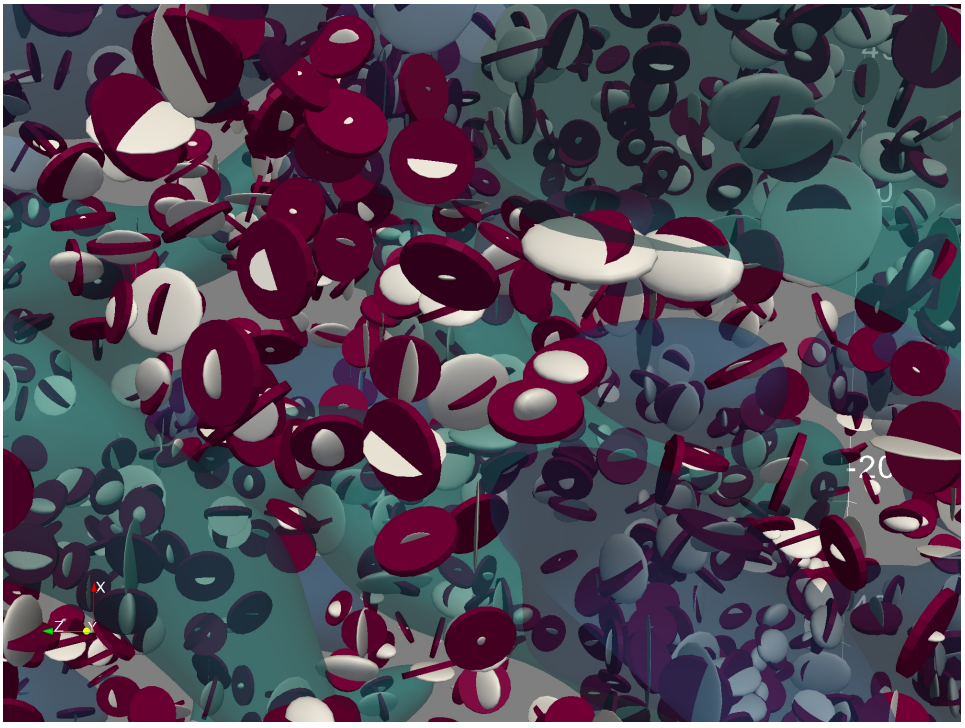

(b) Zoom in and detailed image of misalignments among tidal shear and galaxy shapes.

Figure 3.3: 3D visualisation of the misalignment between the disks (in red) and the tidal shear tensors (in white) over the density field for a box of size 128Mpc h^{-1}. Blue and green contours correspond to $+1\sigma$ and -1σ contours of the density field. The smoothing scale is set to 8Mpc h^{-1}. Disks show the orientations of the galaxies, not their 3D shapes. 2000 galaxies are shown.

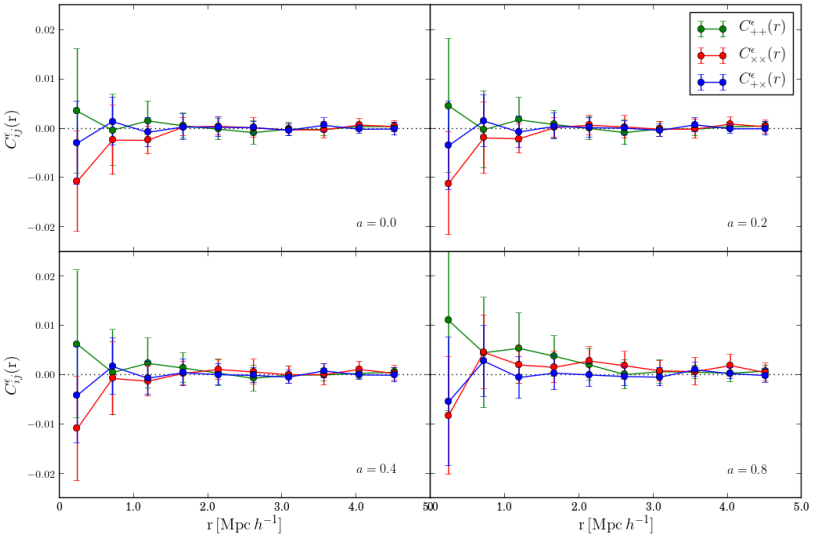

Figure 3.4: Ellipticity correlation functions $C^{\epsilon}_{++}, C^{\epsilon}_{\times\times}$ and cross-correlation $C^{\epsilon}_{+\times}$. While the cross-correlation remains consistent with zero, as expected if statistical parity invariance holds, the other components increase in amplitude as the misalignment parameter increases.

origin. The sphere will be deformed only by the action of the quadratic term of the Taylor expansion, i.e. the tidal field. In fact both the zeroth and the first order are ineffective in terms of shape deformation, since the zeroth term has no physical effect, and the first term (the linear term) only acts by shifting the sphere (this is the case of a constant gravitational field), not inducing any kind of change in its shape. The tidal field, instead, constitutes variations in the gravitational field, which cause different accelerations at different points of the sphere.

The constant C in Eqn. (3.29) is a normalisation factor to be defined, and it can be considered to contain all the information we lack about the relation between the luminous, baryonic galaxy shape and the dark matter halo containing it, other that all the baryonic physics involved in galaxy formation. Therefore Catelan et al. (2001) give an empirical estimate of the constant C by computing the expected rms ellitpicity of individual galaxies and comparing this quantity to the typical source ellipticity in order to fix it.

Specifically, one can imagine that the galactic halo is perturbed by the local tidal field of the LSS and can be either "stretched" or "compressed", respectively ending in an prolate or an oblate halo, whose preferential elongation is along the direction of the tidal field. This is particularly easy to see in the very simple case of a spherical halo in a constant tidal field, i.e. in a constantly varying gravitational field. In such a case the acceleration on a side of the halo is dif-

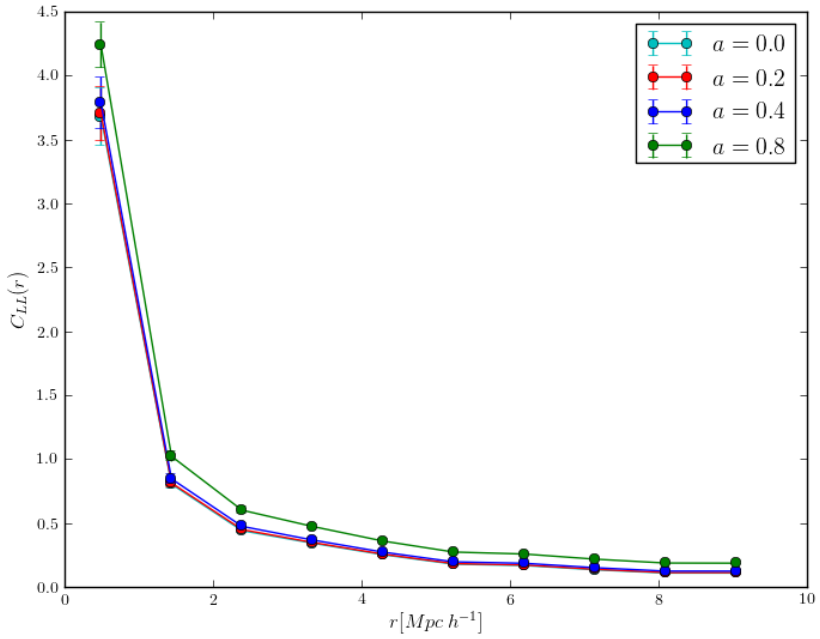

Figure 3.5: Angular momentum correlation function for varying value of the misalignment parameter a. Increasing values of a lead to higher correlations between galactic spins, i.e. the spins keep memory of the underlying tidal shear field.

ferent (stronger or weaker) from the acceleration on the other side, causing the object to be compressed or stretched. This is an ideal and unrealistic situation but still it represents a trend in elongation of halos which could be visible in the population on average.

This model has become the standard model to be used when including intrinsic alignments as a contamination to weak lensing, which we will address in Chap. 4.

3.7 IA and N-body simulations

Throughout the years, due to the higher and higher interest in IA arose in the scientific community, there have been many N-body studies primarily on TTT and its efficacy, as discussed in Chap. 2, and later on also on intrinsic correlations. In fact not only N-body simulations constitute a way to check analytical results, but they constitute themselves an alternative to analytical models. Here we report several studies conducted by means of N-body simulations and their results, many of which also involve a quantitative description of the contamination of IA on weak lensing, which will be discussed in the next chapter.

One of the first simulations carried out to study the effects of tidal torquing on the galactic shape has been (Dubinski, 1992), who also calculated the angular momentum correlation function according to theories based on tidal torquing. It is found that tidal fields are very important for establishing structure and kinematics of dark halos, and they retrieve the tendency of the the angular momentum to lie parallel to the intermediate axis of the tidal shear.

Most notably Lee & Pen (2000), having proposed, within the quadratic model, the parametrisation through the misalignment parameter, find the most suitable value to be $a = 0.24$, which consequently yields to a significant correlation of the shear intermediate principal axis with the direction of angular momentum of the halos, and means at the same time that the shear and inertia eigensystems are misaligned, but still quite strongly correlated. The same result has been obtained by Porciani et al. (2002b), who find that only small deviations of about 10% from perfect alignment of inertia and tidal shear tensors allow the angular momentum to form. Because of this result they argue that any approximation used for calculations of angular momenta or IA which is based on the assumption of complete misalignment between inertia and tidal field leads to wrong estimates. Upon this they also argue that mostly estimations of the angular momentum magnitude may be affected by this wrong assumption (cfr. Catelan & Theuns, 1996a; Lemson & Kauffmann, 1999), and therefore they focus just on the directions of the spins.

At the same time also Croft & Metzler (2000) carried out high resolution N-body simulations to find three-dimensional correlations among the projected ellipticities of DM halos, and find correlations on scales $0.5 \div 30$ Mpch^{-1}, which they then project these both by using Limber's equation (Limber, 1954) and by

projecting the simulation boxes. They compare this result to typical shear signals, finding that the intrinsic signal strongly depends on the redshift width of the galaxy distribution, and that IA could account for $10-20\%$ of the shear signal. Heavens et al. (2000) used N-body simulations in order to find the correlation functions of ellipticities of both elliptical and spiral galaxies, but giving a special attention to spirals for technical reasons (it appeared difficult to numerically resolve the ellipticals due to the small number of particles defining a halo). For spiral galaxies they made the usual assumption of their disk being perpendicular to the angular momentum of the DM halo. They extracted three dimensional correlation functions, and projected them through Limber's equation. Results for these correlations give an order of $\sim 10^{-4}$ at small separations and $\sim 10^{-5}$ on scales of the order of $10'$. Moreover it is found that the signal dominates over weak lensing for shallow surveys, but the contrary appears to be the case for deep surveys (see also Crittenden et al. (2002) for this)

Jing (2002) finally shows that IA can significantly contaminate weak lensing not only on shallow surveys but also in deep surveys. The interest is anyhow specified to study how the simulation resolution affects the determination of the correlation function. This appears to have influence on the final result, by underestimating it of a factor of 2 when the halos contain only 20 particle. More stable results are obtained for halos containing a number larger to 160 particles. The size of the box is instead less relevant.

Finally, Porciani et al. (2002a) find TTT poorly predicts the galaxy spin direction due to nonlinear effects (the mean error being $\sim 50°$) and therefore expect and find poor results also for two point correlation function among spin directions. They also find the correlation function to change with redshift: The signal appears to be much weaker on the same scales at lower redshift ($z = 0$) as compared to higher redshift ($z = 50$). This result is interpreted as a consequence of nonlinear effects diluting the original angular momentum. In fact at high redshift predictions match well the simulation data since TTT still holds and non linearities still did not kick in. These nonlinear effects weakened the linear spin spin correlation on scales ≥ 1 Mpch^{-1} by a factor of a few, making therefore the TTT signal an overestimation of the true signal. The nonlinear effects, by structure not included in TTT, are two-fold in nature: Either the members of galaxy paris get closer, so they correlate at later redshifts at lower separation distances (in which case correlations should shift to smaller scales) or spin directions themselves evolve away from TTT predictions. In the latter case the IA should be weakened at all scales, but non linear halo-halo interactions might occur, such as angular momentum exchange or in falling of material, and they would build up a new correlation signal.

3.8 Summary

In this chapter we have reviewed the theory of intrinsic alignments, how they form, and how they are modelled both for late-type and early-type galaxies. The fundamental steps can be summarised as follows:

- IA's theory is dual in its nature, due to the fact that it aims to describe *local* processes starting from the quantity of the tidal shear tensor, which has long correlation length and is thus *not local* in nature. Other than the tidal shear tensor, another quantity plays a key role in any description of the IA: the inertia tensor which, quite differently from the tidal tensor, has a rather shorter correlation length. The study of intrinsic alignments thus translates into the analysis of how these two tensors intercorrelate among galaxies at different points.

- In this sense, an essential point to make is that, for a same galaxy, the inertia and tidal shear tensors appear to be quite strongly correlated, as shown in numerical simulations (Lee & Pen, 2000; Porciani et al., 2002b).

- spirals' and ellipticals' IA are described via different models, respectively the *quadratic* and *linear* models. Equivalently, late-type ellipticities are proportional to the square of the tidal shear (i.e. second derivatives of the potential), whereas the ellipticals are assumed to be linearly proportional to the tidal shear.

- within the framework of the quadratic model, we have analysed two similar models, ascribable to Crittenden et al. (2002) and Mackey et al. (2002), which we call the CNPT and the MWK models. The models agree in considering the inertia tensors of different galaxies independent one from another (i.e. $P(\mathbf{I}|\mathbf{I}')$ is omitted), but diverge in considering the inertia tensor completely independent of the tidal tensor at the same point (i.e. $P(\mathbf{I}|\mathbf{T})$ is considered for CNPT, but omitted by MWK). Both the models agree in considering the correlations in the tidal field at two different locations the cause of IA, and therefore consider $P(\mathbf{T}|\mathbf{T}')$.

- Specifically, CNPT encode the information contained in $P(\mathbf{I}|\mathbf{T})$ by making use of a parametrisation suggested by Lee & Pen (2000), which introduces an appropriate parameter, the *misalignment parameter* a, able to establish the degree of alignment between inertia and tidal shear tensors, and therefore to track how much the angular momenta keep memory of the tidal shear originating them. A more intuitive and visual way of seeing this property of the misalignment parameter is given in Fig. (3.3), where we used a value of $a = 0.25$;

- IA have been investigated also in numerical simulations throughout the years. The first important confirmation has been that tidal fields are indeed important in the establishment of the structure of the dark halo, and find as a prop-

erty the tendency of the spin to lie parallel to the intermediate axis of the tidal shear.

- Lee & Pen (2000) measure the most suitable value for the misalignment parameter and find it to be $a = 0.24$, indicating that the inertia and tidal shear eigensystems are misaligned, but still quite correlated.

- Non-linear effects on spins and IA were also investigated in numerical simulations. Porciani et al. (2002a) find that non-linearities tend to dilute the initial correlation of the spins at later times, making the correlation function be significantly weaker at low redshift than at high redshift, where instead the predictions of the TTT are much better matched. This yields the correlation function to depend on redshift, and the TTT to over predict spin-spin correlations at low redshift.

Chapter 4

WEAK LENSING

The first observational test of General Relativity was conducted by A. Eddington and F. Dyson in 1919 who, during the solar eclipse in that same year, measured the deflection of the light coming from stars in the region around the Sun due to the gravitational field of the Sun. This provided one of the earliest confirmation of the theory of General Relativity. First proposed by Kaiser (1992) and first measured by (Bacon et al., 2000; Kaiser et al., 2000; Wittman et al., 2000; Van Waerbeke et al., 2000), *gravitational lensing* has become an extremely useful tool for pinning down cosmological parameters, mostly due to the fact that it is able to probe directly the mass distribution therefore bypassing intermediate steps which would require detailed knowledge about the relation between visible and dark matter or between luminosity and matter. We start by a description of the theory of gravitational lensing in Sec. 4.1, followed by the interplay between weak lensing and IA in Sec. 4.2. We focus on the technique of tomography applied to weak lensing in Sec. 4.3, since all the latest surveys are based on this approach, given the enhancement in signal which can be gained from it. In Sec. 4.4 we give a round up of the measurements on IA applied to cosmic shear and we summarise this chapter in Sec. 4.5. This chapter broadly uses the notation and follows the logic of Bartelmann & Schneider (2001).

4.1 Gravitational lens theory

In the most simple picture, a light ray departing from a background source S at angular diameter distance D_s from us (the observers) gets deflected by an angle $\hat{\boldsymbol{\alpha}}$ due to the presence of a mass M (thus called lens) distant from us D_d. This situation is sketched in Fig.(4.1).

General Relativity quantifies this angle which is, in the case of an impact parameter much larger than the Schwarzschild radius of the lens:

$$\hat{\alpha} = \frac{4GM}{c^2\xi}, \tag{4.1}$$

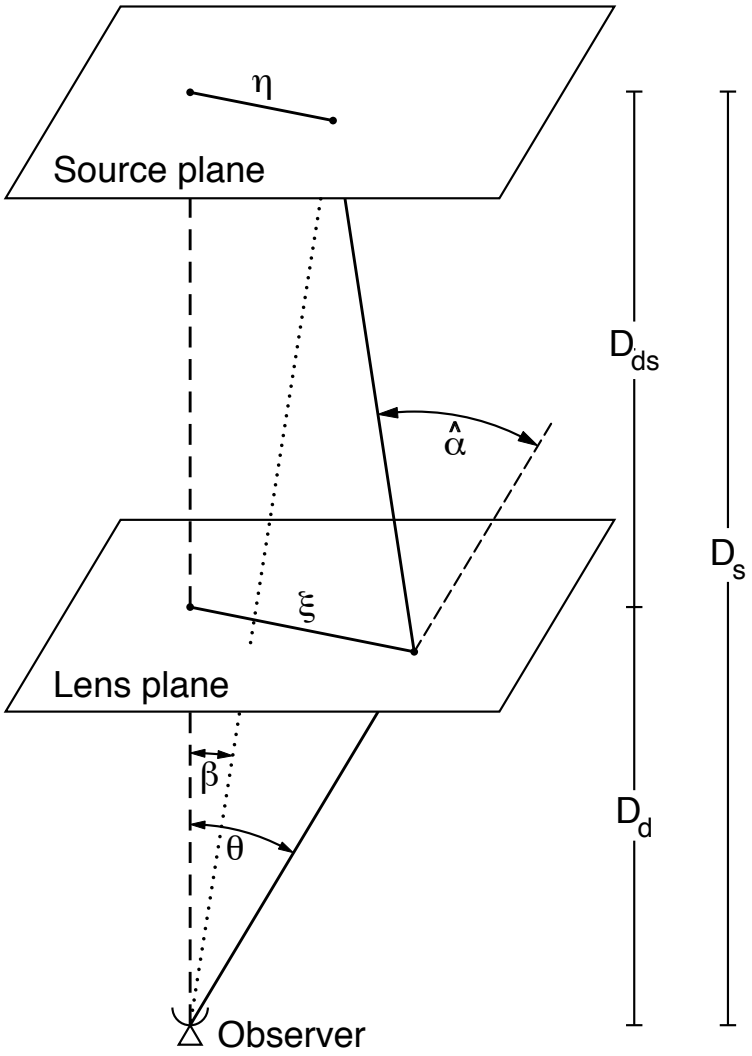

Figure 4.1: This figure is taken by Bartelmann & Schneider (2001) and sketches the typical situation we encounter with gravitational lensing.

This angle is twice the value it would have in Newtonian gravity, and depends on the mass distribution of the lens and the impact parameter ξ.

The theory of gravitational lensing is based on two assumptions:

- *Thin lens approximation*: It is assumed that the extension in redshift Δz of the lens is much smaller compared to the distances $D_{\rm ds}$ and $D_{\rm d}$ (see Fig. (4.1)), i.e. the lens is thin compared to the total extent of the light path;
- *Born approximation*: Given that the deflection angle is very small, the deflected light ray is approximated to a straight line instead of a curved path in proximity to the lens.

This allows us to rewrite the two-dimensional vector $\boldsymbol{\alpha}$ as:

$$\hat{\boldsymbol{\alpha}}(\boldsymbol{\xi}) = \frac{4G}{c^2}\int \mathrm{d}^2\xi'\,\Sigma\boldsymbol{\xi}'\,\frac{\boldsymbol{\xi}-\boldsymbol{\xi}'}{|\boldsymbol{\xi}-\boldsymbol{\xi}'|^2}, \tag{4.2}$$

where we have defined the *surface mass density*:

$$\Sigma(\boldsymbol{\xi}) \equiv \mathrm{d}r_3\,\rho(\xi_1,\xi_2,r_3) \tag{4.3}$$

as the mass density projected onto the lens plane, perpendicularly to the light ray, and where r_3 is the coordinate along the line of sight, and ξ_1, ξ_2 the other two perpendicular coordinates.

Lens equation: The lens equation puts into relation the true position $\boldsymbol{\beta}$ and observed position $\boldsymbol{\theta}$ of the source on the sky by simple geometrical considerations:

$$\boldsymbol{\beta} = \boldsymbol{\theta} - \frac{D_{\rm ds}}{D_{\rm s}}\,\hat{\boldsymbol{\alpha}}(D_{\rm d}\boldsymbol{\theta}) \equiv \boldsymbol{\theta} - \boldsymbol{\alpha}(\boldsymbol{\theta}), \tag{4.4}$$

where we have redefined the deflection angle as the reduced quantity $\boldsymbol{\alpha} = D_{\rm ds}\hat{\boldsymbol{\alpha}}/D_{\rm s}$ from definition (4.1). It is convenient to define the critical surface mass density:

$$\Sigma_{\rm cr} = \frac{c^2}{4\pi G}\frac{D_{\rm s}}{D_{\rm d}D_{\rm ds}}, \tag{4.5}$$

which depends on the combination of the distances $D_{\rm d}$ and $D_{\rm ds}$, and defines the limiting case in which the deflection angle $\boldsymbol{\alpha} = \boldsymbol{\theta}$ and $\boldsymbol{\beta} = 0$. The dimensionless form of the surface mass density is defined as the *convergence*:

$$\kappa(\boldsymbol{\theta}) = \frac{\Sigma(D_{\rm d}\boldsymbol{\theta})}{\Sigma_{\rm cr}}, \tag{4.6}$$

and allows to define the threshold between *strong* and *weak* lenses: a mass distribution with $\kappa > 1$ constitutes a strong lens, i.e. the lens has a surface mass density larger than the critical one, and produces multiple images (note that the

condition $\kappa \geq 1$ is necessary but not suffiecient). The weak lensing regime, instead, is characterised by $\kappa \ll 1$.

Deflection potential: The reduced deflection angle, rewritten in terms of the convergence, becomes:

$$\boldsymbol{\alpha}(\boldsymbol{\theta}) = \frac{1}{\pi}\int \mathrm{d}^2\theta'\, \kappa(\boldsymbol{\theta}')\frac{\boldsymbol{\theta}-\boldsymbol{\theta}'}{|\boldsymbol{\theta}-\boldsymbol{\theta}'|^2}, \tag{4.7}$$

in which we can recognise the last term to be $\boldsymbol{\theta}-\boldsymbol{\theta}'/|\boldsymbol{\theta}-\boldsymbol{\theta}'|^2 = \nabla(\ln|\boldsymbol{\theta}-\boldsymbol{\theta}'|)$ in two dimensions. The deflection angle can be expressed therefore in terms of the *deflection potential*:

$$\psi(\boldsymbol{\theta}) = \frac{1}{\pi}\int \mathrm{d}^2\theta'\, \kappa(\boldsymbol{\theta}')\ln|\boldsymbol{\theta}-\boldsymbol{\theta}'| \tag{4.8}$$

as:

$$\boldsymbol{\alpha} = \nabla\psi. \tag{4.9}$$

The deflection potential is the scaled and projected Newtonian potential Φ of the lens:

$$\psi(\boldsymbol{\theta}) = \frac{D_{\mathrm{ds}}}{D_{\mathrm{d}}D_{\mathrm{s}}}\frac{2}{c^2}\int \mathrm{d}z\, \Phi(D_{\mathrm{d}}\boldsymbol{\theta}, z), \tag{4.10}$$

and its Laplacian is related to the convergence by means of the Poisson equation:

$$\Delta\psi = \frac{2}{c^2}\frac{D_{\mathrm{d}}D_{\mathrm{ds}}}{D_{\mathrm{s}}}\int \mathrm{d}z\, \Delta\Phi = \frac{2}{c^2}\frac{D_{\mathrm{d}}D_{\mathrm{ds}}}{D_{\mathrm{s}}}4\pi G\Sigma = 2\frac{\Sigma(\boldsymbol{\theta})}{\Sigma_{cr}} \equiv 2\kappa(\boldsymbol{\theta}). \tag{4.11}$$

Magnification and distortion: Since the deflection angle is a function of the impact parameter ξ, different light bundles coming from the same source will be differentially deflected, and consequently the image of the source will also be affected by lensing. Hence we are interested in quantifying the effect of gravitational lensing on the shape of the source object, and in relating the latter to the its observed shape.

The feature that lensing conserves the surface brightness of the source can be efficiently used for this purpose. So the surface brightness distribution in the source plane, $I^{(s)}(\boldsymbol{\beta})$, must be equal to the observed surface brightness in the lens plane:

$$I(\boldsymbol{\theta}) = I^{(s)}[\boldsymbol{\beta}(\boldsymbol{\theta})]. \tag{4.12}$$

The lens equation can be locally linearised such that for any point $\boldsymbol{\theta}_0$ in the observed image the corresponding point $\boldsymbol{\beta}_0 = \boldsymbol{\beta}(\boldsymbol{\theta}_0)$ in the source image can be written by means of the linear mapping:

$$\boldsymbol{\beta} = \boldsymbol{\beta}_0 + \mathscr{A}(\boldsymbol{\theta}_0)(\boldsymbol{\theta}-\boldsymbol{\theta}_0). \tag{4.13}$$

this linearisation can be done if the condition that the size of the source is much smaller than the size of variation of the lens is fulfilled. In this case the distortion of the image is the Jacobian of this mapping:

$$\mathscr{A}(\boldsymbol{\theta}) = \frac{\partial \boldsymbol{\beta}}{\partial \boldsymbol{\theta}} = \left(\delta_{ij} - \frac{\partial^2 \psi(\boldsymbol{\theta})}{\partial\theta_i \partial\theta_j}\right) = \begin{pmatrix} 1-\kappa-\gamma_1 & -\gamma_2 \\ -\gamma_2 & 1-\kappa+\gamma_1 \end{pmatrix}, \tag{4.14}$$

where we have introduced the complex *shear*:

$$\gamma \equiv \gamma_1 + i\gamma_2 = |\gamma| e^{2i\phi}, \tag{4.15}$$

whose components are also related to the deflection potential by means of combinations of its second derivatives $\psi_{,ij}$:

$$\begin{aligned} \gamma_1 &= \frac{1}{2}(\psi_{,11} - \psi_{,22}) \equiv \gamma(\boldsymbol{\theta}) \sin(2\phi(\boldsymbol{\theta})) \\ \gamma_2 &= \psi_{,12} = \psi_{,21} \equiv \gamma(\boldsymbol{\theta}) \cos(2\phi(\boldsymbol{\theta})). \end{aligned} \tag{4.16}$$

Notice that the presence of a factor 2 in front of the angle ϕ stands for the symmetry property of the shear, which is a spin-2 field. The term κ is instead the convergence, related to the deflection potential by Eqn. (4.11). Note that this implies that the convergence can be written:

$$\kappa = \frac{1}{2}(\psi_{,11} + \psi_{,22}) = \frac{1}{2}\mathrm{tr}\,\psi_{,ij}. \tag{4.17}$$

The great advantage of weak lensing, therefore, is the fact that its observables are directly linked to the matter density by means of Poisson's equation, making the this technique a great way to directly probe the mass distribution. The Jacobian in Eqn.(4.14) can be rewritten as:

$$\mathscr{A} = (1-\kappa)\begin{pmatrix} 1 & 0 \\ 0 & 1 \end{pmatrix} - \gamma \begin{pmatrix} \cos(2\phi) & \sin(2\phi) \\ \sin(2\phi) & -\cos(2\phi) \end{pmatrix}, \tag{4.18}$$

from which one can extrapolate the meaning of convergence and shear. The convergence is associated with an isotropic focusing of the light rays, and hence the source image is mapped onto an image with the same shape, but larger size. The shear instead introduces anisotropy of magnitude γ and direction ϕ in this mapping. Therefore the total *magnification* is given by both isotropic and anisotropic focusing:

$$\mu = \frac{1}{\det\mathscr{A}} = \frac{1}{(1-\kappa)^2 - |\gamma|^2} \tag{4.19}$$

In presence of both convergence and shear a circular source gets mapped onto an ellipse whose major and minor axes are respectively:

$$\begin{aligned} a &= (1-\kappa-\gamma)^{-1} \\ b &= (1-\kappa+\gamma)^{-1}. \end{aligned} \tag{4.20}$$

It is worth noticing that when a linearisation of the mapping in Eqn. (4.13) is not possible, then higher order derivatives of the deflection potential enter the analysis and the first and second flexions F and G must be considered (Bartelmann, 2010a).

Ellipticities and reduced shear: If $I(\boldsymbol{\theta})$ is the surface brightness of the galaxy at the position $\boldsymbol{\theta}$, then the centre of the image $\bar{\boldsymbol{\theta}}$ can be calculated as the normalised average:

$$\bar{\boldsymbol{\theta}} \equiv \frac{\int \mathrm{d}^2\theta\, q_I[I(\boldsymbol{\theta})]\boldsymbol{\theta}}{\int \mathrm{d}^2\theta\, q_I[I(\boldsymbol{\theta})]}, \tag{4.21}$$

where $q_I[I]$ is a suitable weighting function. The *tensor of second brightness moments* can be then defined as the symmetric tensor:

$$Q_{ij} = \frac{\int \mathrm{d}^2\theta\; q_I[I(\boldsymbol{\theta})]\;(\theta-\bar{\theta}_i)(\theta-\bar{\theta}_j)}{\int \mathrm{d}^2\theta\; q_I[I(\boldsymbol{\theta})]}, \quad i,j \in 1,2 \tag{4.22}$$

Upon this definition one can define:

- the *size* of the image ω by means of two invariants of the tensor Q:

$$\omega = (Q_{11}Q_{22} - Q_{12}^2)^{1/2}; \tag{4.23}$$

- the *shape* of the image by means of the *complex ellipticity* (Bonnet & Mellier, 1995):

$$\epsilon \equiv \frac{Q_{11} - Q_{22} + 2iQ_{12}}{Q_{11} + Q_{22} + 2(Q_{11}Q_{22} - Q_{12}^2)^{1/2}}, \tag{4.24}$$

whose components (cfr. Eqn. (3.2)) are:

$$\epsilon_+ = \frac{Q_{11} - Q_{22}}{Q_{11} + Q_{22} + 2(Q_{11}Q_{22} - Q_{12}^2)^{1/2}} \tag{4.25}$$

and

$$\epsilon_\times = \frac{2Q_{12}}{Q_{11} + Q_{22} + 2(Q_{11}Q_{22} - Q_{12}^2)^{1/2}} \tag{4.26}$$

One can write the tensor of second brightness moments also for the source image, $Q_{ij}^{(s)}$ and use both the property that the surface brightness must be conserved and the linearised lens equation. The relation between the source and observed images is then:

$$Q^{(s)} = \mathscr{A} Q \mathscr{A}^T = \mathscr{A} Q \mathscr{A}, \tag{4.27}$$

where the Jacobian $\mathscr{A}$ is considered at the position $\bar{\boldsymbol{\theta}}$ and we used the property that $\mathscr{A} = \mathscr{A}^T$ in the Born approximation.

In general the ellipticity of the source depends on a combination of convergence and shear, the so-called *reduced shear*:

$$g(\boldsymbol{\theta}) \equiv \frac{\gamma(\boldsymbol{\theta})}{1-\kappa(\boldsymbol{\theta})} \tag{4.28}$$

in terms of which the Jacobian can be written:

$$\mathscr{A} = (1-\kappa)\begin{pmatrix} 1-g_1 & -g_2 \\ -g_2 & 1+g_1 \end{pmatrix} \tag{4.29}$$

Also from this formulation it is clear that the factor $1-\kappa$ affects the size of the image, but not its shape. The sizes of source and observed image is:

$$\omega = \mu(\boldsymbol{\theta})\omega^{(s)}. \tag{4.30}$$

The ellipticity of the source can be related to the observed one by means of (Seitz & Schneider, 1997):

$$\epsilon^{(s)} = \begin{cases} \frac{\epsilon-g}{1-g^*\epsilon} & \text{for } |g| \le 1 \\ \frac{1-g\epsilon^*}{\epsilon^*-g^*} & \text{for } |g| > 1 \end{cases} \tag{4.31}$$

This formulation becomes much simpler in the case of weak lensing, defined by the following conditions:

$$\left.\begin{array}{r} \kappa \ll 1 \\ |\gamma| \ll 1 \end{array}\right\} \Rightarrow |g| \ll 1, \tag{4.32}$$

which then lead to the following expression for the ellipticity in the limit of weak lensing:

$$\epsilon \approx \epsilon^{(s)} + g \approx \epsilon^{(s)} + \gamma. \tag{4.33}$$

This equation practically states that the observed ellipticity is given by the original source ellipticity plus a contribution of deformation due to weak lensing, which amounts to about 1% for cosmic shear (which we are going to discuss now), making it a statistical effect which leads to a significant signal to noise ration only if enough sources are considered.

Cosmic shear: The treatment of weak lensing carried out up to now considered the presence of one lens mass only, whereas a natural assumption would be that light paths covering the entire space between the source from where they depart up to us encounter the large scale structure along their way and undergo lensing several times, as shown in Fig. (4.2). Therefore the expression for the convergence as defined in Eqn. (4.6) must be substituted by another accounting for the distribution of mass between the sources and us: The *effective convergence*:

$$\kappa_{\rm eff}(\boldsymbol{\theta}) = \int_0^{\chi_H} \mathrm{d}\chi\, W_\kappa(\chi)\delta(\chi\boldsymbol{\theta}), \tag{4.34}$$

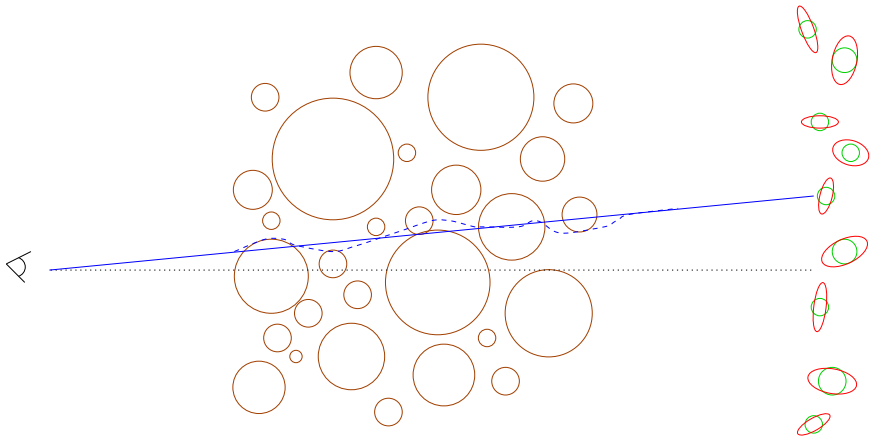

Figure 4.2: Weak lensing operated by the LSS. Figure taken by Refregier (2003).

which contains an integration over the density contrast δ along the line of sight and a weighting function $W_\kappa(\chi)$ which accounts for the fact that the sources are distributed in redshift:

$$W_\kappa(\chi) = \frac{3H_0^2\Omega_{m0}}{2c^2}\frac{D_+(a(\chi))}{a(\chi)}G(\chi)\chi, \quad \text{with} \quad G(\chi) = \int_\chi^{\chi_H} \mathrm{d}\chi'\, n(z)\frac{\mathrm{d}z}{\mathrm{d}\chi'}\frac{\chi'-\chi}{\chi'}, \tag{4.35}$$

where $n(z)$ is the redshift distribution of the sources:

$$n(z)\mathrm{d}z = \frac{\beta}{z_0^3\Gamma(3/\beta)}z^2\exp\left[-\left(\frac{z}{z_0}\right)^\beta\right]\mathrm{d}z. \tag{4.36}$$

Also note that Poisson's equation was used in Eqn. (4.34):

$$\Delta\Phi = \frac{3}{2a\chi_H^2}\Omega_0\delta. \tag{4.37}$$

The effective convergence is thus proportional to the matter density parameter. Throughout the rest of the thesis we will drop the subscript from κ_{eff} and mean by κ the effective convergence.

In order to study the statistical properties of the convergence, we define its power spectrum:

$$C_\kappa(\ell) = \int_0^{\chi_H}\frac{\mathrm{d}\chi}{\chi^2}W_\kappa^2(\chi)P_\delta\left(\frac{\ell}{\chi},\chi\right), \tag{4.38}$$

where P_δ is the density power spectrum, and where the projection due to Limber's equation (Limber, 1954) has been used.

A last important remark is the fact that the statistical properties of convergence and shear, i.e. their power spectra, are the same. If we in fact use the flat

sky approximation, and consider the Fourier transform of the shear, $\hat{\gamma}$, the correlator will be (Bartelmann, 2010b):

$$\langle\hat{\gamma}\hat{\gamma}^*\rangle = \langle|\hat{\gamma}|_1^2\rangle + \langle|\hat{\gamma}|_2^2\rangle = \left[\frac{1}{4}(\ell_1^2-\ell_2^2)^2 + \ell_1^2\ell_2^2\right]\hat{\psi}\hat{\psi}^* = \left[\frac{\ell^4}{4}\right]\hat{\psi}\hat{\psi}^* = \langle\hat{\kappa}\hat{\kappa}^*\rangle, \quad (4.39)$$

where $\ell^2 = \ell_1^2 + \ell_2^2$. Therefore $C_\gamma(\ell) = \langle\hat{\gamma}\hat{\gamma}^*\rangle = C_\kappa(\ell)$.

Shear and mass in aperture: Very useful quantities to measure are the so-called variance in apertures. According to this formulation, which was suggested by Schneider et al. (1992), the variances of quantities such as the shear and the mass could be calculated in apertures of size θ:

$$\langle\kappa^2\rangle(\theta) = \frac{2}{\pi}\int \ell \mathrm{d}\ell\, W_1^2(\ell\theta)\, C_\kappa(\ell), \quad (4.40)$$

and

$$\langle M_\kappa^2\rangle(\theta) = \frac{2}{\pi}\int \ell \mathrm{d}\ell\, W_4^2(\ell\theta)\, C_\kappa(\ell), \quad (4.41)$$

so to give an idea of how the fluctuations scale with varying aperture size. The weighting functions $W_0(x)$, and $W_4(x)$, $x = \ell\theta$, are defined as:

$$W_1(x) = \frac{J_1(x)}{x} \quad \text{and} \quad W_4(x) = \frac{12J_4(x)}{x^2}, \quad (4.42)$$

respectively, for the shear variance averaged in an aperture of size θ and the aperture mass variance. The usefulness of the mass in aperture is also that it can be calculated directly from the convergence without any need for mass reconstruction.

4.2 Weak lensing and intrinsic alignments [1]

When the convergence power spectrum is measured, usually a *shot noise* is added to account for the fact that source galaxies have intrinsic ellipticity variation and are not simply round in shape. The observed ellipticity is not only due to the shear acting along the line of sight. This contribution is assumed to be random, and adds a white noise to the convergence signal (Kaiser, 1992, 1998):

$$C_\kappa^{\mathrm{obs}}(\ell) = C_\kappa(\ell) + \frac{\sigma_\epsilon^2}{\bar{n}}, \quad (4.43)$$

where σ_ϵ^2 is the rms intrinsic shear and $\bar{n}$ is the mean number density of the galaxies in the survey. This approximation, though, reveals itself to be crude. In

[1] Part of this section was inspired by the online tutorial http://gravitationallensing.pbworks.com/w/page/15553247/FrontPage

fact, if we consider the definition of the observed ellipticity in Eqn.(4.33) and then also consider the ensemble average, or correlator between two observed ellipticities at positions $\boldsymbol{\theta}_i$ and $\boldsymbol{\theta}_j$ on the sky, we obtain and expression containing four terms:

$$\langle \epsilon(\boldsymbol{\theta}_i)\epsilon(\boldsymbol{\theta}_j)\rangle = \langle \gamma_i\gamma_j\rangle + \langle \epsilon_i^{(s)}\epsilon_j^{(s)}\rangle + \langle \gamma_i\epsilon_j^{(s)}\rangle + \langle \gamma_j\epsilon_i^{(s)}\rangle. \tag{4.44}$$

The first term is the precisely the *shear-shear* component, also dubbed GG (gravitation -gravitation) component, i.e. the power spectrum of the shear (or, equivalently, of the convergence). The second term is the *intrinsic-intrinsic* component (or II component), and is due to the fact that close galaxies tend to be aligned (see Chap. 3). The third and fourth components are the *shear-intrinsic* components (or GI components), noted for the first time by Hirata & Seljak (2004). They physically represent the same phenomenon, namely the correlation that might arise between the lensed image of a background source and the image of a foreground galaxy which is physically aligned from the tidal filed of the lens. In other words the lens contributes both the the physical alignment of the foreground galaxy and to the lensing of the background one. This contribution actually produces an anticorrelation due to the different kind of shearing of the image (gravitational lensing produces a tangential shear, whereas the intrinsic alignment produces preferentially a radial alignment). So we can write in general for the power spectrum:

$$C_\kappa^{\rm obs}(\ell) = C_\kappa(\ell) + C_\epsilon(\ell) + C_{\kappa\epsilon}(\ell) \tag{4.45}$$

4.2.1 E- and B-modes

The lensing usually produces in the galaxy shapes a pattern. Kaiser (1992); Stebbins (1996) show how a tangential distortion pattern is created by lensing of a point mass. Such pattern is curl-free and is referred to as of E-type pattern, or E-mode. We have seen that the ellipticity is intimately related to the shear field, and this can be written, in the flat sky approximation, as (Kamionkowski et al., 1998):

$$\gamma_{ij} = \begin{pmatrix} \epsilon_+ & \epsilon_\times \\ \epsilon_\times & -\epsilon_+ \end{pmatrix}, \tag{4.46}$$

where $\epsilon_+ = |\epsilon|\cos(2\phi)$ and $\epsilon_\times = |\epsilon|\sin(2\phi)$ are the components of the complex ellipticity (cfr. Eqn.(3.2)). The shear field as a function of space $\mathbf{x}$ can be written in terms of a gradient and a curl component, called the E- and B-modes (Crittenden et al., 2002):

$$\gamma_{ij}(\mathbf{x}) = \left(\partial_i\partial_j - \frac{1}{2}\delta_{ij}\nabla^2\right)\Phi_E(\mathbf{x}) + \left(\epsilon_{kj}\partial_i\partial_k + \epsilon_{ki}\partial_k\partial_j\right)\Phi_B(\mathbf{x}), \tag{4.47}$$

where $\epsilon_i j$ is the anti-symmetric tensor. To extract the E- and B-components it is sufficient to apply the ∇^4 to the shear field, and obtain:

$$\begin{aligned} \nabla^4\Phi_E(\mathbf{x}) &= 2\partial_i\partial_j\gamma_{ij} = \nabla^2\gamma_E \\ \nabla^4\Phi_B(\mathbf{x}) &= 2\epsilon_{ij}\partial_i\partial_k\gamma_{jk} = \nabla^2\gamma_B, \end{aligned} \tag{4.48}$$

where we have defined $\gamma_E \equiv \nabla^2\Phi_E(\mathbf{x})/2$ and $\gamma_B \equiv \nabla^2\Phi_B(\mathbf{x})/2$ (Kamionkowski et al., 1998), and we can see that these are combinations of the derivatives of the ellipticity components:

$$\begin{aligned}\nabla^2\gamma_E &= (\partial_x\partial_x - \partial_y\partial_y)\epsilon_+ + 2\partial_x\partial_y\epsilon_\times \\ \nabla^2\gamma_B &= (\partial_x\partial_x - \partial_y\partial_y)\epsilon_\times - 2\partial_x\partial_y\epsilon_+.\end{aligned} \tag{4.49}$$

For this very reason $\gamma_E(\mathbf{x})$ and $\gamma_B(\mathbf{x})$ are degenerate functions which may differ by a constant and a linear gradient term, yet producing the same ellipticity field. In the case of gravitational lensing the shear field is given by:

$$\gamma_{ij}(\mathbf{x}) = \left(\partial_i\partial_j - \frac{1}{2}\delta_{ij}\nabla^2\right)\psi(\mathbf{x}), \tag{4.50}$$

where ψ is the deflection potential. This immediately shows that for weak lensing $\Phi_E(\mathbf{x}) = \psi(\mathbf{x})$, and $\Phi_B(\mathbf{x}) = 0$ (Kamionkowski et al., 1998), and the only patterns expected are the tangential ones. The patterns for both modes are represented in Fig.(4.3)

Beyond IA, other sources of systematics in shear measurements are constituted by incomplete correction for seeing and optical distortions, selection effects, noise-rectification biases (for technical details, see Hoekstra & Jain, 2008).

4.3 Tomographic Weak Lensing

A new available information from weak lensing surveys is the photometric redshift of the sources, which therefore gives us information on their effective distribution. This information can "sharpen the statistical tools" (power spectrum, bispectrum, etc) we use for extracting the cosmological parameters, increasing the signal to noise ratio for the convergence. The possibility of being able to recover the redshift information up to high redshifts ($z \gtrsim 1$) and therefore the information of the lensing field along the line of sight, provides us with the additional knowledge about the growth of the structure, which can therefore be a means of more tightly constraining cosmological parameters, especially the ones affecting the growth of the structure, such as the dark energy parameter. This also represents a way to cross-check measurements of the dark energy parameter with the other important measurements of SNIa and the CMB.

The idea is to divide the sample of galaxies in redshift bins, and define a redshift distribution within each bin. The convergence will then be (Takada & Jain, 2004):

$$\kappa_i(\boldsymbol{\theta}) = \int_0^{\chi_H} \mathrm{d}\chi\, W_\kappa^{(i)}(\chi)\chi\delta(\chi\boldsymbol{\theta}), \tag{4.51}$$

where this time the window function is:

$$W_\kappa^{(i)}(\chi) = \begin{cases} \frac{3H_0^2\Omega_0}{2c^2} D_+(a(\chi))\chi G_i(\chi) & \text{for } \chi \le \chi_{i+1} \\ 0 & \text{for } \chi > \chi_{i+1} \end{cases} \tag{4.52}$$

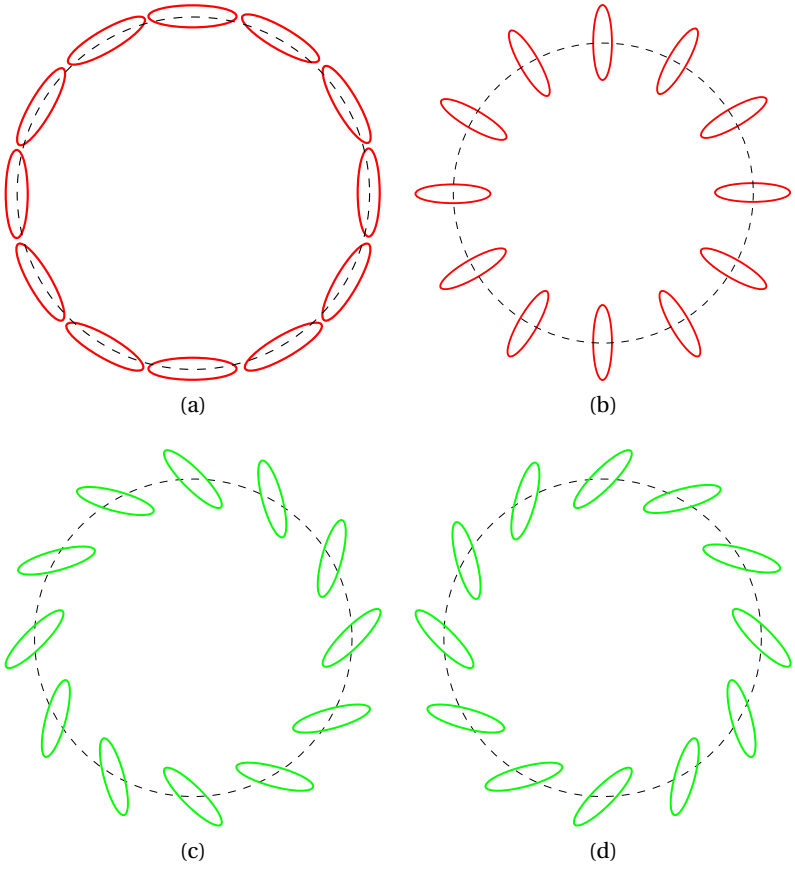

Figure 4.3: Typical patterns expected for the E-modes are shown in (a) and (b) panels, whereas B-modes are shown in panels (c) and (d). The figure was kindly provided by B. M. Schäfer.

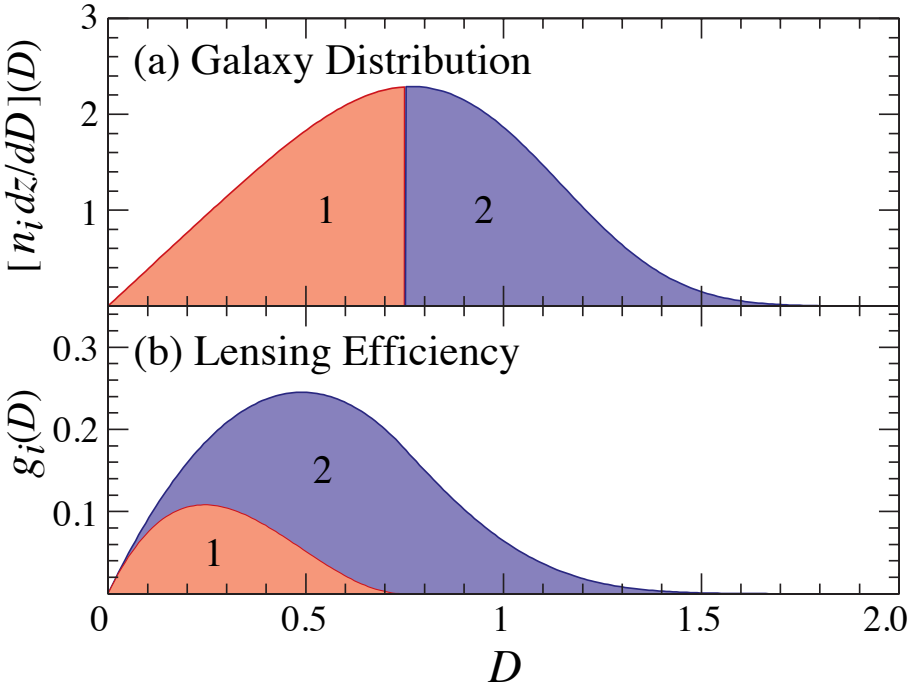

Figure 4.4: Subdivision of the source population taken from Hu (1999). The image shows a division of the galaxy sample in two redshift bins (top panel), and the relative lensing efficiency functions $g_i(D)$ (bottom panel). These correspond to our $W_\kappa^{(i)}$.The clear overlapping of the lensing efficiency is due to the fact that both high and low redshift galaxies undergo the lensing of the same foreground low redshift structures.

where the possible errors for the photometric redshifts are not considered.

In Fig.(4.4) we show an example of partition of the galaxy redshift distribution with $z_{\rm med} = 1$ and the corresponding lensing efficiencies taken from (Hu, 1999). The plots clearly show how a net and clean division of the galaxy redshift sample leads to overlapping lensing efficiencies. This is indicative of the fact that both high and low redshift bins are subject to the lensing of the same foreground structure at low redshift. One furthermore expects the higher redshift bins to yield to a stronger signal, since the structure in-between the source and the observer is larger and provides more lensing (Hu, 1999). Due to the overlapping lensing efficiencies we also expect to have cross-correlation signals between different bins.

Once the convergence of each bin is defined, the power spectrum between two bins i, j becomes (Takada & Jain, 2004):

$$C_{ij}(\ell) = \int_0^{\chi_H} {\rm d}\chi \, W_\kappa^{(i)}(\chi) W_\kappa^{(j)}(\chi) \chi^{-2} P_\delta(\kappa = \frac{\ell}{\chi}, \chi) \tag{4.53}$$

We applied tomography to both the convergence power spectrum $C_\kappa(\ell)$ and the ellipticity spectra $C_E^\epsilon(\ell)$ and $C_B^\epsilon(\ell)$ modelled by means of the CNPT model. Our results are shown in Fig. (4.5) and (4.6). In the first series of plots we show how both the linear and non-linear auto- and cross-power spectra vary with number of bins. We also plot the shape noise typical for the EUCLID survey. As can be evinced from the case of $n = 2$ bins (top right panel) the amplitude of the signal is higher for the auto-spectra relative to the largest bin which, corresponding to a deeper distribution in redshift, collects more weak lensing signal. The gain in amplitude is clearly visible throughout the increasing number of bins. Same considerations apply for the ellipticity spectra $C_E^\epsilon(\ell)$ and $C_B^\epsilon(\ell)$, where the latter spectrum is always lower in amplitude compared to the former. It is clear that a subdivision into a number of bins n larger than ~ 3 would essentially not add much amplitude to the spectra. A practical way of quantifying the amount of information would be to consider the function $R_{ij} = C_{ij}/(C_{ii}C_{jj})^{1/2}$, which is the correlation coefficient between the power spectra of the different bins. In analogy to correlation coefficient in statistical analyses, the function R_{ij} can vary in the range $[0, 1]$. Low values of the correlation coefficient indicate that the number of subdivisions are actually adding new information and that, therefore, the subdivision id profitable. Higher values of R_{ij} tending to 1, instead, correspond to a little gain in power of the spectra, therefore meaning that further subdivisions in redshift bins are not useful anymore.

Finally, in Fig. (4.7) we plot how the signal-to-noise ratio of both the linear and non-linear spectra $C_\kappa(\ell)$ vary for an increasing number of bins. We can see also from here how the gain in information basically saturates for $n = 3$.

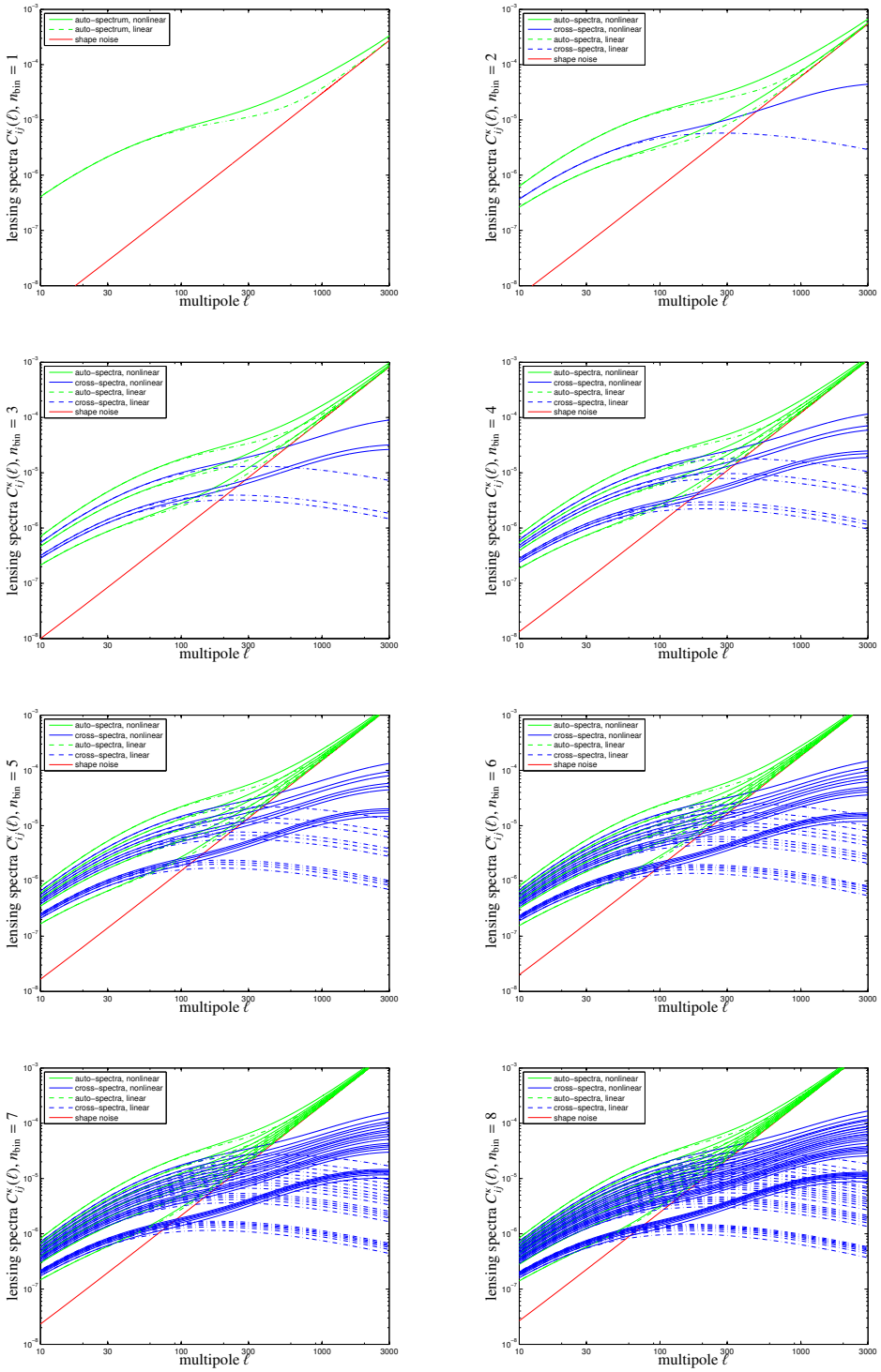

Figure 4.5: Tomographic spectra $C^\kappa_{ij}(\ell)$ for an increasing number n of bins for both linear (dashed curve) and non-linear (solid curve) power spectra. The shape noise is also shown. The amplitudes of the power spectra grow as the number of bins increases, but this effect saturates for $n \sim 3$.

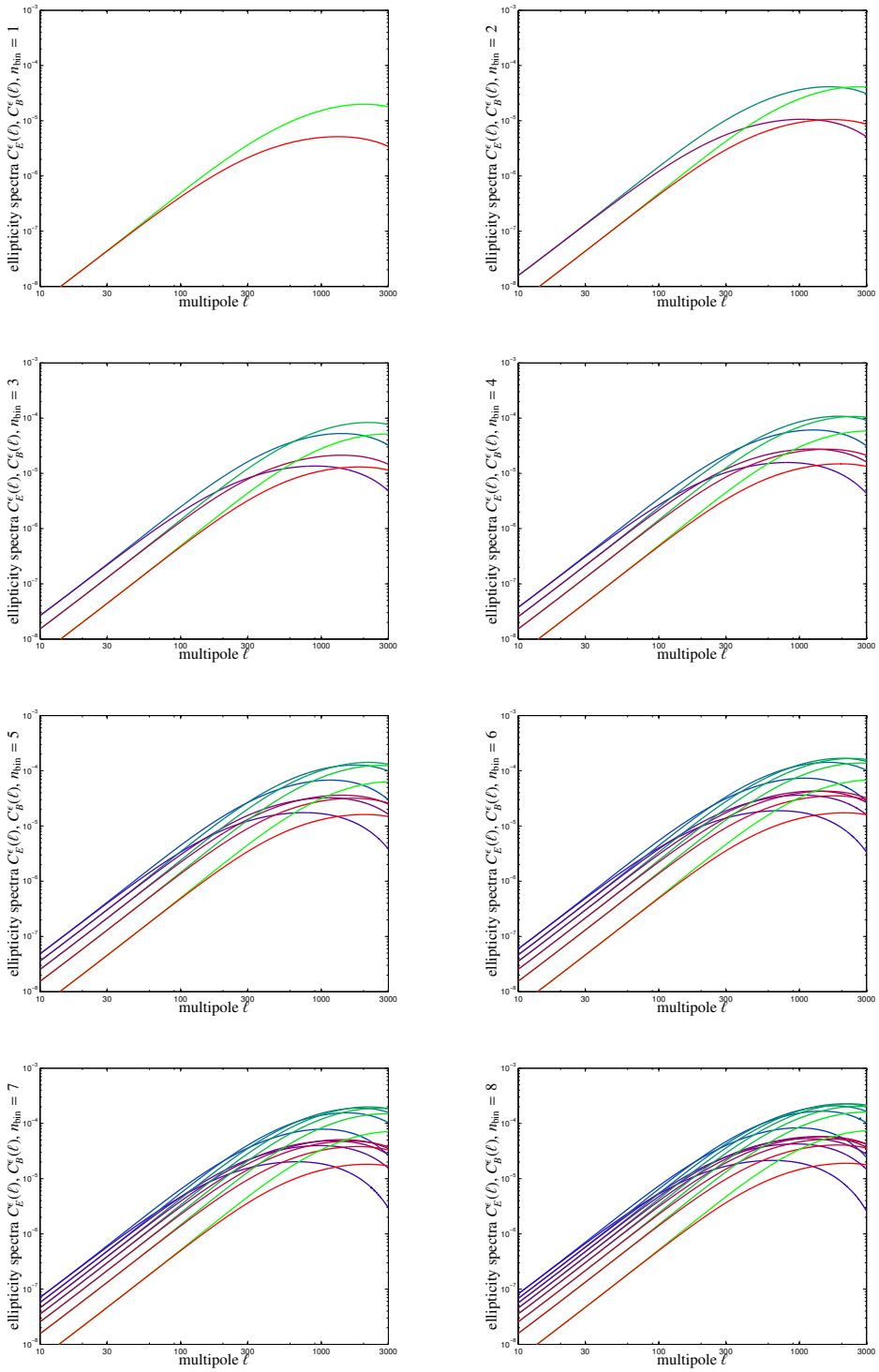

Figure 4.6: Tomographic spectra for the E- and B-modes for an increasing number n of bins. It can be easily seen how the increase in bins leads to less and less gain in information. The essential gap of signal is obtained for a subdivision up to $n = 3$ bins.

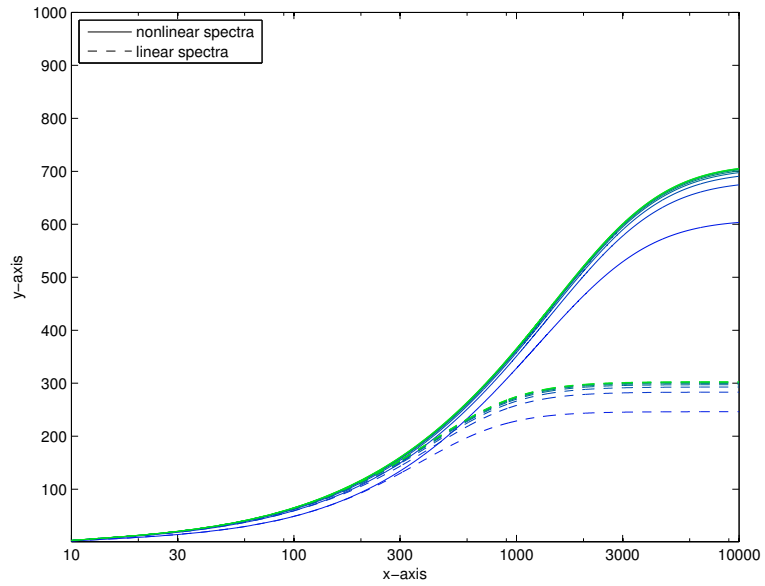

Figure 4.7: Signal-to-noise ratio for the linear and non-linear power spectra $C_\kappa(\ell)$. It is clear that $n = 3$ bins are enough for already obtaining a considerable gain in amplitude.

4.4 Measurements of WL with IA

In the last two decades a tremendous amount of efforts has been put in the numerical and observational investigation of the impact of IA in weak lensing surveys. The IA signal is expected to contaminate the shear signal of about 10% (Bacon et al., 2000; Wittman et al., 2000; Kaiser et al., 2000; Van Waerbeke et al., 2000; Heavens et al., 2000), hampering today the measurements of the weak lensing signal in percent-accuracy surveys and extraction of cosmological parameters therefrom, being though at the same time a precious wealth of information about structure formation and galaxy evolution.

IA and GI alignments The first attempts to study IA of spiral galaxies can be traced back to Croft & Metzler (2000), who investigate IA via numerical simulations and find positive detection of correlations up to scales of 20 Mpch^{-1}, thereby confirming the 10% level of contamination. Heavens et al. (2000); Heymans & Heavens (2003) also used N-body simulations to show how the interplay between weak lensing signal and intrinsic ellipticity signal depends on the redshift depth of the survey: as expected from Crittenden et al. (2001) the weak lensing appears to dominate over the ellipticity correlation if the survey is deep, but the opposite happens for shallow surveys, where the IA effectively dominate. This domination has been repetitively inspected, among others, by analyses of Lee & Pen (2000) and Brown et al. (2002). This claim, though, was later challenged by Hirata & Seljak (2004), who speculated for the first time that not only II correlations could affect weak lensing measurements, but also and more significantly the GI alignments. Hirata & Seljak (2004) therefore estimate the magnitude of the GI alignment for both linear and quadratic models of intrinsic ellipticities (see Sec. 3.6 and Sec. 3.4), finding that while GI alignments dominate significantly over the II in the linear alignment model for a broad redshift distribution, the quadratic model does not produce any GI signal by construction, since if a Gaussian distribution is adopted for the distribution of angular momenta as in Eqn. (3.16), the GI corresponds to an odd moment, and therefore vanishes. In the linear model that the difference between GI and II can be of more than one order of magnitude.

In this direction thus Mandelbaum et al. (2006) perform measurement of both II and GI correlations on a sample of 2.6×10^5 spectroscopic galaxies from SDSS at low redshift ($z \lesssim 0.12$), finding no indication of II alignments (because of the weakness of the signal), but a significant negative signal for the GI alignment which would underestimate the shear signal by 20%. This initial analysis is enhanced by Hirata et al. (2007), who analysed luminous red galaxies from the SDSS and 2SLAQ and focused particularly on GI alignments, finding a $> 3\sigma$ detections affecting scales > 60 Mpch^{-1}. Furthermore they study the scaling of the IA signal with redshift, galaxy luminosity and transverse separation, finding a bias in the parameter σ_8 of $\Delta\sigma_8 = -0.02$.

IA and tomography: Bridle & King (2007) make use of a tomographic analysis to try to pinpoint the bias in the dark energy parameter (since dark enery is very likely to be strongly constrained by tomography) when II and GI alignments are not included. The linear alignment model is adopted. Their analysis leads to a dramatic bias of 50% on the dark energy equation of state. They also study how the photometric redshift scatter affects the results, and stress that great accuracy is needed. Furthermore, if IA are considered then this increases of twice the number of tomographic bins required for obtaining the same results as when only shear correlations are present. Recently a similar analysis has been carried out by Kirk et al. (2012), who also study the effect of IA on dark energy constraints, but adopt the so called non-linear alignment model (NLA), proposed by Hirata & Seljak (2004) for a description of IA. The situation appears to be even more dramatic, with a bias up to tens of σ level on w_0 and w_a if IA are neglected. In order to correct of this they use a flexible grid of nuisance parameters which are the marginalised over. The grid parameters are allowed to vary in scale and redshift. this clearly decreases the constraining power but removes the bias. A similar study, based on flexible grid of parameters, was use by Joachimi & Bridle (2010). They use tomography and perform a joint analysis of ellipticity and galaxy number density correlations, and cross-correlations between them. The attempt is to use the statistical power of the galaxy number density in order to make up for possible biases due to both the galaxy bias and the IA, which constitute the nuisance parameters of their grid. They therefore constrain cosmological parameters while providing a simultaneous self-calibration for IA and galaxy bias contributions. They find that, to this aim, a quality of the redshifts similar to that required in absence of IA must be achieved. The usage of such grids ultimately degrades part of the information of the original signal, as is to be expected.

Heymans et al. (2013) also apply a tomographic weak lensing analysis to the CHFTLenS survey, and attempt to reduce the effect of IA on the constraining power of weak lensing by simultaneously fitting the cosmological model and the intrinsic alignment model. They also increase the constraining power by using as priors other cosmological probes such as CMB constraints from WMAP7, the baryon acoustic oscillations from BOSS and a prior on the Hubble constant from HST. Concerning the IA, they find that the IA contamination depends on the galaxy type, being the IA signal different from zero just for early-type galaxies, but consistent with zero for late-type galaxies.

IA scalings and physical properties of the galaxies: In the last years more attention has been put on the physics contained in the IA and on the attempt of modelling the IAs' dependence on morphology, redshift and luminosity.

Studies of whether and how the IA evolve with redshift have been carried out by Mandelbaum et al. (2011), who increase the redshift depth of the analysis by performing for the first time measurements of IA at intermediate red-

shifts $z \sim 0.6$ for blue (spiral) galaxies by using galaxy images from SDSS and spectroscopic redshifts fro the WiggleZ Dark Energy Survey. They find no significant detection of IA signal for blue galaxies, and perform the analysis by using the linear alignment model for IA. Since in general the linear model is not very suitable for spiral galaxies, they counterbalance this choice by allowing for a power-law redshift evolution of the IA , which should account for effects such as mergers and interactions, i.e. non-linearities able to change the image of the galaxy. They find that constraints on cosmic shear contamination are not significantly weakened by this evolution with redshift. In a similar fashion, Joachimi et al. (2011) studied the IA correlations in the MegaZLRG galaxy sample of more than 8×10^5 luminous red galaxies at intermediate redshift up to $z \sim 0.6$ with photometric redshift information. By adding to this the previous information from SDSS samples they get to redshifts $z \lesssim 0.7$. In their analysis they find that correlations between the galaxy number density and galaxy shapes can improve cosmological parameters constraints, yielding to a bias $< 1\sigma$. The photometric redshift scatter is accounted for, as much as effects of galaxy-galaxy lensing and lensing magnification-shear cross correlations, introduced by photo-z uncertainty. They also assumed zero intrinsic alignments for blue galaxies. The fact that blue galaxies are often not considered in these measurements was questioned by the analysis of Lee & Pen (2007), who instead find that the IA signals of spiral and elliptical galaxies are both detected in the SDSS survey for redshifts $z \lesssim 0.4$. As a further step in the analysis for late-type galaxies, Lee (2010) focuses on the II signal from a spectroscopic late-type galaxy sample of the SDSS DR7 at very low redhsifts: $0 \leq z \leq 0.02$. The signal is detected up to 3.4σ and 2.4σ for spatial separation of ≈ 1 Mpch^{-1} and ≈ 2 Mpch^{-1}. In a different perspective compared to all the aforementioned analyses, the question they address is whether it would be possible to reconstruct the tidal field and thus the density field starting from the ellipticity one, problem they already addressed in a previous work (Lee & Pen, 2000), and whether the assumption often made of null IA signal for spiral galaxies is justifiable.

Joachimi et al. (2012) are interested in which physical ingredients contributes to the observable shapes of the galaxies. They are mainly interested in finding the distribution of galaxy shapes among various galaxy populations, and in finding constraints on the evolution of the dispersion of intrinsic ellipticities with redshift, which both shape the term of white noise, $\sigma_\epsilon / \bar{n}$, usually included in weak lensing analysis. The first aim is interesting since certain galaxy samples, even though being less in density (i.e. having lower $\bar{n}$), could be appropriately selected if they have low ellipticity dispersion σ_ϵ. So they calculate the intrinsic ellipticity dispersions and distributions of ellipticities of 1.5×10^5 galaxies from HST COSMOS Survey and compare these measurements with simulated-based models for the galaxy morphology obtained by exploiting the halo properties of halos in the Millennium Simulation. They consider both spirals and ellipticals and use linear and quadratic model, finding that early-type galaxies have a $\sigma_\epsilon \sim 25\%$ lower than early-type galaxies. The COSMOS Survey also covers four

decades in luminosity and redshifts out to $z \sim 2$, so they can investigate the redshift evolution of the intrinsic ellipticity dispersion, for which they find no evidence.

Suppression of IA: In general there have been attempts for suppressing the IA signal. Concerning II alignments, if photo-z are known, then these can be removed (King & Schneider (2003, 2002); Heymans & Heavens (2003); Takada & White (2004)) since one simply down weights galaxy pairs which have small separation. Crittenden et al. (2002) underline the fact that weak lensing can produce only E-modes, whereas IA can produce both E- and B-modes, and suggest this as a way of disentangling the two, although the B-mode signal is low and difficult to measure. Nevertheless, it appears an important tool for investigating the systematics of weak lensing. Finally, nulling and boosting techniques, adapt for GI alignments too, have been put forward by Joachimi & Schneider (2009) who, with a tomographic analysis, change the weighing functions in such a way that the contribution of the large scale structure inside a tomographic bin is nulled. These techniques have the disadvantage that there is a loss of accuracy in the constraints of the cosmological parameters.

4.5 Summary

- Key quantity in the theory of gravitational lensing is the deflection angle, which typically amounts to ~ 1 arcmin in weak lensing applications.
- The theory of gravitational lensing is based on two approximations, the *thin lens* and the *Born* approximation;
- The true and observed positions of the source on the sky are related by means of the lens equation: $\boldsymbol{\beta} = \boldsymbol{\theta} - \boldsymbol{\alpha}(\boldsymbol{\theta})$;
- The deflection angle can be written in terms of a deflection potential: $\boldsymbol{\alpha} = \nabla\psi$, which is the scaled and projected Newtonian potential Φ of the lens, and can thus also be related to the dimensionless surface mass density, or convergence: $\nabla^2\psi(\boldsymbol{\theta}) = 2\kappa(\boldsymbol{\theta})$;
- A source image undergoes magnification and distortion, information which is contained in the Jacobian $\mathscr{A}$ of the mapping $\boldsymbol{\theta} \mapsto \boldsymbol{\beta}(\boldsymbol{\theta})$: The Jacobian in turn contains the convergence κ and the shear γ.
- Only a combination of convergence and shear, the reduced shear $g = \gamma/(1-\kappa)$, can actually be measured;
- The statistical properties of convergence and shear, i.e. their power spectra, are the same;

- The weak lensing regime is defined by the conditions: $\kappa \ll 1$, $\gamma \ll 1$ and therefore $g \ll 1$ and $g \simeq \gamma$;
- Cosmic shear, i.e. the weak lensing from large scale structure, produces a distortion of the images of about 1%;
- IA constitute an severe contaminant to weak lensing measurements, accounting for $\sim$ 10% of the shear signal, but contain at the same time a wealth of information about galaxy and structure formation;
- While the shear due to gravitation produces as typical patterns tangential patterns, IA are able to produce also curl patterns. These are called respectively the E- and B-modes, as shown in Fig. (4.3), and could be used to disentangle the shear and IA signals.
- Improvements on the amplitude of the weak lensing signal can be obtained by tomography, i.e. by splitting the galaxy sample in different bins. Results we obtained by applying tomography to both weak lensing and intrinsic ellipticities are shown in Figs. (4.5) and (4.6), respectively for linear and non-linear weak lensing, and E- and B-modes. Fig. (4.7) shows the signal-to-noise ratio for the weak lensing tomographic spectra, from which it appears clear that a number of subdivisions of the galaxy redshift distribution higher than $\sim$ 3 leads to no significant gain in amplitude.
- IA signal can be decomposed in two parts: the II (intrinsic intrinsic) alignments, and the GI (gravity-intrinsic) alignments. The latter, suggested by Hirata & Seljak (2004), are actually expected to dominate over the II alignment (as is also found in observations);
- IA have been widely studied throughout the years, both in the attempt of completely removing them from the shear signal (King & Schneider, 2003, 2002; Heymans & Heavens, 2003; Takada & White, 2004; Joachimi & Schneider, 2009) and recovering from them as much information as possible about the structure and galaxy formation conditions (Lee & Pen, 2000, 2007). Latest studies try to model the IA signal and its dependence on several features such as morphology, luminosity and redshift (Lee, 2010; Mandelbaum et al., 2011; Joachimi et al., 2012)

Chapter 5

INTRINSIC ALIGNMENTS AND WEAK LENSING

The content of this chapter entirely reproduces the article Capranico et al. (2012). After a brief introduction about weak lensing and intrinsic alignments, the core of this work can be found in Sections 5.4.2, 5.5 and 5.6. A summary of our results is presented in Sec. 5.7.

5.1 Abstract

Subject of this paper are the statistical properties of ellipticity alignments between galaxies evoked by their coupled angular momenta. Starting from physical angular momentum models, we bridge the gap towards ellipticity correlations, ellipticity spectra and derived quantities such as aperture moments, comparing the intrinsic signals with those generated by gravitational lensing, with the projected galaxy sample of EUCLID in mind. We investigate the dependence of intrinsic ellipticity correlations on cosmological parameters and show that intrinsic ellipticity correlations give rise to non-Gaussian likelihoods as a result of nonlinear functional dependencies. Comparing intrinsic ellipticity spectra to weak lensing spectra we quantify the magnitude of their contaminating effect on the estimation of cosmological parameters and find that biases on dark energy parameters are very small in an angular-momentum based model in contrast to the linear alignment model commonly used. Finally, we quantify whether intrinsic ellipticities can be measured in the presence of the much stronger weak lensing induced ellipticity correlations, if prior knowledge on a cosmological model is assumed.

5.2 Introduction

Weak cosmic shear, i.e. lensing by the gravitational field of the cosmic matter distribution (Blandford et al., 1991; Seitz et al., 1994; Seitz & Schneider, 1994;

Kamionkowski et al., 1998), is considered to be an excellent probe of structure formation processes, precision measurements of cosmological parameters (Hu, 1999, 2002a,b; Takada & White, 2004; Hannestad et al., 2006) and the influence of dark energy on cosmic structure formation (Huterer & Turner, 2001; Huterer, 2002, 2010; Amara & Kitching, 2011; Kunz, 2012). The primary observable are ellipticity correlation functions or their Fourier counterparts (Jain & Seljak, 1997; Hu & Tegmark, 1999; Hu & White, 2001; Hu & Jain, 2004). These shape correlations have been first detected by a number of research groups more than 10 years ago (Van Waerbeke et al., 2000; Kaiser et al., 2000; Bacon et al., 2000; Wittman et al., 2000) and are now routinely used for parameter estimation. Correlations in shapes of galaxies are introduced because light rays from neighbouring galaxies experience correlation distortions due to correlations in the tidal fields through which the respective rays propagate. A common assumption is the absence of intrinsic correlations such that any positive shape correlation can be attributed to the gravitational lensing effect. This hypothesis, however, might be flawed as there are physical mechanisms by which galaxies are intrinsically shape correlated: Due to the fact that neighbouring galaxies form from correlated initial conditions, their respective angular momenta are correlated (Croft & Metzler, 2000; Heavens et al., 2000; Crittenden et al., 2001; Mackey et al., 2002). Assuming that the galactic disks are established with their symmetry axes colinear with the host haloes' angular momentum directions one would observe galaxies at correlated angles of inclination and therefore with correlated ellipticities.

A possible consequence of this new source of ellipticity correlation is its interference with the determination of cosmological parameters from weak lensing data, in particular the properties of dark energy. This issue has been the target of a number of investigations: Commonly, the description of intrinsic ellipticity correlations was based on the linear alignment model (Catelan et al., 2001; Hirata & Seljak, 2004),

$$\epsilon_+ = C\left(\partial_x^2 - \partial_y^2\right)\Phi \qquad \text{and} \qquad \epsilon_\times = 2C\,\partial_x\partial_y\Phi. \tag{5.1}$$

which provides a direct modelling of the ellipticity field on the tidal shears $\partial_\alpha\partial_\beta\Phi$ (here, the z-axis of the coordinate system is aligned with the line-of-sight) and is able to give a consistent description of gradient and vorticity modes of the ellipticity field. The constant of proportionality was fixed by comparison with observations (Bridle & King, 2007; Joachimi et al., 2012).

If galaxy ellipticities are in fact described by an alignment model linear in the tidal fields, cosmological parameters, in particular the dark energy equation of state parameters would be severly biased (Bridle & King, 2007; Joachimi & Bridle, 2010; Kirk et al., 2010, 2011). Apart from ellipticity correlations themselves, ellipticity position-correlations were affected and ellipticity data would exhibit cross-correlations between intrinsic ellipticities and weak lensing (see, in particular, Hirata & Seljak, 2004).

There are basically four ways of dealing with intrinsic aligments. Firstly, they

can be removed from data by using the fact that they are a small scale phenomenon (Heymans & Heavens, 2003; King, 2005; King & Schneider, 2002, 2003) which takes place at the cost of increasing statistical uncertainties. Secondly, one can take advantage of the fact that intrinsic alignments have different statistical properties in comparison to weak lensing ellipticity correlations (Crittenden et al., 2002; King & Schneider, 2003), most notably it is possible to use the statistics of vortical excitations in the ellipticity field which are exclusively sourced by intrinsic alignments. Thirdly, one can design line-of-sight weightings that null out contributions due to intrinsic alignments (King, 2005; Joachimi & Schneider, 2009, 2008) which marginally increase statistical uncertainties on cosmological parameters. Parameter inference from spectra that result from data in this way still yields unbiased estimates. Finally, one can parameterise the intrinsic alignment contribution to weak lensing data and have those model parameters be determined by data alongside the cosmological parameters under consideration. Maginalisation over the parameters entering the intrinsic alignment model then propagates the statistical errors of the alignment model on to the cosmological model. With a physically correct alignment model the estimates of cosmological parameters will remain unbiased. The feasibility of this approach under the assumption of Gaussian likelihoods has been demonstrated (Bridle & King, 2007; Bernstein, 2009; Joachimi & Bridle, 2010; Kirk et al., 2010; Laszlo et al., 2012).

The motivation of this work was to explore intrinsic alignment effects and their observable properties in angular momentum-based alignment models. In these models, the ellipticity is quadratic in the tidal shear field and because they use in principle a mechanical model of angular momentum generation and ellipticity alignment, the model parameters can be constrained from information other than ellipticity data. We will need two physically meaningful variables: a parameter which is related to the angular momentum model and whose value can be measured in structure formation simulations and a disk morphology parameter which is accessible in galaxy surveys. Clearly, quadratic alignment models will differ in their prediction of ellipticity correlations compared to linear alignment models. Together with the above results employing linear alignment models we hope to complete the view on intrinsic alignments and their relevance for future weak lensing surveys.

The aim of this paper is threefold: (i) We investigate and compare two angular-momentum based alignment models in their predictions for ellipticity correlations and formulate these predictions in terms of ellipticity correlation functions, ellipticity spectra and the scale-dependence of the variance of the ellipticity fields and compare these predictions with the equivalent quantities sourced by weak gravitational lensing (Sects. 5.3 and 5.4). (ii) The dependence of the two ellipticity models in consideration on cosmological parameters is investigated and their likelihoods are derived. With this knowledge, we quantify the contamination of weak lensing data with an intrinsic alignment contribution and quantify how this contaminations impacts on the estimation of cosmological parameters (Sect. 5.5). (iii) We investigate if there is a possibility of observing intrinsic

correlations in the presence of much stronger lensing-induced ellipticity correlations and develop statistical methods for answering these questions (Sect. 5.6). Throughout we will focus on intrinsic ellipticity correlations caused by correlated angular momenta, which is an applicable model for spiral galaxies. Those intrinsic alignments are proportional to the squared tidal field, in contrast to the linear alignment model valid for elliptical galaxies. In this limit, we neglect cross-correlations between intrinsic ellipticity alignments with the tidal field and gravitational lensing, as those correlations are proportional to the expectation value of the tidal field cubed, which vanishes in the case of Gaussian statistics. Specifically, we consider the case of EUCLID's weak lensing survey (Amendola et al., 2012).

The reference cosmological model used is a spatially flat wCDM cosmology with Gaussian adiabatic initial perturbations in the cold dark matter density field. The parameter choice is motivated by the WMAP7 results (Komatsu et al., 2011; Larson et al., 2011): $\Omega_m = 0.25$, $n_s = 1$, $\sigma_8 = 0.8$, $\Omega_b = 0.04$ and $H_0 = 100\,h\,\mathrm{km/s/Mpc}$, with $h = 0.72$. The dark energy equation of state is set to $w = -0.95$.

5.3 Cosmology

Dark energy cosmologies

In spatially flat Friedmann-Lemaître Robertson-Walker cosmologies with the matter density parameter Ω_m and a dark energy component with equation of state $w(a)$, the Hubble function $H(a) = \mathrm{d}\ln a/\mathrm{d}t$ is given by

$$\frac{H^2(a)}{H_0^2} = \frac{\Omega_m}{a^3} + (1-\Omega_m)\exp\left(3\int_a^1 \mathrm{d}\ln a\,(1+w(a))\right). \tag{5.2}$$

The value $w \equiv -1$ corresponds to the cosmological constant Λ. The Hubble function describes the time evolution of the metric and can be used for relating comoving distance χ and scale factor a:

$$\chi = c\int_a^1 \mathrm{d}a\,\frac{1}{a^2 H(a)}, \tag{5.3}$$

in units of the Hubble distance $\chi_H = c/H_0$. The Hubble function also determines the critical density, $\rho_{\mathrm{crit}} \equiv 3H^2/(8\pi G)$.

5.3.1 CDM power spectrum

The linear CDM density power spectrum $P(k)$ describes the fluctuation amplitude of the Gaussian homogeneous density field δ,

$$\langle\delta(\mathbf{k})\delta(\mathbf{k}')\rangle = (2\pi)^3\delta_D(\mathbf{k}+\mathbf{k}')P(k), \tag{5.4}$$

and is given by the ansatz $P(k) \propto k^{n_s} T^2(k)$ with the transfer function $T(k)$. In cosmologies with low Ω_m, $T(k)$ is fitted by (Bardeen et al., 1986; Sugiyama, 1995):

$$T(q) = \frac{\ln(1+2.34q)}{2.34q}\left(1+3.89q+(16.1q)^2+(5.46q)^3+(6.71q)^4\right)^{-\frac{1}{4}}. \tag{5.5}$$

The wave number k is rescaled with the shape parameter $\Gamma \simeq \Omega_m h$, $q = k/\Gamma$. The spectrum $P(k)$ is normalised to the variance σ_8 of the density field on scales of $R = 8\,\mathrm{Mpc}/h$,

$$\sigma_R^2 = \frac{1}{2\pi^2}\int \mathrm{d}k\, k^2 P(k) W^2(kR) = \int \mathrm{d}\ln k\, \Delta^2(k) W^2(kR). \tag{5.6}$$

$W(x) = 3j_1(x)/x$ is the Fourier-transformed spherical top hat filter function. $j_\ell(x)$ refers to the spherical Bessel function of the first kind of order ℓ (Abramowitz & Stegun, 1972a; Arfken & Weber, 2005) and the dimensionless variance per logarithmic wavenumber $\Delta^2(k) = k^3 P(k)/(2\pi^2)$ can be used instead of the CDM spectrum $P(k)$. In computing ellipticity correlation functions and ellipticity spectra we will employ a smoothed CDM spectrum $P(k) \to P(k)\exp(-(kR)^2)$ with a smooothing scale R that corresponds to a mass cutoff at a halo mass M. Those two quantities are related by $M = 4\pi/3\,\Omega_m \rho_{\mathrm{crit}} R^3$.

5.3.2 Linear structure growth

As long as the amplitudes in the cosmic density field are small, $\delta \ll 1$, the density field grows in a homogenous way, $\delta(\mathbf{x}, a) = D_+(a)\delta(\mathbf{x}, a=1)$. The growth function $D_+(a)$ results from solving the growth equation (Turner & White, 1997; Wang & Steinhardt, 1998; Linder & Jenkins, 2003),

$$\frac{\mathrm{d}^2}{\mathrm{d}a^2}D_+(a) + \frac{1}{a}\left(3+\frac{\mathrm{d}\ln H}{\mathrm{d}\ln a}\right)\frac{\mathrm{d}}{\mathrm{d}a}D_+(a) = \frac{3}{2a^2}\Omega_m(a) D_+(a). \tag{5.7}$$

Nonlinear structure formation enhances the CDM-spectrum $P(k,a)$ on small scales by one and a half order of magnitude, which is described by the fit suggested by Smith et al. (2003).

5.3.3 Angular momenta from tidal shearing

Angular momenta of dark matter haloes embedded in potential flows in the large-scale structure are generated by a mechanism refered to as tidal shearing, where the differential motion of mass elements inside a protohalo gives rise to a torquing moment (Hoyle, 1949; Sciama, 1955; Peebles, 1969; Doroshkevich, 1970; White, 1984):

$$L_\alpha = a^3 H(a)\frac{\mathrm{d}D_+}{\mathrm{d}a}\epsilon_{\alpha\beta\gamma} I_{\beta\delta}\Phi_{\delta\gamma}, \tag{5.8}$$

i.e. it is the variation $\partial_\alpha v_\beta$ of the velocities $v_\beta \sim \partial_\beta\Phi$ across the protohalo and hence the tidal field $\Phi_{\alpha\beta}$

$$\Phi_{\alpha\beta} = \partial_\alpha\partial_\beta\Phi \tag{5.9}$$

which is responsible for angular momentum generation. The mass distribution inside the protohalo itself is described by its inertia tensor $I_{\alpha\beta}$,

$$I_{\alpha\beta} = \Omega_m \rho_{\rm crit}\, a^3 \int_{V_L} \mathrm{d}^3 q\, (\mathbf{q}-\bar{\mathbf{q}})_\alpha (\mathbf{q}-\bar{\mathbf{q}})_\beta \tag{5.10}$$

i.e. the second moments of the matter distribution, with the centre of mass at the position $\bar{\mathbf{q}}$ and the integration comprising the Lagrangian volume of the protohalo. Throughout, we use Einstein's summation convention.

The Levi-Civita-symbol in Eqn. (5.8) generates the interesting misalignment property between the shear and inertia eigensystems which is required for generating angular momentum: Only the antisymmetric contribution $X^-_{\beta\gamma}$, derived from the commutator $X^-_{\beta\gamma} = [I_{\beta\gamma}, \Phi_{\beta\gamma}]$, to the product between the tensors $I_{\beta\gamma}$ and $\Phi_{\beta\gamma}$ is non-vanishing in contraction with the antisymmetric $\epsilon_{\alpha\beta\gamma}$ and therefore relevant for angular momentum generation. The symmetric contribution $X^+_{\beta\gamma}$, which can be isolated using the anticommutator $X^+_{\beta\gamma} = \{I_{\beta\gamma}, \Phi_{\beta\gamma}\}$ cancels in the contraction. This means that for angular momentum build-up, the tidal shear and the inertia tensors are not allowed to have a common eigensystem and be skewed relative to each other (Schäfer, 2009; Schäfer & Merkel, 2012). Likewise, degeneracies in this relation evoked by spatial symmetries in the two tensors can prohibit the generation of angular momentum. Alternative models of galaxy angular momenta assume that the haloes are spun up by non-central, anisotropic infall in filaments (see, for instance, Pichon et al., 2010; Kimm et al., 2011; Codis et al., 2012).

5.3.4 Galaxy ellipticities

Ellipticity correlations between galaxies are traced back to correlated angular momenta of their host haloes. CDM haloes acquire their angular momentum by tidal shearing and due to the fact that neighbouring galaxies experience correlated tidal fields, their angular momenta are correlated in consequence. The direction of the angular momentum $\mathbf{L}$ in turn determines the angle of inclination under which the galactic disk is viewed, and ultimately the ellipticity which is attributed to the galactic disk (Heavens et al., 2000; Crittenden et al., 2001, 2002; Mackey et al., 2002; Heymans & Heavens, 2003): Linking the angular momentum direction $\hat{\mathbf{L}} = \mathbf{L}/L$ to the components of the complex ellipticity ϵ using the above argument yields

$$\epsilon = \epsilon_+ + \mathrm{i}\epsilon_\times \quad \text{with} \quad \epsilon_+ = \alpha \frac{\hat{L}_x^2 - \hat{L}_y^2}{1+\hat{L}_z^2}, \quad \epsilon_\times = 2\alpha \frac{\hat{L}_x \hat{L}_y}{1+\hat{L}_z^2}, \tag{5.11}$$

if the coordinate system is aligned with its z-axis being parallel to the line of sight. A rotation of the coordinate frame by φ causes the complex ellipticity to rotate twice as fast, $\epsilon \to \exp(2\mathrm{i}\varphi)\epsilon$. α is a free parameter weakening the dependence between inclination angle and ellipticity for thick galactic disks and has

been determined to be $\alpha \simeq 0.75$ in the APM sample (Crittenden et al., 2001) with a large uncertainty.

It should be emphasised that the assumption of a galactic disk forming perpendicularly to the host halo angular momentum direction is a very strong one, which seems suggestive but has only little support from structure formation simulations. In fact, a number of studies point at possibly large misalignments and underline the complexity of the baryonic physics on galactic scales (van den Bosch et al., 2002; Navarro et al., 2004; Bailin et al., 2005; Bailin & Steinmetz, 2005; Mayer et al., 2008; Kimm et al., 2011).The disk thickness and the degree of misalignment between the symmetry axis of the galactic disk and the angular momentum axis of the host halo therefore have a decisive role in the description of galaxy formation, and appear to be degenerate physical quantities. In our analysis, misalignments could be incorporated in choosing a smaller value for the disk thickness parameter α, which will play the role of normalising the ellipticity spectra. The angular momentum-based alignment model is only able to capture the physics of tidal alignment of spiral galaxies. In the case of elliptical galaxies, a model which is linear in the tidal shear is more appropriate.

5.3.5 Weak gravitational lensing

The weak lensing convergence κ provides a weighted line-of-sight measurement of the matter density δ (for reviews, see Mellier, 1999; Bartelmann & Schneider, 2001; Huterer, 2002; Hoekstra & Jain, 2008; Bartelmann, 2010b)

$$\kappa = \int_0^{\chi_H} \mathrm{d}\chi \, W_\kappa(\chi)\delta, \tag{5.12}$$

with the weak lensing efficiency $W_\kappa(\chi)$ as the weighting function,

$$W_\kappa(\chi) = \frac{3\Omega_m}{2\chi_H^2}\frac{D_+}{a}G(\chi)\chi, \text{ with } G(\chi) = \int_\chi^{\chi_H} \mathrm{d}\chi' \, n(z)\frac{\mathrm{d}z}{\mathrm{d}\chi'}\frac{\chi'-\chi}{\chi'}. \tag{5.13}$$

$n(z)$ denotes the redshift distribution of the lensed background galaxies (with the parameterisation introduced by Smail et al., 1995),

$$n(z) = n_0\left(\frac{z}{z_0}\right)^2 \exp\left(-\left(\frac{z}{z_0}\right)^\beta\right)\mathrm{d}z \quad \text{with} \quad \frac{1}{n_0} = \frac{z_0}{\beta}\Gamma\left(\frac{3}{\beta}\right). \tag{5.14}$$

z_0 has been chosen to be $\simeq 0.64$ such that the median of the redshift distribution is 0.9, which is anticipated for the EUCLID galaxy sample (Amara & Réfrégier, 2007; Amendola et al., 2012). With these definitions, one can carry out a Limber-projection (Limber, 1954) of the weak lensing convergence for obtaining the angular convergence spectrum $C_\kappa(\ell)$,

$$C_\kappa(\ell) = \int_0^{\chi_H} \frac{\mathrm{d}\chi}{\chi^2} \, W_\kappa^2(\chi)P(k=\ell/\chi), \tag{5.15}$$

which describes the fluctuation statistics of the convergence field. We will always work in the weak lensing regime, $\kappa, \gamma \ll 1$, and approximate the reduced shear $g \equiv \gamma/(1-\kappa)$ with the lensing shear γ, which has the same statistical properties as the weak lensing convergence κ.

5.4 Ellipticity correlations

5.4.1 Angular momentum induced ellipticity correlations

The idea behind intrinsic correlations is that neighbouring galaxies build up their angular momenta with correlated tidal shears because the galaxy separation is typically smaller than the correlation length of the tidal shear field. Under the assumption that the galactic disk orients itself perpendicular to the angular momentum direction of the host halo (for a review on angular momenta of galactic disks, see Romanowsky & Fall, 2012; Bryan et al., 2012), one perceives neighbouring galactic disks under correlated angles of inclination, and therefore the apparent shapes are correlated, which is measured in terms of ellipticities. We use two ellipticity correlation models in this paper, which are both constructed on the idea of correlated angular momenta, but which differ in their particular ansatz. The first model, proposed by Crittenden et al. (2001) establishes the link between the angular momentum direction to the tidal shear field in a random process in real space, whereas the second model, which is due to Mackey et al. (2002), directly formulates the ellipticity field in Fourier space, which makes it easier to quantify ellipticity spectra, but whose parameterisation is not as clear as in the first case.

Ellipticity correlations

Correlations of the two ellipticity components ϵ_+ and $\epsilon_\times$ between two points θ_1 and θ_2 separated by an angular distance θ can be described using two correlation functions $C_{++}(\theta) = \langle\epsilon_+(\theta_1)\epsilon_+(\theta_2)\rangle$ and $C_{\times\times}(\theta) = \langle\epsilon_\times(\theta_1)\epsilon_\times(\theta_2)\rangle$, which are conveniently combined into two correlation functions $C_\pm(\theta)$,

$$C_+(\theta) = C_{++}(\theta) + C_{\times\times}(\theta) \tag{5.16}$$

$$C_-(\theta) = C_{++}(\theta) - C_{\times\times}(\theta) \tag{5.17}$$

using $C_{+\times}(\theta) = \langle\epsilon_+(\theta_1)\epsilon_\times(\theta_2)\rangle = 0$. Finally, ellipticity correlation functions can be transformed to the spectra $C_E^\epsilon(\ell)$ and $C_B^\epsilon(\ell)$ of the gradient and vorticity modes of the ellipticity field,

$$C_E^\epsilon(\ell) = \pi \int \theta \mathrm{d}\theta \, [C_+(\theta) J_0(\ell\theta) + C_-(\theta) J_4(\ell\theta)] \,, \tag{5.18}$$

$$C_B^\epsilon(\ell) = \pi \int \theta \mathrm{d}\theta \, [C_+(\theta) J_0(\ell\theta) - C_-(\theta) J_4(\ell\theta)] \,, \tag{5.19}$$

by Fourier transform (Kaiser, 1992; Schneider et al., 2002; Schneider & Kilbinger, 2007; Fu & Kilbinger, 2010). Gravitational lensing in the lowest approximation is only able to excite E-modes in the ellipticity field.

Configuration space approach

In this work we use the angular momentum-based ellipticity correlation model proposed by Crittenden et al. (2001) (referred to as the CNPT-model), who trace ellipticity correlations back to tidal shear correlations using the conditional probability distribution $p(\mathbf{L}|\Phi_{\alpha\beta})\mathrm{d}\mathbf{L}$ introduced by Lee & Pen (2001): In this model, the distribution $p(\mathbf{L}|\Phi_{\alpha\beta})\mathrm{d}\mathbf{L}$ is assumed as being Gaussian which is then being marginalised over the magnitude of the angular momentum vector, retaining only its directional dependence. Writing down the ellipticity components as a function of the angular momentum direction and employing the covariance $\langle L_\alpha L_\beta\rangle$ as a function of the squared tidal shear tensor, as advocated by Lee and Pen, it is possible to relate the tidal shear correlations to the spectrum of the density field.

Angular momenta $\mathbf{L}$ are described as being coupled to the tidal shear by means of a Gaussian random process $p(\mathbf{L}|\Phi_{\alpha\beta})\mathrm{d}\mathbf{L}$ involving tidal fields $\Phi_{\alpha\beta}$ shaping the covariance $\mathrm{cov}(L)_{\alpha\beta}$ of the Gaussian distribution (Lee & Pen, 2001),

$$\mathrm{cov}(L)_{\alpha\beta} = \langle L_\alpha L_\beta\rangle = \frac{\langle \mathbf{L}^2\rangle}{3}\left(\frac{1+a}{3}\delta_{\alpha\beta} - a\,(\hat{\Phi}^2)_{\alpha\beta}\right), \tag{5.20}$$

with the misalignment parameter a, which describes the average orientation of the protohalo's inertia to the tidal shear eigensystem. a has been measured in numerical simulation to be close to 0.25 which we will assume in this work. $\hat{\Phi}$ is the unit normalised traceless tidal shear with the properties $\mathrm{tr}(\hat{\Phi}) = 0$ and $\mathrm{tr}(\hat{\Phi}^2) = 1$. This description is valid on scales where the correlations between inertia tensors are negligible.

The conditional probability density can be used for establishing a direct relation between ellipticity ϵ and tidal shear $\hat{\Phi}_{\alpha\beta}$ by integrating out angular momentum direction and magnitude:

$$\epsilon(\hat{\Phi}_{\alpha\beta}) = \int \mathrm{d}\hat{\mathbf{L}}\,\epsilon(\hat{\mathbf{L}}) \int L^2 \mathrm{d}L\, p(\mathbf{L}|\Phi_{\alpha\beta}) \tag{5.21}$$

With this relation, one can write down the two correlation functions $\langle\epsilon_+(\mathbf{x}_1)\epsilon_+(\mathbf{x}_2)\rangle$ and $\langle\epsilon_\times(\mathbf{x}_1)\epsilon_\times(\mathbf{x}_2)\rangle$ of the three-dimensional ellipticity field in terms of moments $\zeta_n(r)$ (see Crittenden et al., 2001) of the tidal shear field. Those moments, in turn, are expressed as weighted integrals over the CDM-spectrum, where we impose a Gaussian smoothing on a scale of $10^{11}\,M_\odot/h$, which is typical for galaxies.

The correlation function of the 3-dimensional ellipticity field can then be projected onto the angular correlation function of the ellipticity components by

using the configuration-space Limber-equation (Limber, 1954):

$$C_{++}(\theta) = \int \mathrm{d}\chi_1 W_\epsilon(\chi_1) \int \mathrm{d}\chi_2 W_\epsilon(\chi_2) \langle \epsilon_+(\mathbf{x}_1)\epsilon_+(\mathbf{x}_2)\rangle \tag{5.22}$$

$$C_{\times\times}(\theta) = \int \mathrm{d}\chi_1 W_\epsilon(\chi_1) \int \mathrm{d}\chi_2 W_\epsilon(\chi_2) \langle \epsilon_\times(\mathbf{x}_1)\epsilon_\times(\mathbf{x}_2)\rangle \tag{5.23}$$

with the distance distribution $W_\epsilon(\chi) = n(z(\chi))\mathrm{d}z/\mathrm{d}\chi$ resulting for a given cosmology from the observed redshift distribution $n(z)\mathrm{d}z$ of background galaxies (see Eqn. 5.14). The separation distance entering the three dimensional correlation functions is completely determined by the two line-of-sight distances χ_1, χ_2 and the angle of separation θ. Giahi-Saravani & Schäfer (2012) have shown that distorsions of the intrinsic ellipticity pattern due to the peculiar motion of galaxies is very small for multipoles up to $\ell = 1000$.

Fourier-approach

We extend our analysis by the approach of Mackey et al. (2002) (abbreviated as MWK). Similar to Crittenden et al. (2001) they also work in the framework of tidal torque theory and relate intrinsic ellipticity to angular momentum assuming that the disk of a galaxy forms perpendicular to its spin axis. However, when computing the angular momentum the MWK-model entirely neglects any correlation between the tidal field and the tensor of inertia. They argue that due to the different correlation lengths involved (while the correlations for the inertia tensor primarily arise from smaller scales the correlations in the tidal field are long-ranged) a successive averaging-process is permissible. First, they perform an average over inertia tensors then over the tidal field expecting the ellipticity correlation arising from long-range correlations of the latter. In contrast to this, the CNPT-model takes explicitly the correlations of the inertia tensor and the tidal field via the misalignment parameter a into account.

One more simplification made by MWK is to drop the dependence of the observed ellipticity on the z-component of the angular momentum of the galaxy, i.e.

$$\epsilon_+ = C\left(L_x^2 - L_y^2\right) \qquad \text{and} \qquad \epsilon_\times = 2C\,L_x L_y. \tag{5.24}$$

with a constant C. Accordingly, the intrinsic ellipticity scales quadratically with the modulus of the angular momentum, leaving faster spinning galaxies more flattened. Note that by the basic structure of this relation the symmetry properties of the ellipticity field are the same ones as in Eqn. (5.1).

Assuming shear and inertia being statistically independent allows to work completely in harmonic space, which greatly facilitates the computation. Since we aim at the power spectra of the intrinsic ellipticity it is convenient to introduce the parity conserving (E-mode) and parity violating (B-mode) part of the

intrinsic ellipticity field

$$\begin{aligned} E(\mathbf{k})\,k^2 &= \left(k_x^2 - k_y^2\right)\epsilon_+(\mathbf{k}) + 2k_x k_y \epsilon_\times(\mathbf{k}) \\ B(\mathbf{k})\,k^2 &= -2k_x k_y \epsilon_+(\mathbf{k}) + \left(k_x^2 - k_y^2\right)\epsilon_\times(\mathbf{k}). \end{aligned} \tag{5.25}$$

Focusing on modes perpendicular to the line of sight one can derive the following dimensionless ellipticity power spectra for the E- and B-mode, respectively

$$\begin{aligned} \Delta_X^2(k) &= \frac{C}{225}\left(\frac{3}{2}\Omega_m H_0^2\right)^4 \int_0^\infty \frac{\mathrm{d}\alpha}{\alpha}\Delta^2(\alpha k) \\ &\quad \times \int_{-1}^{1} \mathrm{d}\mu \frac{\Delta^2(k\sqrt{1+\alpha^2-2\alpha\mu})}{(1+\alpha^2-2\alpha\mu)^{7/2}} g_X(\alpha,\mu). \end{aligned} \tag{5.26}$$

Here $X \in \{E, B\}$ and g_X is a polynomial given in Eqn. (17) of Mackey et al. (2002) together with a detailed derivation of the expressions given above. As before, we smooth the linear power spectrum on an appropriate length scale with a Gaussian filter function.

Finally, in order to get the corresponding angular power spectra we have to again make use of the Fourier-space variant of Limber's projection (Limber, 1954)

$$\frac{\ell(2\ell+1)}{4\pi} C_X^\epsilon(\ell) = \frac{\pi}{\ell}\int_0^\infty \chi\,\mathrm{d}\chi\, W_\epsilon^2(\chi)\Delta_X^2(\ell/\chi) \tag{5.27}$$

with the weighting function $W_\epsilon(\chi)\mathrm{d}\chi = n(z)\mathrm{d}z$ already introduced in Eqn. (5.14).

Mackey et al. (2002) determine the constant C by computing the expectation value of the squared angular momentum modulus and adjusting C to match the mean-square source ellipticity typically observed in galaxy surveys. For our purpose, however, it makes more sense to choose C in such a way that the angular power spectra obtained with the two different approaches coincide on largest scales. This is justified by the expectation that the large-scale power will be least effected by the differences in the two approaches under consideration. Hence, we first compute the spectra using formulae (5.18) and (5.19) for appropriately chosen misalignment parameter a and galaxy thickness parameter α and subsequently determine C, so that the two models yield identical predictions for the variance of the intrinsic ellipticity field on large scales.

Comparison of the two ellipticity-models

The ellipticity correlation functions $C_{++}(\theta)$ and $C_{\times\times}(\theta)$ resulting from both models are plotted in Fig. 8.2 as a function of angle of separation θ, where the projection was carried out for the EUCLID galaxy redshift distribution. The plot suggests correlation lengths of ~ 10 arcminutes for the ellipticity field and shows that under the normalisations chosen, the correlation functions resulting from the CNPT-model achieves 50% higher amplitudes in comparison to those predicted by the MWK-model, but otherwise the general shape is in very good agreement.

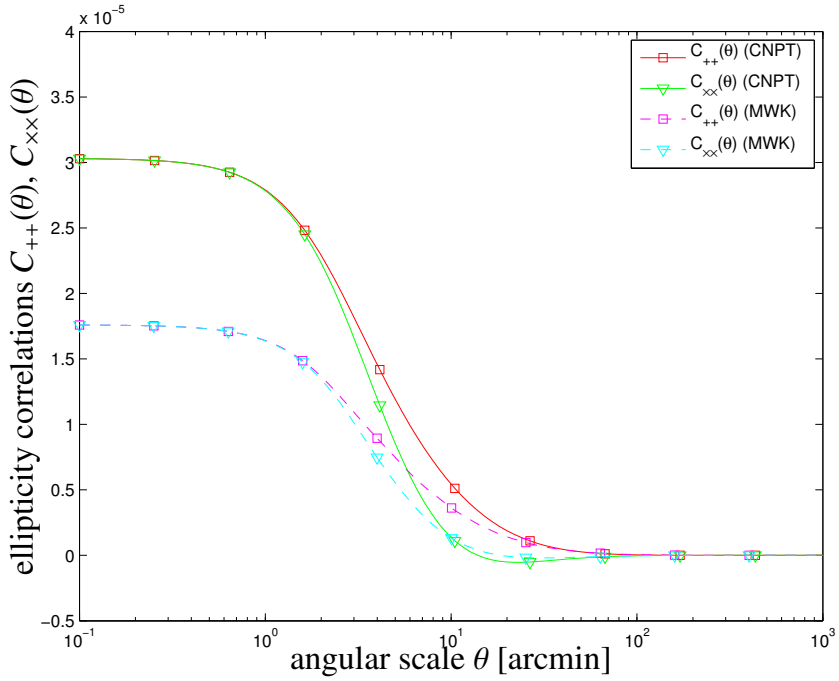

Figure 5.1: Angular ellipticity correlation functions $C_{++}(\theta)$ (green and magenta lines) and $C_{\times\times}(\theta)$ (red and cyan lines), for a smoothing scale of $M = 10^{11} M_{\odot}/h$, a misalignment parameter $a = 0.25$ and a disk thickness of $\alpha = 0.75$. The correlation functions were derived using the CNPT- and MWK-models with the relative normalisation as discussed in the text.

Computing the spectra $C_E^\epsilon(\ell)$ and $C_B^\epsilon(\ell)$ yields Fig. 10, where for comparison the linear and nonlinear spectra $C_\kappa(\ell)$ for the weak lensing convergence and the EUCLID shape noise levels σ_ϵ^2/n are plotted. The shape of the ellipticity spectra shows constant amplitudes up to scales of $\ell \sim 300$, where individual ellipticities are uncorrelated, and correlations between ellipticities are present on smaller angular scales. The spectra exhibit a wide maximum on multipoles of $\ell \sim 10^3$ before dropping in amplitude, which is caused by imposing the mass cutoff. For comparison and motivating our analysis we plot predictions for the weak lensing spectrum $C_\kappa(\ell)$ for linear and nonlinear CDM spectra, as well as the anticipated shot-noise for EUCLID. Clearly, intrinsic ellipticity correlations are subdominant compared to weak lensing induced ellipticity correlations, but can in amplitude amount to up to 30% of the lensing signal on multipoles of $\ell \simeq 10^3$ before the shape noise makes measurements difficult. Comparing the two ellipticity models show that, if the normalisation is chosen as explained, the MWK-model predicts lower spectra than the model by CNPT by about 50% on high multipoles as in the case of the correlation function at small separations, but both models predict similar ratios between $C_E^\epsilon(\ell)$ and $C_B^\epsilon(\ell)$ amounting to about a factor of 5 at high multipoles. Interestingly, intrinsic ellipticity correlations would dominate over the weak lensing signal if the lensing prediction was derived using linear structure growth only. Comparing the spectra $C_E^\epsilon(\ell)$ and $C_\kappa(\ell)$ with the shape noise levels of EUCLID clearly demonstrate the importance of intrinsic ellipticity correlations in weak lensing data.

The B-mode spectrum $C_B^\epsilon(\ell)$, which is sourced by intrinsic alignments, is smaller by more than one order of magnitude compared to the E-mode spectrum $C_E^\epsilon(\ell)$ at high multipoles but might dominate over other higher-order lensing effects which are able to excite parity-violating modes in the ellipticity field such as source-lens clustering (Schneider et al., 2002), multiple lensing along the line-of-sight or violations of the Born-approximation (Cooray & Hu, 2002; Shapiro & Cooray, 2006; Schäfer et al., 2012).

5.4.2 Variance in apertures

Quantities derived from the weak lensing spectrum $C_\kappa(\ell)$ are weighted variances of the convergence inside apertures of varying size θ, introduced by Schneider (1996):

$$\langle \kappa^2 \rangle(\theta) = \frac{2}{\pi} \int \ell \mathrm{d}\ell \, W_1^2(\ell\theta) \, C_\kappa(\ell), \tag{5.28}$$

and

$$\langle M_\kappa^2 \rangle(\theta) = \frac{2}{\pi} \int \ell \mathrm{d}\ell \, W_4^2(\ell\theta) \, C_\kappa(\ell), \tag{5.29}$$

which measure the scale-dependence of fluctuations' variance in the respective field. The weighting functions $W_0(x)$, and $W_4(x)$, $x = \ell\theta$, are defined as:

$$W_1(x) = \frac{J_1(x)}{x} \quad \text{and} \quad W_4(x) = \frac{12 J_4(x)}{x^2}, \tag{5.30}$$

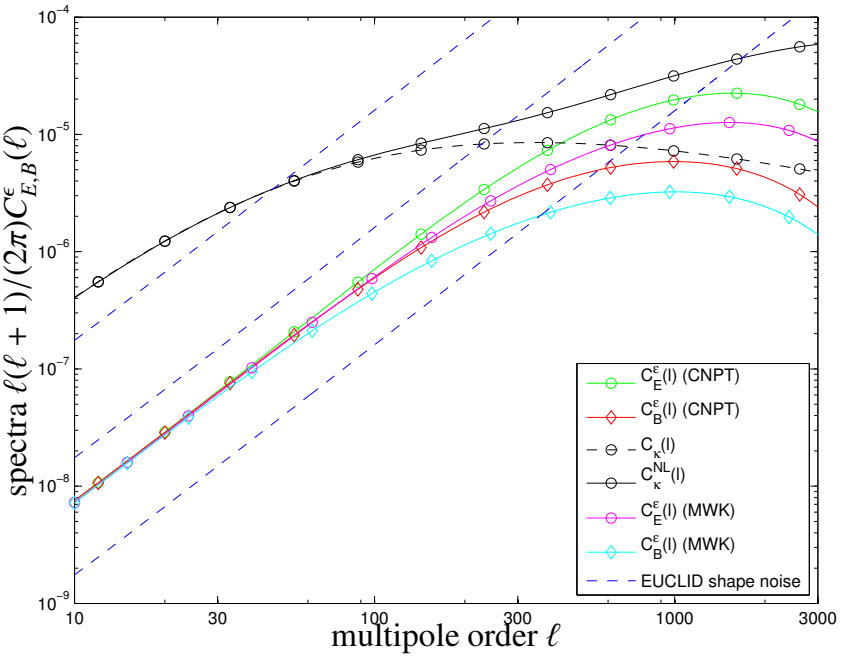

Figure 5.2: Ellipticity spectra $C^{\epsilon}_{E}(\ell)$ (green and magenta lines) and $C^{\epsilon}_{B}(\ell)$ (red and cyan lines) derived with the CNPT- and MWK-models, with weak convergence power spectrum $C_{\kappa}(l)$, both linear and nonlinear (black dashed and solid lines, respectively), and the EUCLID shape noise $\sigma^2_{\epsilon}/\bar{n}$, with $10^n \times \sigma^2_{\epsilon}/\bar{n}$, $n = 0, 1, 2$ (blue dashed lines).

respectively, for the shear variance averaged in an aperture of size θ and the aperture mass variance. The weak lensing power spectrum is substituted in the previous definitions with $C_E^\epsilon(\ell)$, and $C_B^\epsilon(\ell)$ in order to obtain:

$$\langle\epsilon_+^2\rangle(\theta) = \frac{2}{\pi}\int \ell \mathrm{d}\ell\, W_1^2(\ell\theta) C_E^\epsilon(\ell), \tag{5.31}$$

$$\langle M_{\rm ap}^2\rangle(\theta) = \frac{2}{\pi}\int \ell \mathrm{d}\ell\, W_4^2(\ell\theta) C_E^\epsilon(\ell), \tag{5.32}$$

$$\langle\epsilon_\times^2\rangle(\theta) = \frac{2}{\pi}\int \ell \mathrm{d}\ell\, W_1^2(\ell\theta) C_B^\epsilon(\ell), \tag{5.33}$$

$$\langle M_\perp^2\rangle(\theta) = \frac{2}{\pi}\int \ell \mathrm{d}\ell\, W_4^2(\ell\theta) C_B^\epsilon(\ell), \tag{5.34}$$

which are analogous quanitites if the origin of ellipticity correlations would be purely intrinsic and generated by correlated angular momenta.

In Fig. 5.3 we show, how the aperture-weighted variances of the intrinsic ellipticity field should behave in the EUCLID galaxy sample as a function of angular scale in comparison to that of the weak lensing field. We consider both tangential and radial shears and compare the results between the two different intrinsic ellipiticity models.

The aperture-weighted variances derived from intrinsic ellipticities decrease in magnitude which of course is a generally expected behaviour caused by the weighting functions $W_n(\ell\theta)$, and exhibit lower amplitudes compared to the lensing ones, as can be expected from the relative magnitudes of the spectra. From angular scales of 100 arcminutes on intrinsic alignments have dropped to zero, which is compatible with them being a small-scale phenomenon, while weak lensing still has a considerable signal. As expected, the differnece in magnitude of the variances sourced by E-modes and B-modes is smaller than the difference in spectra on small scales because of the averaging in multipole ℓ, and an analogous argument applies to the predictions by the two models under consideration.

5.5 Parameter likelihood

In this section, the dependence of the intrinsic ellipticity spectrum on the cosmological parameter set is investigated. This is of particular relevance because of their contaminating effect in weak lensing data by introducing spurious ellipticity correlations, and because they depend on the cosmological model in a very nonlinear way, much stronger than e.g. the weak lensing convergence: We point out that in our models, the angular momentum $\mathbf{L}$ reflects the squared tidal shears $\partial_i\partial_j\Phi$, and the ellipticity field ϵ in turn has a very complex dependence on the angular momentum direction, which can be approximated to be quadratic for small line of sight-components of the angular momentum direction. In the following, we keep the parameter α in our ellipticity model constant,

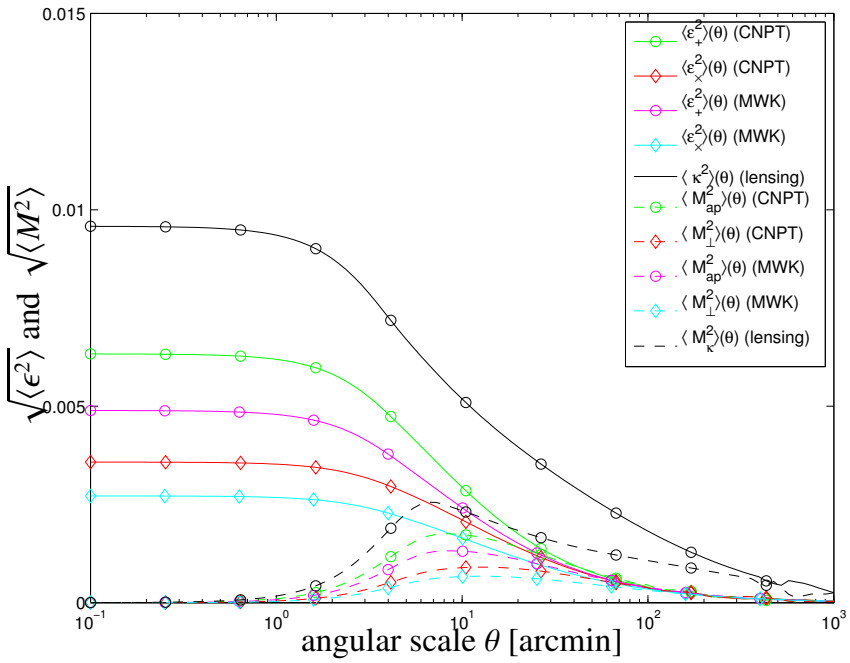

Figure 5.3: Standard deviation of the averaged ellipticity and aperture mass as a function of aperture size θ for the CNPT- and MWK-models: tangential ellipticity $\langle\epsilon_+^2\rangle$ (solid green and magenta lines), radial ellipticity $\langle\epsilon_\times^2\rangle$ (solid red and cyan lines), aperture mass $\langle M_{\rm ap}^2\rangle$ (dashed green and magenta lines) along with $\langle M_\perp^2\rangle$ (dashed red and cyan lines), all for the EUCLID galaxy sample in comparison to the same quantities derived from the weak lensing convergence (corresponding black lines).

because it can in principle be determined by analysing morphological data, as Crittenden et al. (2001) demonstrated. The misalignment parameter a replaces σ_8 because it fixes the normalisation of the spectra, and is completely degenerate with α.

5.5.1 Parameter dependences of intrinsic alignments

When considering the angular spectra describing the ellipticity field, the parameter sensitivity of intrinsic alignments can be nicely illustrated by considering derivatives of the spectra with respect to cosmological parameters, weighted by the inverse noise. For illustration, we assume that weak lensing-induced ellipticity alignments were absent from the data, and that the ellipticity shape noise would be that of EUCLID. Therefore the sensitivities, i.e. the derivative of the observables with respect to the parameters to be estimated in units of the noise,

$$\frac{1}{\sqrt{\mathrm{cov}_X(\ell)}}\frac{\partial C_X^\epsilon}{\partial x_\mu}, \quad X\in\{E,B\}\,, \tag{5.35}$$

correspond to the contributions $\sqrt{\mathrm{d}F_{\mu\mu}/\mathrm{d}\ell}$ to the diagonal entries of a Fisher-matrix $F_{\mu\nu}$, which describes the parameter dependence of the spectra $C_E^\epsilon(\ell)$ and $C_B^\epsilon(\ell)$ on a cosmological model. It is worth to mention that derivatives respect to the parameter or respect to the logarithm of the parameter are substantially equal in our case, given the fact that the parameters themselves are of the order of unity. The covariances of acquire a cosmic variance error and a Poissonian shape measurement error,

$$\mathrm{cov}_X(\ell)=\frac{2}{2\ell+1}\frac{1}{f_\mathrm{sky}}\left(C_X^\epsilon(\ell)+\frac{\sigma_\epsilon^2}{n}\right)^2 \tag{5.36}$$

with $\sigma_\epsilon=0.3$, $n=30/\mathrm{arcmin}^2$ as the number density of galaxies per square steradian and the sky fraction $f_\mathrm{sky}=1/2$.

We depict these quantities in Fig. 5.4 for the basic set of cosmological parameters considered here: $x_\mu\in\{\Omega_m,a,h,w\}$, where n_s has been omitted due to its very weak influence on the spectra. Clearly, the E-mode and B-mode spectra exhibit an identical behaviour on large, cosmic variance dominated scales, where they reflect identical dependence on the physical processes of angular momentum generation and disk orientation, before differening on multipoles $\ell\gtrsim 300$, where weaker B-modes start being influenced by the noise level. The effectively non-existent dependence of the ellipticity spectra on the dark energy equation of state parameter w is particularly interesting and suggests that intrinsic alignments contaminations in weak lensing can be investigated almost independently from the dark energy model assumed. Conversely, the dependences on Ω_m and a are particularly strong, because a determines the amplitude of the spectra in much the same way as σ_8 fixes the normalisation of the weak lensing spectra.

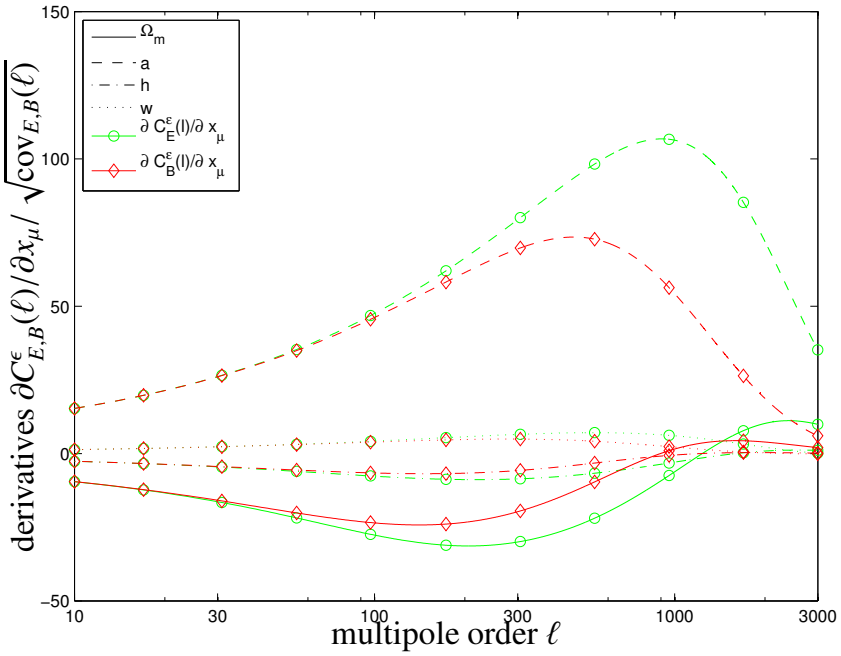

Figure 5.4: Sensitivities $\partial C_E^\epsilon(\ell)/\partial x_\mu$ (green lines) and $\partial C_B^\epsilon(\ell)/\partial x_\mu$ (red lines) in units of $\sqrt{\mathrm{cov}_X(\ell)}$ as a function of maximum multipole order ℓ, with respect to the cosmological parameters Ω_m (dashed lines), a (solid lines), h (dash-dotted lines) and w (dotted lines). The spectra were computed with the CNPT-model.

5.5.2 Non-Gaussian likelihoods

This section is intended to check whether our assumption of Gaussianity for the parameters likelihood is well-grounded. In order to achieve this we compare the Gaussian likelihoods derived by using the Fisher-formalism,

$$\mathscr{L} \propto \exp\left(-\frac{(x_\mu - x_\mu^{\rm fid})^2}{2\sigma_\mu^2}\right) \quad \text{with} \quad \sigma_\mu^2 = \frac{1}{F_{\mu\mu}} \tag{5.37}$$

where the Fisher-matrix is determined from the curvature of the logarithmic likelihood,

$$F_{\mu\nu} = \sum_{\ell=\ell_{\rm min}}^{\ell_{\rm max}} \frac{\partial C_E^\epsilon(\ell)}{\partial x_\mu} \frac{1}{{\rm cov}_E(\ell)} \frac{\partial C_E^\epsilon(\ell)}{\partial x_\nu} \tag{5.38}$$

with a direct evaluation of the respective likelihood function, derived using the relation:

$$\mathscr{L} \propto \exp\left(-\chi^2(x_\mu)/2\right) \tag{5.39}$$

where the χ^2-functional is given by

$$\chi^2(x_\mu) = \sum_{\ell=\ell_{\rm min}}^{\ell_{\rm max}} \frac{1}{{\rm cov}_E(\ell)} \left[C_E^\epsilon(\ell|x_\mu) - C_E^\epsilon(\ell|x_\mu^{\rm fid})\right]^2, \tag{5.40}$$

and quantifies the goodness-of-fit of a parameter choice x_μ in the space spanned by the set of cosmological parameters $\{\Omega_m, a, h, w, n_s\}$. It is important to specify that due to the weakness of the intrinsic ellipticity correlations we consider only conditional errors, i.e. we let one parameter vary at a time, keeping the remaining fixed and focus only on the stronger E-mode spectrum $C_E^\epsilon(\ell)$. The reduced dimensionality allows us to compute the likelihood directly on a grid without having to make use of Monte-Carlo sampling techniques for evaluating the likelihood.

Any deviation from a Gaussian shape of the likelihood $\mathscr{L}$ is caused by a nonlinear dependence of the spectrum $C_E^\epsilon(\ell)$ on a model parameter x_μ, which is due to the fact that the χ^2-functional deviates from a parabolic shape if the model parameter is varied. The likelihood assumes an approximately Gaussian shape if it is sufficiently peaked such that a Taylor-expansion of the nonlinear parameter dependences is applicable in the region around the fiducial parameter choice. In our case, non-Gaussian shapes have been observed if the summation in Eqn. (5.40) was restricted to the multipole range $10 \leq \ell \leq 100$ and quickly became Gaussian if the summation was carried out to higher multipoles.

The non-Gaussian likelihoods $\mathscr{L}(\Omega_m)$ and $\mathscr{L}(w)$ for the matter density and the dark energy equation of state can be seen in Fig. 5.5 in comparison to their Gaussian approximation. All likelihoods are centered on the fiducial model value $x_\mu^{\rm fid}$ and scaled with the width σ_μ derived with the Fisher formalism. This new normalized variable allows the curves to range in the same interval and to be comparable. Likelihoods have also been normalized to unity. Most notably, the

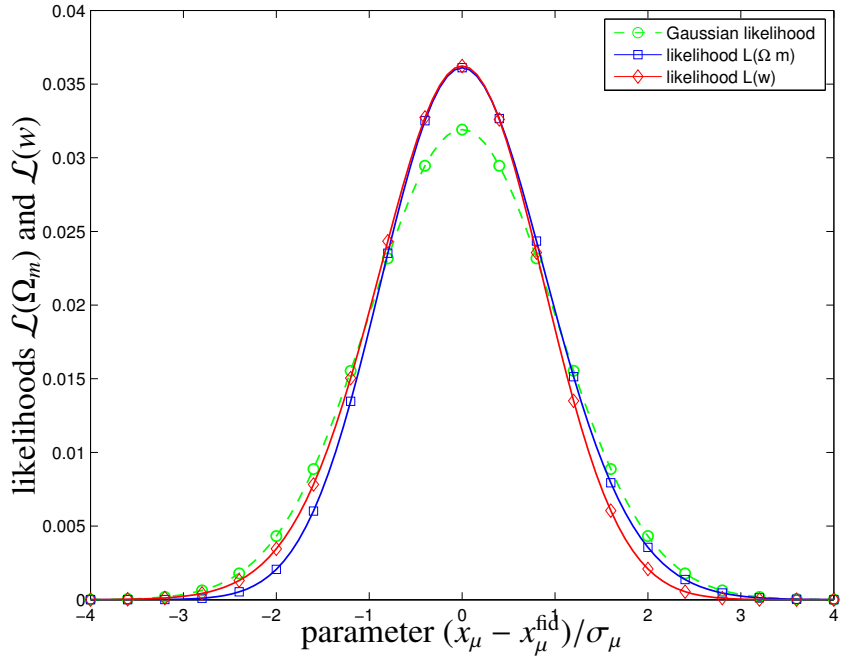

Figure 5.5: Conditional likelihoods $\mathscr{L}(\Omega_m)$ (solid blue line) and $\mathscr{L}(w)$ (solid red line), along with their Gaussian approximations derived with the Fisher-formalism ($\sigma_\mu = 1/\sqrt{F_{\mu\mu}}$, dashed green line), for an observation of ellipticity spectrum $C_E^\epsilon(\ell)$ with the EUCLID survey characteristics with all other parameters fixed to their fiducial values. The multipole range was set to $10 \leq \ell \leq 100$ and the spectrum $C_E^\epsilon(\ell)$ entering the likelihood-calculation resulted from the CNPT-model.

likelihoods are more strongly peaked than their Gaussian counterparts, with slight asymmetries of $\mathscr{L}(\Omega_m)$ towards large values and of $\mathscr{L}(w)$ towards small parameter values. It should be noted, that the misalignment parameter a (together with the disk thickness α) is a linear parameter in our models and its likelihood $\mathscr{L}(a)$ is always of Gaussian shape. We conclude that the amount of deviation from the ideal shape is not a serious impediment for applying the Fisher-formalism for investigating intrinsic alignments, keeping in mind that in reality one observes alignments over a much wider multipole range such that the likelihoods are closer to Gaussianity.

5.6 Interference with weak lensing

In this section we show how the intrinsic alignments can affect measurements of the convergence spectrum by quantifying the parameter biases arising when

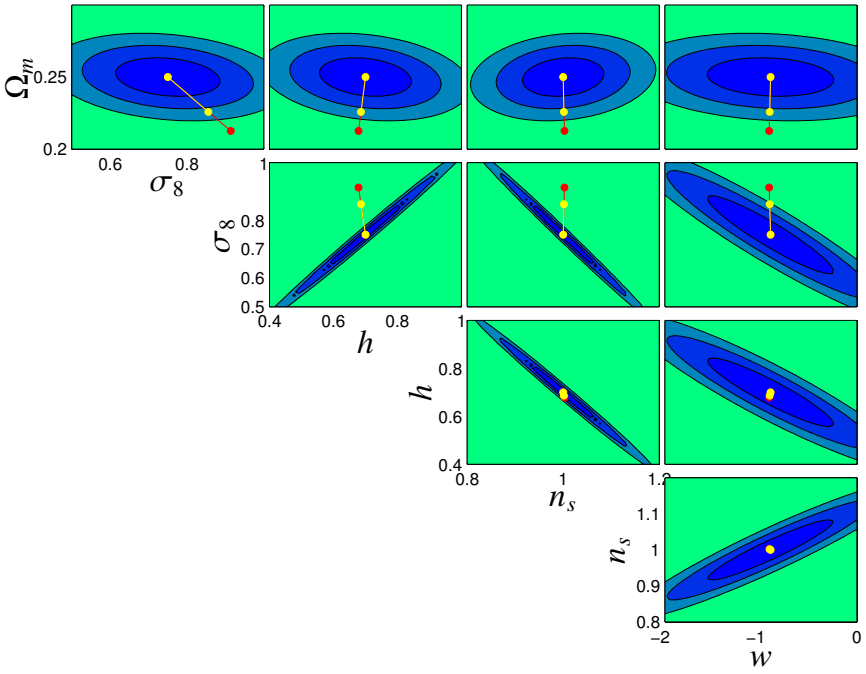

Figure 5.6: Parameter estimation biases in Ω_m, σ_8, h, n_s and w obtained respectively with the CNPT-model (in red) and with the MWK-model (in yellow) for EUCLID's observation of the weak lensing spectrum $C_\kappa(\ell)$, which is contaminated by intrinsic alignments $C_E^\epsilon(\ell)$ on small scales. The misalignment parameter is set to $a = 0.25$; the disk thickness parameter is set to $\alpha = 0.75$, the multipole range was $10 \leq \ell \leq 3000$ and as a noise amplitude we considered $\sigma_\epsilon = 0.3$. The ellipses give $1, 2, 3\sigma$ statistical uncertainties on the cosmological parameters from the weak lensing spectrum $C_\kappa(\ell)$ from the same multipole range.

trying to explain the data consisting of both weak lensing-induced ellipticity correlations and intrinsic alignments by a model that only accounts for weak lensing and neglects intrinsic alignments. We consider the case of EUCLID's weak lensing survey in a non-tomographic setup and give an estimation of the biases, if intrinfsic alignments are not removed from data (as proposed by King, 2005; Joachimi & Schneider, 2009, 2008) or not properly modelled (King & Schneider, 2003, 2002). We aim to supplement previous analysis of intrinsic alignment contaminations such as Hirata & Seljak (2004), Bridle & King (2007) and Kitching et al. (2008) by using a physically motivated and well described alignment model for spiral galaxies with a small number of parameters which can be accessed by morphological galaxy samples (the disk thickness parameter α) and cosmological simulations (the misalignment parameter a).

5.6.1 Parameter constraints

Statistical errors on constraints on the cosmological parameters from the projected weak lensing power spectrum $C_\kappa(l)$ when ignoring the intrinsic ellipticity spectrum can be easily obtained by using the Fisher matrix formalism, where the Fisher-matrix $F_{\mu\nu}$ measures the curvature of the logarithmic likelihood $\ln \mathscr{L}$ in all parameter directions (Tegmark et al., 1997):

$$F_{\mu\nu} = \sum_{\ell=\ell_{\min}}^{\ell_{\max}} \frac{\partial C_\kappa(\ell)}{\partial x_\mu} \frac{1}{\mathrm{cov}_\kappa(\ell)} \frac{\partial C_\kappa(\ell)}{\partial x_\nu} \tag{5.41}$$

where the covariance is given by:

$$\mathrm{cov}_\kappa(\ell) = \frac{2}{2\ell+1} \frac{1}{f_{\mathrm{sky}}} \left(C_\kappa(\ell) + \frac{\sigma_\epsilon^2}{n} \right)^2 . \tag{5.42}$$

In the latter expression EUCLID's noise σ_ϵ^2/n was used as well as $f_{\mathrm{sky}} = 1/2$ for the sky fraction, and the parameter space is spanned by the cosmological parameters $x_\mu \in \{\Omega_m, \sigma_8, h, n_s, w\}$. We will use the covariance $\mathrm{cov}_\kappa(\ell)$ throughout this chapter and neglect small contributions due to intrinsic alignments to the covariance of the ellipticity field, as the covariance and therefore the sampling noise is dominated by weak lensing.

The statistical $n\sigma$-ellipses obtained as cross-sections through the Gaussian-approximated likelihood for all pairs of parameters are shown in Fig. 5.6 together with the systematical errors in parameter estimation if intrinsic alignments are not taken care of. The extend to which weak lensing parameter likelihoods are Gaussian is investigated in detail by Wolz et al. (2012).

5.6.2 Parameter estimation biases

Ultimately our analysis aims to quantify how biased the parameter estimation with EUCLID-data will be if intrinsic alignments as predicted from angular momentum models were present in the data but if we were to interpret the data

with a model which does not take intrinsic ellipticities into account. We therefore identify a true model which includes intrinsic alignments

$$C_t(\ell) = C_\kappa(\ell) + C_E^\epsilon(\ell) + \frac{\sigma_\epsilon^2}{n} \tag{5.43}$$

and a false model, which omits intrinsic alignments and considers the ellipticities as random,

$$C_f(\ell) = C_\kappa(\ell) + \frac{\sigma_\epsilon^2}{n}. \tag{5.44}$$

For both models, one can specify a goodness-of-fit parameter which in the case of Gaussian errors is the χ^2-functional. If the data, which follows the model $C_t(\ell)$, is interpreted with the wrong model $C_f(\ell)$, the corresponding χ^2-functional will exhibit its minimum at a position in parameter space shifted from the true parameter choice, because the incomplete model is forced to provide a fit to the data by detuning the parameter set away from the fiducial values. The way to achieve this goal was proposed by a number of authors (Cabré et al., 2007; Amara & Réfrégier, 2008; Taburet et al., 2009; March et al., 2011; Schäfer & Heisenberg, 2012) in different contexts: Taking the second-order Taylor expansion of the wrong χ_f^2-functional around the best-fit point x_t of the true model one retrieves an expression involving the vector δ:

$$\chi_f^2(\mathbf{x}_f) = \chi_f^2(\mathbf{x}_t) + \sum_\mu \frac{\partial}{\partial x_\mu}\chi_f^2(\mathbf{x}_t)\delta_\mu + \frac{1}{2}\sum_{\mu,\nu}\frac{\partial^2}{\partial x_\mu \partial x_\nu}\chi_f^2(\mathbf{x}_t)\delta_\mu\delta_\nu, \tag{5.45}$$

being $\delta \equiv \mathbf{x}_f - \mathbf{x}_t$. For weak systematics, this approach has been demonstrated to yield very accurate results for the estimation biases by comparison with the shift of the likelihood peak evaluated by MCMC-techniques (Taburet et al., 2010).

Now, by extremising the ensamble-averaged $\langle\chi_f^2(\mathbf{x}_f)\rangle$ one gets the best-fit position $\mathbf{x}_f$. This operation yields a linear system of equations:

$$\sum_\nu G_{\mu\nu}\delta_\nu = a_\mu \quad \rightarrow \quad \delta_\mu = \sum_\nu (G^{-1})_{\mu\nu}a_\nu \tag{5.46}$$

and can be inverted directly leading to the estimation bias δ. Substitution gives expressions for the quantities $G_{\mu\nu}$ and a_μ which involve derivatives of the spectra,

$$\begin{aligned} G_{\mu\nu} &\equiv \sum_{\ell=\ell_{\min}}^{\ell_{\max}} \frac{1}{\mathrm{cov}_\kappa}\left[\frac{\partial C_\kappa(\ell)}{\partial x_\mu}\frac{\partial C_\kappa(\ell)}{\partial x_\nu} - C_E^\epsilon(\ell)\frac{\partial^2 C_\kappa(\ell)}{\partial x_\mu \partial x_\nu}\right], \\ a_\mu &\equiv \sum_{\ell=\ell_{\min}}^{\ell_{\max}} \frac{1}{\mathrm{cov}_\kappa}\left[C_E^\epsilon(\ell)\frac{\partial C_\kappa(\ell)}{\partial x_\mu}\right]. \end{aligned} \tag{5.47}$$

It is worth to notice that the espression for $G_{\mu\nu}$ simplifies to $F_{\mu\nu}$ when the correct model is used, and the bias vector is therefore zero. A consequence of this argument is that the inclusion of a Gaussian prior $F_{\mu\nu}^{\mathrm{prior}}$ would reduce the parameter

estimation bias due to the transformation $G_{\mu\nu} \to G_{\mu\nu} + F_{\mu\nu}^{\text{prior}}$, leading to smaller values for δ_μ in the inversion of the linear system Eqn. (5.46).

Fig. 5.6 shows the biases in the estimation of the cosmological parameters induced by considering the intrinsic ellipticities. We computed the 1,2, and 3σ ellipses by means of the Fisher matrix, as explained in Sect. 5.6.1, and we considered the full range of multipoles going from $\ell_{\text{min}} = 10$ to $\ell_{\text{max}} = 3000$ well into the noise-dominated regime. We calculated the biases for both the CNPT and the MWK models of the intrinsic alignments: In what concerns the CNPT-model we considered the value of the misalignment parameter found in n-body simulations (Lee & Pen, 2000) $a = 0.25$, and $\alpha = 0.75$ for the thickness of the disk. The biases are shown respectively in red for the CNPT-model, and in yellow for the MWK-model. All parameters apart from the dark energy equation of state w and the slope n_s are significantly biased, and in almost all cases the shift is not along the primary statistical degeneracy. The differences in the biases between the CNPT- and MWK-models reflect the difference in amplitude they predict, which is in our case due to the choice of normalisation.

The first thing to notice is how the biases depend on the parameters. Evidently Ω_m and σ_8, parameters on which the convergence spectrum $C_\kappa(\ell)$ highly depends, seem to be mostly affected. This is in line with the fact that the presence of $C_E^\epsilon(\ell)$ increases the normalisation and adds power to the high-ℓ part of the spectrum, therefore requiring larger values of σ_8, but also causes a tilting of the spectrum which instead asks for lower Ω_m-values. The other parameters are instead very weakly affected by the presence of intrinsic alignments.

5.6.3 Scaling of the estimation bias

It is necessary to investigate how the estimation bias scales with the normalisation of the intrinsic alignment spectra, as the parameters a and α in the CNPT-model and the resulting normalisation C in the MWK-model have a large uncertainty. It is worth recalling that the misalignment parameter a is measured in n-body simulations of structure formation, and the galaxy disk thickness α is taken from data on galaxy morphologies.

In Fig. 5.7 we focus on the CNPT-model, by plotting the biases in units of the conditional error $\sigma_\mu^2 = 1/F_{\mu\mu}$ as a function of the misalignment parameter a while keeping α fixed at 0.75. An increasing value of a means a higher misalignment between shear and inertia tensors (Lee & Pen, 2000; Crittenden et al., 2001; Schäfer, 2009), and hence a higher correlation between angular momenta, or, differently phrased, less randomness in their directions. This means that, within the model, the angular momenta trace the underlying tidal shear field in a tighter way. The lower limit $a = 0$ indicates therefore complete randomness and absence of any link of the angular momenta to the gravitational potential, as described in Lee & Pen (2000). It is visible how the biases grow fast for greater values of the parameter a, simply meaning that stronger intrinsic correlations would represent a stronger contamination to the covergence spectrum, but that

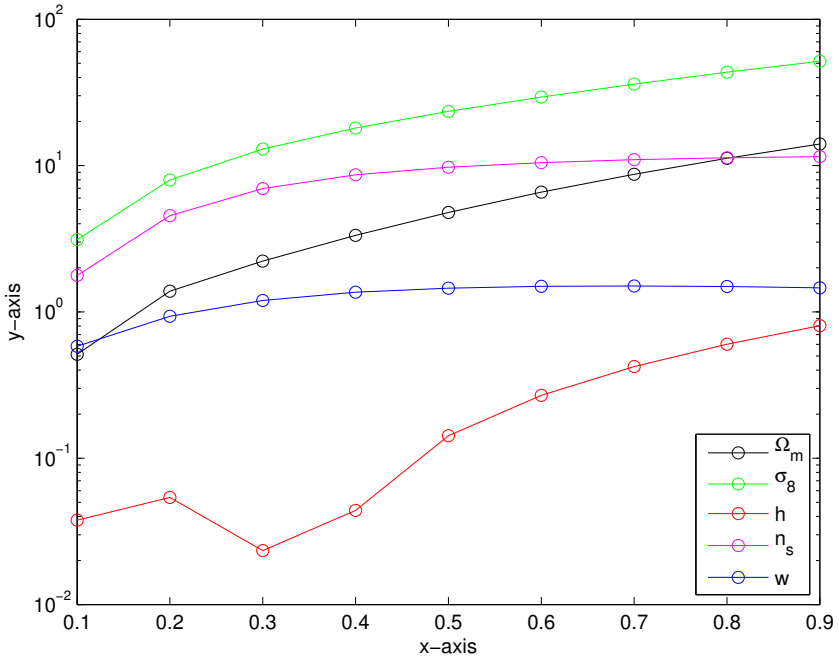

Figure 5.7: Biases b_μ in units of the statistical error σ_μ for the cosmological parameters Ω_m (black line), σ_8 (green line), h (red line), n_s (magenta line) and w (blue line), as a function of the misalignment parameter a of the CNPT-model.

for very large values of a the dependence of the parameter estimation bias with a is saturated and it evolves weaker with increasing a, and even decreases in the case of the parameter n_s. Given the fact that the estimation biases δ_μ/σ_μ change by almost two decades as a is varied, it is vitally important to determine a beforehand, either from independent observations or from simulations of structure formation.

5.6.4 Observations of intrinsic alignments

Another approach to gain infomation about the intrinsic alignments relies on the subtraction of the weak lensing signal from the overall signal that is measured. This is, roughly speaking, the inverse of what is usually done with nulling techniques (for details see Joachimi & Schneider, 2008, 2009, 2010), whose aim is to clear up the weak lensing signal from intrinsic alignments. The idea behind this is that if we know with high accuracy the model describing the cosmology, we can then predict how, according to this model, the weak lensing spectrum must be. By subtracting the latter from the measured spectrum, the remaining part is ascribable to intrinsic ellipticities. More precisely, if the uncertainty on the convergence power spectrum is small enough to still allow for the extrac-

tion of the intrinsic ellipticity signal, then it means that we will be able, in future surveys, to notice this weak signal in the presence of the much stronger weak lensing spectrum.

It is worth to remark, at this point, that the intrinsic alignments we consider in this work, also known as II (intrinsic-intrinsic) alignments, are not the only contaminant to the weak lensing spectrum, usually referred to as the GG (gravitational shear-gravitational shear) signal. For instance, another source of contamination are the GI (gravitational shear-intrinsic ellipticity) correlations, which might occur when the alignment produced by a dark matter halo on a closeby galaxy correlates with the shear signal that the same halo induces on a background galaxy. This effect, first suggested by Hirata & Seljak (2004), is difficult to remove, and is not considered in our treatment. Likewise, we do not consider complications arising from the statistical uncertainty in estimating the combined spectrum $C_\kappa(\ell) + C_E^\epsilon(\ell)$.

The problem is therefore now to understand whether the uncertainty at which the lensing spectrum can be predicted for a given cosmology is enough to attribute a high-ℓ excess in the ellipticity spectrum to intrinsic alignments. In order to quantify the uncertainty on the covergence spectrum $\Delta C_\kappa(\ell)$, we consider a multivariate Gaussian likelihood for the cosmological parameters, draw from this distribution simultaneously a sample of five parameters, and compute for those the weak lensing spectrum. This gives us a bundle of spectra around the fiducial spectrum $C_\kappa(\ell|x_\mu^{\rm fid})$, and allows us to define the uncertainty as the standard deviation:

$$\Delta C_\kappa(\ell)^2 = \frac{1}{n}\sum_{i=1}^{n}\left[C_\kappa(\ell|x_\mu^{(i)}) - \langle C_\kappa(\ell|x_\mu^{\rm fid})\rangle\right]^2, \tag{5.48}$$

at each multipole ℓ where the index i runs over the samples $x_\mu^{(i)}$ of parameter sets drawn from the multivariate Gaussian likelihood. In short, this sampling of a parameter set and measuring the variance of the resulting spectra is a method of propagating the statistical parameter uncertainty described by the likelihood to an error-tube around $C_\kappa(\ell)$ reflecting the prediction uncertainty in the spectrum. This allows now to compare the magnitude of the intrinsic ellipticity spectrum $C_E^\epsilon(\ell)$ to this uncertainty and to quantify the significance. We have considered here, as throughout the whole paper, the semi-analytical expression for the non-linear power spectrum derived by (Smith et al., 2003) without taking into account possible uncertainties in this expression, but only uncertainties on the parameters, since our goal is primarily to give a qualitative description of how the intrinsic alignment signal could be extracted from the convergence signal. Nonetheless, the Cosmic Emulators have found a discrepancy of $5-10\%$ between the semi-analytical fit and the simulations (Heitmann et al., 2010, 2009; Lawrence et al., 2010). This would increase the uncertainty on $C_\kappa(\ell)$ by an amount considerably smaller than the order of magnitude which separates $C_{E,B}(\ell)$ from $\Delta C_\kappa(\ell)$, therefore not affecting the robustness of our result.

Fig. 5.8 shows the uncertainties $n \times \Delta C_\kappa(\ell)$ with $n = 1 \ldots 5$ obtained by using this technique. The likelihood from which samples on the wCDM-parameter set including Ω_m, σ_8, h, n_s and w were drawn is the one describing the knowledge on the cosmological parameters if EUCLID's measurement of baryon acoustic oscillations, EUCLID's weak lensing data (both in a 10-bin tomographic measurement) and PLANCK's CMB data were present, with a theoretical prior on spatial flatness. The PLANCK-likelihood was marginalised over the baryon density Ω_b. The error tube $\Delta C_\kappa(\ell)$ can be clearly separated into two multipole ranges, the first region where the linear CDM-spectrum is dominating in the generation of the weak lensing spectrum, and the second region where the nonlinear enhancement of $P(k)$ is important and where the error tube is much wider.

With such small uncertainties and with the choice of a cosmological model with low complexity the predictive uncertainty on $C_\kappa(\ell)$ is much smaller than the amplitude of the intrinsic alignments from multipoles of $\ell \simeq 30$ on, $\Delta C_\kappa(\ell) \ll C_E^\epsilon(\ell)$. We verified that the PLANCK CMB likelihood alone would not be sufficient for extracting the intrinsic ellipticity spectrum. Likewise, a more complex model with a larger number of parameters would have much larger uncertainties, $\Delta C_\kappa(\ell) \gg C_E^\epsilon(\ell)$ for most of the multipole range.

5.7 Summary

Subject of this paper are the statistical properties of intrinsic, angular momentum induced ellipticity alignments, and their dependence on the cosmological parameter set, in comparison to ellipticity correlations induced by weak gravitational lensing. We carry out our computations with the EUCLID ellipticity data sample in mind, and use the projected EUCLID galaxy redshift distribution and shape noise for making forecasts.

1. We base our predictions for the spectra $C_E^\epsilon(\ell)$ and $C_B^\epsilon(\ell)$ describing fluctuations in the ellipticity field on physical models for angular momentum correlations in the large-scale structure (Crittenden et al., 2001; Mackey et al., 2002). The two models under consideration link the angular momentum field to the tidal shear field, and model the ellipticity of a galaxy by assuming that the galactic disk is formed perpendicular to the host halo's angular momentum direction. The two models differ in describing these physical processes in configuration space versus Fourier space, and use different normalisations. For comparability, we have normalised the MWK-model such that it displays the same amplitudes as the CNPT-model on large angular scales. The CNPT-model in turn uses 3 parameters, which are the mass-scale of the galaxies, imposed by an Gaussian filter acting on the CDM-spectrum $P(k)$, a misalignment parameter a, which is determined to have the numerical value $a \simeq 0.25$ in numerical simulations (Lee & Pen, 2001) and finally the disk thickness parameter α, which

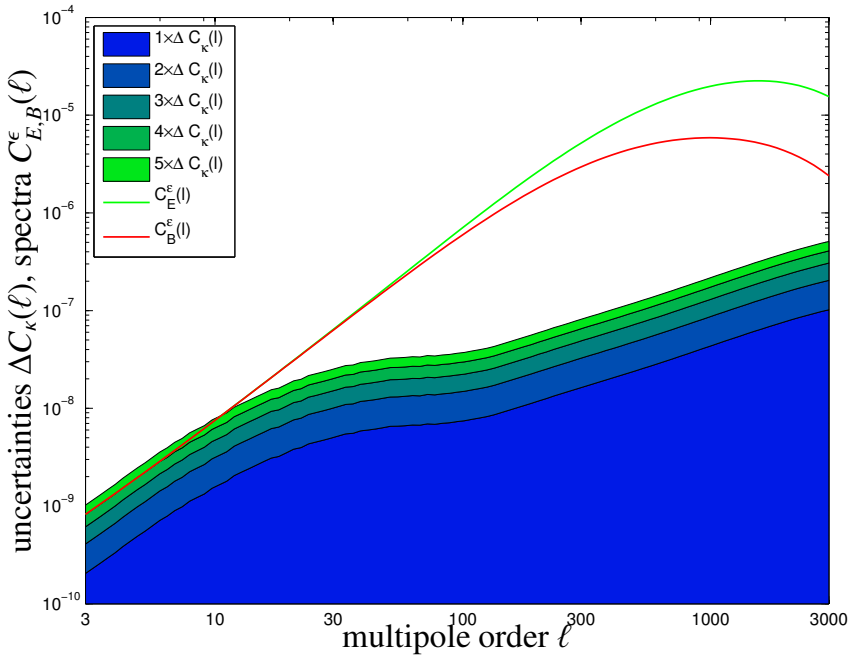

Figure 5.8: Uncertainties $\Delta C_\kappa(\ell)$ (shaded area) in the prediction of the nonlinear weak lensing spectra $C_\kappa(\ell)$ from drawing samples for Ω_m, σ_8, h, n_s and w from a Gaussian parameter likelihood, for which we use a prior on the wCDM-model combining baryon acoustic oscillations, lensing and the CMB (EUCLID 10-bin BAO spectra, EUCLID 10-bin weak lensing spectra and PLANCK CMB temperature and polarisation spectra). The uncertainty is compared to the ellipticity spectra $C^\epsilon_E(\ell)$ (green line) and $C^\epsilon_B(\ell)$ (red line) determined with the CNPT-model.

has been measured to be $\alpha \simeq 0.75$ in the APM-galaxy sample (Crittenden et al., 2001).

2. Computing the ellipticity spectra $C_E^\epsilon(\ell)$ and $C_B^\epsilon(\ell)$ for the galaxy sample of EUCLID from both models yields spectra which are constant on large angular scales and drop off exponentially on small scales, while the E-mode spectrum is larger by about an order of magnitude compared to the B-mode spectrum on multipoles of $\ell \simeq 1000$. By themselves, the spectrum $C_E^\epsilon(\ell)$ would be significantly larger than the linear weak lensing convergence spectrum $C_\kappa(\ell)$, which is comparable in amplitude to the spectrum $C_B^\epsilon(\ell)$ on these multipoles. Nonlinear structure formation, however, increases the variance of the cosmic density field strongly, such that intrinsic ellipticities contribute only $\sim 20\%$ to the total variance of the ellipticity field at $\ell = 1000$. Aperture weighted variances give a similar impression: The averaged shear and the aperture mass of the nonlinear weak lensing convergence dominate the variance on all relevant scales, and intrinsic alignments are smaller by at least a factor of two in this observable.

3. Investigating the dependence of the ellipticity spectra on cosmological parameters gives a result very different compared to other cosmological probes. Due to the dependence of the angular momentum field on the angular momentum direction and not the magnitude, σ_8 is entirely replaced by the misalignment parameter a. n_s, Ω_m and h determine the CDM spectrum $P(k)$ (the latter two by fixing the shape parameter Γ) and Ω_m is of course appearing in the conversion between comoving distance and redshift at the stage of applying the Limber equation. Computing the derivatives $\partial C_E^\epsilon(\ell)/\partial x_\mu$ and $\partial C_B^\epsilon(\ell)/\partial x_\mu$ of the spectra with respect to the cosmological parameters and expressed in units of their covariance suggests that the parameters a and Ω_m are the ones most important for intrinsic alignments, with only minor dependences on the dark energy equation of state w and the Hubble-parameter h. At the same time Ω_m and σ_8 are the ones best constrained by lensing, so that it is suggestive to expect the largest estimation biases in those two parameters, if the intrinsic alignments are not properly removed or modelled.

4. In the next step we quantified the likelihood $\mathscr{L}(\Omega_m, a, w)$ of the intrinsic alignment spectrum $C_E^\epsilon(\ell)$ if lensing was not present. One could expect this likelihood to have non-Gaussian contributions because of the nonlinearities present in an angular momentum-based alignment model: firstly, the angular momentum depends on the quadratic tidal shear and the ellipticity depends on the squared angular momentum direction. For a restricted multipole $\ell_{\max} \lesssim 100$ range one can see clear deviations from Gaussianity, which quickly vanish if the multipole range is extended. The misalignment parameter a, which describes the normalisation of the spectra, is described by a Gaussian likelihood and enters as a prefactor.

5. We compute estimation biases on the wCDM parameter set if intrinsic alignments are not removed from the ellipticity spectrum, i.e. if the data is in reality described by $C_\kappa(\ell) + C_E^\epsilon(\ell)$ and wrongly fitted by $C_\kappa(\ell)$ only. The strongest biases are present in Ω_m, which is measured to low and σ_8, which is estimated too high, both at the level of $\sim 2\sigma$, making the estimation biases significant. Interestingly, the dark energy equation of state is almost unbiased, indicating that dark energy investigations are not directly affected by intrinsic alignments. Changing the magnitude of the intrinsic alignment contamination by increasing the misalignment parameter a shows an monotonic increase of the estimation biases for all parameters except n_s where the estimation bias saturates at $a \simeq 0.5$ and drops for higher amplitudes. Clearly, these results demand a good external prior on a, either from independent measurements or from numerical simulations.

6. Finally we investigate if the weak lensing convergence spectrum $C_\kappa(\ell)$ can be predicted precisely enough such that a deviation can be attributed to a contribution $C_E^\epsilon(\ell)$. For this purpose, we develop a technique for propagating the uncertainty in the set of cosmological parameters to the variance $\Delta C_\kappa(\ell)^2$ around $C_\kappa(\ell)$ for the fiducial cosmology. Comparing this uncertainty with the amplitudes $C_E^\epsilon(\ell)$ suggests that it should be measurable at high multipoles. In this process we used a Gaussian likelihood $\mathscr{L}$ on a standard wCDM-cosmology reflecting the knowledge on the cosmological parameters from EUCLID's BAO- and weak lensing spectra and from the temperature and polarisation spectra of the cosmic microwave background measured by PLANCK.

We plan to extend our research to the intrinsic alignment contamination of tomographic weak lensing data, and to include cross-correlations between the weak lensing shear and the intrinsic ellipticity field, the so-called GI-alignments, which we aim to derive from angular momentum-based alignment models and which enter the ellipticity spectra at higher order. These GI-alignments are challenging to describe as they introduce ellipticity correlations across tomography bins. Additionally, we aim to include a linear alignment model for elliptical galaxies and to work with a proper morphological mix of ellipticities, working towards a more complete physical description of alignments in tomographic weak lensing data.

Chapter 6

EXTREME VALUE STATISTICS: THE TOOLKIT

6.1 Extreme values: why?

The first investigations on the statistics of the extreme values (EVS hereafter) were conducted in1709 by N. Bernoulli who was interested in the extreme constituted by the the mean duration of life of the last survivor of a group of n men of equal age who die after t years. In the following century tests and criterions for the acceptance or rejection of outlying values were studied B. Peirce (1852), W. Chauvenet (1878), and systematically established by P. Rider in 1933. In 1923 studied extreme values for normal distributions. L. H. C.Tippett conducted studies in this direction in 1925 too. But the normal distribution is not the natural environment of extreme values, which occur in higher rates actually in probability distributions parting from the Gaussian one. Studies on other distributions were carried out by E. L. Dodd in 1923, and most notably by M. Fréchet in 1927 (Fréchet, 1927), who not only found one of the asymptotic distributions of the largest value, but introduced the stability postulate (see Sec. 6.4.1). The basic work for extreme values is rooted in the work of R. Fisher and L. Tippett (Fisher & Tippett, 1928), who found the other two asymptotic distributions, and E. Gumbel who, together with Fisher and Tippett, pioneered the field of extreme value statistics.

There are many fields where the statistics of extremes can be implemented: from meteorology, finance, risk management, engineering and hydrology to astronomy.

To bring the problem to something more tangible, we can consider the example of floods. Considering a river and having available the annual data $\{x_1 ... x_{365}\}$ of the daily flow for N years, we can consider the set of the maxima throughout the N years $\{X_1 ... X_N\}$, and ask ourselves some basic questions:

- what is the probability that a flood will exceed a certain value x the next year?

- what is the probability that a future flood exceeds all the previous ones?
- what is the expectance time before the occurrence of a specific value of an extreme?

These are the typical questions addressed by EVS (Embrechts, 1994, 1997). In particular, the second question corresponds to the so-called exceedance problem. One could therefore grasp the important difference between EVS and the usual statistics (e.g. the study of the moments of a distribution): EVS focuses on the asymptotic behaviour of a random process at the tails of the distribution, where events are rare but extreme, instead of considering the central part of the distribution. This appears to be particularly interesting when non-linear processes, which usually enhance the probability of extreme events (and therefore the tails of the distribution), are involved. In the next section we are going to revisit some key concepts which are very useful when working with EVS. In Sec. 6.3 we give the exact distribution for the extreme values, while we discuss the approximate distributions for increasing number of samples in Sec. 6.4. Sec. 6.5 describes the exceedance theory and introduces the Pareto distribution. We give a round up of the usage of EVS in cosmology in Sec. 6.6, and we summarise the main points of this chapter in Sec. 6.7.

6.2 Key concepts and definitions

In this section we provide the statistical concepts which are used in the construction of the EVS. Given a generic probability density function (PDF) $p(x)\mathrm{d}x$ of a continuous random variable x, we can define a series if quantities:

Moments of the distribution: The moments of a distribution completely define and characterise the distribution. Different definitions of the moments are possible: The n-th *raw moment* of the PDF $p(x)\mathrm{d}x$ is calculated about zero, and is defined as the expectation value of x^n; The n-th *central moment*, which is the moment calculated about the mean μ; The n-th *standardised moment*, defined as the n-th central moment divided by the n-th power of the standard deviation σ: μ_n/σ^n.

$$\begin{aligned}
\gamma_n^{(r)} &= E[x^n] = \int_{-\infty}^{+\infty} x^n p(x)\mathrm{d}x, \\
\gamma_n &= E[(x-E[x])^n] = \int_{-\infty}^{+\infty} (x-\mu)^n p(x)\mathrm{d}x, \\
\gamma_n^{(s)} &= E\left[\left(\frac{(x-E[x])}{E[(x-E[x])^2]}\right)^n\right] = \int_{-\infty}^{+\infty} \left(\frac{(x-\mu)}{\sigma}\right)^n p(x)\mathrm{d}x,
\end{aligned} \tag{6.1}$$

The zero-th moment of any PDF is equal to 1, since it corresponds to the normalisation of the PDF, while the first raw moment of a distribution corresponds

to the mean, and the second central moment corresponds to the standard deviation. In the case of standardised moments we find that the first moment is zero, the second is 1, and we can define the third and fourth moments, the *skewness* $\gamma_3^{(s)}$ and the *kurtosis* $\gamma_4^{(s)}$:

$$\begin{aligned} \gamma_3^{(s)} &= \frac{\gamma_3}{\sigma^3} \\ \gamma_4^{(s)} &= \frac{\gamma_4}{\sigma^4}, \end{aligned} \tag{6.2}$$

the skewness $\gamma_3^{(s)}$ arising as soon as the PDF is asymmetric. The skewness can take positive or negative values respectively if the mode is smaller than the median or vice versa (this is only valid if multimodal distributions are not considered, but gives a good rule of thumb). The fourth standardised moment is instead a measure of how much peaked a distribution is. A positive kurtosis leads to more acute peak around the mean, and fatter tails; a negative kurtosis flattens the peak, making it wider, and makes the tails thin.

The moments of a distribution can be extracted by the *moment generating function*:

$$M_x(t) = E[e^{xt}] = \int_{-\infty}^{+\infty} e^{tx}\, p(x)\, \mathrm{d}x, \quad t \in \mathbb{R}. \tag{6.3}$$

If this function, which is the Laplace transform of $p(x)$, exists, the moments of order n are the n-th derivative at $t = 0$.

Cumulative distribution function: Finally, a key concept used for approaching the study of EVS is the cumulative probability distribution P(x), defined as the probability that the random variable x distributed as $p(x)$ is to be found at a value less or equal than a certain value x', $Pr(x \leq x')$:

$$P(x') = \int_{-\infty}^{x'} p(x)\mathrm{d}x. \tag{6.4}$$

6.3 Extreme values: the exact distribution

If we consider a random variable x with the PDF $p(x)\mathrm{d}x$, and we sample N times from this distribution, which we can call the parent distribution, the probability that one value x_i is less than certain value x is the cumulative distribution $F(x)$. Following Gumbel (2004) and his notation, the probability that all the n observations are less than x is just $P^N(x) = Pr(x_1, ..., x_N \leq x) = Pr(x_1 \leq x)Pr(x_2 \leq x)...Pr(x_N \leq x)$. The probability that just one value is found to be larger than x (which corresponds to the probability of the complementary event) is therefore:

$$P_+(x) = 1 - P^N(x). \tag{6.5}$$

This is still a cumulative function, and the related probability distribution of the maxima is:

$$p_+(x) = \frac{\mathrm{d}P^n(x)}{\mathrm{d}x}. \tag{6.6}$$

Following the same logical path, we can find that the probability of the n values x_i to be systematically larger than or equal to the value x is given by $[1-P(x)]^N$, being $[1-P(x)]$ the probability of just one value x_i to be larger than x. Therefore, if we are interested in the probability of the minima, we seek the probability that just one value is found to be lower than the value x, and this is the cumulative distribution for the minima:

$$P_-(x) = 1 - [1-P(x)]^N, \tag{6.7}$$

Once more the probability distribution of the minima can be computed by differentiation:

$$p_-(x) = \frac{\mathrm{d}[1-P(x)]^N}{\mathrm{d}x}. \tag{6.8}$$

Some properties and consequences of this distribution are:

- the probability that a given x is the largest one decreases with increasing number of the sample size N;
- the different curves $P^N(x)$ for a set of curves which do not intersect and shift to the right with increasing N, which means that modes and means of the largest values also shift towards larger values;
- even if the initial distribution is symmetric, the distribution of largest value is no longer symmetric. This can be seen if we consider the case of a parent distribution about median zero, for which we would have:

$$1 - P^N(x) \neq P^N(-x). \tag{6.9}$$

  An asymmetry is therefore introduced by the fact that we are picking extreme values of a single type, either maxima or minima.

6.4 Asymptotic distributions and the General Extreme Values distribution

We are now interested in knowing to which distribution the distribution of extreme values tends as a function of the sample size. Gumbel (1954, 2004) shows that it is possible to find the exact distributions of the extremes for certain initial distributions, e.g. the so-called exponential and Cauchy distributions. In general, though, it is very complicated to extract an analytical exact formulation for the distribution of the extremes, but it can be shown that the latter can tend to three possible asymptotic distributions for large values of N (being N the

number of samples we are considering). Each asymptote assumes a specific behaviour for absolute large values of the initial distributions. In this section we will therefore dwell upon the asymptotic distributions and try to give an explanation

6.4.1 The Stability Postulate

At the heart of this derivation, carried out by Fisher & Tippett (1928) and finally reformulated by Gnedenko (1943), there is the so called *Stability Postulate*. We consider to sample from an initial distribution N times, each sample being of size M. We will have, for each sample, a maximum value (the maximum of the M values we have), and we will have a maximum of all these N maximum values. The latter is the largest value of all the NM samplings (or observations) we have done. Now we can consider that the distribution of the largest values as obtained by having NM samplings and the one obtained by having N samples will both tend to the same asymptotic expression. This is basically equal to saying that the samples are statistically equivalent.

What can be further used is the invariance of a the shape of a distribution under a linear transformation. So if the cumulative distribution for the largest value is $P^N(x)$, then it must be:

$$P^N(x) = P(a_N x + b_N), \tag{6.10}$$

where a_n, b_n are two parameters functions of n. This equation is the Stability Postulate. Note that cumulative distribution $P^N(x)$ corresponds to the probability $Pr\{M_N \leq x\}$ that the maximum value of all the samples $M_N = \text{Max}\{x_1, ..., x_N\}$ is lower than x. Using now a linear transformation for x equals to requiring:

$$Pr\left\{\frac{M_N - b_N}{a_N} \leq x\right\}, \tag{6.11}$$

and corresponds to a renormalisation of M_N, where we also find that $a_N \geq 0$.

Basically, in analogy to the *Central Limit Theorem* which finds the asymptotic limit to the mean of a sufficient large number n of independent and identically distributed (i.i.d.) variables $\{x_i\}$ with specific mean μ and finite variance σ^2 to be a normal distribution:

$$\bar{x} = \frac{1}{n}\sum_{i=1}^{n} x_i \longrightarrow N(\mu, \sigma^2/n), \tag{6.12}$$

we find a similar theorem for M_n, where the asymptote is one of the three functions constituting the family of the General Extreme Value distribution (Colombi et al., 2011).

6.4.2 General Extreme Value Distribution

The three asymptotic distributions can mathematically be obtained from eqn. (6.10) by considering the cases $a_n = 1$, $a_n \neq 1$, or $P(0) = 1$. We are not going to

show the detailed calculations, for which we refer to Gumbel (2004), but the interesting feature is that these three cases can be grouped in one synthetic form, the *General Extreme Value Distribution* (Fisher & Tippett, 1928; Gnedenko, 1943):

$$P_{GEV}(x) = \exp\left[-x^{-\gamma\frac{x-\alpha}{\beta}}\right], \tag{6.13}$$

where α, β and γ are the location, scale and shape parameters. Once can recover the *Gumbel distribution* (or Type I distribution) when $\gamma = 0$, the *Fréchet distribution* (or Type II distribution) for $\gamma > 0$ and the *Weibull distribution* (or Type III distribution) for $\gamma < 0$.

It is rather interesting to note that one recovers these asymptotes according to the ranges of definition of the random variable of the original distribution. In the first case, the variate is unbounded ($-\infty \leq x \leq +\infty$), whereas in the second and third cases the variate is respectively lower bounded ($x \geq x'$) and upper bounded ($x \leq x'$). In addition to this it is interesting to note that, in the case of unbounded variates, the distribution of the maxima (and minima) will naturally tend to the Gumbel distribution for very large N. In fact, starting from the exact expression $P^N(x)$, we can rewrite this as:

$$\begin{aligned} P^N(x) &= \exp\left[\ln P^N(x)\right] = \exp\left[N \ln P(x)\right] = \exp\left[\ln(1-(1-P(x)))\right] \\ &\sim \exp\left[N[-(1-P(x)) - (1-P(x))^2 - ...]\right] \sim \\ &\sim \exp[-N[1-P(x)]]. \end{aligned} \tag{6.14}$$

$(1-P(x))$ is then approximated with a gaussian distribution, and $P^N(x)$ can therefore be expressed as an exponential function, which can be shown (Gumbel, 2004) to always tend to a Gumbel distribution for an unlimited variate x.

It is very easy to show that, given the cumulative Gumbel distribution:

$$P_{Gum}(x) = \exp\left[-\exp\left[-z\right]\right], \tag{6.15}$$

where $z = (x-\alpha)/\beta$, and the probability function is:

$$p_{Gum}(x) = \frac{1}{\beta}\exp[-z - \exp[-z]], \tag{6.16}$$

The mode is α, the median is $\alpha - \beta\ln(\ln 2)$ and the mean is $\alpha + \gamma'\beta$, where γ' is the Euler-Mascheroni constant ($\gamma' \sim 0.5772$ Abramowitz & Stegun, 1972a).

6.5 Exceedance theory and the Pareto Distribution

Another way to approach the study of extreme values is to deal with their frequencies. In other words, instead of requiring an initial distribution function from which to derive the distribution of minima and maxima, one might want to forecast the number of cases surpassing the current extreme value. Mathematically we require the variate x considered just to be continuous, and not to

be distributed as a certain initial PDF (in the flood example, this means that if there is an inundation, it is uninteresting to know by how much water the soil has been covered, but it is more interesting to know what are the chances of getting an even more severe inundation Gumbel, 2004). This way of investgating the extreme values is called *exceedance theory*. Waizmann et al. (2012b) provide a very insightful description for calculating the probability associated to this question, and we therefore follow their notation. Given an event x coming from an underlying distribution F, and set a threshold t, we want to know the probability that x exceeds t by the amount y. This equals to considering the conditional probability distribution:

$$Pr\{x > t + y | x > t\} = \frac{1 - F(t+y)}{1 - F(t)}, \quad \text{for} y > 0. \tag{6.17}$$

For very high thresholds and if the extremes are distributed as the GEV, then the distribution of the exceedances i given by the *generalised Pareto distribution* (GDP):

$$P_{GPD}(y) = \begin{cases} 1 - \left[1 + \kappa^{y/\tilde{\beta}}\right]^{-1/\kappa} & \text{for} \quad \kappa \neq 0, \\ 1 - \exp[-y/\tilde{\beta}] & \text{for} \quad \kappa = 0. \end{cases}$$

The GPD parameters are related to the GEV ones by means of the following relations:

$$\begin{aligned} \kappa &= \gamma \\ \tilde{\beta} &= \beta + \gamma(t - \alpha). \end{aligned} \tag{6.18}$$

6.6 Extreme Value Statistics in cosmology

Attempts to study extreme values and quantify their distributions by considering an underlying Gaussian field were made by Colombi et al. (2011), who find an analytical probability distribution of the maximum of the density field in a patch of a certain size in the case of a smoothed Gaussian random field. By using the cell-in-counts formalism they find good fitting with the type III distribution of the Generalised Extreme Value distributions (GEV), the Weibull distribution. A similar analysis was conducted by Davis et al. (2011) who also calculate an analytic formulation for the complete probability distribution of the most massive dark matter halos (or galaxy clusters) in a specific region of the universe, starting from Gaussian initial conditions. They find an expression for the three parameters characterising the GEV distributions by assuming as limit condition that the distribution of halos for very large sizes of the patches has to tend to a Poisson distribution (due to the homogeneity on large scales). Bias effects due to clustering are also considered and lead to no significant change in the extreme values distribution for the Gaussian case. Results are compared to N-body simulations and find strong agreement.

A great deal of effort has been put to study extremely massive galaxy clusters and the possibility that their existence at high redshifts could rule out the current ΛCDM paradigm or alternative models. To summarise the work carried out in the last years, we could say that there are different possible ways to investigate extremes, which respectively try to find answers to two questions.

The first question is: What is the expected mass of the most massive clusters given a cosmological model? Holz & Perlmutter (2012) went in this direction by focusing on the highest mass tail of the mass function as a probe for the validity of the ΛCDM model. They quantified the expected mass of the most massive clusters in ΛCDM model and then compared this result with observations. They find disagreement with just one cluster, but remark, in this respect, that the power of this method precisely relies on the fact that even a single object (found to have too large or too small mass) could be enough to disprove a cosmological model. They furthermore find the expected range of masses to strongly depend on redshift, making the analysis a good test also for the evolution according to ΛCDM. Their results were questioned by Hotchkiss (2011) who finds a strong bias on the studies on the rareness of high mass clusters at high redshift. This bias is basically due to an ill-defined probability of finding such rare clusters which makes these clusters appear less likely than they actually are. In proposing new suitable methods which also keep into account biasing on non-Gaussian initial conditions, he finds less tension with ΛCDM than the previous authors. The same is confirmed by the analysis of Waizmann et al. (2011) and Waizmann et al. (2012b). In the first paper a measure of the cumulative distribution function of the most massive objects is extracted from a sample of volumes of same size and redshift depth by using GEV. By considering the case of an hypothetical survey compatible with surveys such as EUCLID, they then fit the observational results to the GEV calculated for a set of different cosmologies in order to study which of the three parameters of the GEV is more adequate to distinguish between different models, and in which ranges of masse. They find that the shift parameter, i.e. the parameter of the GEV closely related to the peak of the distribution for the most massive clusters, is the best suited to test the validity of ΛCDM in the case of a large-area surveys with $M_{\rm lim} \sim 10^{14.5} M_\odot h^{-1}$ and redshifts above $z = 1$ or $M_{\rm lim} \sim 10^{14} M_\odot h^{-1}$ and $z = 1.5$, and that in general the real impact of errors in mass estimations must be evaluated. In the second paper they apply these theoretical results to the four most massive clusters at high redshift and the four most massive low redshift clusters, finding no tension with ΛCDM.

The other possible way to tackle the problem is to ask for a quantification of the excess of galaxy clusters over a certain high-mass threshold. This kind of analysis, which is also called statistics of *exceedances*, was carried out by Waizmann et al. (2012a). Motivated by the fact that surveys like the ones based on the Sunyaev-Zel'dovich effect are mass-limited with constant limit up to high redshift, they make use of a new tool: The Generalised Pareto distribution (GPD) which is precisely the distribution of exceedances. They investigate the depen-

dence of the distributions on different thresholds and on redshift ranges, and study how much the survey area affects the mean excess above a given mass threshold. They recover their previous results that ΛCDM is proven to be in agreement with observations. They furthermore compare the results obtained via GPD and GEV statistics for a given value of the threshold, finding strong concordance if the galaxy cluster is very rare, but strong deviation for less rare clusters. They conclude by commenting on the possibility of using the GPD as a cosmological probe, which seems disfavoured compared to the GEV.

Beyond tests on the cosmological constant model alone, other possible scenarios have been investigated through the statistics of extremes. We report here the studies of Baldi & Pettorino (2011) and Mortonson et al. (2011), who tested respectively coupled dark energy models and quintessence models. The first authors considered the case of a very massive cluster at high redshift detected by Jee et al. (2009) and shown by the latter to have a discrepancy of 3σ with the assumed model (ΛCDM with Gaussian initial conditions). Hence this requires revisiting the model either in terms of the initial Gaussian conditions, or of alternatives to the cosmological constant. In this direction they investigate coupled dark energy models, finding that these enhance the cumulative halo mass function at any epoch compared to models for the cosmological constant, and thus giving a possible interpretation of the detection of Jee et al. (2009). Mortonson et al. (2011) instead analyse predictions on abundance of clusters of a given mass and redshift using quintessence models. They point out that any observations falsifying ΛCDM would automatically falsify also quintessence, since quintessence models generate a suppression in the abundance of rare clusters similar to ΛCDM. They also include in the analysis possible sources of bias and variance, stressing the importance of high accuracy on the estimation of the mass, given the fact that even just one single event could rule out a model. Therefore they argue the necessity of including the Eddington bias in any analysis. Other possible sources of variance are the parameter variance (i.e. that fact that values of the parameters lie within a range which is bounded by current data) and the sample variance (i.e. the fact that counting rare objects in a finite volume introduces a Poissonian noise). When including all of these sources of bias they also find no tension with ΛCDM. Their analysis is further broadened by calling attention to the fact that solutions invoking dark energy would also have difficulties if high mass clusters appear only at high redshift: In fact phantom or clustered dark energy mostly affects structure growth, because the acceleration of the Universe is a rather recent event. So the behaviour of extremely large mass clusters must be investigated also at low redshift. The same would apply for modified gravity or interacting dark energy models.

Concerning lensing, extreme values statistics analyses were motivated by considerations about the largest Einstein radius measured. Zitrin et al. (2009) calculate a probability distribution function for Einstein radii to try to explain this rare event. This probability was then used to calculate the number of clusters expected above a certain redshift able to produce such Einstein radii in the

standard ΛCDM, finding that this number is extremely low, of the order of 10^{-7}. Waizmann et al. (2012) pick up this study and analyse the same largest observed Einstein radius as the previous authors. They question the feasibility of ruling out the ΛCDM model by means of just one single extreme galaxy cluster. By using Monte Carlo simulations they create the distribution of triaxial halo population, from which they sample. They then fit the result of the sampling with GEV distribution finding the best fit to be the Fréchet (or type II) distribution. These distributions are used to find the probability of occurrence of the observed extremes, which shows agreement with the ΛCDM model. They also investigate how the extremes are affected by the choice of the mass function and the triaxiality. They find the first not to affect the results much, but the latter to affect the distribution of the largest Einstein radii strongly, in the way that the more elongated objects are present, the higher the tail of the extreme value distributions. A step further in this field was taken by Redlich et al. (2012), who study the impact of mergers on the distribution of the largest Einstein radii, which have been found able to significantly increase the strong lensing efficiency of individual clusters. They conclude that semi-analytic studies must include the effect of mergers in order to be realistic and to make statements about the validity of the standard cosmological model based on the statistics of extremely giant gravitational arcs.

The CMB has also been field of investigation through extreme value statistics. Martinez-Gonzalez & Sanz (1989) study the statistics of the hot and cold spots (i.e. found above a certain temperature threshold) starting from two primordial power spectra: the white noise and the Zel'dovich spectrum. They find a probability of 10% for the hottest or coldest spot. Studies on spot-spot and temperature-weighted correlation functions of hot and cold spots were carried out by Larson & Wandelt (2005) who use a frequentist hypothesis test to the study non-Gaussianities in the CMB on WMAP data. Hou et al. (2009) study the one- and two-point statistics of local extremes in the five year WMAP release and compare these to Gaussian simulations to check for the differences. They find compatibility with the Gaussian model usually used, but find extremely low variance for the local extremes and a north-south asymmetry (for more details about the statistics and discriminators between Gaussian and non-Gaussian random fields we refer to Coles, 1988).

Mikelsons et al. (2009) study the statistics of extremes within patches of a fixed area. They use Gumbel statistics and fit the extreme distributions to CMB data and then to simulated Gaussian maps, comparing these results to investigate possible differences. Finally, they devote part of the study to the possibility of detection of non-Gaussianities with the CMB, finding that the Gumbel statistics would not be able to detect $f_{\rm NL}$ lower than ~ 1000. Concerning non-Gaussianities, also Mortonson et al. (2011) studied the feasibility of future measurements to detect primordial non-Gaussianities, but in the context of the statistics of the largest mass clusters. In fact they expect that if $f_{\rm NL}$ is larger than zero this would increase the abundance of high redshift massive clusters. They

find, though, that a very high value for $f_{\rm NL}$ would be required (~ 400). Chongchitnan & Silk (2012) also studied how the presence of local non-Gaussianities, parametrised by $f_{\rm NL}$, could affect the distribution of objects of extreme mass. In doing this they investigate uncertainties in the mass function by considering Press-Schechter, Sheth-Tormen and Tinker mass functions, which give similar extreme value distributions at low redshift, but largely depart one from another for high redshifts and high values of $f_{\rm NL}$. They include in the analysis non-Gaussian corrections of mass function and bias, Eddington corrections, sky coverage and redshift. They find that $f_{\rm NL}$ induces a shift in the extreme mass cluster to higher values but is degenerate with an increase in σ_8. Cayón et al. (2011) refer to the detection of the highest mass cluster XMM2235 of Jee et al. (2009) and extend the previous work of Holz & Perlmutter (2012) to study how the probability of finding XMM2235 to be most massive cluster within the survey is affected by non-Gaussianity. They use the parametrisation through the $f_{\rm NL}$ parameter for which they find constraints of $f_{\rm NL} = 529 \pm 194$.

6.7 Summary

In this chapter we provided an overview over the basic properties of EVS, which can be summarised as follows:

- EVS allows to draw statistical conclusions from rare and extreme events described by the tails of a distribution.
- Given an initial cumulative distribution $P(x)$ for a variate x, the exact formulations for the distributions of maxima and minima are mathematically defined as $1 - P^N(x)$ and $1 - [1 - P(x)]^N$, (where N is the number of samples) but are often quite difficult to analytically calculate.
- In any case, for large value of the number of samples N, these distributions can tend to one of the three asymptotic distributions of the family of GED, depending on whether the variate considered is bounded or unbounded.
- For unbounded variates, the distribution always tends to the Gumbel distribution.
- As much as one can tackle the problem of extreme values by asking which is the probability distribution function for maxima and minima, one can also consider the exceedance, and ask what is the probability that a certain event surpasses a threshold (which might be the current extreme value). This is of particular relevance in hydrology, where, given an inundation, one is interested in knowing what is the chance that an even more severe inundation might occur.
- EVS has been used recently in literature in the context of cosmology. Fields of application are the study of extremely massive galaxy clusters, dark energy

models, strong lensing, non-Gaussianities and the CMB. In general, the methods employed are similar in all the cases: The attempt is to study the extremes in order to either check the validity of a certain model, e.g. the ΛCDM, or rule out possible categories of models, as is the case for dark energy or non-Gaussainity models. The other possible way to carry out this analysis is instead to use the statistics of exceedances. The ΛCDM paradigm has so far passed these tests.

Chapter 7

PRIMORDIAL NON-GAUSSIANITIES

7.1 Introduction

The Cosmological Principle, on which we base cosmology, asserts that the Universe is homogeneous and isotropic on large scales. This property of the Universe, firstly assumed by Einstein at the beginning of the twentieth century without any empirical prove but for simplicity in the calculations, was observationally confirmed at the end of the same century.

This fact is translated in the statistical statement that observables such as the temperature of the CMB, or the density field, are assumed to be distributed as a Gaussian (concerning the CMB, this is the EhlersÐGerenÐSachs theorem). At the same time, though, the Universe's pool of information appears as a good balance between a large scale homogeneity and a small scale inhomogeneity. As we have seen in Chap. 6, the latter yields to departures from Gaussianity. Therefore the study of non-Gaussianities has become of paramount importance and interest.

When considering possible mechanisms able to generate deviations from a Gaussian behaviour of an observable, there are essentially two processes to account for: the quantum fluctuations, which are believed to grow due to gravitational instability, and therefore provide the seeds of the inhomogeneities, and the large scale structure (LSS) non-linearities, whose contribution becomes dominant when $\delta \gg 1$. In this chapter we focus on the first type of non-Gaussianity, which is built upon the theory of inflation. Inflation, in fact, is able to explain at the same time homogeneity and isotropy of the Universe, but also its level of inhomogeneity, by creating a link between the microscopical features of this Universe (quantum fluctuations) and its macroscopical features (large amount of symmetry on large scales). Inflation furthermore operates in a regime in which the energies are extremely high, and could not be reproduced in the accelerators and thus constitutes a necessary and unique test for high energy physics as well. We will start by introducing the horizon and flatness problems in Sec. 7.2, to which inflation (Sec. 7.3) finds a solution. In this section we also talk

about the slow-roll and slow-roll conditions. Sec. 7.4 dwells upon primordial non-Gaussianities, describing the so-called "shapes" of non-Gaussianities, and Sec. 7.5 summaries the chapter. [1].

7.2 The two problems

Despite the successes of the Big Bang theory, and the fact that it offers a very consistent picture of the evolution of the Universe (see Chap. 1), it was known already in the 50s that the Big Bang would lead to some problems (Rindler, 1956; Weinberg, 1972; Misner et al., 1973). Essentially the reason for this lies in the fact that the Big Bang theory is not able to give a description of what happened before the Planck time $t_{\rm PL} \sim 10^{-43}$s, simply because at that time, when quantum field theory is expected to become as important as general relativity and the two theories should merge, our treatment of the equations (which is based purely on general relativity) breaks down. The problems aforementioned are the horizon and the flatness (or entropy) problems, and will be examined in the following.

The horizon problem: As we saw in Chap. 1, the concept of horizons is a key concept in cosmology. In particular, we stress once more that there is a difference between the particle horizon and Hubble radius, for which we repeat the definitions:

$$R_{\rm PH}(t) = a(t)\int_0^t \frac{c\,{\rm d}t'}{a(t')} \tag{7.1}$$

$$R_{\rm H}(t) = \frac{c}{H(t)} = \frac{ca}{\dot{a}}. \tag{7.2}$$

The particle horizon defines the region within objects (particles) are in causal contact, i.e. it is the distance light can have traveled from $t = 0$ to a certain time t. The Hubble radius, which is not an horizon, is instead defined as the distance at which objects appear receding from us at the speed of light. If two objects (or particles) are separated by a distance larger than $R_{\rm PH}$ then they were never causally connected, and therefore they could have never communicated. If two particles are separated by distances larger than the Hubble radius, they could not communicate to each other at time t (Dodelson, 2003) but, in principle, they can be causally connected at another time.

Of course the causal connection is crucial for the assumption we make that the Universe is homogeneous since, roughly speaking, we need particles to have had the chance to interact at some point of their history in order to justify the homogeneity of their properties we see today. One of the best support we have for

[1] The content of this chapter is based on the lectures notes of Prof. Dr. M. Bartelmann:
http://www.ita.uni-heidelberg.de/research/bartelmann/Lectures/cosmology/cosmology.pdf,
and of Prof. Dr. Riotto:
http://www.cbpf.br/~iijtsc/lectures/A_Riotto_Notes.pdf

homogeneity is the CMB, or the surface of last scattering, when atoms formed and when photons could travel through optically thin space, only $3 \cdot 10^5$ years after the Big Bang (cfr. Sec. 1.7). As we have seen, the CMB is homogeneous in temperature up to fluctuations of order 10^{-5}. We can measure the angular size of the particle horizon at the time of recombination as $\theta_{\rm rec} = a_{\rm rec} r_{\rm PH}(a_{\rm rec})/D_A(a_{\rm rec})$, with $r_{\rm PH}(a_{\rm rec})$ being the comoving particle horizon at recombination:

$$r_{\rm PH}(a_{\rm rec}) = \frac{2c}{H_0}\sqrt{\Omega_m a_{rec}} \approx 175\sqrt{\Omega_0}\,{\rm Mpc}h^{-1}, \tag{7.3}$$

where we used the fact that the Universe is matter-dominated at recombination, and D_A is the angular diameter distance:

$$D_A(a_{\rm rec}) \approx \frac{2c}{H_0} a_{\rm rec}(1-\sqrt{a_{\rm rec}}) \approx \frac{2c}{H_0} a_{\rm rec} \approx 5\,{\rm Mpc}h^{-1}. \tag{7.4}$$

Be obtain thus an angular size of

$$\theta_{\rm rec} \approx 1.7^\circ\sqrt{\Omega_m}, \tag{7.5}$$

which is very small compared to the size of the microwave sky. The question arises of how is it possible that the CMB temperature is so similar everywhere on the sky, also between angular sizes greater than $\theta_{\rm rec}$, if the photons had the chance of interact and "communicate" within patches of only roughly 2°.

Another useful way to picture this problem (Wang, 2013) is to imagine that there are two competing processes in determining what portion of information we will access as observers at a certain time $t_{\rm obs}$: on the one hand, as the time passes ($t > t_{\rm obs}$), the particle horizon increases and our past light cone gets larger enabling us to access more information, but on the other hand the expansion of the Universe will make the constituents of the Universe drift apart, therefore decreasing our chances to access to more information. This basically results into the competition between two length scales: the one associated with the particle horizon, λ, and the other associated with the Hubble radius $\sim (H)^{-1}$. If $\lambda < H^{-1}$ then the scale λ is within the Hubble radius. Otherwise, the scale is outside the horizon.

The flatness problem: The second problem can be expressed by the statement that the condition $\Omega \sim 1$ is an unstable one. In fact, if we consider the Friedmann equation without cosmological constant but with curvature Ω_K:

$$H^2(a) = \frac{8\pi G}{3}\rho - \frac{Kc^2}{a^2}, \tag{7.6}$$

we can rewrite it as:

$$H^2(a) = H^2(a)\left[\Omega(a) - \frac{Kc^2}{a^2H^2}\right]. \tag{7.7}$$

Therefore:

$$\Omega(a) - 1 = \frac{Kc^2}{a^2 H^2}, \tag{7.8}$$

which means that if the Universe is perfectly flat ($K = 0$), then the condition $\Omega = 1$ must hold throughout all cosmic history. We know today that the geometry of the Universe is almost flat, i.e. $\Omega \sim 1$ (Planck has shown consistency with spacial flatness to percent level precision Planck Collaboration et al., 2013a), and it is legitimate to ask what should have been the value of Ω in the past such that today we can observe an almost flat Universe. We can choose the very early Universe, and compare the deviation of Ω from unity at the Planck time $t_{\rm PL}$ and compare it to the deviation today:

$$\frac{|\Omega - 1|_{t=t_{PL}}}{|\Omega - 1|_{t=t_0}} \approx \left(\frac{a_{PL}^2}{a_0^2}\right) \approx \left(\frac{T_0^2}{T_{\rm PL}^2}\right), \tag{7.9}$$

where we have used the relation $T \propto a^{-1}$ and assumed that the Universe was always radiation dominated, and therefore $H^2 \propto \rho_r \propto a^{-4}$ and:

$$\Omega - 1 \propto \frac{1}{a^2 a^{-4}} \propto a^2. \tag{7.10}$$

If we do so, we find that:

$$\frac{|\Omega - 1|_{T=T_{PL}}}{|\Omega - 1|_{T=T_0}} \approx O(10^{-64}), \tag{7.11}$$

where we have used the fact that $T_{\rm PL} \sim 10^{19}$ GeV and $T_0 \sim 10^{-13}$ GeV today. This means that the deviation from unity must have been fine-tuned to values extremely close to zero but yet not zero at times as early as the Planck time.

The horizon problem would be solved if the Hubble radius could have shrank in the past for a certain amount of time, so to bring closer to each other (and hence accessible to each other, and causally connected) portions of the Universe which would have not been causally connected otherwise. This phase needs to end at some point, so that the Universe starts expanding again as we observe today. Specifically, we require the comoving Hubble radius $c/(aH)$ to shrink. This would in principle also solve the second problem: In fact the right-hand side of Eqn. (7.8) is precisely $KR_{\rm H}^{\rm com}$, which would tend to zero for a shrinking comoving Hubble radius. Then one would naturally recover $\Omega \longrightarrow 1$.

Requiring that the the comoving Hubble radius shrinks equals to require:

$$\frac{\mathrm{d}}{\mathrm{d}t}\left(\frac{c}{aH}\right) = \frac{\mathrm{d}}{\mathrm{d}t}\left(\frac{c}{\dot{a}}\right) = -\frac{c\ddot{a}}{\dot{a}^2} < 0, \tag{7.12}$$

We therefore require that $\ddot{a} > 0$, i.e. that the Universe expands accelerating for a certain lapse of time. Note that this equals to requiring that the physical scale length λ grows faster than the Hubble radius, such that:

$$\frac{\mathrm{d}}{\mathrm{d}t}\left(\frac{\lambda}{H^{-1}}\right) > 0. \tag{7.13}$$

If this expansion is adiabatic, we can use the Friedmann equations. By looking at the second Friedmann equation (Riotto, 2002) we see that, in absence of any cosmological constant, an accelerated expansion is only possible if:

$$\rho c^2 + 3p < 0, \tag{7.14}$$

which means that we need a fluid with negative pressure following the relation:

$$p < -\frac{\rho c^2}{3}. \tag{7.15}$$

If we consider the simplest case of a cosmological constant $p = -\rho c^2$ we find the *de Sitter* universe. In such a Universe ρ = const and H = const and the expansion is therefore exponential:

$$a \propto e^{Ht}. \tag{7.16}$$

7.3 Inflation

A possible solution to the problems explained above was proposed by Guth (1981a) and further developed by (Starobinsky, 1982a; Linde, 1982; Albrecht & Steinhardt, 1982; Starobinskiĭ, 1979), and goes under the name of *inflation*. The fluid needed, characterised by a negative pressure such that it enables expansion, can be given by a self-interacting scalar field Φ, the *inflaton*, with potential $V(\Phi)$. Its form is not known exactly but its Lagrangian density comes from the *ansatz* (Mukhanov & Winitzki, 2007):

$$\mathscr{L} = \frac{1}{2}\partial_\mu \Phi \partial^\mu \Phi - V(\Phi), \tag{7.17}$$

and consequently its action is:

$$S = \int \mathrm{d}^4x \sqrt{-g}\mathscr{L} = \int \mathrm{d}^4x \sqrt{-g}\left[\frac{1}{2}\partial_\mu \Phi \partial^\mu \Phi - V(\Phi)\right]. \tag{7.18}$$

The equations of motion can now be obtained by Euler-Lagrange equations:

$$\partial^\mu \frac{\delta(\sqrt{-g}\mathscr{L})}{\delta \partial^\mu \Phi} - \frac{\delta(\sqrt{-g}\mathscr{L})}{\delta \Phi} = 0, \tag{7.19}$$

where $\sqrt{-g} = a^3$ is a volume which, multiplied by the Lagrangian density, gives us back the Lagrangian. By solving we find the equation of motion of the inflaton:

$$\ddot{\Phi} + 3H\dot{\Phi} - \frac{\nabla^2 \Phi}{a^2} + \frac{\mathrm{d}V(\Phi)}{\mathrm{d}\Phi} = 0. \tag{7.20}$$

An interesting feature in this equation is the presence of a friction term, $3H\dot{\Phi}$, known as the Hubble friction, and due to the expansion of the Universe, which affects the scalar field rolling down its potential.

In order to quantify the requirement given by Eqn. (7.15) in the case of the inflation, we consider the energy-momentum tensor:

$$T_{\mu\nu} = \partial_\mu \Phi \partial_\nu \Phi - g_{\mu\nu}\mathscr{L} \tag{7.21}$$

whose time-time component is the energy density and whose space-space components give the pressure density:

$$\rho c^2 = \frac{1}{2}\dot{\Phi}^2 + V(\Phi) + \frac{(\nabla\Phi)^2}{2a^2} \tag{7.22}$$

$$p = \frac{1}{2}\dot{\Phi}^2 - V(\Phi) + \frac{(\nabla\Phi)^2}{6a^2}. \tag{7.23}$$

The terms $\nabla\Phi$ vanish due to homogeneity, and Eqn. (7.15) becomes:

$$\frac{1}{2}\dot{\Phi}^2 - V(\Phi) < -\frac{1}{3}\left(\frac{1}{2}\dot{\Phi}^2 - V(\Phi)\right), \tag{7.24}$$

which corresponds to the condition:

$$\frac{\dot{\Phi}^2}{2} \ll V(\Phi). \tag{7.25}$$

In order to have a negative pressure and thus an accelerated expansion of the Universe, the scalar field's kinetic energy has to be lower than its potential energy, meaning that the field Φ needs to slowly roll down its potential. This also names this period of the Universe the *slow-roll*.

7.3.1 Slow-roll conditions

It is useful to use some parameters to describe the slow-roll conditions. In order to do this we insert the energy density in the Friedmann equation, considering that in this epoch the inflation energy density dominates over all the other components, which will be therefore neglected:

$$H^2 \simeq \frac{8\pi G}{3}\left[\frac{1}{2}\dot{\Phi}^2 + V(\Phi)\right] \simeq \frac{8\pi G}{3}V(\Phi). \tag{7.26}$$

This leads to a new equation of motion:

$$3H\dot{\Phi} = -\frac{\mathrm{d}V(\Phi)}{\mathrm{d}\Phi}. \tag{7.27}$$

The slow-roll condition in Eqn. (7.25), in addition to the latter equation, lead to the requirements:

$$\dot{\Phi}^2 \ll V(\Phi) \Longrightarrow \frac{(V')^2}{V} \ll H^2, \tag{7.28}$$

where $V' = \mathrm{d}V(\Phi)/\mathrm{d}t$, and

$$\ddot{\Phi} \ll 3H\dot{\Phi} \Longrightarrow V'' \ll H^2. \tag{7.29}$$

We can define the slow-roll parameters, ϵ and η, as:

$$\epsilon = -\frac{\dot{H}}{H^2} = 4\pi G \frac{\dot{\Phi}}{H^2} = \frac{1}{16\pi G}\left(\frac{V'}{V}\right)^2, \tag{7.30}$$

$$\eta = \frac{1}{8\pi G}\left(\frac{V''}{V}\right) = \frac{1}{3}\frac{V''}{H^2}, \tag{7.31}$$

and their combination (Riotto, 2002):

$$\delta = \eta - \epsilon = -\frac{\ddot{\Phi}}{H\dot{\Phi}}. \tag{7.32}$$

The parameter ϵ is a quantification of the variation of the Hubble parameter over the period of inflation. Given that:

$$\frac{\dot{a}}{a} = \dot{H} + H^2 = (1-\epsilon)H^2, \tag{7.33}$$

inflation is only possible if $\epsilon < 1$. More in general, slow-roll inflation imposes the conditions that $\epsilon \ll 1$ and $\eta \ll 1$. Physically, the two slow-roll parameters η and ϵ guarantee respectively that the duration of the inflation is long enough (i.e. that the the roll is slow enough), and that the pressure is negative enough (remember that the condition $w < 1/3$ must hold). During inflation, since the potential is flat, these parameters remain almost constant, but inflation ends when the condition $\epsilon < 1$ ceases to be true, i.e. when the potential energy of the inflation is lower than its kinetically energy. When inflation ends, it leaves the Universe extremely cool and with a very low entropy, which is not what we see. In order to reconcile the conditions of the Universe just after inflation with a Universe radiation-dominated, an intermediate process must have taken place. In this period, dubbed *reheating*, the energy in Φ is used for producing particles at high temperatures.

7.3.2 Solution of the horizon and flatness problems

In order to give a more quantitative reasoning of why the inflation theory solves the two problems, we consider the inflation as a de-Sitter epoch whose Hubble size, c/H_I, is constant, and whose scale factor increases as:

$$a = a_I e^{H_I(t-t_I)}, \tag{7.34}$$

where a_I, H_I, t_I are the scale factor, the Hubble parameter and the time at inflation.

The particle horizon therefore exponentially grows during inflation:

$$R_{\mathrm{PH}}(t) = a(t)\int_{t_I}^{t}\frac{c\,\mathrm{d}t'}{a(t')} = -\frac{ca_I e^{H_I(t-t_I)}}{H_I}\left[e^{-H_I(t-t_I)}\right]_{t_I}^{t} \simeq \frac{ca(t)}{H_I}, \tag{7.35}$$

and the comoving Hubble radius

$$R_{\rm H} = \frac{c}{aH_I} = \frac{c}{H_I} e^{-H_I(t-t_I)} \tag{7.36}$$

exponentially shrinks. In order to understand how much the inflation must have lasted to solve the horizon problem we consider t_I and t_F to be the time of the beginning and the end of the inflation epoch. Then it is possible to define the number of e-foldings N as:

$$N = \ln[H_I(t_F - t_I)]. \tag{7.37}$$

By imposing the condition that the present Hubble radius c/H_0 must have been reduced to a value smaller than the Hubble radius at time of inflation:

$$\frac{c}{H_0}\left(\frac{a(t_F)}{a(0)}\right)\left(\frac{a(t_I)}{a(t_F)}\right) = \frac{c}{H_0}\left(\frac{T_0}{T_F}\right)e^{-N} \lesssim \frac{c}{H_I} \tag{7.38}$$

we obtain:

$$N \gtrsim \ln\left(\frac{T_0}{H_0}\right) - \ln\left(\frac{T_F}{H_I}\right) \approx 67 + \ln\left(\frac{T_F}{H_I}\right), \tag{7.39}$$

which gives $N \gtrsim 70$.

This automatically solves also the flatness problem, since during inflation:

$$\frac{|\Omega - 1|_{t=t_F}}{|\Omega - 1|_{t=t_I}} = \left(\frac{a_I}{a_F}\right)^2 = e^{-2N}, \tag{7.40}$$

since $\Omega - 1 \propto a^{-2}$ given that the Hubble rate is constant during inflation. If we require $|\Omega - 1|_{t=t_I}$ to be of the order of unity, we see that a period of inflation lasting longer than $N \approx 70$ e-foldings is enough to guarantee that the present day value of Ω_0 is unity with a great precision, thus solving the flatness problem.

We have considered here the first and simplest of the so-called single-field models, which have in common the assumption that only one quantum field drives the inflation. There is a very wide plethora of other models, including multi-field models, non-canonical kinetic term models, non-adiabatic vacuum models which we will not discuss here(for more details see Bartolo et al., 2004).

7.4 Primordial non-Gaussianities

Inflation has received such a wide consensus because not only it solves the problems of flatness and horizon, but it remarkably solves also the problem of explaining what generated the inhomogeneities of the Universe in the way we observe them today. The idea is in fact that the inflaton field underwent vacuum fluctuations before the inflation. During the inflation time these microscopic fluctuations were stretched up to the point of exiting the horizon, when they froze. When the inflation stopped these fluctuations entered again the horizon,

and hence had the chance to grow once again due to gravitational instability, yielding to the temperature anisotropies we see in the CMB and forming the large scale structure we see today (for reviews see Riotto, 2002; Bartolo et al., 2004; Chen, 2010; Langlois, 2011; Wang, 2013). If we therefore want to learn about these early fluctuations we must certainly look in the imprints they left both on CMB and in the large scale structure. In this section what we are interested in are the statistical properties of these underlying primordial fluctuations. Most of the inflationary scenarios predict for them small deviations from Gaussianity due to the violation of slow-roll conditions (Allen et al., 1987; Falk et al., 1992; Gangui et al., 1994; Lesgourgues et al., 1997; Gangui et al., 2002). Other scenarios (for example isocurvature fluctuations or the curvaton mechanism), instead, predict very high departures from Gaussianity (Mollerach, 1990; Linde & Mukhanov, 1997; Lyth & Wands, 2002). Any kind of non-Gaussianity could have left signatures in the distributions of CMB anisotropies and of the large scale structure which could shed light on the physics and the processes characterising the early Universe and, even more importantly, could help to discriminate among different inflation scenarios. Primordial non-Gaussian imprints in the CMB have been extensively studied (as an example, see Komatsu, 2010), whereas studies on the non-Gaussian signal in the large scale structure have been carried out, for example, by Desjacques & Seljak (2010a).

Other than the CMB and the LSS, weak lensing as well can be used to probe and study primordial non-Gaussianities, but with smaller sensitivities (Fedeli et al., 2011; Jeong et al., 2011a; Marian et al., 2011; Schäfer et al., 2012a).

The core difference between any Gaussian and non-Gaussian distribution is the fact that a Gaussian distribution is fully described just by its first and second moments. When dealing with fields such as the temperature field in the case of the CMB and the density field for the LSS, this corresponds to saying that the second-order correlator, i.e. the correlation function, or its Fourier pair, the power spectrum are enough to fully describe the statistics of the observable. In the more general case of a non-Gaussian distribution this property does not apply, and one must study higher-order correlators of the distribution of primeval curvature perturbations ζ. The primordial perturbations ζ can be related to the Bardeen potential curvature perturbations Φ (Bardeen, 1980; Bardeen et al., 1983a) and to the temperature of the CMB by means of:

$$\zeta = \frac{5}{3}\Phi \tag{7.41}$$

$$\frac{\Delta T}{T} = -\frac{\Phi}{3} \tag{7.42}$$

(see Sachs & Wolfe, 1967). By making the following *local ansatz* for the potential (Komatsu & Spergel, 2001a; Okamoto & Hu, 2002):

$$\begin{aligned}\Phi(\mathbf{x}) &= \Phi_L(\mathbf{x}) + f_{\rm NL}\left[\Phi_L^2(\mathbf{x}) - \langle\Phi_L^2(\mathbf{x})\rangle\right] \\ &+ g_{\rm NL}\left[\Phi_L^3(\mathbf{x}) - 3\langle\Phi_L^2(\mathbf{x})\rangle\Phi_L(\mathbf{x})\right] + \mathscr{O}(\Phi_L^4),\end{aligned} \tag{7.43}$$

where Φ_L represents Gaussian linear perturbations, we have two parameters quantifying the amplitudes of the primordial non-Gaussianity: $f_{\rm NL}$ and $g_{\rm NL}$. By using this ansatz we can obtain the higher order correlators in Fourier space, i.e. the three-point function, or *bispectrum*:

$$\langle \Phi(\mathbf{k_1})\Phi(\mathbf{k_2})\Phi(\mathbf{k_3})\rangle = (2\pi)^3\delta^D(\mathbf{k_1}+\mathbf{k_2}+\mathbf{k_3})\, B_\Phi(k_1,k_2,k_3), \tag{7.44}$$

and the four-point function, or *trispectrum*:

$$\langle \Phi(\mathbf{k}_1)\Phi(\mathbf{k}_2)\Phi(\mathbf{k}_3)\Phi(\mathbf{k}_4)\rangle = (2\pi)^3\delta_D(\mathbf{k}_1+\mathbf{k}_2+\mathbf{k}_3+\mathbf{k}_4)\, T_\Phi(k_1,k_2,k_3,k_4), \tag{7.45}$$

where δ_D is the Dirac delta function and imposes the condition that the sum of the wavevectors is zero in order to have non-vanishing bi- and trispectra. This means that the wavevectors have to form, respectively, a triangle for the bispectrum, and a tetrahedron for the trispectrum. Creminelli (2003) and Babich et al. (2004) showed how different shapes of the triangles can be used to discriminate between different models for inflation, and paved the way to many analyses of the *shapes of the non-Gaussianities*.

Before analysing in more detail the shapes of non-Gaussianities it is worth quantifying at least by orders of magnitude the expected amplitudes for $f_{\rm NL}$ in different scenarios: while the case of non-linearity in the inflation or single field models lead to $f_{\rm NL} \sim O(10^{-1})$ and second order gravity leads to $f_{\rm NL} \gtrsim \mathcal{O}(1)$, cases such as isocurvature fluctuations, features or curvatons can lead to $f_{\rm NL} \gg 1$ (Komatsu et al., 2005). This automatically implies that any measurement of $f_{\rm NL} \gg 1$ would disfavour certain models. This statement was made even stronger by Maldacena (2003); Acquaviva et al. (2003) and Creminelli & Zaldarriaga (2004), who proved that the entire family of inflation models based on a single scalar field would be ruled out in the case of $f_{\rm NL} \gg 1$.

7.4.1 The shape of the non-Gaussianities

The most general classification of the various shapes of the non-Gaussianities for the bispectrum is the following: squeezed ($k_1 \simeq k_2 \gg k_3$), elongated ($k_1 = k_2 + k_3$), folded ($k_1 = 2k_2 = 2k_3$), isosceles ($k_2 = k_3$), equilateral ($k_1 = k_2 = k_3$). As mentioned above, different physical models for producing non-Gaussianities produce signals which peak at specific triangle shapes:

- the squeezed triangles are usually representative for models with multiple light fields during inflation;
- the equilateral triangles are typical at the peak f bispectra coming from models with high-derivative interactions;
- the folded triangles are typical for models with non-standard initial conditions.

The elongated and isosceles triangles represent intermediate cases.

The bispectrum $B_\Phi(k_1,k_2,k_3)$ depends on these different shapes of the triangles, and it is convenient to picture the contribution of each shape by plotting the magnitude of the quantity $B_\Phi(k_1,k_2,k_3)(k_2/k_1)^2(k_3/k_1)^2$ as a function of (k_2/k_1) and (k_3/k_1) for a value of k_1, given the condition $k_1 \geq k_2 \geq k_3$ (Komatsu, 2010). In this section we are going to focus on the three shapes which are mostly analysed in the literature: The *local*, the *equilateral* and the *orthogonal* shapes.

Local form: The local form bispectrum takes its name from the fact that it can arise from the curvature perturbation $\Phi(\mathbf{x}) = \Phi_L(\mathbf{x}) + f_{\rm NL}\left[\Phi_L^2(\mathbf{x}) - \langle\Phi_L^2(\mathbf{x})\rangle\right]$, although this is not the only way of producing such a bispectrum. It is given by the following relation (Gangui et al., 1994; Komatsu & Spergel, 2001a; Verde et al., 2000a):

$$\begin{aligned} B_\Phi^{\rm local}(k_1,k_2,k_3) &= 2f_{\rm NL}^{\rm local}[P_\Phi(k_1)P_\Phi(k_1) + P_\Phi(k_1)P_\Phi(k_1) + P_\Phi(k_1)P_\Phi(k_1)] \\ &= 2A^2 f_{\rm NL}^{\rm local}\left[k_1^{n_s-4}k_2^{n_s-4} + (2\ \text{perm})\right], \end{aligned} \tag{7.46}$$

where $P_\Phi = A/k^{4-n_s}$ is the power spectrum of the potential Φ and A its normalisation factor. If we consider the normalised amplitude $B_\Phi^{\rm local}(k_2/k_1)^2(k_3/k_1)^2$ we see that has a peak at the squeezed triangle, i.e. for wavevector magnitudes arranged as $k_1 \simeq k_2 \gg k_3$.

Equilateral form: The equilateral form, given by Creminelli et al. (2006) is :

$$\begin{aligned} B_\Phi^{\rm equil}(k_1,k_2,k_3) &= 6A^2 f_{\rm NL}^{\rm equil} \\ &\times \left[-2(k_1k_2k_3)^{2(n_s-4)/3}\right. \\ &- [(k_1k_2)^{n_s-4} + (2\ \text{perm})] \\ &+ \left.[k_1^{n_s-4}k_2^{2(n_s-4)/3}k_3^{(n_s-4)} + (5\ \text{perm})]\right], \end{aligned} \tag{7.47}$$

This form is an approximation for the bispectrum forms which arise from the class of scalar fields with non-canonical kinetic terms, and peaks at the equilateral configuration. Local and equilateral forms are almost orthogonal to each other, allowing for almost independent measurements.

Orthogonal form: The orthogonal form is constructed in such a way to be almost orthogonal to both the local and equilateral forms (Senatore et al., 2010) and is given by:

$$\begin{aligned} B_\Phi^{\rm ortho}(k_1,k_2,k_3) &= 6A^2 f_{\rm NL}^{\rm ortho} \\ &\times \left[-8(k_1k_2k_3)^{2(n_s-4)/3}\right. \\ &- 3[(k_1k_2)^{n_s-4} + (2\text{perm})] \\ &+ \left.3[k_1^{n_s-4}k_2^{2(n_s-4)/3}k_3^{(n_s-4)} + (5\ \text{perm})]\right], \end{aligned} \tag{7.48}$$

This form arises when specific linear combinations of equilateral shapes are considered. This would in fact lead to this particular shape, orthogonal to both local and equilateral shapes. The orthogonal shape has a peak at the equilateral configuration, and a negative valley along the elongated configurations.

In order to quantitatively complete this picture we also give the relation for the trispectrum in the case of local non-Gaussianitites:

$$\begin{aligned} T_\Phi(\mathbf{k}_1,\mathbf{k}_2,\mathbf{k}_3,\mathbf{k}_4) &= 6g_{\rm NL}\left[(k_1k_2k_3)^{n_s-4}+(3\text{ perm})\right] \\ &+ \frac{25}{18}\tau_{\rm NL}\left[(k_1k_2)^{n_s-4}[P_\Phi(k_{13})P_\Phi(k_{14})]+(11\text{ perm})\right] \end{aligned} \tag{7.49}$$

where $k_{ij}\equiv|\mathbf{k}_i+\mathbf{k}_j|$, which is the term giving rise to another parameter compared to Eqn.(7.43) quantifying the amplitude of the spectrum in Fourier space, $\tau_{\rm NL}$.

The current measures from the *Planck* mission (Planck Collaboration et al., 2013b) are:

$$\begin{aligned} f_{\rm NL}^{\rm local} &= 2.7\pm5.8 \\ f_{\rm NL}^{\rm equil} &= -42\pm75 \\ f_{\rm NL}^{\rm ortho} &= -25\pm39 \end{aligned} \tag{7.50}$$

at 68% CL. These values therefore appear to be compatible with the absence of any primordial non-Gaussianity for these shapes. Further constrains on the trispectrum are also given, although it is specified that the signal of the reconstructed trispectrum is consistent with zero apart from one large term, which is anyhow thought not to be of primordial origin. The constraint $\tau_{\rm NL}<2800$ (95% CL) is therefore given by allowing the signal to be primordial. The amplitude $g_{\rm NL}$, instead, has not been constrained by Planck.

7.5 Summary

In this chapter we have reviewed the basics of the theory of inflation and we have introduced primordial non-Gaussianities. The main content of this chapter can be summarised as follows:

- Inflation is a theory able to explain at the same time both the level of homogeneity and of inhomogeneity of the Universe. In fact, on the one hand t gives a theoretical framework (an exponential expansion of the Universe at very early times), able to account for the facts that large portions of the Universe must have come into causal contact during the early times in order to appreciate the homogeneity today (horizon problem), and that the departure from unity of the geometry parameter Ω must have been finely tuned in the early Universe to make this parameter be roughly unity today (flatness problem). On

the other hand, it provides a theory for quantum fluctuations, which would be the seeds, grown via gravitational instability, of the structures we observe today.

- Statistically, most inflation scenarios predict a nearly Gaussian distribution for these primordial fluctuations. Any primordial departure from Gaussainity, therefore, could have a key role in discriminating between different inflation scenarios. Primordial non-Gaussianities can be studied by means the higher-order correlators of the underlying distribution of the fluctuations. In Fourier space the three- and four-point correlators are the bispectrum and the trispectrum. The amplitude of these spectra are parametrized by means of the parameters $f_{\rm NL}$, $g_{\rm NL}$ and $\tau_{\rm NL}$.

- Concerning the bispectrum, it has been shown that specific shapes of non-Gaussianities are able to discriminate very well among inflation scenarios. Different bispectrum forms, in fact, peak at different shape configurations, each one of which is in turn are suitable for describing certain scenarios. The shapes described in this chapter are the three types usually studied in the literature.

- The latter constraints given on the parameters for different shapes come from the *Planck* mission, and are reported in Eqn.(7.50). Although appearing compatible with absence of non-Gaussianity, these constraints only apply to the three shapes analysed, which are not the only existing ones.

Chapter 8

EVS: AN APPLICATION TO WEAK LENSING AND PRIMORDIAL NON-GAUSSIANITIES

The content of this chapter entirely reproduces the article Capranico et al. (2013). While the introduction focusses on the theory of EVS and gives the cosmological background, the analysis we have carried out can be found in Sec. 8.3. A summary of our results is presented in Sec. 8.4.

8.1 Abstract

Cosmic inflation is a mechanism by which the early Universe underwent a period of exponential accelerated expansion and has been invoked in order to solve the flatness and horizon problems (Guth, 1981b). In addition, it provides a natural explanation for the seed fluctuations from which the cosmic large-scale structure grew by gravitational instability (for reviews, see Bartolo et al., 2004; Wang, 2013; Martin et al., 2013; Lesgourgues, 2013). A very important signature of inflationary theories are the statistical properties of the perturbations they cause in the cosmic distribution of matter (Bardeen et al., 1983b; Starobinsky, 1982b). These fluctuations are expected to be almost Gaussian, with small deviations from Gaussianity due to violated slow-roll conditions. The most general observable of a certain inflationary model is the sequence of polyspectra which describe the fluctuations in the density field (or in the gravitational potential) in Fourier-space. Their amplitudes are given by the non-Gaussianity parameters, and we focus in this work on the lowest order parameters: $f_{\rm NL}$ which characterises the bispectrum and $g_{\rm NL}$ which determine the magnitude of the inflationary trispectrum. In observations of the cosmic microwave background or of the cosmic large-scale structure one aims at constraining the non-Gaussianity parameters as well as at measuring the variation of the polyspectra in their dependence on the wave vector configuration. In this way it is possible to distinguish

different inflationary scenarios.

Currently, the tightest constraints on the lowest order non-Gaussianity parameters in a non-Gaussianity model of the local type come from the analysis of the cosmic microwave background by the PLANCK surveyor, who report $f_{\rm NL} = 2.7 \pm 5.8$ for the bispectrum amplitude (Planck Collaboration et al., 2013c,d). Previous studies with WMAP have found bounds on these parameters to be $-7.4 \times 10^5 < g_{\rm NL} < 8.2 \times 10^5$ and $-0.6 \times 10^4 < \tau_{\rm NL} < 3.3 \times 10^4$ (Smidt et al., 2010) and $-5.6 \times 10^5 < g_{\rm NL} < 6.4 \times 10^5$ (Vielva & Sanz, 2010). Data from the large-scale structure put bounds on the non-Gaussianity parameters at similar orders of magnitude: Desjacques & Seljak (2010b) quote the range $-2.5 \times 10^5 < g_{\rm NL} < 8.2 \times 10^5$.

In this paper we focus on constraining the non-Gaussianity parameters $f_{\rm NL}$ and $g_{\rm NL}$ in a local model with extreme value statistics, i.e. where the measurement consists in determining the largest (or smallest) weak lensing shear in apertures of varying size. Because $f_{\rm NL}$ describes the skewness of the distribution of the weak lensing convergences and $g_{\rm NL}$ the kurtosis, one would expect that those parameters influence the occurrence of extreme values of the weak lensing convergence. In contrast to the direct estimation of polyspectra our measurement averages over the configuration dependence of the non-Gaussianity model and is primarily targeted at measuring the non-Gaussianity parameters themselves rather than at distinguishing configuration dependences. The specific observable we consider is the weak lensing convergence which has the advantage of being proportional to the density field. All statistical properties of the observable, including polyspectra, will be proportional to those of the field to be investigated. We use the characteristics of the EUCLID weak lensing survey, which will reach out to redshifts of unity and cover half of the sky.

Extreme value statistics (for the mathematical foundation, please refer to Gumbel, 1954; Beirlant et al., 2004; Gumbel, 2004) has been applied to a range of problems in cosmology, most notably in the "pink-elephant"-argument of massive high-redshift clusters that should not have formed in ΛCDM cosmologies at the redshifts they have been observed, and to extreme features in the cosmic microwave background such as the cold spot (Cruz et al., 2005, 2007; Vielva, 2010). The common motivation is a reliable description of rare events: Of course with a sufficient high number of trials one would be able to observe even very unlikely events in a Gaussian random process, but it is necessary to draw conclusions on the fundamental random process from the observation of single, unlikely events (Coles, 2002; Colombi et al., 2011). Extreme value statistics aims to provide such a description and differs from the measurement of e.g. moments of the random process in the important respect that it focuses on the asyptotic behaviour of the random process at large amplitudes instead of the core of the distribution.

In this spirit, clusters of galaxies reflecting extreme values of the underlying density field have been investigated in their power to probe the cosmological model (Enqvist et al., 2011; Hotchkiss, 2011; Waizmann et al., 2011, 2012b,a; Davis et al., 2011), where the samples are mostly resulting from X-ray surveys. With these samples, statistical tests of ΛCDM or of non-Gaussian initial condi-

tions have been carried out (Cayón et al., 2011; Holz & Perlmutter, 2012; Baldi & Pettorino, 2011; Chongchitnan & Silk, 2012; Mortonson et al., 2011). Apart from the primary application in cluster catalogues, extreme value statistics has been used in statistical analysis of the temperature pattern of the cosmic microwave background (Coles, 1988; Martinez-Gonzalez & Sanz, 1989; Larson & Wandelt, 2005; Hou et al., 2009; Mikelsons et al., 2009) and finally to the strong lensing signal of galaxy clusters (Waizmann et al., 2012; Redlich et al., 2012; Zitrin et al., 2009)

The motivation of this paper is the question if it was possible to derive constraints on inflationary non-Gaussianities from a very simple lensing experiment: If one averages the lensing signal in patches of size angular size θ and if one derives the distribution of averaged weak lensing convergences, there will be a patch with the smallest lensing convergence and one with the largest convergence. If the underlying statistics of the convergence field exhibits non-Gaussianities from inflation, the occurrence of these extreme values of the lensing convergence will be different from those expected for a Gaussian random field. In this way, we aim to constrain non-Gaussianities not from the central part of the distribution by estimating moments but rather from the wings of the distribution by quantifying the occurence of extreme values. Because the proposed measurement is a one-point statistic, it suffers from averaging over all bi- and trispectrum configurations where sensitivity is lost, but we would like to investigate if the focus on the asymptotic behaviour of the distribution far away from the mean makes up for this loss. As the non-Gaussianity model we assume the most basic local non-Gaussianity shape, but it can in principle extended to other types of inflationary non-Gaussianity or structure formation non-Gaussianity.

After summarising the necessary cosmology background including the local model for non-Gaussianities in Sect. 8.2, we introduce the distribution of weak lensing convergence by means of a Gram-Charlier distribution in Sect. 8.3 and investigate the distribution of extreme values and quantify their sensitivity on the non-Gaussianity parameters. We summarise and discuss our results in Sect. 8.4.

We present all computations for a spatially flat wCDM cosmology, with the specific parameter choices motivated by the recent PLANCK-results (Planck Collaboration et al., 2013e): $\Omega_m = 0.3$, $n_s = 1$, $\sigma_8 = 0.8$, $\Omega_b = 0.04$ and $H_0 = 100h$km/s/Mpc, with $h = 0.7$. The dark energy equation of state was set to be $w = -0.95$. The non-Gaussianities due to inflation are taken to be of local type and described by the two non-Gaussianity parameters $f_{\rm NL}$ and $g_{\rm NL}$. We derive extreme value distributions for the case of the EUCLID weak lensing survey with a median redshift of 0.9 and a solid angle of $\Delta\Omega = 2\pi$ (Amara & Réfrégier, 2007; Refregier, 2009).

8.2 Cosmology

8.2.1 Dark energy cosmologies

In Friedmann-Lemaître cosmologies with zero curvature and the matter density parameter Ω_m, the Hubble function $H(a)$ is given by

$$\frac{H^2(a)}{H_0^2} = \frac{\Omega_m}{a^3} + (1-\Omega_m)\exp\left(3\int_a^1 \mathrm{d}\ln a\,(1+w(a))\right), \tag{8.1}$$

where $w(a)$ is the dark energy equation of state describing the ratio between pressure and density of the dark energy fluid. Comoving distances χ can be computed from the scale factor a by integration,

$$\chi = \int_a^1 \mathrm{d}a\,\frac{c}{a^2 H(a)}, \tag{8.2}$$

where the Hubble distance $\chi_H = c/H_0$ can be identified as the natural cosmological distance scale.

8.2.2 CDM power spectrum

The linear CDM density power spectrum $P(k)$ describes Gaussian fluctuations of the CDM-density field δ in Fourier space, $\langle\delta(\mathbf{k}_1)\delta(\mathbf{k}_2)\rangle = (2\pi)^3\delta_D(\mathbf{k}_1+\mathbf{k}_2)P(k_1)$ and this variance is diagonal if the fluctuation properties are homogeneous. Inflationary models suggest

$$P(k) \propto k^{n_s}T^2(k), \tag{8.3}$$

with the transfer function $T(k)$ and the spectral index n_s close to unity. $T(k)$ describes the passage of modes through horizon re-entry and is approximately given by Bardeen et al. (1986),

$$T(q) = \frac{\ln(1+2.34q)}{2.34q}\left(1+3.89q+(16.1q)^2+(5.46q)^3+(6.71q)^4\right)^{-\frac{1}{4}}, \tag{8.4}$$

if the matter density is low. In Eqn. (8.4), the wave vector $q = k/\Gamma$ is substituted in units of the shape parameter $\Gamma = \Omega_m h$. A nonzero baryon density causes a small correction to Γ (Sugiyama, 1995),

$$\Gamma = \Omega_m h\exp\left(-\Omega_b\left(1+\frac{\sqrt{2h}}{\Omega_m}\right)\right). \tag{8.5}$$

The normalisation of the spectrum $P(k)$ is taken to be the variance σ_8^2 on the scale $R = 8\,\mathrm{Mpc}/h$,

$$\sigma_R^2 = \int \frac{\mathrm{d}k}{2\pi^2}\,k^2P(k)W^2(kR) \tag{8.6}$$

with a Fourier transformed spherical top hat filter function, $W(x) = 3j_1(x)/x$. $j_\ell(x)$ is the spherical Bessel function of the first kind of order ℓ (Abramowitz & Stegun, 1972b).

Because the focus of this paper is on large-scale, inflationary non-Gaussianities, the time-evolution of all polyspectra can be predicted from linear structure formation, where $\delta(\mathbf{x}, a) = D_+(a)\delta(\mathbf{x}, a = 1)$. The linear growth function $D_+(a)$ is the growing-mode solution to the growth equation (Turner & White, 1997; Wang & Steinhardt, 1998; Linder & Jenkins, 2003),

$$\frac{\mathrm{d}^2 D_+(a)}{\mathrm{d}a^2} + \frac{1}{a}\left(3 + \frac{\mathrm{d}\ln H}{\mathrm{d}\ln a}\right)\frac{\mathrm{d}D_+(a)}{\mathrm{d}a} = \frac{3}{2a^2}\Omega_m(a)D_+(a). \tag{8.7}$$

which is applicable as long as non-linearities in the structure formation equations are weak. From the spectrum of the CDM density fluctuations one can construction the spectrum $P_\Phi(k)$ of the gravitational potential, $\langle\Phi(\mathbf{k}_1)\Phi(\mathbf{k}_2)\rangle = (2\pi)^3\delta_D(\mathbf{k}_1+\mathbf{k}_2)\,P_\Phi(k_1)$,

$$P_\Phi(k) = \left(\frac{3\Omega_m}{2\chi_H^2}\right)^2 k^{n_s-4}\,T(k)^2 \tag{8.8}$$

by application of the comoving Poisson equation $\Delta\Phi = 3\Omega_m/(2\chi_H^2)\delta$. We focus on large angular scales, where most of the lensing signal is generated by linear structures, and extend the CDM-spectrum to nonlinear scales in some cases, by employing a nonlinear transfer function derived by Smith et al. (2003).

8.2.3 Primordial non-Gaussianities

Non-Gaussianities of the local type are introduced as quadratic and cubic perturbations of the potential at a given point $\mathbf{x}$ (Gangui, 1994; Verde et al., 2000b; Komatsu & Spergel, 2001b),

$$\Phi(\mathbf{x}) \to \Phi(\mathbf{x}) + f_{\rm NL}\left(\Phi^2(\mathbf{x}) - \langle\Phi^2\rangle\right) + g_{\rm NL}\left(\Phi^3(\mathbf{x}) - 3\langle\Phi^2\rangle\Phi(\mathbf{x})\right), \tag{8.9}$$

with two parameters $f_{\rm NL}$ and $g_{\rm NL}$, which lead in Fourier-space to a bispectrum:

$$\langle\Phi(\mathbf{k}_1)\Phi(\mathbf{k}_2)\Phi(\mathbf{k}_3)\rangle = (2\pi)^3\delta_D(\mathbf{k}_1+\mathbf{k}_2+\mathbf{k}_3)\,B_\Phi(\mathbf{k}_1,\mathbf{k}_2,\mathbf{k}_3), \tag{8.10}$$

$$\begin{aligned} B_\Phi(\mathbf{k}_1,\mathbf{k}_2,\mathbf{k}_3) &= 2f_{\rm NL}\left(\frac{3\Omega_m}{2\chi_H^2}\right)^3 \left((k_1k_2)^{n_s-4} + (k_2k_3)^{n_s-4} + (k_1k_3)^{n_s-4}\right)\times \\ &\times\ T(k_1)T(k_2)T(k_3), \end{aligned} \tag{8.11}$$

and a corresponding trispectrum

$$\langle\Phi(\mathbf{k}_1)\Phi(\mathbf{k}_2)\Phi(\mathbf{k}_3)\Phi(\mathbf{k}_4)\rangle = (2\pi)^3\delta_D(\mathbf{k}_1+\mathbf{k}_2+\mathbf{k}_3+\mathbf{k}_4)\;T_\Phi(\mathbf{k}_1,\mathbf{k}_2,\mathbf{k}_3,\mathbf{k}_4), \tag{8.12}$$

$$\begin{aligned} T_\Phi(\mathbf{k}_1,\mathbf{k}_2,\mathbf{k}_3,\mathbf{k}_4) &= 6g_{\rm NL}\left(\frac{3\Omega_m}{2\chi_H^2}\right)^4 \times \\ &\times\ \left((k_1k_2k_3)^{n_s-4} + (k_1k_2k_4)^{n_s-4} + (k_1k_3k_4)^{n_s-4} + (k_2k_3k_4)^{n_s-4}\right)\times \\ &\times\ T(k_1)T(k_2)T(k_3)T(k_4). \end{aligned} \tag{8.13}$$

The normalisation of each mode $\Phi(\mathbf{k})$ is set to be consistent with the normalisation σ_8 of the CDM-spectrum $P(k)$.

8.2.4 Weak gravitational lensing

Weak gravitational lensing refers to the shape distortions of light bundles in their propagation through the tidal fields of the cosmic large-scale structure (see Bartelmann & Schneider, 2001, as a review). The lensing potential ψ is a projection of the gravitational potential Φ along the line of sight, $\psi = 2\int \mathrm{d}\chi\, W_\psi(\chi)\Phi$ with the weighting function $W_\psi(\chi)$,

$$W_\psi(\chi) = \frac{D_+(a)}{a}\frac{G(\chi)}{\chi}. \tag{8.14}$$

$G(\chi)$ is the lensing-efficiency weighted galaxy redshift distribution,

$$G(\chi) = \int_\chi^{\chi_H} \mathrm{d}\chi'\, p(\chi')\frac{\mathrm{d}z}{\mathrm{d}\chi'}\left(1-\frac{\chi}{\chi'}\right) \tag{8.15}$$

with $\mathrm{d}z/\mathrm{d}\chi' = H(\chi')/c$. For the redshift distribution $p(z)\mathrm{d}z$ we choose a standard parameterisation,

$$p(z)\mathrm{d}z = p_0\left(\frac{z}{z_0}\right)^2 \exp\left(-\left(\frac{z}{z_0}\right)^\beta\right)\mathrm{d}z \quad \text{with} \quad \frac{1}{p_0} = \frac{z_0}{\beta}\Gamma\left(\frac{3}{\beta}\right),. \tag{8.16}$$

The lensing observables follow from the lensing potential ψ by taking second derivatives $\psi' = \partial^2\psi/\partial\theta_i\partial\theta_j$ and contracting this tensor with the Pauli-matrices σ_α (Abramowitz & Stegun, 1972b). Specifically, the weak lensing convergence κ is given by $\kappa = \mathrm{tr}(\psi'\sigma_0)/2 = \Delta\psi/2$ and the two shear components $\gamma_+ = \mathrm{tr}(\psi'\sigma_1)/2$, $\gamma_\times = \mathrm{tr}(\psi'\sigma_3)/2$. Although the shear is the primary observable in weak lensing, we carry out our statistical investigations with the convergence as it has identical statistical properties and, being scalar, is easier to handle. For EUCLID, $z_0 \simeq 0.64$ such that the median redshift is 0.9.

8.2.5 Polyspectra of the weak lensing convergence

With the relation $\Delta\psi = 2\kappa$ is is straightforward to compute the angular spectrum $C_\kappa(\ell)$ of the weak lensing convergence from the spectrum $P_\Phi(k)$ of the gravitational potential,

$$C_\kappa(\ell) = \ell^4\int_0^{\chi_H}\frac{\mathrm{d}\chi}{\chi^2}\,W_\psi^2(\chi)P_\Phi(k) \tag{8.17}$$

by application of the Limber-equation (Limber, 1954). Generalisation of the Limber-projection and repeated substitution of $\kappa = \ell^2\psi/2$ yields for the convergence bispectrum $B_\kappa(\mathbf{L}_1,\mathbf{L}_2,\mathbf{L}_3)$,

$$B_\kappa(\mathbf{L}_1,\mathbf{L}_2,\mathbf{L}_3) = (\ell_1\ell_2\ell_3)^2\int_0^{\chi_H}\frac{\mathrm{d}\chi}{\chi^4}\,W_\psi^3(\chi)B_\Phi(\mathbf{k}_1,\mathbf{k}_2,\mathbf{k}_3) \tag{8.18}$$

and finally for the convergence trispectrum $T_\kappa(\mathbf{L}_1,\mathbf{L}_2,\mathbf{L}_3,\mathbf{L}_4)$,

$$T_\kappa(\mathbf{L}_1,\mathbf{L}_2,\mathbf{L}_3,\mathbf{L}_4) = (\ell_1\ell_2\ell_3\ell_4)^2\int_0^{\chi_H}\frac{\mathrm{d}\chi}{\chi^6}\,W_\psi^4(\chi)T_\Phi(\mathbf{k}_1,\mathbf{k}_2,\mathbf{k}_3,\mathbf{k}_4). \tag{8.19}$$

With these polyspectra it is then possible to derive cumulants of the convergence density field which can be smoothed on the angular scale θ by a function $W(\ell\theta)$, which we take to be Gaussian,

$$W(\ell\theta) = \exp\left(-\frac{(\ell\theta)^2}{2}\right). \tag{8.20}$$

Consequently, the variance σ^2 of the smoothed convergence field reads

$$\kappa_2 = \sigma^2 = \int \frac{\ell \mathrm{d}\ell}{2\pi}\, W(\ell\theta)^2\, C_\kappa(\ell), \tag{8.21}$$

which is equal to the second cumulant κ_2 of the distribution $p(\kappa)\mathrm{d}\kappa$. The third cumulant κ_3 then follows from integration of the smoothed bispectrum (Bernardeau et al., 2002b),

$$\kappa_3 = \int \frac{\mathrm{d}^2\ell_1}{(2\pi)^2} W(\ell_1\theta) \int \frac{\mathrm{d}^2\ell_2}{(2\pi)^2} W(\ell_2\theta) \int \frac{\mathrm{d}^2\ell_3}{(2\pi)^2} W(\ell_3\theta)\, B_\kappa(\mathbf{L}_1, \mathbf{L}_2, \mathbf{L}_3), \tag{8.22}$$

and lastly, the fourth cumulant κ_4 can be obtained in complete analogy with

$$\kappa_4 = \int \frac{\mathrm{d}^2\ell_1}{(2\pi)^2} W(\ell_1\theta) \int \frac{\mathrm{d}^2\ell_2}{(2\pi)^2} W(\ell_2\theta) \int \frac{\mathrm{d}^2\ell_3}{(2\pi)^2} W(\ell_3\theta) \int \frac{\mathrm{d}^2\ell_4}{(2\pi)^2} W(\ell_4\theta)\, T_\kappa(\mathbf{L}_1, \mathbf{L}_2, \mathbf{L}_3, \mathbf{L}_4). \tag{8.23}$$

The Gaussian cumulant $\kappa_2 = \sigma^2$, and the two non-Gaussian contributions $\kappa_3/f_{\rm NL}$ and $\kappa_4/g_{\rm NL}$ are depicted in Fig. 8.1 as a function of angular scale θ. Quite generally, the two non-Gaussian cumulants will be proportional to the non-Gaussianity parameters $f_{\rm NL}$ and $g_{\rm NL}$, and all cumulants are decreasing with smoothing scale, because the fluctuations are wiped out and the cumulants as an integrated measure of the fluctuation amplitude decrease. As emphasised by Jeong et al. (2011b), the non-Gaussianity in the observable is weakened due to the central limit theorem because in the line of sight integration many non-Gaussian values for the gravitaitonal potential are added that yield an approximately Gaussian result.

The cumulant κ_4 is very small for $\tau_{\rm NL}$-type non-Gaussianity, about three orders of magnitude less relative to that generated by $g_{\rm NL}$, which is the reason why we do not include it in the subsequent calculations. The reason of this behaviour derives from the fact that the weigthing functions $W(\ell_i\theta)$ downweight contributions from large multipoles ℓ_i. The integrations in Eqns. (8.22) and (8.23) needed for the cumulants κ_3 and κ_4 are carried out in polar coordinates with a Monte-Carlo scheme (specifically, with the CUBA-library by Hahn, 2005, who provides a range of adaptive Monte-Carlo integration algorithms), which reduces the computational complexity considerably.

8.3 Extreme value statistics

8.3.1 Gram-Charlier series

If a Gaussian distribution with zero mean and variance $\sigma^2 = \kappa_2$ is weakly perturbed by the presence of a non-vanishing third and fourth cumulant κ_3 and

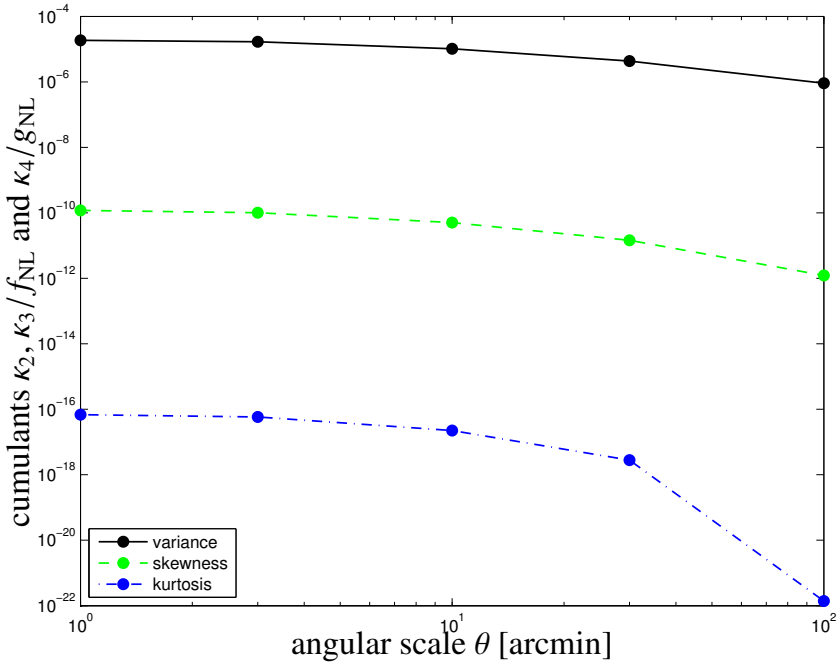

Figure 8.1: Cumulants κ_2, $\kappa_3/f_{\rm NL}$ and $\kappa_4/g_{\rm NL}$ as a function of angular scale θ for a Gaussian smoothing function $W(\ell\theta)$.

κ_4, respectively, the distribution $p(\kappa)\mathrm{d}\kappa$ can be approximated with the Gram-Charlier-series (see Wallace, 1958; Greenwood & Durand, 1955; Durand & Greenwood, 1957; Colombi, 1994; Juszkiewicz et al., 1995; Bernardeau et al., 2002b, who in addition quantify the limits of applicability of the expansion),

$$p(\kappa)\mathrm{d}\kappa = \frac{1}{\sqrt{2\pi\sigma^2}} \exp\left(-\frac{\kappa^2}{2\sigma^2}\right) \times \left[1 + \frac{\kappa_3}{3!\sigma^3} H_3\left(\frac{\kappa}{\sigma}\right) + \frac{\kappa_4}{4!\sigma^4} H_4\left(\frac{\kappa}{\sigma}\right)\right] \mathrm{d}\kappa \tag{8.24}$$

with the argument $x = \kappa/\sigma$ of the Hermite polynomials $H_n(x)$, which can be computed by n-fold differentiation of a Gaussian,

$$H_n\left(\frac{\kappa}{\sigma}\right) = (-\sigma)^n \exp\left(\frac{\kappa^2}{2\sigma^2}\right) \frac{\mathrm{d}^n}{\mathrm{d}\kappa^n} \exp\left(-\frac{\kappa^2}{2\sigma^2}\right). \tag{8.25}$$

It is worth noting that the perturbation of $p(\kappa)\mathrm{d}\kappa$ with H_3 and H_4 do not change the mean and the variance. Specifically, the Hermite-polynomials needed read (Abramowitz & Stegun, 1972b):

$$\begin{aligned} H_1(x) &= x, \quad H_2(x) = x^2 - 1, \\ H_3(x) &= x^3 - 3x, \quad H_4(x) = x^4 - 6x^2 + 3, \\ H_5(x) &= x^5 - 10x^3 + 15x. \end{aligned} \tag{8.26}$$

By substituting Eqn. (8.25) and integrating by parts the cumulative function $P(\kappa)$ of the Gram-Charlier-distribution $p(\kappa)\mathrm{d}\kappa$ can be written down analytically,

$$P(\kappa) = \int_{-\infty}^{\kappa} \mathrm{d}\kappa'\, p(\kappa') = \Phi\left(\frac{\kappa}{\sigma}\right) - \frac{1}{\sqrt{2\pi\sigma^2}} \exp\left(-\frac{\kappa^2}{2\sigma^2}\right) \left[\frac{\kappa_3}{3!\sigma^2} H_2\left(\frac{\kappa}{\sigma}\right) + \frac{\kappa_4}{4!\sigma^3} H_3\left(\frac{\kappa}{\sigma}\right)\right] \tag{8.27}$$

where the cumulative function $\Phi(\kappa/\sigma)$ of the Gaussian distribution is expressed in terms of the error function $\mathrm{erf}(\kappa/\sigma)$,

$$\Phi\left(\frac{\kappa}{\sigma}\right) = \frac{1}{2}\left(1 + \mathrm{erf}\left(\frac{\kappa}{\sqrt{2}\sigma}\right)\right), \tag{8.28}$$

as defined by Abramowitz & Stegun (1972b). By using the derivative relation

$$\frac{\mathrm{d}}{\mathrm{d}\kappa} H_n\left(\frac{\kappa}{\sigma}\right) = \frac{n}{\sigma} H_{n-1}\left(\frac{\kappa}{\sigma}\right) \tag{8.29}$$

of the Hermite polynomials $H_n(x)$, the derivative of the Gram-Charlier distribution takes the compact analytical form,

$$\frac{\mathrm{d}}{\mathrm{d}\kappa} p(\kappa) = -\frac{1}{\sqrt{2\pi\sigma^2}} \exp\left(-\frac{\kappa^2}{2\sigma^2}\right) \times \left[\frac{\kappa}{\sigma^2} + \frac{\kappa_3}{3!\sigma^4} H_4\left(\frac{\kappa}{\sigma}\right) + \frac{\kappa_4}{4!\sigma^5} H_5\left(\frac{\kappa}{\sigma}\right)\right]. \tag{8.30}$$

The moment generating function $M(k)$ can be computed analytically as well,

$$M(k) = \int \mathrm{d}\kappa\, \exp(k\kappa)\, p(\kappa) = \exp\left(\frac{\sigma^2 k^2}{2}\right) \times \left[1 + \frac{\kappa_3}{3!} k^3 + \frac{\kappa_4}{4!} k^4\right], \tag{8.31}$$

from which the moments of order n can be obtained by n-fold differentiation and setting k to zero. We would like to add that the Gram-Charlier expansion in Eqn. (8.24) is only applicable for weak non-Gaussianities in which $\kappa_3 \ll \sigma^3$ and $\kappa_4 \ll \sigma^4$, because otherwise the Hermite-polynomials could cause negative values for $p(\kappa)\mathrm{d}\kappa$. The regime of weak non-Gaussianity in the weak lensing signal would be left if $f_{\rm NL} \gtrsim 10^4$ and $g_{\rm NL} \gtrsim 10^8$, depending on angular scale.

8.3.2 Number of samples

We compute an estimate of the number N of samples from the correlation function $C_\kappa(\beta)$ of the convergence field κ that has been smoothed on the scale θ,

$$C_\kappa(\beta) = \int \frac{\ell \mathrm{d}\ell}{2\pi} W(\ell\theta)^2 C_\kappa(\ell)\, J_0(\ell\beta), \tag{8.32}$$

which is depicted in Fig. 8.2 for a range of smoothing scales and for a Gaussian window function $W(\ell\theta) = \exp(-(\ell\theta)/2)$. The correlation function allows us to define a correlation length β at which the value of $C_\kappa(\beta)$ has dropped to a fraction $\exp(-1)$ of its value at zero lag, $C_\kappa(\beta = 0) = \sigma^2 = \kappa_2$. The number of samples N can then be estimated with the relation $N \times \pi\beta^2 = 4\pi f_{\rm sky}$, i.e. the number of patches of area $\pi\beta^2$ that could be fitted in the survey solid angle. In this approximated picture, the smoothed random field is taken to assume independent values κ in patches of size β. The number of available samples N as a function of smoothing scale θ is given in Fig. 8.3, where we consider the case of the EUCLID mission with the sky fraction $f_{\rm sky} = 1/2$: N drops from $\simeq 4 \times 10^4$ if there is hardly any smoothing at $\theta = 1$ arcmin to a few hundred if a strong smoothing on the scale $\theta = 100$ arcmin is applied.

We choose the smoothing scale $\theta = 10$ arcmin for the subsequent analysis in order to have sufficiently interesting sample sizes while avoiding a possible strong contamination from non-Gaussianities that evolve in nonlinear structure formation. Fig. 10 contained in Appendix A compares smoothed convergence spectra resulting from linear and nonlinear CDM-spectra and we found a contamination of the variance σ^2 amounting to $\simeq 7\%$ at $\theta = 10$ arcmin, compared to $\simeq 1\%$ at $\theta = 30$ arcmin and $\simeq 18\%$ at $\theta = 3$ arcmin.

We would like to point out that in drawing extreme values it would be incorrect to generate a vector of N random deviates for κ and identify in this vector the largest and smallest sample. Instead, one needs to carry out the numerical experiment for finding the largest and the smallest sample separately. The reason for this is the fact that samples for extreme values are compared to each other for finding the extrema, and for this process N samples are needed, which must not be reused as would be the case in the first approach: Each time a new value is drawn, it must be given the chance (and hence probability) of being larger than the current maximum but at the same time smaller than the current minimum. Therefore, every time a new value is drawn, the comparison with the current largest value and the comparison with the smallest one must be separate

processes. The importance of this separation can be clearly seen when considering the very first value which is drawn, since this value is at the same time the largest and the smallest one. This actually also reduces the effective number of samples by 1.

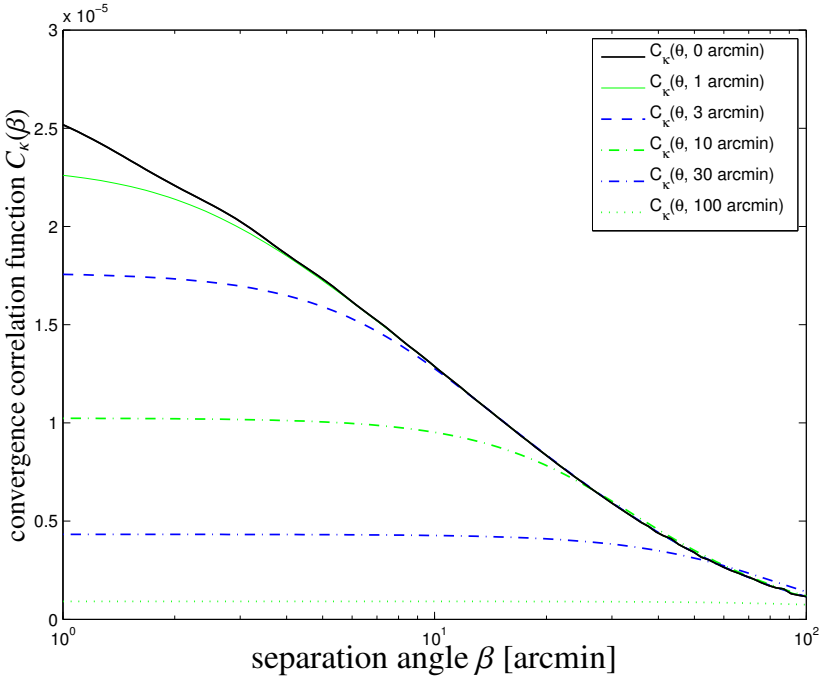

Figure 8.2: The angular correlation function $C_\kappa(\beta)$ is shown as a function of separation angle β (black solid line) and for a range of smoothing scales, $\theta = 1, 3, 10, 30, 100$ arcmin, for a Gaussian filter.

8.3.3 Sampling from the Gram-Charlier distribution

With the analytical form Eqn. (8.27) of the cumulative distribution $P(\kappa)$ it is possible to sample from the Gram-Charlier-distribution $p(\kappa)\mathrm{d}\kappa$ by using its invertibility: From a sample y of the uniform distribution from the unit interval one can obtain a sample of κ by setting $\kappa = P^{-1}(y)$. This inverse always exists because $P(\kappa)$ as an integral of a positive function is monotonically increasing and therefore invertible. Likewise, samples from the extreme value distributions can be generated by drawing N random numbers from the uniform distribution, and by mapping the largest (and the smallest) of those samples onto κ. Because the cumulative distribution $P(\kappa)$ is monotonic, the largest sample of y will be converted to the largest value in κ, and likewise the smallest sample of y will be the smallest κ-value. This approach has advantages over direct sampling from

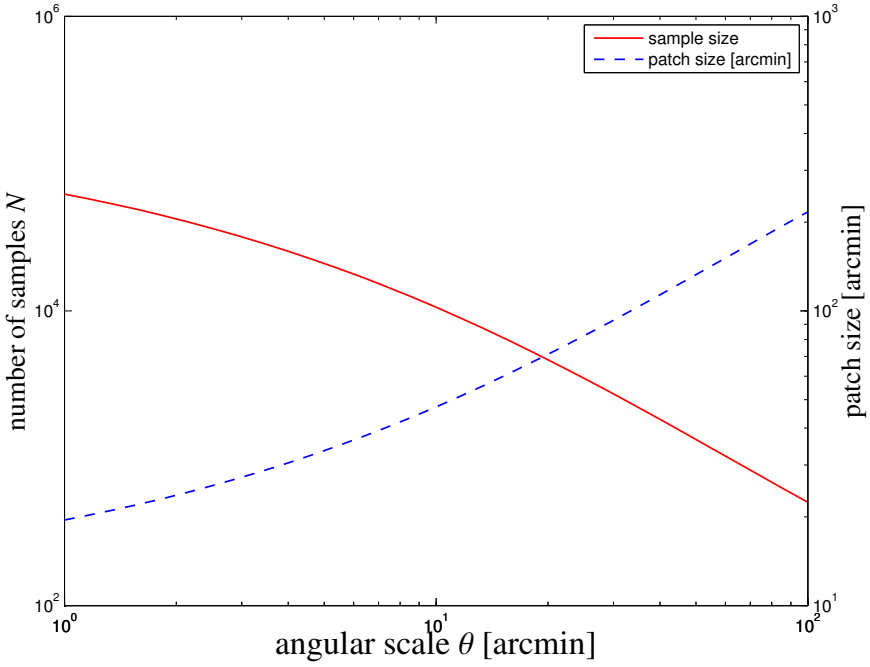

Figure 8.3: Sample size N as a function of smoothing scale θ employed in calculating the cumulants κ_n, $n = 2,3,4$. The sample size is computed from the angular scale at which the correlation function drops to a fraction of $\exp(-1)$ of its value at zero lag.

the Gram-Charlier distribution and finding the extrema, because the inversion $y \to \kappa$ has to be carried out only once.

8.3.4 Extreme value distributions

The reasoning behind extreme value distributions is very instructive (Gumbel, 1954, 2004): The cumulative distribution $P(\kappa)$ gives the probability that a sample is drawn with a value $< \kappa$, and consequently $P(\kappa)^N$ indicates the probability that N independent samples are all smaller than κ. The probability of the complementary event, i.e. that at least a single one of the samples is larger than κ would then be given by $P_+(\kappa) = 1 - P(\kappa)^N$. Differentiation yields the distribution $p_+(\kappa)\mathrm{d}\kappa$ of the maximum values drawn from $p(\kappa)\mathrm{d}\kappa$ in N trials:

$$p_+(\kappa) = \frac{\mathrm{d}}{\mathrm{d}\kappa} P_+(\kappa) = N P(\kappa)^{N-1} p(\kappa), \tag{8.33}$$

which can be computed analytically with Eqns. (8.24) and (8.27). The argumentation for the smallest samples proceeds in complete analogy: Again, the cumulative distribution $1 - P(\kappa)$ states the probability that a sample is $> \kappa$, and the probability that N independent samples are all larger than κ would be given by $(1 - P(\kappa))^N$. The complementary case of a single sample being smaller than κ is computed with $P_-(\kappa) = 1 - (1 - P(\kappa))^N$, which can be differentiated to get the extreme value distribution $p_-(\kappa)\mathrm{d}\kappa$ of the minimum obtained in N draws,

$$p_-(\kappa) = \frac{\mathrm{d}}{\mathrm{d}\kappa} P_-(\kappa) = N(1 - P(\kappa))^{N-1} p(\kappa) \tag{8.34}$$

By the derivation of the extreme value distribution $p_\pm(\kappa)\mathrm{d}\kappa$ as the N-fold exponentiation of the cumulative function $P(\kappa)$ the distribution acquires naturally a strong sensitivity on the asymptotic behaviour of the distribution $p(\kappa)\mathrm{d}\kappa$. In our case, the distribution will be influenced by the presence of a non-vanishing third and fourth cumulant are sourced by the three lowest-order inflationary non-Gaussianity parameters f_{NL} and g_{NL}. Local non-Gaussianity from the τ_{NL}-term influences κ_4 only weakly and will be neglected in the analysis.

The Gram-Charlier distribution $p(\kappa)\mathrm{d}\kappa$ along with the two extreme value distributions $p_\pm(\kappa)\mathrm{d}\kappa$ are shown for $f_{\mathrm{NL}} = 30$ and for $\theta = 10$ arcmin (corresponding to $N = 10597$ on EUCLID's survey cone) in Fig. 8.4. While there is a very small asymmetry in the distribution $p(\kappa)\mathrm{d}\kappa$ of the convergences themselves, the skewness introduced by f_{NL} gives rise to a much larger asymmetry in the extreme value distributions $p_\pm(\kappa)\mathrm{d}\kappa$. Positive f_{NL} skew the distribution in the direction of positive values, making large maxima more likely and large minima less likely. The samples for the Gram-Charlier distribution and the direct sampling of the extreme value distributions corresponds very well to the analytical expressions. Even without the influence of non-Gaussianities one sees that values as large as $\kappa = 0.012$ are the most likely to be expected for the sample size, corresponding to random events at a distance of $\simeq 3.4\sigma$ away from the mean

at zero. Extreme value of that magnitude are consistent with the fact that with $N \simeq 10^4$ samples it is possible to probe the wings of the Gaussian distribution at probabilities of $\mathrm{erfc}(3.4/\sqrt{2}) \simeq 6 \times 10^{-4}$.

Fig. 8.5 shows the Gram-Charlier distribution $p(\kappa)\mathrm{d}\kappa$ with the two corresponding extreme value distributions $p_\pm(\kappa)\mathrm{d}\kappa$ with $g_{\mathrm{NL}} = 3 \times 10^5$ and on an angular scale $\theta = 10$ arcmin. Introducing a positive kurtosis into the distribution is difficult to see in the distribution itself, but makes large extremes much more likely. Overall, the sensitivity of the extreme values to a non-Gaussian kurtosis is much weaker compared to that of a non-Gaussian skewness, and there is a very good correspondence between the sampled distributions and the analytical expressions.

8.3.5 Posterior statistics of the Gram-Charlier distribution

In this section we investigate the properties of the extreme value distributions $p_\pm(\kappa)\mathrm{d}\kappa$ in more detail by deriving its average, its most likely value and its median and by relating its first moments to the standard parameters of the Gumbel distribution. We focus on particular on the position of the extreme value distribution as a function of smoothing θ which influences both the magnitudes of the cumulants κ_n as well as the number of samples N, which is the dominating quantity. As seen in the two previous plots, the extreme value statistics generates a much stronger difference between extreme values from small differences in the parent distributions.

The average $\bar{\kappa}_\pm$ of the extreme value distribution $p_\pm(\kappa)\mathrm{d}\kappa$ is given by

$$\bar{\kappa}_\pm = \int \mathrm{d}\kappa\, \kappa\, p_\pm(\kappa). \tag{8.35}$$

The most likely value $\hat{\kappa}_\pm$ follows from solving:

$$\frac{\mathrm{d}}{\mathrm{d}\kappa} p_\pm(\kappa) = 0, \tag{8.36}$$

where the analytical form eqn. (8.30) of the derivative $\mathrm{d}p(\kappa)/\mathrm{d}\kappa$ is particularly useful. Likewise, the median $\tilde{\kappa}_\pm$ can be computed by solving

$$P_\pm(\kappa) = \frac{1}{2}. \tag{8.37}$$

Figs. 8.6 and 8.7 give an impression of how fast the extreme value distribution shifts away from the parent distribution if the smoothing scale θ is varied, due to changes in the cumulants κ_n and the number of available samples N, the latter being the driving factor, as mentioned previously. As already apparent from Figs. 8.4 and 8.5, a nonzero positive f_{NL} skews the distribution and shifts the maximum distribution $p_+(\kappa)\mathrm{d}\kappa$ towards larger values and the minimum distribution $p_-(\kappa\mathrm{d}\kappa)$ towards less negative values. Non-zero g_{NL} causes larger absolute values for both $p_+(\kappa)\mathrm{d}\kappa$ and $p_-(\kappa)\mathrm{d}\kappa$. As expected for a unimodal distribution, the means $\bar{\kappa}_\pm$, the most likely values $\hat{\kappa}_\pm$ and the median values $\tilde{\kappa}_\pm$ show

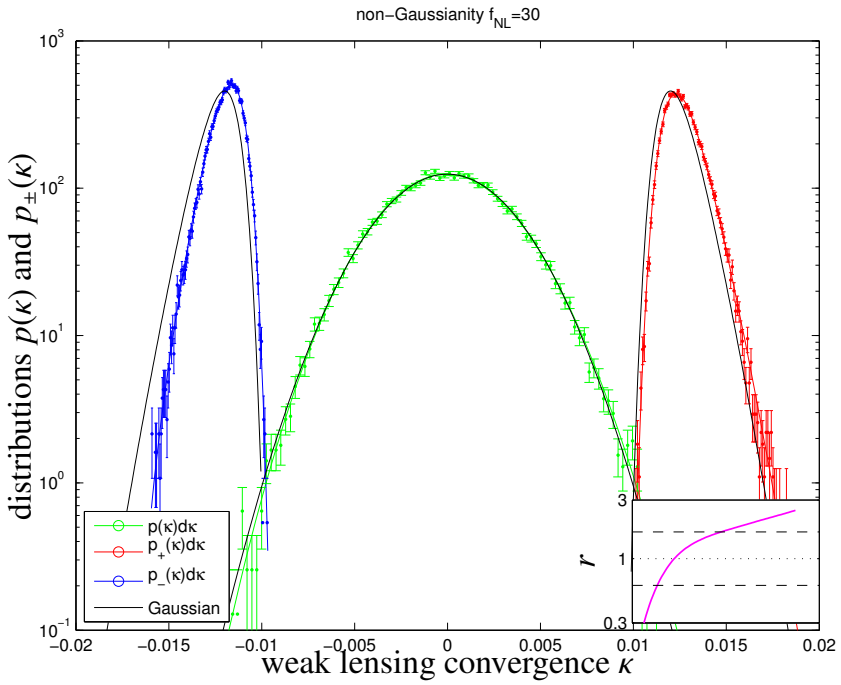

Figure 8.4: Gram-Charlier distribution $p(\kappa)\mathrm{d}\kappa$ and the two extreme value distributions $p_{\pm}(\kappa)\mathrm{d}\kappa$ with the non-Gaussianity parameters $f_{\mathrm{NL}} = 30$ and $g_{\mathrm{NL}} = 0$ on the angular scale $\theta = 10$ arcmin, with a yield of $N = 10597$ samples. Additionally, we show show samples from the Gram-Charlier distribution $p(\kappa)\mathrm{d}\kappa$ including Poissonian errors and the two extreme value distributions $p_{\pm}(\kappa)\mathrm{d}\kappa$ for the Gaussian reference model. The inset figure shows the ratio of the extreme value distributions $p_{+}(\kappa)\mathrm{d}\kappa$ between the Gaussian and the non-Gaussian model, with varying κ along with lines marking the ratios $\exp(\pm 1/2)$ indicating an equivalent 1σ change in likelihood.

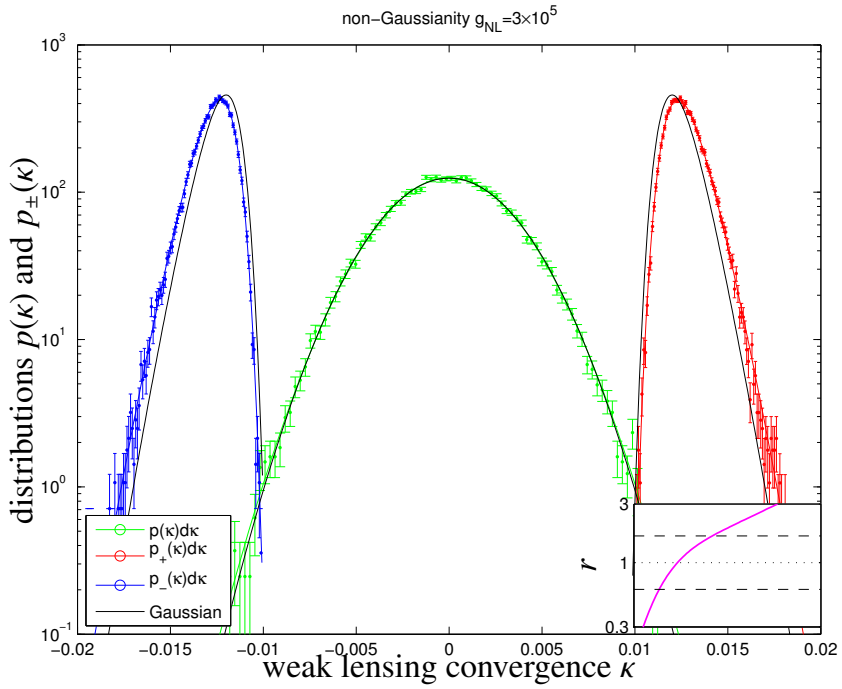

Figure 8.5: Gram-Charlier distribution $p(\kappa)\mathrm{d}\kappa$ and the two extreme value distributions $p_{\pm}(\kappa)\mathrm{d}\kappa$ with the non-Gaussianity parameters $g_{\mathrm{NL}} = 3\times10^5$ and $f_{\mathrm{NL}} = 0$ on the angular scale $\theta = 10$ arcmin, yielding $N = 10597$ samples. Additionally, we show show samples from the Gram-Charlier distribution $p(\kappa)\mathrm{d}\kappa$ including Poissonian errors and the two extreme value distributions $p_{\pm}(\kappa)\mathrm{d}\kappa$ for the Gaussian reference model. The inset gives the ratio between the extreme value distributions $p_{+}(\kappa)\mathrm{d}\kappa$ for the Gaussian and the non-Gaussian parent distribution $p(\kappa)\mathrm{d}\kappa$, with lines indicating the ratios $\exp(\pm1/2)$, which corresponds to a 1σ change in likelihood.

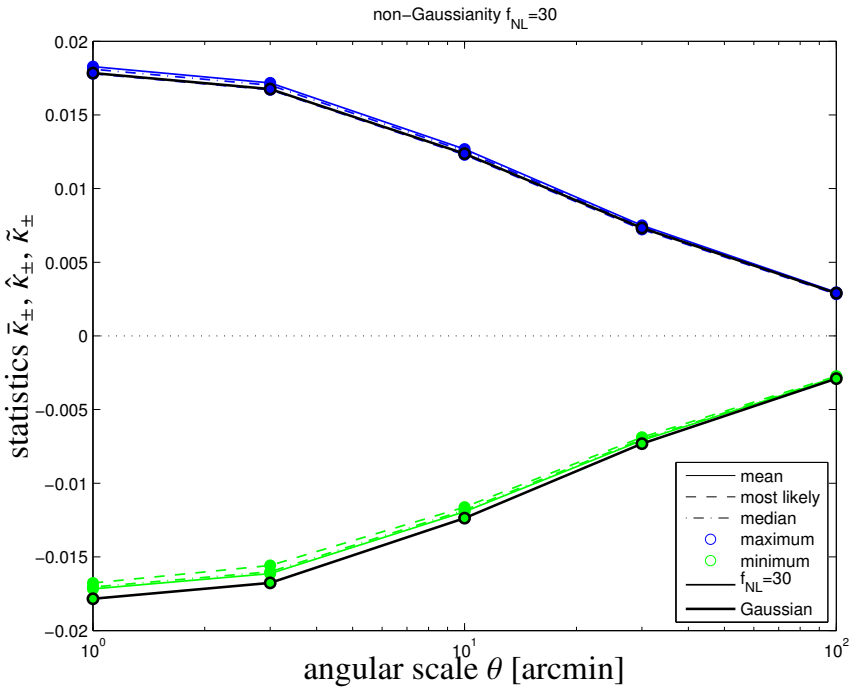

Figure 8.6: The mean value $\bar{\kappa}_\pm$, the most likely value $\hat{\kappa}_\pm$ and the median $\tilde{\kappa}_\pm$ of the extreme value distribution $p_\pm(\kappa)\mathrm{d}\kappa$ for a non-Gaussian model with $f_{\rm NL} = 30$ and $g_{\rm NL} = 0$ in comparison to a Gaussian model, as a function of angular scale θ.

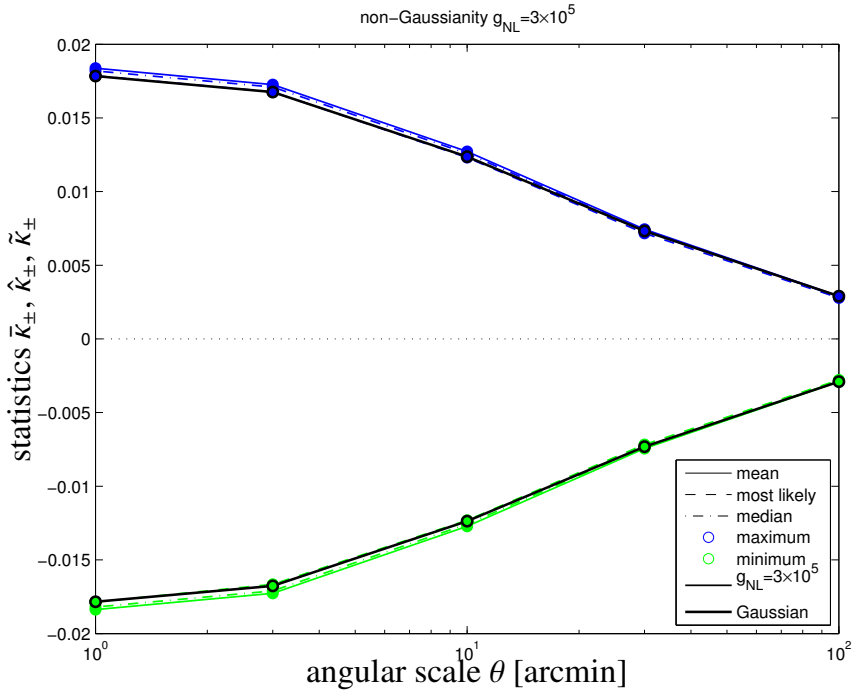

Figure 8.7: The median value $\bar{\kappa}_\pm$, the most likely value $\hat{\kappa}_\pm$ and the median $\tilde{\kappa}_\pm$ of the extreme value distribution $p_\pm(\kappa)\mathrm{d}\kappa$ for a non-Gaussian model with $g_{\rm NL} = 3\times10^5$ and $f_{\rm NL} = 0$ in comparison to a Gaussian model, as a function of angular smoothing scale θ.

a very similar behaviour. In both cases, the position of the extreme value distribution tends towards zero with increasing smoothing scale θ, which reduces the sample number N as well as the numerical value of all cumulants.

8.3.6 Relation to the Gumbel-distribution

The parameters μ and β of the standard Gumbel distribution can be derived from the mean and the variance of $p_{\pm}(\kappa)\mathrm{d}\kappa$,

$$\frac{\beta^2\pi^2}{6} = \int \mathrm{d}\kappa\,\kappa^2 p_{\pm}(\kappa) \quad \text{and} \quad \mu+\gamma\beta = \int \mathrm{d}\kappa\,\kappa\, p_{\pm}(\kappa). \tag{8.38}$$

with the Euler-Mascheroni-constant, $\gamma \simeq 0.57721$ (Abramowitz & Stegun, 1972b). One naturally recovers the shape of the Gumbel distribution in the limit of large N which can be seen from the cumulative distribution $P_+(\kappa) = P^N(\kappa) = \exp\left(N\ln P(\kappa)\right) = \exp\left(N\ln\left(1-(1-P(\kappa))\right)\right) \simeq \exp\left(-N(1-P(\kappa))\right)$ applying a Taylor expansion of the logarithm in the last step. Substituting the Gaussian distribution $p(\kappa)/\kappa$ as a approximation for $1-P(\kappa)$ for large κ one obtains the Gumbel distribution $P_+(\kappa) \simeq \exp(-N/\kappa\,\exp(-\kappa^2/(2\sigma^2)))$ (Gumbel, 2004).

Fig. 8.8 illustrates the variation of the two parameters μ and β with angular scale if the Gaussian distribution is approximated with an extreme value distribution of the Gumbel-shape. Clearly, the position of the mean value distribution described by μ decreases if the sample number and the variance of the parent distribution decrease, and the same argument applies to the width of the extreme value distribution. Because the perturbation with Hermite polynomials in the Gram-Charlier distribution does not introduce a different asymptotic behaviour than that of a Gaussian distribution, the extreme value distribution is of approximate Gumbel-shape and weak non-Gaussianities do not affect the general shape of the extreme value distribution.

8.3.7 Inference from extreme values

Although extreme value statistics seems to be applicable in situations where models are excluded because they might be implausible in generating a certain observed extreme value, they can in fact it can be used for parameter inference, e.g. for the non-Gaussianity parameters f_{NL} and g_{NL}: When observing a certain extreme value κ, one can consider the distribution $p_{\pm}(\kappa|f_{\mathrm{NL}})$ with its dependence on the parameter set f_{NL} as a likelihood, and compare different likelihoods by their ratio r,

$$r(\kappa, f_{\mathrm{NL}}) = \frac{p_{\pm}(\kappa|f_{\mathrm{NL}})}{p_{\pm}(\kappa|f_{\mathrm{NL}}=0)} \quad \text{or} \quad r(\kappa, g_{\mathrm{NL}}) = \frac{p_{\pm}(\kappa|g_{\mathrm{NL}})}{p_{\pm}(\kappa|g_{\mathrm{NL}}=0)}, \tag{8.39}$$

which, according to the Neyman-Pearson lemma, is the most effective test for distinguishing the likelihoods that certain parameter choices provide an explanation of the data, i.e. the observed extreme value κ in our case. The likelihood

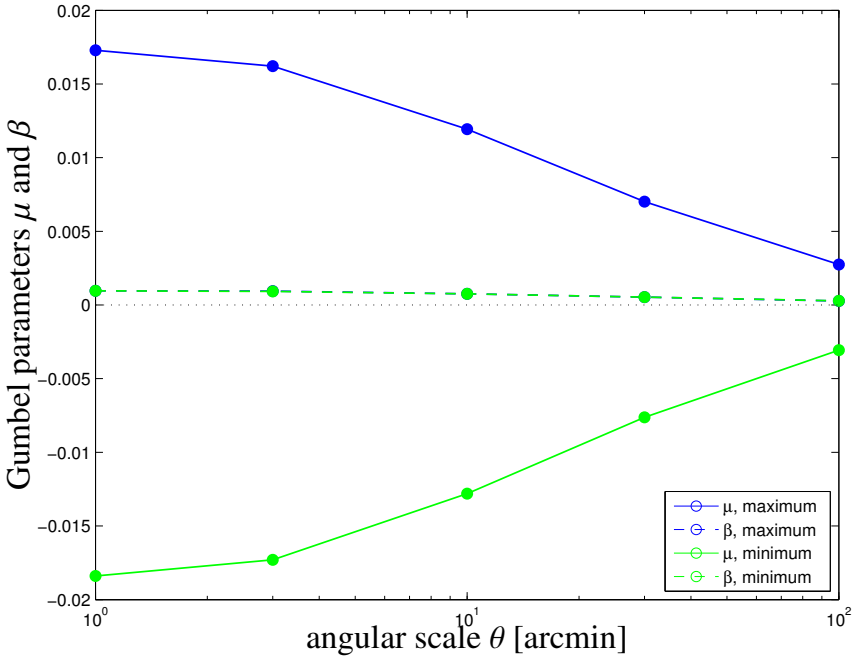

Figure 8.8: Gumbel parameters μ and β for the extreme value distributions $p_{\pm}(\kappa)\mathrm{d}\kappa$ resulting from a Gaussian parent distribution $p(\kappa)\mathrm{d}\kappa$, as a function of angular scale θ.

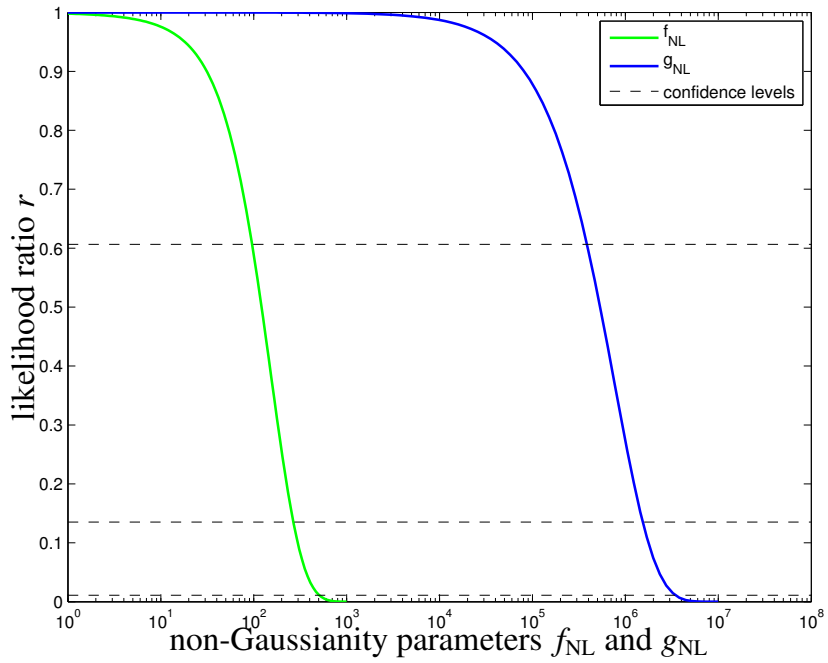

Figure 8.9: Likelihood ratios r for varying $f_{\rm NL}$ (green line) and $g_{\rm NL}$ (blue line) evaluated at the most likely maximum value obtained in the Gaussian reference model with $f_{\rm NL} = g_{\rm NL} = 0$. The angular smoothing scale is set to 10 arcmin, resulting in $N = 10597$ samples. The horizontal lines indicate confidence levels corresponding to $n\sigma$, $n = 1,2,3$.

ratios $r(f_{\rm NL})$ and $r(g_{\rm NL})$ in our example would quantify the plausibility of a cosmological model with nonzero non-Gaussianities $f_{\rm NL}$ or $g_{\rm NL}$ relative to a purely Gaussian fiducial model in providing an explanation to an observed extreme value.

The insets in Figs. 8.4 and 8.5 show the likelihood ratios r as a function of κ between the extreme value distributions from the non-Gaussian and the Gaussian model. For weak non-Gaussianities, the likelihood ratio r as a function of κ assumes values close to unity if the extreme sample is close to the most likely sample for a particular Gram-Charlier-distribution but would assumes values differing significantly from one if the sample is much larger or smaller than the most likely value.

Fig. 8.9 shows the likelihood ratios r as a function of either $f_{\rm NL}$ or $g_{\rm NL}$ if the reference model is Gaussian with $f_{\rm NL} = g_{\rm NL} = 0$. We choose to evaluate the likelihood ratio for a value of κ that occurs in the random experiment with the highest probability, i.e. the most likely value $\hat{\kappa}$ derived with Eqn. (8.36) for $p_+(\kappa)\mathrm{d}\kappa$. We

focus on the maximum value of the convergence $\hat{\kappa}_+$ which can be computed analytically for the Gram-Charlier-distribution. The choice of $\hat{\kappa}_\pm$ for estimating the width of the likelihood corresponds to the average $\langle\chi^2\rangle$ of the χ^2-functional in conventional fits for unbiased models. In this sense, we are attempting to carry out a fit with a single measurement and estimate the precision of the parameter inference from that single measurement. Fig. 8.9 suggests constraints of the order $\Delta f_{\rm NL} \simeq 10^2$ and $\Delta g_{\rm NL} \simeq 10^5$ from extreme value statistics, i.e. an observation of the single extreme value for such a non-Gaussianity would be incompatible with a Gaussian parent distribution.

We conclude similarly to Mikelsons et al. (2009); Chongchitnan & Silk (2012) that the extreme values are not competitive in their sensitivity to weak non-Gaussianities, at least for typical extrema, even though the simplicity of the measurement could be attractive. While extreme values of the lensing convergence might provide a consistency check for constraints on $f_{\rm NL}$, their very weak sensitivity on $g_{\rm NL}$ makes it doubtful if meaningful constraints on primordial trispectra can be derived from extreme value statistics, even less so for $\tau_{\rm NL}$-type non-Gaussianity. By running a direct estimate of the primordial bispectrum in a non-tomographic setup very similar constraints on $f_{\rm NL}$ of $\sim 10^2$ are within reach with EUCLID (Schäfer et al., 2012b), and corresponding constraints on $g_{\rm NL}$ are of the order of $\sim 10^5$, while these values can be improved substantially by lensing tomography. In comparison, large-scale structure probes other than lensing are able to provide constraints close to order unity on $f_{\rm NL}$, likewise the cosmic microwave background.

8.4 Summary

Subject of this paper is the extreme value statistics of the weak lensing convergence in the presence of primordial inflationary non-Gaussianities. We would like to answer the question if the most extreme values of the weak lensing convergence averaged in apertures of a certain angular size is indicative of the non-Gaussianity parameters $f_{\rm NL}$ and $g_{\rm NL}$ in a basic local non-Gaussianity model.

1. For this purpose, we perturb a Gaussian distribution for the lensing convergence with Hermite polynomials whose amplitudes are the cumulants of third and fourth order, i.e. with a Gram-Charlier series. These two cumulants are proportional to the parameters $f_{\rm NL}$ and $g_{\rm NL}$ and are computed from the local non-Gaussianity bi- and trispectra in a configuration space integration for which we use a very efficient adaptive Monte-Carlo integration. For investigating the dependence on angular scale, we introduce a Gaussian smoothing into the polyspectra and we find all cumulants to be decreasing functions with smoothign scale. We made sure that the smoothing is sufficiently strong such that small-scale structure formation non-Gaussianities have a small impact on the cumulants. The $\tau_{\rm NL}$-term provides a much smaller contribution to the weak lensing trispectrum in

comparison to the $g_{\rm NL}$-part and for that reason we neglect it in our investigation.

2. The Gram-Charlier distribution has the convenient property of analytical expressions for the cumulative distribution, the derivative of the distribution and the moment-generating function. We provide analytical expressions for the extreme value distributions for drawing N samples, which alleviates the usage of the generic Gumbel-distribution which would be recovered in the limit of large N. In EUCLID's weak lensing survey one can expect individual extreme values of the weak lensing convergence of a percent on the scale $\theta = 10$ arcmin. If Gaussian statistics is assumed, the most likely extreme value differs from the mean by $\simeq 3.4\sigma$.

3. We propose an efficient sampling scheme for drawing Gram-Charlier distributed random numbers based on drawing uniformly distributed numbers from the unit interval and determining the extremes of this distribution before mapping it onto the weak lensing convergence with the inverse of the cumulative distribution $P(\kappa)$. We verified the correspondence between analytical results and samples from the extreme value distribution and found excellent agreement. The number of samples is estimated from the correlation length of the random field, where we make estimate the correlation length of the field by requiring that the correlation function has dropped to a fraction of $\exp(-1)$ from its value at zero lag and by tiling the survey area with circular patches of this size.

4. We investigated the sensitivity of extreme value distributions on constraining inflationary non-Gaussianity parameters. While non-Gaussianities change the parent distribution only weakly, the difference between a non-Gaussian and a Gaussian model is amplified in the extreme value distribution.

5. We characterised the extreme value distribution and related it to the generic shape of the Gumbel-distribution, which is always recovered in the case of large sample numbers for a unrestricted random process. The mean value, the most likely value and the median of the extreme value distribution reflect the non-Gaussianity in the parent distribution and decrease with stronger smoothing because of two reasons: firstly, the cumulants decrease in value of a stronger smoothing is applied, and secondly, the number of available samples decreases because the correlation length of the convergence field increases.

6. By considering the likelihood ratio between the hypothesis that a non-Gaussian distribution provides and explanation of an extreme value compared to the null-hypothesis of a Gaussian parent distribution we show that individual extreme values can provide constraints on $f_{\rm NL}$ of the order 10^2 and on $g_{\rm NL}$ of the order 10^5. One can expect a significant improvement

in these constraints if the sequence of the nth largest extrema is considered, similarly to Waizmann et al. (2012b) for the observation of massive clusters of galaxies. Due to the smallness of the contribution of the $\tau_{\rm NL}$-term to the fourth cumulant κ_4 we did not derive a limit on $\tau_{\rm NL}$.

In summary we would like to point out the simplicity of the statistical inference from weak lensing extreme values. We are in the process of extending our studies for the related case of structure formation non-Gaussianities, where an effective description of the convergence field with the lognormal distribution is applicable, and to the case of non-zero covariances between individual samples (as an application of the formalism by Bertin & Clusel, 2006).

Conclusions

Cornerstone of this thesis is the weak lensing, a statistical tool which has become, in the last two decades, of paramount importance, mostly due to its ability of providing a direct measurement of the mass distribution without any need of invoking secondary intermediate assumptions such as the link between baryonic and dark matter nor between brightness and mass.

Objects of this thesis are two analyses departing from the different considerations on the weak lensing. On one side measurements of weak lensing are hampered by the contamination induced by intrinsic alignments (IA), physical phenomenon able to mimic the weak lensing signal by producing correlations between shapes of close-by galaxies due to similar conditions intervening in their formation processes. On the other weak lensing is expected to inherit the statistical properties of the density field to it associated, and therefore any departure from the initial Gaussian distribution of the primordial fluctuations throughout the history of the Universe must also be imprinted in the consequent weak lensing convergence distribution.

Intrinsic Alignments: The study of intrinsic alignments appears nowadays to stand on two complementary aspects, and to be necessary and compelling at the same time. On the one hand, in fact, it appears fundamental to approach to a better understanding of IA in the context of weak lensing, because we face an epoch of extraordinary increasingly detailed measurements, which are able to provide stringent constraints on parameters and hence ask for more precise modelling from the theoretical side. On the other, intrinsic alignments contain a wealth of encoded information that could possibly lead us to a better understanding of the physics of galaxy and structure formation. In this direction possibilities of retrieving the potential field and hence reconstructing the matter distribution appear to be interesting and important goals which must be supported, again, by a thorough theoretical framework.

A great deal of effort is being put right now by the scientific community in studying possible and viable ways to suppress of intrinsic alignments regardless of the information they might encode in order to cleanse the spurious signal for weak lensing. This effort is mostly concentrated on decontaminating the shear signal from the GI alignments, whereas the II contribution to the ellipticity cor-

relation seems to be more easy to discriminate in general, and even more in upcoming surveys, where photometric redshifts allow to recognise neighbouring pairs of galaxies, which can then be simply discarded from the analysis. Of course this procedure increases the shot noise by decreasing the average number of galaxies.

Our analysis, in this sense, stands in the crossroads between the two basic approaches used in literature. It is, in fact, subordinated to weak lensing, but at the same time it preserves a rigorous physical approach, which is often moved to the background in other studies of IA applied to weak lensing, in favour of simpler descriptions.

In this work we have focused on intrinsic alignments of II type for late-type galaxies applied to upcoming surveys such as EUCLID. We have modelled the IA by means of the ellipticity spectra $C_E^\epsilon(\ell)$ and $C_B^\epsilon(\ell)$ by using two forms of the quadratic model proposed in literature: the CNPT and the MWK models, which are both based on the TTT but differ in the hypotheses they make. The CNPT model is more precise in the description of the intercorrelations between inertia and tidal shear tensor eigensystems, parametrizing it by means of the misalignment parameter a. MWK, instead, assume that inertia and shear tensor are completely independent. For both the basic assumption is made that the angular momentum is perpendicular to the disk of the galaxy, and thus correlations between angular momenta moulded by the tidal shear are reflected in the correlations between shapes of galaxies. Furthermore, only the direction of the spin is important for the goal of studying intrinsic correlations. We forecasted how the cosmological parameters can be affected by a modelling of the shear signal which neglects the contribution of IA for a wCDM cosmology. It is important to notice that GI alignments in quadratic models automatically vanish, justifying our restriction to II alignments. We used a Fisher matrix approach to compute the biases on the cosmological parameters. Our findings can be summarised as follows:

- we computed the ellipticity spectra $C_E^\epsilon(\ell)$ and $C_B^\epsilon(\ell)$ for multipoles in the range $10 \leq \ell \leq 3000$. As expected, the ellipticity spectra show a peak at large values of ℓ, i.e. small scales, where the intrinsic correlations among close galaxies are present.

- we calculated the biases as the difference, in parameter space, between the best fit values associated with the χ^2-functionals for the true and false models (corresponding respectively to the cases of including and not including IA): A link between these values can be made by Taylor-expanding the χ_f^2-functional for the false model around the best fit parameters $\mathbf{x}_t$ of the true model;

- the most affected parameters appear to be Ω_m and σ_8, by an amount $\gtrsim 3\sigma$: This can be explained by considering the fact that the convergence spectrum mostly depends on these parameters, and thus any difference in how the convergence signal is modelled will tend to compensate by shifting the values of

these parameters.

- Differently from other analyses we found that the dark energy equation of state parameter w is not affected at all by the inclusion of IA. This can most certainly be explained by the fact that the other analyses use tomographic weak lensing, which is very sensible to the parameter w since it influences the growth function only weakly.

- In the spirit of physically modelling as best as possible the IA signal in order to maximise the inference of physical information therefrom, we investigated the chance of retrieving, in the future, the intrinsic ellipticity spectrum $C_E^e(\ell)$ in the case in which the weak lensing convergence spectrum $C_\kappa(\ell)$ can be predicted precisely enough. This basically corresponds to comparing the uncertainty of the convergence spectrum with the amplitudes of the ellipticity spectrum. This uncertainty is a propagation of the uncertainty on the cosmological parameters to the convergence power spectrum. Thus it can be made small when multiple independent priors for the parameters are used. We find that, by using EUCLID's BAO- and weak lensing spectra and from the temperature and polarisation spectra of the cosmic microwave background measured by PLANCK, it is possible to measure the intrinsic signal at high multipoles.

Important further steps can be made to improve this analysis. The first is to include tomography to check whether this, together with such a detailed physics description of the IA, would lead to significant biases also on the parameter w, thus recovering previous results. Another important consideration concerns the morphologies of the galaxies. It seems in fact essential to try to model the distribution of morphologies of the galaxies with redshift, in order to provide a weighted IA signal based on both linear and quadratic models accounting for late- and early type-galaxies. This must be considered mostly with tomographic surveys, since if there is a dependence of the morphology on redshift, then the intrinsic alignment signal must be weighted according to the redshift. A great improvement would also be obtained in shaping the GI alignments, which are the largest contamination to weak lensing. GI alignments arise in tomography when computing the cross-correlations between different redshift bins, and are non-vanishing just for the linear model. Thus knowing how to weight the contribution of linear and quadratic models to IA has a great influence on the resulting GI alignments.

Extreme Values: The study of extreme values represents a new and valuable tool offering many possible applications in cosmology. It appears to be preferable to common statistical analyses focusing on the central part of the distribution because its specific object of study are the tails of the distributions involved. In this sense Extreme Value Statistics (EVS) proves to be more appropriate when dealing with asymmetric and non-Gaussian distributions which derive from non-

linear processes. Our analysis aims to investigate the possibility that, by subdividing the sky in N patches of certain aperture, the extreme values of each patch collect into the two extreme values distributions which could be indicative of primordial non-Gaussianities amplitudes $f_{\rm NL}$ and $g_{\rm NL}$. This analysis can be summarised in the following basic points:

- Weak non-Gaussianities induced in the simplest case of local primordial non-Gaussianties are described via the Gram-Charlier distribution, which gives a perturbation to a Gaussian in terms of the Hermite polynomials. The amplitude of these perturbations are the third and fourth order cumulants, which are, in the case of primordial non-Gaussianities, the amplitudes $f_{\rm NL}$ and $g_{\rm NL}$. These can be calculated by means of integrations over the bi- and tri-spectra of the local primordial non-Gaussianty.

- We find a very precise agreement between the analytical expressions we calculate for the distributions of the extremes in the case of a Gram-Charlier distribution and the data we find by numerically sampling the maxima and minima from this parent distribution.

- We aimed to study the features of the distributions of the extreme values we obtain when we sample the sky in N independent patches of different apertures. Of course we expect these features, namely the mean, median and the most likely value to depend on this subdivision in the sky, and thus on the number of patches, or interchangeably the size of the patch. The number of independent samples was estimated by evaluating when the correlation function related to the convergence power spectrum would drop to a fraction of $\exp(-1)$ from its value at zero lag. We found that mean, median and the most likely value decrease with increasing smoothing scale.

- We found that the weak non-Gaussianity present in the parent distribution is reflected very well in the extreme distributions, which significantly depart from the ones one would obtain in the Gaussian case. We also recover the fact that, for a large number N of samplings, the extreme distributions tend to the Gumbel distribution.

- At last, we speculated over the possibility of setting constraints on the primordial non-Gaussianities amplitudes $f_{\rm NL}$ and $g_{\rm NL}$ by studying the single extreme values of the observed convergence in a weak lensing survey. Basically this corresponds to answering to the question of what is the probability that the single largest and lowest values of a data set are ascribable to a non-Gaussian parent distribution due to inflationary primordial non-Gaussianities rather than to a model with a Gaussian parent distribution. We find that the constraints set on the two parameters $f_{\rm NL}$ and $g_{\rm NL}$ are not as stringent as hoped, being of the order of 10^2 for the $f_{\rm NL}$ and of 10^5 for $g_{\rm NL}$.

Concluding, we emphasise once more the key role of weak lensing in offering a unique tool for extracting information on the mass distribution, but

also in offering a wide range of other possible applications aimed to investigate and deepen the still considerable (fortunately) amount of unanswered questions permeating our current understanding of the Universe.

APPENDIX A

.1 Smoothed convergence spectra

For completeness we show the angular spectrum $C_\kappa(\ell)$ of the weak lensing convergence in Fig. 10 with a Gaussian smoothing $W(\ell\theta)$ applied on a range of scales θ which cuts off contributions on smaller multipoles ℓ with increasing θ. From the smoothed spectrum we compute the smoothed convergence correlation functions $C_\kappa(\beta)$ by Fourier transform, and estimate in this way the correlation length of the convergence field κ. Furthermore, it gives the largest multipole ℓ for the numerical computation of the cumulants κ_3 and κ_4 needed at a given smoothing scale. Differences between spectra computed for linear and nonlinear CDM-spectra are small if θ is chosen large enough.

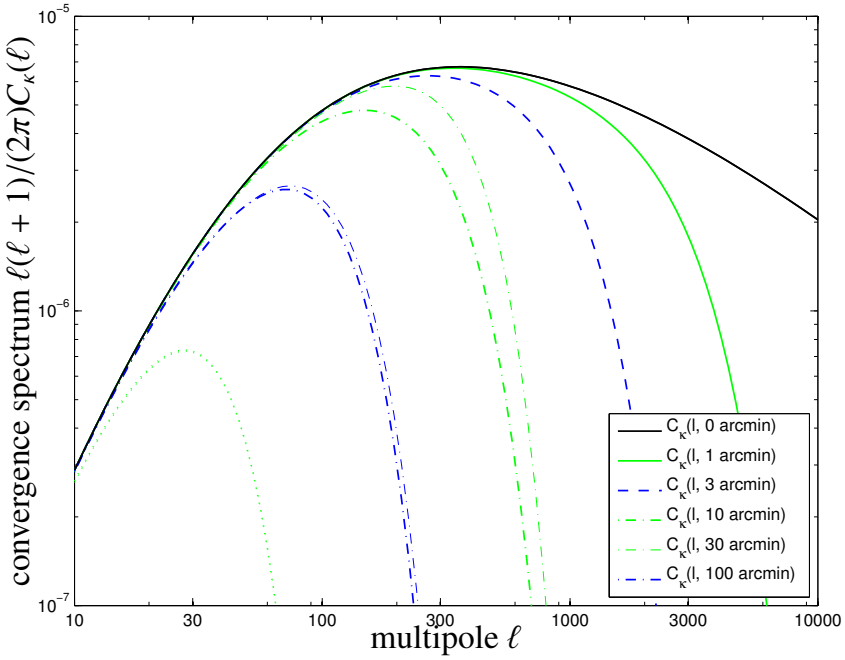

Figure 10: Angular convergence spectrum $C_\kappa(\ell)$ (black solid line) and with a Gaussian smoothing $W(\ell\theta)$ applied on a range of scales, $\theta = 1, 3, 10, 30, 100$ arcmin. The faint lines for $\theta = 10, 30, 100$ arcmin are derived with a nonlinear CDM spectrum, whereas the thick lines are computed with a linear CDM-spectrum.

Bibliography

Abramowitz M., Stegun I. A., 1972a, Handbook of Mathematical Functions

Abramowitz M., Stegun I. A., 1972b, Handbook of Mathematical Functions. Handbook of Mathematical Functions, New York: Dover, 1972

Acquaviva V., Bartolo N., Matarrese S., Riotto A., 2003, Nuclear Physics B, 667, 119

Albrecht A., Steinhardt P. J., 1982, Physical Review Letters, 48, 1220

Allen T. J., Grinstein B., Wise M. B., 1987, Physics Letters B, 197, 66

Amara A., Kitching T. D., 2011, MNRAS, 413, 1505

Amara A., Réfrégier A., 2007, MNRAS, 381, 1018

Amara A., Réfrégier A., 2008, MNRAS, 391, 228

Amendola L. et al., 2012, ArXiv e-prints 1206.1225

Aragón-Calvo M. A., van de Weygaert R., Jones B. J. T., van der Hulst J. M., 2007, ApJL, 655, L5

Arfken G. B., Weber H. J., 2005, Mathematical methods for physicists 6th ed.

Babich D., Creminelli P., Zaldarriaga M., 2004, JCAP, 8, 9

Bacon D. J., Refregier A. R., Ellis R. S., 2000, MNRAS, 318, 625

Bailin J. et al., 2005, ApJL, 627, L17

Bailin J., Steinmetz M., 2005, ApJ, 627, 647

Baldi M., Pettorino V., 2011, MNRAS, 412, L1

Bardeen J. M., 1980, Phys. Rev. D, 22, 1882

Bardeen J. M., Bond J. R., Kaiser N., Szalay A. S., 1986, ApJ, 304, 15

Bardeen J. M., Steinhardt P. J., Turner M. S., 1983a, Phys. Rev. D, 28, 679

Bardeen J. M., Steinhardt P. J., Turner M. S., 1983b, Phys. Rev. D, 28, 679

Barnes J., Efstathiou G., 1987, ApJ, 319, 575

Bartelmann M., 2010a, ArXiv e-prints

Bartelmann M., 2010b, Classical and Quantum Gravity, 27, 233001

Bartelmann M., Schneider P., 2001, Physics Reports, 340, 291

Bartolo N., Komatsu E., Matarrese S., Riotto A., 2004, Physics Reports, 402, 103

Beirlant J., Goegebeur Y., Segers J., Teugels J., De Waal D., Ferro C., 2004, Statistics of Extremes: Theory and Applications. Wiley Series in Probability and Statistics, John Wiley & Sons

Bernardeau F., Colombi S., Gaztañaga E., Scoccimarro R., 2002a, Physics Reports, 367, 1

Bernardeau F., Colombi S., Gaztañaga E., Scoccimarro R., 2002b, Physics Reports, 367, 1

Bernstein G. M., 2009, ApJ, 695, 652

Bertin E., Clusel M., 2006, Journal of Physics A Mathematical General, 39, 7607

Binney J., 1978, MNRAS, 183, 501

Binney J., Tremaine S., 2008, Galactic Dynamics: Second Edition. Princeton University Press

Blandford R. D., Saust A. B., Brainerd T. G., Villumsen J. V., 1991, MNRAS, 251, 600

Bonnet H., Mellier Y., 1995, A&A, 303, 331

Bouchet F. R., 1996, in Bonometto S., Primack J. R., Provenzale A., eds, Dark Matter in the Universe. p. 565

Bouchet F. R., Juszkiewicz R., Colombi S., Pellat R., 1992, ApJL, 394, L5

Bridle S., King L., 2007, New Journal of Physics, 9, 444

Brown M. L., Taylor A. N., Hambly N. C., Dye S., 2002, MNRAS, 333, 501

Brunino R., Trujillo I., Pearce F. R., Thomas P. A., 2007, MNRAS, 375, 184

Bryan S. E., Kay S. T., Duffy A. R., Schaye J., Dalla Vecchia C., Booth C. M., 2012, ArXiv e-prints 1207.4555

Buchalter A., Jimenez R., Kamionkowski M., 2001, MNRAS, 322, 43

Buchert T., 1994, MNRAS, 267, 811

Buchert T., 1996, in Bonometto S., Primack J. R., Provenzale A., eds, Dark Matter in the Universe. pp 543–564

Bullock J. S., Kolatt T. S., Sigad Y., Somerville R. S., Kravtsov A. V., Klypin A. A., Primack J. R., Dekel A., 2001, MNRAS, 321, 559

Burkert A., 2009, in Jogee S., Marinova I., Hao L., Blanc G. A., eds, Astronomical Society of the Pacific Conference Series Vol. 419, Galaxy Evolution: Emerging Insights and Future Challenges. p. 3

Burles S., Nollett K. M., Turner M. S., 1999, ArXiv Astrophysics e-prints

Cabré A., Fosalba P., Gaztañaga E., Manera M., 2007, MNRAS, 381, 1347

Capranico F., Fotios Kalovidouris A., Schaefer B. M., 2013, ArXiv e-prints

Capranico F., Merkel P., Schaefer B. M., 2012, ArXiv e-prints

Carroll S. M., Press W. H., Turner E. L., 1992, ARA&A, 30, 499

Catelan P., 1995, MNRAS, 276, 115

Catelan P., Kamionkowski M., Blandford R. D., 2001, MNRAS, 320, L7

Catelan P., Porciani C., 2001, MNRAS, 323, 713

Catelan P., Theuns T., 1996a, MNRAS, 282, 436

Catelan P., Theuns T., 1996b, MNRAS, 282, 455

Catelan P., Theuns T., 1997, MNRAS, 292, 225

Cayón L., Gordon C., Silk J., 2011, MNRAS, 415, 849

Chen X., 2010, Advances in Astronomy, 2010

Chongchitnan S., Silk J., 2012, Phys. Rev. D, 85, 063508

Codis S., Pichon C., Devriendt J., Slyz A., Pogosyan D., Dubois Y., Sousbie T., 2012, ArXiv e-prints 1201.5794

Coles P., 1988, MNRAS, 234, 509

Coles P., 2002, in Metcalfe N., Shanks T., eds, Astronomical Society of the Pacific Conference Series Vol. 283, A New Era in Cosmology. p. 56

Coles P., Lucchin F., 2002, Cosmology: The Origin and Evolution of Cosmic Structure, Second Edition

Colless M. et al., 2001, MNRAS, 328, 1039

Colombi S., 1994, ApJ, 435, 536

Colombi S., Davis O., Devriendt J., Prunet S., Silk J., 2011, MNRAS, 414, 2436

Cooray A., Hu W., 2002, ApJ, 574, 19

Creminelli P., 2003, JCAP, 10, 3

Creminelli P., Nicolis A., Senatore L., Tegmark M., Zaldarriaga M., 2006, JCAP, 5, 4

Creminelli P., Zaldarriaga M., 2004, JCAP, 10, 6

Crittenden R. G., Natarajan P., Pen U., Theuns T., 2001, ApJ, 559, 552

Crittenden R. G., Natarajan P., Pen U., Theuns T., 2002, ApJ, 568, 20

Croft R. A. C., Metzler C. A., 2000, ApJ, 545, 561

Cruz M., Cayón L., Martínez-González E., Vielva P., Jin J., 2007, ApJ, 655, 11

Cruz M., Martínez-González E., Vielva P., Cayón L., 2005, MNRAS, 356, 29

Dalcanton J. J., Spergel D. N., Summers F. J., 1997, ApJ, 482, 659

Davies R. L., Efstathiou G., Fall S. M., Illingworth G., Schechter P. L., 1983, ApJ, 266, 41

Davis O., Devriendt J., Colombi S., Silk J., Pichon C., 2011, MNRAS, 413, 2087

Desjacques V., Seljak U., 2010a, Classical and Quantum Gravity, 27, 124011

Desjacques V., Seljak U., 2010b, Phys. Rev. D, 81, 023006

Dodelson S., 2003, Modern cosmology

D'Onghia E., 2008, in Bureau M., Athanassoula E., Barbuy B., eds, IAU Symposium Vol. 245, IAU Symposium. pp 51–54

D'Onghia E., Navarro J. F., 2007, MNRAS, 380, L58

Doroshkevich A. G., 1970, Astrofizika, 6, 581

Dubinski J., 1992, ApJ, 401, 441

Durand D., Greenwood J. A., 1957, Ann. Math. Statist., 28, 978

Efstathiou G., Jones B. J. T., 1979, MNRAS, 186, 133

Efstathiou G., Silk J., 1983, Fundamental Cosmic Physics, 9, 1

Einstein A., 1916, Annalen der Physik, 354, 769

Embrechts P. Klüppelberg C. M. T., 1997, Springer-Verlag

Embrechts P. S. H., 1994, Mathematical Methods of Operations Research, 39

Enqvist K., Hotchkiss S., Taanila O., 2011, JCAP, 4, 17

Falk T., Rangarajan R., Srednicki M., 1992, Phys. Rev. D, 46, 4232

Fall S. M., Efstathiou G., 1980, MNRAS, 193, 189

Fedeli C., Carbone C., Moscardini L., Cimatti A., 2011, MNRAS, 414, 1545

Fisher R. A., Tippett L. H. C., 1928, Proceedings of the Cambridge Philosophical Society, 24, 180

Fréchet M., 1927, Ann. Soc. Polon. Math., 6

Fu L., Kilbinger M., 2010, MNRAS, 401, 1264

Gamow G., 1952, Phys. Rev., 86, 251

Gangui A., 1994, Phys. Rev. D, 50, 3684

Gangui A., Lucchin F., Matarrese S., Mollerach S., 1994, ApJ, 430, 447

Gangui A., Martin J., Sakellariadou M., 2002, Phys. Rev. D, 66, 083502

Giahi-Saravani A., Schäfer B. M., 2012, ArXiv e-prints 1202.1196

Gnedenko B., 1943, Ann. Math., 44

Governato F., Mayer L., Brook C., 2008, in Funes J. G., Corsini E. M., eds, Astronomical Society of the Pacific Conference Series Vol. 396, Formation and Evolution of Galaxy Disks. p. 453

Governato F. et al., 2004, ApJ, 607, 688

Governato F., Willman B., Mayer L., Brooks A., Stinson G., Valenzuela O., Wadsley J., Quinn T., 2007, MNRAS, 374, 1479

Greenwood J. A., Durand D., 1955, Ann. Math. Statist., 26, 233

Gumbel E., 1954, Statistical theory of extreme values and some practical applications: a series of lectures. Applied mathematics series, U. S. Govt. Print. Office

Gumbel E., 2004, Statistics of Extremes. Dover Books on Mathematics Series, Dover Publ.

Guth A. H., 1981a, Phys. Rev. D, 23, 347

Guth A. H., 1981b, Phys. Rev. D, 23, 347

Hahn O., Porciani C., Carollo C. M., Dekel A., 2007, MNRAS, 375, 489

Hahn T., 2005, Computer Physics Communications, 168, 78

Hannestad S., Tu H., Wong Y. Y., 2006, JCAP, 6, 25

Heavens A., Peacock J., 1988, MNRAS, 232, 339

Heavens A., Refregier A., Heymans C., 2000, MNRAS, 319, 649

Heitmann K., Higdon D., White M., Habib S., Williams B. J., Lawrence E., Wagner C., 2009, ApJ, 705, 156

Heitmann K., White M., Wagner C., Habib S., Higdon D., 2010, ApJ, 715, 104

Heymans C. et al., 2013, ArXiv e-prints

Heymans C., Heavens A., 2003, MNRAS, 339, 711

Hirata C. M., Mandelbaum R., Ishak M., Seljak U., Nichol R., Pimbblet K. A., Ross N. P., Wake D., 2007, MNRAS, 381, 1197

Hirata C. M., Seljak U., 2004, Phys. Rev. D, 70, 063526

Hoekstra H., Jain B., 2008, Annual Review of Nuclear and Particle Science, 58, 99

Holz D. E., Perlmutter S., 2012, ApJL, 755, L36

Hotchkiss S., 2011, JCAP, 7, 4

Hou Z., Banday A. J., Górski K. M., 2009, MNRAS, 396, 1273

Hoyle F., 1949, MNRAS, 109, 365

Hu W., 1999, ApJL, 522, L21

Hu W., 2002a, Phys. Rev. D, 66, 083515

Hu W., 2002b, Phys. Rev. D, 65, 023003

Hu W., Jain B., 2004, Phys. Rev. D, 70, 043009

Hu W., Tegmark M., 1999, ApJL, 514, L65

Hu W., White M., 2001, ApJ, 554, 67

Hubble E., 1929, Proceedings of the National Academy of Science, 15, 168

Huterer D., 2002, Phys. Rev. D, 65, 063001

Huterer D., 2010, General Relativity and Gravitation, 42, 2177

Huterer D., Turner M. S., 2001, Phys. Rev. D, 64, 123527

Jain B., Seljak U., 1997, ApJ, 484, 560

Jee M. J. et al., 2009, ApJ, 704, 672

Jeong D., Schmidt F., Sefusatti E., 2011a, Phys. Rev. D, 83, 123005

Jeong D., Schmidt F., Sefusatti E., 2011b, Phys. Rev. D, 83, 123005

Jing Y. P., 2002, MNRAS, 335, L89

Joachimi B., Bridle S. L., 2010, A&A, 523, A1

Joachimi B., Mandelbaum R., Abdalla F. B., Bridle S. L., 2011, A&A, 527, A26

Joachimi B., Schneider P., 2008, A&A, 488, 829

Joachimi B., Schneider P., 2009, A&A, 507, 105

Joachimi B., Schneider P., 2010, A&A, 517, A4

Joachimi B., Semboloni E., Bett P. E., Hartlap J., Hilbert S., Hoekstra H., Schneider P., Schrabback T., 2012, ArXiv e-prints 1203.6833

Juszkiewicz R., Weinberg D. H., Amsterdamski P., Chodorowski M., Bouchet F., 1995, ApJ, 442, 39

Kaiser N., 1992, ApJ, 388, 272

Kaiser N., 1998, ApJ, 498, 26

Kaiser N., Wilson G., Luppino G. A., 2000, ArXiv e-prints 000338

Kamionkowski M., Babul A., Cress C. M., Refregier A., 1998, MNRAS, 301, 1064

Kimm T., Devriendt J., Slyz A., Pichon C., Kassin S. A., Dubois Y., 2011, ArXiv e-prints 1106.0538

King L., Schneider P., 2002, A&A, 396, 411

King L. J., 2005, A&A, 441, 47

King L. J., Schneider P., 2003, A&A, 398, 23

Kirk D., Bridle S., Schneider M., 2010, MNRAS, 408, 1502

Kirk D., Laszlo I., Bridle S., Bean R., 2011, ArXiv e-prints 1109.4536

Kirk D., Rassat A., Host O., Bridle S., 2012, MNRAS, p. 3339

Kitching T. D., Taylor A. N., Heavens A. F., 2008, MNRAS, 389, 173

Komatsu E., 2010, Classical and Quantum Gravity, 27, 124010

Komatsu E. et al., 2011, ApJS, 192, 18

Komatsu E., Spergel D. N., 2001a, Phys. Rev. D, 63, 063002

Komatsu E., Spergel D. N., 2001b, Phys. Rev. D, 63, 063002

Komatsu E., Spergel D. N., Wandelt B. D., 2005, ApJ, 634, 14

Kunz M., 2012, ArXiv e-prints 1204.5482

Langlois D., 2011, Progress of Theoretical Physics Supplement, 190, 90

Larson D. et al., 2011, ApJS, 192, 16

Larson D. L., Wandelt B. D., 2005, ArXiv Astrophysics e-prints

Larson R. B., 1969, MNRAS, 145, 405

Larson R. B., 1974, MNRAS, 166, 585

Larson R. B., 1975, MNRAS, 173, 671

Larson R. B., Tinsley B. M., 1974, ApJ, 192, 293

Laszlo I., Bean R., Kirk D., Bridle S., 2012, MNRAS, 423, 1750

Lawrence E., Heitmann K., White M., Higdon D., Wagner C., Habib S., Williams B., 2010, ApJ, 713, 1322

Lee J., 2010, ArXiv e-prints

Lee J., 2013, ArXiv e-prints

Lee J., Pen U., 2000, ApJL, 532, L5

Lee J., Pen U., 2001, ApJ, 555, 106

Lee J., Pen U., 2008, ApJ, 681, 798

Lee J., Pen U.-L., 2007, ApJL, 670, L1

Lemaître G., 1927, Annales de la Societe Scietifique de Bruxelles, 47, 49

Lemson G., Kauffmann G., 1999, MNRAS, 302, 111

Lesgourgues J., 2013, ArXiv e-prints 1302.4640

Lesgourgues J., Polarski D., Starobinsky A. A., 1997, Nuclear Physics B, 497, 479

Libeskind N. I., Hoffman Y., Knebe A., Steinmetz M., Gottlöber S., Metuki O., Yepes G., 2012, MNRAS, 421, L137

Libeskind N. I., Hoffman Y., Steinmetz M., Gottlöber S., Knebe A., Hess S., 2013, ApJL, 766, L15

Limber D. N., 1954, ApJ, 119, 655

Linde A., Mukhanov V., 1997, Phys. Rev. D, 56, 535

Linde A. D., 1982, Physics Letters B, 108, 389

Linder E. V., Jenkins A., 2003, MNRAS, 346, 573

Lynden-Bell D., 1967, MNRAS, 136, 101

Lyth D. H., Wands D., 2002, Physics Letters B, 524, 5

Mackey J., White M., Kamionkowski M., 2002, MNRAS, 332, 788

Maldacena J., 2003, Journal of High Energy Physics, 5, 13

Mandelbaum R. et al., 2011, MNRAS, 410, 844

Mandelbaum R., Hirata C. M., Ishak M., Seljak U., Brinkmann J., 2006, MNRAS, 367, 611

March M. C., Trotta R., Amendola L., Huterer D., 2011, MNRAS, pp 612–+

Marian L., Hilbert S., Smith R. E., Schneider P., Desjacques V., 2011, ApJL, 728, L13

Martin J., Ringeval C., Vennin V., 2013, ArXiv e-prints 1303.3787

Martinez-Gonzalez E., Sanz J. L., 1989, MNRAS, 237, 939

Mayer L., Governato F., Kaufmann T., 2008, Advanced Science Letters, 1, 7

Mellier Y., 1999, ARA&A, 37, 127

Meza A., Navarro J. F., Steinmetz M., Eke V. R., 2003, ApJ, 590, 619

Mikelsons G., Silk J., Zuntz J., 2009, MNRAS, 400, 898

Misner C. W., Thorne K. S., Wheeler J. A., 1973, Gravitation

Mo H. J., Mao S., White S. D. M., 1998, MNRAS, 295, 319

Mollerach S., 1990, Phys. Rev. D, 42, 313

Mortonson M. J., Hu W., Huterer D., 2011, Phys. Rev. D, 83, 023015

Mukhanov V., Winitzki S., 2007, Introduction to Quantum Effects in Gravity

Navarro J. F., Abadi M. G., Steinmetz M., 2004, ApJL, 613, L41

Okamoto T., Hu W., 2002, Phys. Rev. D, 66, 063008

Patiri S. G., Prada F., Holtzman J., Klypin A., Betancort-Rijo J., 2006, MNRAS, 372, 1710

Peebles P. J. E., 1967, ApJ, 147, 859

Peebles P. J. E., 1969, ApJ, 155, 393

Peebles P. J. E., 1971a, Physical cosmology

Peebles P. J. E., 1971b, A&A, 11, 377

Perlmutter S. et al., 1999, ApJ, 517, 565

Pichon C., Gay C., Pogosyan D., Prunet S., Sousbie T., Colombi S., Slyz A., Devriendt J., 2010, in Alimi J.-M., Fuözfa A., eds, American Institute of Physics Conference Series Vol. 1241, American Institute of Physics Conference Series. pp 1108–1117

Planck Collaboration et al., 2013a, ArXiv e-prints

Planck Collaboration et al., 2013e, ArXiv e-prints 1303.5076

Planck Collaboration et al., 2013c, ArXiv e-prints 1303.5082

Planck Collaboration et al., 2013b, ArXiv e-prints

Planck Collaboration et al., 2013d, ArXiv e-prints 1303.5084

Porciani C., Dekel A., Hoffman Y., 2002a, MNRAS, 332, 325

Porciani C., Dekel A., Hoffman Y., 2002b, MNRAS, 332, 339

Press W. H., Schechter P., 1974, ApJ, 187, 425

Redlich M., Bartelmann M., Waizmann J.-C., Fedeli C., 2012, A&A, 547, A66

Refregier A., 2003, ARA&A, 41, 645

Refregier A., 2009, Experimental Astronomy, 23, 17

Riess A. G. et al., 1998, Astronomical Journal, 116, 1009

Rindler W., 1956, MNRAS, 116, 662

Riotto A., 2002, ArXiv High Energy Physics - Phenomenology e-prints

Romanowsky A. J., Fall S. M., 2012, ArXiv e-prints 1207.4189

Sachs R. K., Wolfe A. M., 1967, ApJ, 147, 73

Scannapieco C., Tissera P. B., White S. D. M., Springel V., 2008, MNRAS, 389, 1137

Schäfer B. M., 2009, International Journal of Modern Physics D, 18, 173

Schäfer B. M., Grassi A., Gerstenlauer M., Byrnes C. T., 2012a, MNRAS, 421, 797

Schäfer B. M., Grassi A., Gerstenlauer M., Byrnes C. T., 2012b, MNRAS, 421, 797

Schäfer B. M., Heisenberg L., 2012, MNRAS, p. 3168

Schäfer B. M., Heisenberg L., Kalovidouris A. F., Bacon D. J., 2012, MNRAS, 420, 455

Schäfer B. M., Merkel P. M., 2012, MNRAS, 421, 2751

Schneider P., 1996, MNRAS, 283, 837

Schneider P., Ehlers J., Falco E. E., 1992, Gravitational Lenses

Schneider P., Kilbinger M., 2007, A&A, 462, 841

Schneider P., van Waerbeke L., Mellier Y., 2002, A&A, 389, 729

Sciama D. W., 1955, MNRAS, 115, 3

Seitz C., Schneider P., 1997, A&A, 318, 687

Seitz S., Schneider P., 1994, A&A, 287, 349

Seitz S., Schneider P., Ehlers J., 1994, Classical and Quantum Gravity, 11, 2345

Senatore L., Smith K. M., Zaldarriaga M., 2010, JCAP, 1, 28

Shapiro C., Cooray A., 2006, Journal of Cosmology and Astro-Particle Physics, 3, 7

Slipher V. M., 1917, Proceedings of the American Philosophical Society, 56, 403

Smail I., Hogg D. W., Blandford R., Cohen J. G., Edge A. C., Djorgovski S. G., 1995, MNRAS, 277, 1

Smidt J., Amblard A., Byrnes C. T., Cooray A., Heavens A., Munshi D., 2010, Phys. Rev. D, 81, 123007

Smith R. E. et al., 2003, MNRAS, 341, 1311

Sousbie T., Colombi S., Pichon C., 2009, MNRAS, 393, 457

Sousbie T., Pichon C., Colombi S., Novikov D., Pogosyan D., 2008, MNRAS, 383, 1655

Starobinskiĭ A. A., 1979, Soviet Journal of Experimental and Theoretical Physics Letters, 30, 682

Starobinsky A. A., 1982a, Physics Letters B, 117, 175

Starobinsky A. A., 1982b, Physics Letters B, 117, 175

Stebbins A., 1996, ArXiv Astrophysics e-prints

Steinmetz M., Bartelmann M., 1995, MNRAS, 272, 570

Steinmetz M., Navarro J. F., 2002, New Astronomy, 7, 155

Sugerman B., Summers F. J., Kamionkowski M., 2000, MNRAS, 311, 762

Sugiyama N., 1995, ApJS, 100, 281

Taburet N., Aghanim N., Douspis M., Langer M., 2009, MNRAS, 392, 1153

Taburet N., Douspis M., Aghanim N., 2010, MNRAS, 404, 1197

Takada M., Jain B., 2004, MNRAS, 348, 897

Takada M., White M., 2004, ApJL, 601, L1

Tegmark M., Taylor A. N., Heavens A. F., 1997, ApJ, 480, 22

Toomre A., 1977, in Tinsley B. M., Larson D. Campbell R. B. G., eds, Evolution of Galaxies and Stellar Populations. p. 401

Toomre A., Toomre J., 1972, ApJ, 178, 623

Turner M. S., White M., 1997, Phys. Rev. D, 56, 4439

van den Bosch F. C., Abel T., Croft R. A. C., Hernquist L., White S. D. M., 2002, ApJ, 576, 21

Van Waerbeke L. et al., 2000, A&A, 358, 30

Verde L., Wang L., Heavens A. F., Kamionkowski M., 2000a, MNRAS, 313, 141

Verde L., Wang L., Heavens A. F., Kamionkowski M., 2000b, MNRAS, 313, 141

Vielva P., 2010, Advances in Astronomy, 2010

Vielva P., Sanz J. L., 2010, MNRAS, 404, 895

Vitvitska M., Klypin A. A., Kravtsov A. V., Wechsler R. H., Primack J. R., Bullock J. S., 2002, ApJ, 581, 799

von Weizsäcker C. F., 1951, ApJ, 114, 165

Waizmann J.-C., Ettori S., Moscardini L., 2011, MNRAS, 418, 456

Waizmann J.-C., Ettori S., Moscardini L., 2012a, MNRAS, 420, 1754

Waizmann J.-C., Ettori S., Moscardini L., 2012b, MNRAS, 422, 3554

Waizmann J.-C., Redlich M., Bartelmann M., 2012, A&A, 547, A67

Wallace D. L., 1958, Annals of Mathematical Statistics, 29, 635

Wang L., Steinhardt P. J., 1998, ApJ, 508, 483

Wang Y., 2013, ArXiv e-prints

Warren M. S., Quinn P. J., Salmon J. K., Zurek W. H., 1992, ApJ, 399, 405

Weinberg S., 1972, Gravitation and Cosmology: Principles and Applications of the General Theory of Relativity

White S. D. M., 1984, ApJ, 286, 38

Wick G. C., 1950, Phys. Rev., 80, 268

Wittman D. M., Tyson J. A., Kirkman D., Dell'Antonio I., Bernstein G., 2000, Nature, 405, 143

Wolz L., Kilbinger M., Weller J., Giannantonio T., 2012, ArXiv e-prints 1205.3984

Zavala J., Okamoto T., Frenk C. S., 2008, MNRAS, 387, 364

Zitrin A., Broadhurst T., Rephaeli Y., Sadeh S., 2009, ApJL, 707, L102

Acknowledgements

"Every beginning
is but a continuation,
and the book of events
is never more than half open."

Wislawa Szymborska

We eventually always come to this point, where we need to take stock of the situation of ending something we started. At the end of this PhD, indeed there are people I want to thank. So here it goes.

First and foremost I feel to thank you, Björn: I owe you among everything what I have learnt and the privilege of being here. Thank you even more for your silent understanding, your support, your kindness. Thank you, Matthias, for the enthusiasm you remind us being the ground of any valuable achievement.

I would like to thank Prof. Luca Amendola for having accepted to be my second referee at the very last moment, and the other members of my commission, Prof. Kellerbauer and Prof. Eva Grebel, whom I also especially thank, together with Prof. Wambsganss, for having hosted our group in ARI for the majority of our time here. A special thank goes to whom made the bureaucracy much less cumbersome: Saskia Mayer, Hildrun Pisch, Diana Schwalbe and Anna Zacheus, for being so kind and available for any question or problem.

ARI has been my first "house", so I will start from here. Frederik, thanks for having been a constant presence in the time spent in ARI since my very beginning: thanks for the fruitful exchanges of ideas and for having dedicated part of your time in teaching me photography. I know nowadays how valuable being taught is, mostly when passion is involved. Anna and Emanuela, my italian ARI creek, thank you. Anna, your support made of experience and understanding was precious as much as our funny chats. Emanuela, I appreciate so much your sarcasm and bluntness! Thanks Jan for the beautiful breakfasts in ARI you so persistently organised. Raoul, thanks to you too for the many nice short visits you made by dropping by at our office. You have been one of the first friendly faces I have met there.

To the people I now share my working place with, and mostly to Christian, Alex, Matthias, Felix, Tim, Korbinian, Matteo, Luigi: thanks for sharing enjoyable lunches together and for your kind attempt (unfortunately not so fruitful) of making me take breaks in this last period. I would also like to thank Francesco, who is always part of ITA in my mind. I am really grateful to you for your helpfulness and availability during the GR tutoring: I learnt so much!

Of course - how could I possibly not mention him - thank you Angelos, for nobody, but really *nobody* is like you are. Sharing the office with you has been an exceptional experience, which I certainly know I will always look back to with a smile.

I cannot avoid putting in this list the Bar Centrale members. I have been introduced to Bar Centrale sessions late and I regret I haven't started earlier! You guys have been an important and extremely delightful light motif over these last years. Ana, I feel to say I am so happy for you! I am glad we had the chance to know each other better. We eventually shared much more than just Friday evenings and some typical working frustrations. Emanuel, you have been a slow discovery, one I really am happy I had the chance to make. Benoît, a special thought goes to you, and the strength, braveness and sweetness I had the luck to experience. Smirnov! I really am glad I met you. Thanks for our proficous tandem, and for being always so gentle and caring: I really know few people who can be as much as you are. Wise Adi: you have moulded Bar-Centrale's meetings as only you could have done: with lightness and tremendous aggregation spirit. I truly had a great time with you.

Dear Agnese, your sweetness, calmness and curiosity in front of life, of differences, are inspiring. Hold on to them, and remember: always hold on to yourself and your capabilities. Iva, you're the latest entry in my life but I feel I know you from so much longer than that. Eleonora, we have walked at the same pace since the very beginning, and what a long way since then! I witnessed many changes in your life, and I think this is always a blessing for a friendship. The laughters with you, Jc, in the Hauptstrasse in the December of my first year here are memorable, and still indeed in the top-ten-list of the best laughters of my life. Laughing with someone so heartily is something one (and mostly me) can never forget. I hope for many more to come.

Going back to the older creek, I feel to thank Giovanni for our conversations which, as we know, are either absolutely trivial or extremely deep. And, most of all, thanks for sharing with me your quest for composing a "canzone-pop-di-successo". I am sure you will succeed! Olga, it has been nice to spend time with you and learn how far one can get with grit and endurance.
Massimo: you are upright in front of life, and you go about it with your head held high. I admire this, and I am mostly glad I had the chance to know also the very tender part you undoubtably have. I am deeply grateful for your presence, balance and support, which have really made the difference sometimes. Denija...what could I say to you? I feel your presence, your words, but most importantly the silences you have been able to alternate in-between have been pre-

cious to me. Thank you for having weighted so well these ingredients in delicate moments, and for taking part to my joys as much as my sorrows.

With you, Gisella, I have walked together slowly and persistently and I am proud we can witness today how life eventually puts everything into place. I bring you with me since a long time now, Viviana and Sara, and life has brought us on very similar paths throughout time. We have been able to build new memories on old hurtful ones, and I feel to thank you both for all the long chats, drinks at P11, confessions and intense moments we shared: I really felt with you a sense of belonging which we all yearn for. But no good life is really good without having fun, and I do have beautiful memories of this too, like fighting against mosquitos at 5 in the morning, or meeting every wednesday for our usual, necessary and delightful "cochina".

Melania, we met almost by chance, but eventually tightened this bond. You are a solid rock and I admire your persistence and determination. Thanks for spending time together and for talking about books, movies, and life experiences.

I would like to thank you, Johanna, for sharing with me not only a flat. I am very proud of our neighbours saying how loud we could be able to get by laughing sometimes (!), and of how cozy we managed to make our flat since the very fist moment. Valentina, thanks also to you for being my flatmate as well. Although it was not for a long time, it has been a precious and very nice one.

I would like now to also thank people who were not physically here, but managed to be close to me in all these years, contrasting an unfortunate distance. Marco, Simona, Stefano, Lara, Grazia, Emanuele and Alessandro: grazie semplicemente per essere i buoni amici che siete, perché essere capaci di stare vicini con costanza pur essendo lontani non è comune abilità! Isa, porto sempre con me l'esempio del tuo dinamismo, apertura e curiosità. Grazie per essere stata la prima ad atterrare sui suoli tedeschi per venire a visitarmi! Cecilia, mi riesce quasi incredibile pensare che sono ben trent'anni che ci conosciamo. E nonostante le rotte diverse ed i differenti orizzonti che ci si sono parati di fronte, ci siamo tenute vicino, considerandoci l'una sicuro e costante approdo per l'altra. Sono fiera di noi. Paolo, nuovi ricordi si accumulano sui tanti più vecchi anche con te! È stato bello, in questi anni, poter fuggire di tanto in tanto e venirti a trovare, e sono sempre stata accolta dal caldo ambiente di casa che tu sai così bene creare. Quanto spero che possa sempre essere così. Federica I.: i grandi dolori della vita ci scavano in profondità, ma creano uno spazio in noi che può essere nuovamente colmato. Sento di essere stata, con estrema gioia, parte attiva nell'aver contribuito a riempire almeno un poco di quello spazio. Grazie soprattutto per avermelo concesso. Federica F., è sempre estremamente ricco e fruttuoso quel che condivido con te. Francesca, quante novità nella tua vita! Grazie per essere venuta a trovarmi qui, è un ricordo che caramente porterò con me. Giovi: certamente non puoi mancare tu in questa lista. Quante cose sono cambiate, eppure quante son rimaste immutate ed intonse. Sei un constante specchio di fronte a me capace di vedermi ed accettarmi. Grazie!

Un grazie incondizionato va alla mia famiglia per il sostegno, la presenza e la cura che mi hanno dedicato nel tempo. La tenacia, la voglia di fare, di sperimentare, di lottare, di fallire e di riuscire le ho apprese da voi tutti. Prenderebbe molto più che un paragrafo ringraziarvi tutti, ma soprattutto sento necessario ringraziare mia madre, per avermi infuso coraggio ogni volta che ho tremato, ho temuto, che mi sono bloccata: non posso ringraziarti abbastanza per aver davvero sempre creduto in me. Ringrazio mio padre, perchè i migliori ricordi assieme si trovano proprio in mezzo a questi duri anni, e sono soprattutto tutte le belle, lunghe e leggere conversazioni che, in mezzo al trambusto, ai problemi, alle sofferenze ed i timori, abbiamo avuto la capacità di ricreare ogni volta. Pur non avendole registrate, le porto con me. Stefano, quanto coraggio ho potuto ammirare in come hai condotto la tua vita in questi ultimi anni, e quanta forza e umiltà nell'andare avanti, passo dopo passo, anche quando la fatica ti ha stremato. Grazie per esserti occupato e preoccupato dei molti ed onerosi problemi lungo questo cammino. Sono soprattutto felice, oggi, di poter nuovamente condividere con te. Andrea, le nostre lunghe conversazioni al telefono, mentre passeggiavo nel giardino del mio ufficio, su tutto - dal lavoro ai progetti futuri alla filosofia ai problemi del quotidiano ai commenti sui tuoi lavori. Mi rende felice averti riscoperto, aver toccar con mano quanto le nostre visioni del mondo spesso coincidano. E tutto senza esserlo mai detto prima.

Grazie anche a mia nonna, a nonna Adele, a mia zia Ida, a Domenico, ed alle piccole creature che mi hanno accompagnata nel lungo viaggio dall'infanzia fino ad oggi. Quello che potrò sempre fare è tenere viva la vostra memoria.

Finally, I would like to thank the two who shaped, in such many different ways, great part of the time and my stay here in Heidelberg. Alessandra, I think no words can really express how much in debt I feel with life for having put you in the place right next to mine in these long, intense and beautiful years. You have seen the worse, you have seen the best. I know for myself I want to keep you in that place.
Baybars thanks, for true bonds survive space and time. Ve en önemlisi, cheers!

Heidelberg, July 2013